Investigating the Therapeutic Potential of Adult Mouse Cerebellum derived Neural Stem Cells and the Morphological Characterisation of Extracellular Vesicles



UNITED KINGDOM · CHINA · MALAYSIA

Zubair Ahmed Nizamudeen MSc, BSc

School of Medicine

Division of Cancer and Stem Cells

Thesis submitted to The University of Nottingham for the degree of

Doctor of Philosophy

April 2019

Acknowledgments

All praise to Allah, the most gracious, the most merciful, and the all-knowing. I would like to thank my family and friends for their support throughout my research. Particularly, I would like to thank my father Mr Nizamudeen NSA, for funding my tuition fee and providing financial support throughout my PhD course.

I would like to thank my supervisors Dr Virginie Sottile and Dr Lisa Chakrabarti for their constant encouragement and guidance during my PhD.

I would like to thank my colleagues and collaborators from mine and neighbouring labs for their training, help and support while facing challenging research questions. To name a few, not limited to, Nigel M, Anaid L, Ashley R, Katherine P, Maria E, Abdul A, Emma C, Nguyen T N Vo, Ana T, Jordan T, Rachael X, Kiran S, Kiran M, Maria B, Jayson B, Paula O, Dr Sarah M, Dr Alexander K, Dr Lara L, Dr Laura M, Dr Sara P, Dr Diogo M, Dr Jamie B, Dr Ksenija V, Dr Amal S, Dr Shelanah S, Dr Azaz A, Dr James S, Dr D Onion, Dr Chris P, Dr Robert M, Dr Gell C, Dr Rajani S, Dr Lodge R (University of Nottingham) and Dr Mark P (University of Loughborough).

I would like to thank the CBS administration staff and the facility coordinators for their support during my research.

Thesis statement and contributions

The work presented in this thesis is mine (Zubair Ahmed Nizamudeen: ZN), unless otherwise declared. This project was supervised by Dr Virginie Sottile (VS) and Dr Lisa Chakrabarti (LC).

In Figure 4.1 (page 177), the negative staining and the transmission electron microscopy (TEM) of EVs was performed by Dr Rhys Lodge (RL) and ZN. In Figure 4.8 (page 188), the qNano analysis was performed by Dr Mark Platt (MP). In Figure 6.1 (page 263), the negative staining and the TEM of EVs was performed by Kiran Suain (KS) and ZN. In Figures 4.2 (page 179), 6.3 (page 268) and 6.4 (page 270), the cryo-TEM was performed by Dr Christopher Parmenter (CP) and was assisted by ZN. In Figures 5.8 (page 236), 5.9 (page 238) and 5.10 (page 240), the immunostaining of mouse tissues was performed by Dr Shelanah Salih (SS). In Figure 6.5 (page 272), the flow cytometry was performed by Dr David Onion (DO). Dr Robert Markus (RM) and ZN developed and optimised the d-STORM approach together (section 2.11, page 106; Figure 2.4, page 109). RM developed the macro for d-STORM image analysis (section 2.11, page 106, Appendix Macro 1). In Figure 4.6 (page 184), the d-STORM images were captured by RM and ZN. In Figure 6.2 (page 263), the DLS experiments were performed by Rachael Xerri (RX) and ZN.

Publications

Results from Chapter 3 have been published in Stem Cell Research journal. Nizamudeen, Z.A., Chakrabarti, L., and Sottile, V. (2018). Exposure to the ROCK inhibitor fasudil promotes gliogenesis of neural stem cells *in vitro*. Stem Cell Res. *28*, 75–86. DOI: 10.1016/j.scr.2018.02.001

Results from Chapter 4 have been published in BBA Molecular Cell Research. Nizamudeen, Z., Markus, R., Lodge, R., Parmenter, C., Platt, M., Chakrabarti, L., and Sottile, V. (2018). Rapid and accurate analysis of stem cell-derived extracellular vesicles with super resolution microscopy and live imaging. Biochim. Biophys. Acta BBA - Mol. Cell Res. 1865, 1891–1900. DOI: 10.1016/j.bbamcr.2018.09.008

A conference meeting report on 'Abam and the Node's Adult Neurogenesis 2018, Dresden' was published in Node community website which was peer reviewed by conference speakers. Link: http://thenode.biologists.com/adult-neurogenesis-2018-highlights/highlights/

Results from Chapters 5 and 6 are in submission stage to journals Development and Journal of Extracellular Vesicles, respectively.

Poster presentations

'Fasudil based medium promotes enhanced gliogenesis of neural stem cells in vitro' Poster presentation in Adult Neurogenesis 2018, Dresden, Germany.

'*Rapid and accurate analysis of stem cell-derived extracellular vesicles with super resolution microscopy and live imaging'* Poster presentation in Mercia Stem Cell Alliance 2018, Nottingham, UK.

Abstract

Neural stem cells (NSCs) in the adult mammalian brain have been identified in the sub-ventricular zone (SVZ) of the lateral ventricles (LV) and the sub-granular zone (SGZ) of the hippocampus. Recently, the Bergmann glia (BG) of the adult mammalian cerebellum have been proposed as a NSC population of the adult brain. However, their regenerative potential is largely unclear. This project aims to investigate the properties of LV-derived and cerebellum-derived NSCs from the adult mouse brain by developing and optimising protocols to (a) differentiate primary NSCs, and (b) characterise extracellular vesicles (EV) secreted by NSCs.

The first results chapter focuses on testing a clinical drug called fasudil for neural differentiation *in vitro*. Fasudil is a a ROCK (Rho associated kinase) inhibitor which has been recently shown to differentiate C17.2 cell line. Here, the results show that fasudil can promote radial-like gliogenesis in primary LV-NSCs with increase in radial-like movement, radial glial markers GFAP and Sox2, and reduction in the neuronal marker βIII-tubulin. Moreover, this effect was consistent in multiple culture conditions including changes in serum concentration, substrate coating, and the batch of primary NSCs. Fasudil-based medium was thus used to study *in vitro* differentiation of primary NSCs.

The second results chapter focuses on developing an innovative tool to characterise EVs secreted by stem cells by using direct stochastic optical

reconstruction microscopy (d-STORM- a super resolution imaging technique), and a lipid-based dye called DiD. The result show that the d-STORM approach was a reliable and a rapid alternative to conventional techniques used for EV characterisation including electron microscopy (EM), nanoparticle tracking analysis (NTA), and tunable resistive pulse sensing (TRPS). d-STORM provided superior sensitivity (20 nm to 30 nm) and speed (<1 hour) for analysing the EV size and count. The approach was further demonstrated to be useful to study intracellular uptake and trafficking of EVs in neural cells.

The third results chapter focuses on using the tools developed in the previous results chapters, including the fasudil-based NSC differentiation protocol and the d-STORM-based EV characterising approach, to investigate the NSC properties of BG isolated from the adult mouse cerebellum. Results showed that BG-NSCs can multiply and differentiate into neurons (expressing βIII-tubulin) and glia (expressing GFAP, S100b), similar to LV-NSCs. Image analysis of immunostained cerebellum sections from *pcd* (Purkinje cell degeneration) mutant mice model showed that BG increase in number during late stages of neurodegeneration. It was found that BG-NSCs secreted EVs that promote neuronal growth in a 2-D neuronal culture system, similar to LV-NSCs. BG-NSCs also showed some distinctive features compared to LV-NSCs such as the difference in morphology at early passages during cell culture, longer doubling time, producing larger neuronal bodies, expressing Calbindin in neural extensions, and secretion of 10-times more EVs per cell.

The fourth result chapter focuses on discovering the undesired effects of low-power sonication during EV analysis for future refinement of EV processing protocols. Results show that low-power sonication induces changes in size distribution, surface membrane properties and its functional effect including cellular uptake. Importantly, by comparing sonicated vs non-sonicated EVs in a 2-D neuronal culture system, it is shown that sonication of EVs is necessary for the neuronal outgrowth promoted by NSC derived EVs observed in the previous chapter. This chapter hence provides insights into the future considerations during EV research.

Taken together, this project provides a deeper understanding into NSC properties of BG, which was investigated by developing protocols to study cellular differentiation and extracellular vesicle characterisation.

Table of Contents

Investigating the Therapeutic Potential of Adult Mouse Cerebellum derived Neural Stem Cells and the Morphological Characterisation of Extracellular Vesicles 1

Acknowledgments 2

Thesis statement and contributions 3

Publications 4

Poster presentations 5

Abstract 6

Table of Contents 9

Table of Figures 20

Table of Tables 32

Abbreviations 33

1. Introduction 35

1.1. Adult neural stem cells and glia 37

1.1.1. Radial Glia 37

1.1.2. Adult neurogenesis in the mammalian brain 39

1.1.3. Markers of neural cells 43

1.1.4. Therapeutic properties of NSCs 47

1.1.5. Astroglia 49

1.2. The Cerebellum 51

1.2.1. Structure of the adult cerebellum 51

1.2.2. Cerebellar Development: Interaction of Purkinje neuron and Bergmann glia 54

1.2.3. Adult cerebellum stem cells: NSC characteristics of Bergmann glia 59

1.3. Neurogenic effect of ROCK inhibitor - fasudil 64

1.3.1. Rho-ROCK cascade in central nervous system 65

1.3.2. Fasudil as a clinical drug for neurological disorders 68

1.4. Extracellular vesicles 70

1.4.1. Classification of EVs 71

1.4.2. Biogenesis and secretion of EVs 73

1.4.3. EVs in the CNS 80

Aims of the project 84

2. Materials and methods 86

2.1. Cell Culture 86

2.1.1. Primary mouse neural stem cells 87

2.1.2. C17.2 cerebellar progenitor cell line 90

2.1.3. Mouse D1 mesenchymal stem cell line 90

2.2. Neurite outgrowth analysis 91

2.3. Pico Green assay 91

2.4. Presto Blue assay 92

2.5. Immunohistochemistry 93

2.5.1. Paraffin embedding and dewaxing of brain tissues 93

2.5.2. Standard immunostaining protocol 94

2.6. Immunofluorescence imaging 96

2.6.1. Considerations while imaging using Nikon 90i Eclipse 96

2.6.2. Immunofluorescence quantification using ImageJ software 97

2.6.3. Operetta high throughput imaging 99

2.6.4. Immunofluorescence quantification using Harmony software 99

2.6.5. Immunofluorescence neurite quantification using MetaXpress 100

2.7. Real-time analysis of 2-D neural migration 102

2.7.1. Live imaging settings for neural stem cells using Operetta system 102

2.7.2. Module construction in Harmony software for migratory cell selection 103

2.7.3. Quantification of neural migration using Harmony software 103

2.8. PCR 104

2.8.1. RNA extraction 105

2.8.2. cDNA synthesis 105

2.8.3. RT-PCR 106

2.8.4. Gel electrophoresis 106

2.8.5. Quantitative real-time PCR 107

2.9. EV isolation 108

2.10. EV characterisation using conventional methods 109

2.10.1. Transmission electron microscopy (TEM) and cryo-TEM 109

2.10.2. Nanoparticle tracking analysis (NTA) 110

2.10.3. Tunable resistive pulse sensing (TRPS) 111

2.10.4. Dynamic light scattering (DLS) 112

2.11. Direct stochastic reconstruction microscopy (d-STORM) based EV characterisation 112

2.12. Analysis of EV uptake 116

2.12.1. Seeding of labelled EVs onto cells 116

2.12.2. Confocal, real-time wide-field and structured illumination microscopy (SIM) imaging for EVs 117

2.12.3. Flow cytometry 119

2.13. Dot blot 119

2.14. Statistical analysis 120

3. *In vitro* differentiation of primary LV-NSCs to radial-like glia using fasudil 121

3.1. Introduction 121

3.2. Aims 122

3.3. Results 123

3.3.1.1. Changes in metabolic and morphological properties of postnatal Cell_LVsg and Cell_C17.2 on exposure to fasudil 123

3.3.2. GFAP and βIII-Tubulin expression of fasudil treated postnatal LV-NSCs and C17.2 cells 130

3.3.3. Migratory properties of fasudil treated postnatal Cell_LVsg and Cell_C17.2 141

3.3.4. Changes in morphology, metabolic activity and NSC marker expression during FAS-differentiation compared to RET-differentiation of adult Cell_LVsg 145

3.3.5. Divergent differentiation responses of adult Cell_LVsg under FAS- and RET-based conditions 153

3.3.6. Effect of changes in substrate coating, serum concentration and source of LV-NSCs on fasudil mediated radial-like glial differentiation 158

3.4. Discussion 166

3.4.1. 100 µM fasudil concentration is non-toxic to primary LV-NSC derived neural cells. 166

3.4.2. Fasudil promotes radial-like gliogenesis of primary LV-NSCs 167

3.4.3. Sox2 expression is maintained in LV-NSCs during FAS-treatment 168

3.4.4. Serum concentration and substrate coating can improve FAS-mediated glial differentiation of LV-NSCs. 170

3.4.5. Source of NSCs and the state of LV-NSCs can significantly impact FAS-mediated glial differentiation 171

3.5. Conclusion..... 173

4. Development of a reliable EV characterisation technique using d-STORM super resolution imaging and subsequent EV uptake analysis using real-time wide-field and confocal imaging 174

4.1. Introduction 174

4.2. Aims 178

4.3. Results 179

4.3.1. Sample analysis of MSC-derived EVs by TEM, cryo-TEM and immuno-dot blot 179

4.3.2. d-STORM imaging of MSC-derived EVs 184

4.3.3. Size and concentration characterisation of stem cell-derived EVs using d-STORM vs NTA and TRPS 189

4.3.4. Imaging of EV uptake in stem cell culture using confocal, SIM and live-epifluorescence microscopy 193

4.3.5. Neuronal response, cellular uptake and localisation of Cell_LVwt derived EVs in neuronal culture system 200

4.3.6. Particle size distribution, concentration and changes in secretion rate of EVs derived from differentiating LV-NSCs 208

4.4. Discussion 212

4.4.1. d-STORM is an efficient alternative to conventional EV characterisation techniques 212

4.4.2. Vybrant DiD is an efficient label for tracking EVs 213

4.4.3. Investigation of EV trafficking using live-imaging 215

4.4.4. Further research to investigate *in vitro* neuronal differentiation using NSC-derived EVs 216

4.4.5. EV release characterisation can be used to monitor neuronal differentiation *in vitro* 218

4.5. Conclusion 220

5. Cellular and acellular properties of Bergmann glia (BG)-NSCs derived from adult mouse cerebellum 221

5.1. Introduction 221

5.2. Aims 224

5.3. Results 225

5.3.1. Morphological and cell growth properties of Cell_BGwt *in vitro* 225

5.3.2. *In vitro* differentiation properties of Cell_BGwt 231

5.3.3. *In vivo* response of BG in pcd^{5J} mouse 237

5.3.4. Neuronal response, cellular uptake and localisation of Cell_BGwt derived EVs in neuronal culture system 243

5.3.5. Particle size distribution, concentration and secretion rate of EVs derived from Cell_BGwt 250

5.4. Discussion 254

5.4.1. Distinct stem cell properties of BG 254

5.4.2. BG-NSCs display the potential to produce cerebellar neurons 255

5.4.3. Nestin is an activated stem-cell state of adult BG 257

5.4.4. BG can be a source of reactive glial stem cells 258

5.5. Conclusion 260

6. Effect of low-power sonication on isolated extracellular vesicles in addition to disaggregation 261

6.1. Introduction 261

6.2. Aims 263

6.3. Results 264

6.3.1. Effect of sonication on disaggregation of EVs analysed by TEM 264

6.3.2. Effect of sonication on EV distribution analysed by DLS, NTA and d-STORM imaging 265

6.3.3. Effect of sonication on EV membrane morphology analysed by cryo-TEM 268

6.3.4. Flow cytometry analysis of cellular uptake of sonicated vs non-sonicated EVs 273

6.3.5. Neuronal response, cellular uptake and localisation of sonicated vs non-sonicated NSC derived EVs in a 2-D neuronal culture system 274

6.4. Discussion 283

6.4.1. EVs are a heterogeneous population containing vesicles with varying shape and membrane properties. 283

6.4.2. Sonication of EVs may bias the EV sample towards lipoproteins 284

6.4.3. Unmonitored sonication leads to variability in EV research 286

6.5. Conclusion 288

7. Concluding discussion and future perspectives 289

7.1. Investigating the effect of fasudil on primary NSCs 289

7.1.1. Fasudil as a pro-neuroglial agent to investigate gliogenesis *in vitro* 289

7.1.2. Rho-ROCK cascade as an NSC modulating signalling pathway 290

7.2. D-STORM approach can be used to study EVs 293

7.2.1. D-STORM proves advantageous over conventional high-throughput techniques for EV characterisation 294

7.2.2. Methods of choice for characterising EVs 297

7.3. Bergmann glial stimulation as a potential cerebellum repair strategy 298

7.3.1. *In vitro* NSC potential of BG 298

7.3.2. The distinct NSC properties of BG 300

7.3.3. BG heterogeneity *in vivo* 300

8. Final conclusion 303

9. References 305

10. Appendix document 333

Table of Figures

Figure 1.1: Neural stem cells are reported to be present in multiple sites of the adult mouse brain 43

Figure 1.2: Candidate markers for neural and glial lineages (adapted from Zhang and Jiao, 2015). 47

Figure 1.3: Anatomy of adult rat cerebellum showing the fissures, lobules and hemispheres.. 52

Figure 1.4: Simplified representation of cellular organisation in the adult mammalian cerebellum. 54

Figure 1.5: Isthmus related genes and organizing activity. 55

Figure 1.6: Birthdate of cerebellar neurons from rhombic lip and the ventricular zone (adapted from Leto et al., 2006). 56

Figure 1.7: Progenitors and neurons in the cerebellum. 57

Figure 1.8: Migration of granule cells to granule cell layer via Bergmann fibres during the first postnatal week of cerebellar development. 59

Figure 1.9: Key discoveries supporting BG as NSCs of adult cerebellum.. 61

Figure 1.10: Evidence for BG (Bergmann glia) neurogenesis in the cerebellar cortex of adult mice. 63

Figure 1.11: Summary of fasudil (Adapted from Chen et al., 2013). 64

Figure 1.12: Graphical overview of Rho-ROCK cascade in axonal growth inhibition of neurons. 67

Figure 1.13: Classification of EVs as exosomes and microvesicles. ... 72

Figure 1.14: Formation of EVs in cells via ESCRT- dependent and ESCRT independent machineries.. 75

Figure 1.15: Release of EVs and major components proposed to be associated with the EV release. 77

Figure 1.16: Mechanisms of EV uptake into recipient cells. 79

Figure 1.17: Graphical representation of the role of EVs in the CNS. (Adapted from Holm et al., 2018)..... 82

Figure 0.1: Diagrammatic representation of thesis project plan..... 85

Figure 2.1: ImageJ manual thresholding of (A) neurons and (B) glia... 98

Figure 2.2: Masking of neurites for counting total neurite processes in an image using Neurite outgrowth module in MetaXpress. 101

Figure 2.3: Graphical representation of the parameters used for cell-track types..... 104

Figure 2.4: Image analysis of EVs captured using d-STORM super resolution microscopy..... 116

Figure 2.5: Testing for fluorescence channel leakage into the far-red (DiD) channel..... 118

Figure 3.1: Morphological changes of Cell_LVsg_FAS and Cell_C17.2_FAS at day 2 and day 4 compared to day 0. 124

Figure 3.2: βIII-tubulin staining of Cell_LVsg_FAS. 126

Figure 3.3: βIII-tubulin staining of Cell_C17.2_FAS. 128

Figure 3.4: Brightfield cell count analysis of Cell_LVsg_FAS and Cell_C17.2_FAS. 129

Figure 3.5: Change in metabolic activity of (A) postnatal LV-NSCs and (B) C17.2 cells after FAS-treatment at day 2 and day 4 compared to day 0 and undifferentiated (UD) controls. 130

Figure 3.6: Marker expression analysis in postnatal Cell_LVsg exposed to FAS-treatment. 132

Figure 3.7: RT-PCR analysis of postnatal Cell_LVsg treated with FAS-medium. 134

Figure 3.8: Marker expression analysis in Cell_C17.2 exposed to FAS-treatment.. 135

Figure 3.9: RT-PCR analysis of Cell_C17.2 treated with FAS-medium. 137

Figure 3.10: Marker expression analysis in overgrown cultures of postnatal Cell_LVsg compared to FAS-treated cultures. 139

Figure 3.11: Marker expression analysis in overgrown cultures of Cell_C17.2 compared to FAS-treated cultures. 140

Figure 3.12: Comparative time-lapse analysis of postnatal Cell_LVsg and Cell_C17.2 during FAS-treatment..... 142

Figure 3.13: Percentage of dividing cells (S-S type) tracked in postnatal Cell_LVsg and Cell_C17.2 samples. 143

Figure 3.14: Quantitative analysis showing the total distance migrated by postnatal Cell_LVsg and Cell_C17.2 cells treated with FAS medium vs. undifferentiated cells..... 145

Figure 3.15: Brightfield images showing morphological response of adult LV-NSCs during RET- and FAS-differentiation on day 2 and day 10.. 146

Figure 3.16: Metabolic response (normalised to DNA content) of adult LV-NSCs during RET- and FAS-differentiation on (A) day 2 and (B) day 10. 147

Figure 3.17: Cell count and metabolic profiling of adult LV-NSCs in response to different concentrations of FAS..... 148

Figure 3.18: Morphological assessment of radial-like outgrowth of adult LV-NSCs in response to different concentrations of FAS. 149

Figure 3.19: Nestin and Sox2 expression in adult LV-NSCs under FAS- and RET-differentiation protocols. 151

Figure 3.20: (A-D) Quantitation of immunofluorescence images of (A and B) Nestin and (C and D) Sox2 detection in adult LV-NSCs under FAS-

and RET-differentiation protocols at day 2 (A and C) and day 10 (B and D) of treatment compared to day 0 controls. 152

Figure 3.21: GFAP and βIII-tubulin expression (red) in Cell_LVsg under FAS- and RET-differentiation protocols. 154

Figure 3.22: (A-D) Quantitation of immunofluorescence images of (A and B) GFAP and (C and D) βIII-tubulin detection in adult Cell_LVsg under FAS- and RET-differentiation protocols at day 2 (A and C) and day 10 (B and D) of treatment compared to day 0 controls. (E-F) qPCR analysis of (E and F) GFAP and (G and H) βIII-tubulin detection in Cell_LVsg under FAS- and RET-differentiation protocols at day 2 (E and G) and day 10 (F and H) of treatment compared to day 0 controls. 155

Figure 3.23: S100b and DCX expression in Cell_LVsg under FAS- and RET-differentiation protocols (day 10).. 157

Figure 3.24: Effect of change in serum concentration and surface coating during FAS-treatment of Cell_LVsg. 159

Figure 3.25: Vacuolar formation in FAS-treated Cell_LVsg. 161

Figure 3.26: Number of neuronal bodies produced by adult Cell_LVsg (Sox1+/-GFP) and Cell_LVwt (Wildtype C57BL6/N) after day 10 RET-treatment. 163

Figure 3.27: (A-D) Immunohistochemistry for GFAP (green) and βIII-Tubulin (red) during (A) day 0, (B) day 10 RET- and (C) day 10 FAS-treatment of (A-C) adult Cell_LVwt. 164

Figure 3.28: βIII-Tubulin immunostaining detection in FAS- and RET treated Cell_LVwt (day 10). 165

Figure 4.1: TEM images of MSC-derived EVs. (A) TEM showing EV structures of 100 to 250 nm in size. Zoomed-in box shows cup-shaped morphology of a vesicle (black arrow) and non-cup-shaped white vesicular structures below 50 nm in size (red arrow). (B) 100 nm vesicle, black arrow showing membrane fold. (C) 20 nm cup-shaped EV (black arrow). (D) 50 nm cup-shaped EV structure (black arrow) along with other white, non-cup-shaped vesicular structures of 5 to 100 nm in size (red arrows). Staining performed and images captured by RL and ZN. 180

Figure 4.2: Cryo-TEM images of MSC-derived EVs. 182

Figure 4.3: Dot blot immunodetection of CD63, TSG101 and GM130 proteins in (A) EV lysate and (B) cell lysate samples isolated from MSCs. 183

Figure 4.4: Photo-blinking frequency of DiD-labelled EVs isolated from MSCs during d-STORM imaging. 185

Figure 4.5: Graphical representation of EV sample scanning pattern with snapshots of areas 1, 2 and 3 recorded in TIRF..... 186

Figure 4.6: d-STORM images of MSC-derived EVs showing (A) TIRF (white), (B) rSWF (sum of wide field frames over the experiment) (green 75), (C) d-STORM (magenta) and (D) merge of rSWF and d-STORM. (E) Cross-sectional line-profiling of two EVs imaged in TIRF, rSWF and d-

STORM as shown in (A) to (D), measured across the line indicated as dotted arrow in (A). 187

Figure 4.7: Absolute frequency of photon number recorded in [DiD in PBS] (green), [DiD in Exo-E medium] (red), [DiD in serum-free Exo-E medium] (purple) and DiD-labelled EV sample (blue)..... 189

Figure 4.8: Particle size distribution of MSC-derived EVs analysed by (A) d-STORM imaging, (B) qNANO (TRPS; performed by MP) and (C) NTA. (Mean ± SEM; n=3). 191

Figure 4.9: (A) Standard curve from DiD-labelled MSC-derived EV dilutions to determine the working range for d-STORM particle count, shown in the boxed area. (B) EV concentration measurements produced by d-STORM and TRPS based approaches..... 193

Figure 4.10: Confocal microscopy imaging of live DiO-labelled NSCs (green) with nuclear counterstain (blue), incubated in the (A) presence or (B) absence of DiD-labelled MSC-derived EVs (magenta). Arrows show DiD-labelled EVs in magnified view of boxed area. 195

Figure 4.11: SIM imaging of DiD-labelled MSC-derived EVs (magenta) uptake by DiO-labelled NSCs (green), with magnified areas 1 and 2 showing intracellular DiD-labelled EVs (arrows). 197

Figure 4.12: Real-time time-lapse snapshots of MSC-derived DiD-labelled EVs (magenta) inside DiO-labelled NSCs (green). 199

Figure 4.13: (A) Metabolic assay and (B) brightfield imaging of 2-DN cultures under different stock concentrations of EVs derived from Cell_LVwt_D0 on day 10. 202

Figure 4.14: Changes in number of neuronal processes upon addition of EV_LVwt_D0 (day 10). 204

Figure 4.15: Immunofluorescence and subsequent 3-D reconstruction imaging of EV_LVwt_D0 uptake by 2-DN cultures (day 10). 207

Figure 4.16: Immunofluorescence and subsequent 3-D reconstruction imaging of the soma of neurons after addition of EV_LVwt_D0 in 2-DN cultures (day 10). 208

Figure 4.17: Particle size distribution of LV-NSC derived EVs. (A to C) EVs derived from (A) day 0, and day 4 (B) RET-treated and (C) FAS-treated LV-NSC_SG. (D to F) EVs derived from (A) day 0, and day 4 (E) RET-treated and (F) FAS-treated LV-NSC_WT.. 209

Figure 4.18: Average concentration and size determination of LV-NSC derived-EVs. 211

Figure 5.1: Brightfield images showing (A) Cell_BGwt-and (B) Cell_LVwt in culture. 226

Figure 5.2: Brightfield images showing the morphological appearance of (A and B) Cell_BGwt, (C and D) Cell_LVwt at (A and C) passage 2 and (B and D) passage 20. 228

Figure 5.3: (A) Doubling time of Cell_BGwt and Cell_LVwt in culture. (B) Viability of NSCs after Accutase treatment. Student's t-test, n=3 (C) Change in cell count at day 4 of differentiation compared to day 0 in Cell_BGwt and Cell_LVwt. One-way ANOVA, Tukey's multiple comparison tests, n=3. (D) Brightfield images showing the size of neuronal bodies in Cell_BGwt_RET and Cell_LVwt_RET cultures. (E) Quantitation of neuronal perikaryon size in Cell_BGwt_RET and Cell_LVwt_RET cultures. 230

Figure 5.4: Immunofluorescence imaging of (A, C, E and G) Cell_BGwt and (B, D, F and H) Cell_LVwt during differentiation. 232

Figure 5.5: Immunofluorescence detection of calbindin (green) in (A-D) Cell_BGwt and (E-H) Cell_LVwt from day 0 to day 7 of RET treatment (with brightfield merge).. 234

Figure 5.6: Immunofluorescence detection of GFAP (green) in (A, C and E) Cell_BGwt and (B, D and F) Cell_LVwt at (A and B) day 0, (C and D) day 7 of RET-treatment and (E and F) day 7 of FAS-treatment. 235

Figure 5.7: Immunofluorescence detection of S100b (red) in (A, C and E) Cell_BGwt and (B, D and F) Cell_LVwt at (A and B) day 0, (C and D) day 7 of RET-treatment and (E and F) day 7 of FAS-treatment. 236

Figure 5.8: Expression of NSC associated markers in the BG of adult mice. 238

Figure 5.9: Double immunostaining of (A) Nestin and (B) Ki67 (both brown) with Calbindin (blue) in the adult mouse cerebellum. 240

Figure 5.10: (A) Expression of Sox1, Sox2 and Sox9 in postnatal day 104 *pcd* mutant mice. (B) Quantitation of Sox1, Sox2, Sox9 in the PCL of mice cerebellum on P104 (..... 242

Figure 5.11: Double immunostaining of GFAP (brown) with Calbindin (blue) showing the BG fibres situated in ML of (A) WT and (B) pcd mutant cerebellum at P100..... 243

Figure 5.12: (A) Metabolic assay and (B) brightfield imaging of Cell_LVwt_RET under different stock concentrations of EVs derived from Cell_BGwt on day 10..... 245

Figure 5.13: Changes in number of neuronal processes upon addition of EV_BGwt_D0 (day 10). 247

Figure 5.14: Immunofluorescence and subsequent 3-D reconstruction imaging of EV_BGwt_D0 uptake by 2-DN cultures (day 10). 249

Figure 5.15: Particle size distribution analysis of EVs derived from Cell_BGwt using d-STORM at (A) day 0, (B) day 4 RET-treated and (C) day 4 FAS-treated. 251

Figure 5.16: Average concentration and size determination of Cell_BGwt derived-EVs..... 252

Figure 5.17: (A) Average size of EVs and (B) Average EV released per cell by Cell_LVwt and Cell_BGwt. 253

Figure 6.1: TEM images of non-sonicated (ns) and sonicated (s) EVs. (a) Non-sonicated and (b) sonicated EVs embedded onto holey carbon grids. 265

Figure 6.2: Characterisation of (A, C, E and G) ns- and (B, F and H) s-EVs by (A and B) DLS, (C and D) NTA, (E and F) TIRF and (G and H) d-STORM. 267

Figure 6.3: Cryo-TEM images of non-sonicated MSC-derived EV samples. 270

Figure 6.4: Cryo-TEM images of sonicated MSC-derived EV samples. 272

Figure 6.5: Cellular uptake of EVs by MSCs analysed by flow cytometry. 274

Figure 6.6: (A) Metabolic assay and (B) brightfield imaging of Cell_LVwt_RET under the incubation of 0.1x concentration of sonicated vs non-sonicated EVs derived from Cell_LVwt_D0 and Cell_BGwt_D0 (day 10). 276

Figure 6.7: Changes in number of neuronal processes upon addition of sonicated (s-) vs non-sonicated (ns-) NSC-derived EVs (day 10). 278

Figure 6.8: Immunofluorescence images of EV_LVwt_D0 uptake by Cell_LVwt_RET (day 10). 280

Figure 6.9: Immunofluorescence images of EV_BGwt_D0 uptake by Cell_LVwt_RET (day 10). 282

Figure 7.1: Schematic flowchart of the d-STORM approach used in this study to characterise EVs. 294

Figure 7.2: Summary of EV characterisation techniques used in this study, with their key advantages and disadvantages. 296

Figure 7.3: Flowchart depicting future perspective for BG-NSC research. BG-Bergmann glia. 302

Table of Tables

Table 1.1: The effects of fasudil against CNS disorders in clinic or animal models: potential mechanism(s) and the delivery and dosage used. .. 68

Table 2.1: Cell and EV sample nomenclature used in this study 89

Table 4.1: Concentration of EVs from Cell_LVwt used for neuronal cell response study 201

Table 5.1: Concentration of EVs isolated from BG-NSCs used for neuronal cell response study 244

Table 6.1: Average size of EVs calculated by DLS, NTA and d-STORM techniques 268

Table 10.1: Details of antibodies used for immunostaining experiments 333

Table 10.2: List of primers used in RT-PCR 334

Table 10.3: Primers used for qPCR 334

Table 10.4: Details of antibodies used for immunoblotting experiments. 334

Abbreviations

(B-E)	‘BEGIN’ to ‘END’ type
(S-S)	‘SPLIT’ to ‘SPLIT’ type
AD	Alzheimer’s disease
ALIX	ALG2 interacting protein X
ATP	Adenosine tri-phosphate
BDNF	Brain-derived growth factor
bFGF	Basic fibroblast growth factor
BG	Bergmann glia
BGwt	BG-NSCs derived from C57BL6/N mice
CDD	Cerebellar dysfunctional disorders
CDNA	Complementary DNA
CNS	Central nervous system
DCX	Doublecortin
DMSO	Dimethyl sulfoxide
DMEM	Dulbecco’s modified Eagle’s medium
DNA	Deoxyribonucleic acid
d-STORM	Direct stochastic optical reconstruction microscopy
EGF	Epidermal growth factor
EGL	External germinal layer
EM	Electron microscopy
eNOS	Endothelial NO synthase
ERK	Extracellular signal-regulated protein kinases
ESCRT	Endosomal sorting complex required for transport
EV	Extracellular vesicle
Exo-E	EV-enrichment medium
FAS or ‘FAS medium’	Fasudil-based medium
FBS	Fetal bovine serum
GC	Granule cell
GCL	GC layer
GDP	Guanosine diphosphate
GFAP	Glial fibrillary acidic protein
GLAST	Glutamate aspartate transporter
GTP	Guanosine triphosphate
HCL	Hydrochloric acid
ILV	Intra-luminal vesicles
IN	Interneurons
iNSCs	Induced NSCs
iPSCs	Induced pluripotent stem cells
LV	Lateral ventricle

LVsg	LV-NSCs derived from Sox1 ± GFP mice
LVwt	LV-NSCs derived from C57BL6/N mice
MBP	Myelin basic protein
MHB	Midbrain-hindbrain boundary
MLC	Myosin light chain
MSC	Mesenchymal stem cell
sEVs	Sonicated EVs
NO	Nitric oxide
NSC	Neural stem cells
nsEVs	Non-sonicated EVs
NTA	Nanoparticle tracking analysis
PBS	Phosphate buffered saline
PBT	PBS + 0.1% Tween 20
PC	Purkinje cells
PCL	PC layer
PCP	Purkinje progenitor cell
PCR	Polymerase chain reaction
PFA	Paraformaldehyde
PSD	Particle size distribution
qPCR	Quantitative PCR
RAB	Ras-related protein
RET or ‘RET medium’	Retinoic acid analogue treated-based medium
RNA	Ribonucleic acid
ROCK	Rho-associated protein kinase
rSWF	Reconstructed standard widefield
RT-PCR	Reverse transcription PCR
SAH	Subarachnoid haemorrhage
SDW	Sterile distilled water
SGZ	Sub-granular zone
SIM	Structured illumination microscopy
STD or ’STD medium’	Standard medium
SVZ	Sub-ventricular zone
TEM	Transmission electron microscopy
TIRF	Total internal reflection microscopy
TRPS	Tunable resistive pulse sensing

1. Introduction

According to recent estimations, 13% of global disease prevalence records for brain disorders, exceeding cancer and cardiovascular disorders (Collins et al., 2011). In Europe alone, brain disorders have cost the economy a total of €798 billion in 2010, of which only 37% was accounted as direct health care cost (European Brain Council) (Olesen et al., 2012); non-medical direct costs for neurological and neurodegenerative disorders are estimated to be 40% of their sum total, in contrast to other mental disorders (Olesen et al., 2012).

Cerebellar dysfunctional disorders (CDDs) are associated with a variety of neurodegenerative disorders including Alzheimer's Disease (AD), Parkinson's Disease, Huntington's Disease, autism and amyotrophic lateral sclerosis (Bede et al., 2015; Guo et al., 2016; Rüb et al., 2013; Wu and Hallett, 2013). Demands for therapeutic strategies for CDDs of the brain have significantly increased over the past decade in clinical as well as socio-economical fields. Majority of the current treatments including physio-, occupational- and symptomatic- therapies are inadequate to target the source of the disorders. CDDs have become increasingly challenging, primarily due to the lack of knowledge to rescue or replace the degenerating neurons in the brain.

Neural stem cells (NSCs) have shown the ability to generate new neural cells (neurons and glia) and replace damaged and/or lost cells in the adult mammalian brain. It has been established that NSCs can also

secrete a variety of neurogenic factors and promote cell recovery and health in an acellular (indirect) manner (refer to section 1.4.3.1). Therefore, researchers have focused on developing a variety of tools to understand and harness the potential of NSCs to treat neurodegenerative disorders. However, actively dividing adult NSCs are restricted in localisation to the sub-ventricular zone (SVZ) and the sub-granular zone (SGZ), which makes distant regions of the adult mammalian brain, including the cerebellum, hard to repair (Ming and Song, 2005, 2011). Recently, a distinct population of cells known as the Bergmann glia (BG), isolated from the adult mammalian cerebellum, have been characterised as NSCs (Alcock and Sottile, 2009). However, the potential of BG-NSCs to rescue the cerebellar neurons upon degenerative insult is largely unknown.

Here, novel tools were developed to study the cellular and acellular potential of adult BG-NSCs. First, a pro-glial differentiation protocol for primary SVZ-NSCs was developed using the clinical drug called fasudil. In parallel, an innovative approach to characterise extracellular vesicles (EVs) isolated from NSCs was developed which contributed to revealing the effect of NSC-derived EVs on neuronal maturation. Finally, the developed tools were used to characterise and investigate the cellular (*in vitro* differentiation) and acellular (EV mediated effect) neurogenic potential of BG-NSCs. The study presented here thus broadly contributes to 1) the development in NSC research, 2) the development in EV research, and 3) investigation of BG-NSCs, a cell population that can be used to develop a potential strategy to combat ataxic neurodegeneration.

1.1. Adult neural stem cells and glia

Neural stem cells (NSCs) have the potential to multiply and produce multiple cell types in the central nervous system (CNS) including neurons and glia. NSCs of the CNS are found throughout development (from embryonic stages to adulthood) (Gage and Temple, 2013). During the embryonic period, the radial glial NSCs produce majority of the cells that make up the CNS. At later stages of development, the radial glial NSCs reduce in number drastically, and by adulthood, relatively few NSCs (derived from radial glial NSCs) serve as adult NSCs in discrete and distinct locations in the brain.

1.1.1. Radial Glia

Radial glia are descendants of the neuroepithelial cells present during the embryonic development of the CNS, and they produce majority of the neurons and glia of the adult brain (Kriegstein and Alvarez-Buylla, 2009; Kriegstein and Götz, 2003). Using a lox-Cre system to permanently track neonatal radial glia and BrdU labelling to track mitotic cells and their progeny, a study has reported that radial glia give rise to adult NSCs in the SVZ (Merkle et al., 2004). Specialised glial cells in the adult brain including the Bergmann Glia (BG) of the cerebellum and the Muller glia of the retina are also suggested to be rare persistence of radial glia into mammalian adulthood (Alcock and Sottile, 2009; Bernardos et al., 2007). Therefore the radial glia are key players of neurogenesis of the brain.

Radial glia possess unique biophysical and biomechanical properties in the CNS compared to neural progenitors and mature neurons and glia. Radial glia have been observed possess smooth cytoplasmic extensions (or 'radial extensions') via which they display a unique phenomenon known as interkinetic nuclear movement (INM), a feature they share with their parent neuroepithelial cells (Elkabetz et al., 2008; Kriegstein and Alvarez-Buylla, 2009; Kriegstein and Götz, 2003; Spear and Erickson, 2012a, 2012b). INM is the cell cycle regulatory migration of the cell body (of radial glia and neuroepithelial cells) along the radial fibres which is known to modulate neurogenesis of the developing brain (Spear and Erickson, 2012b, 2012a). In contrast to neuroepithelial cells however, the radial glia express astroglial proteins including GLAST, Tenascin C, BLBP, and NSC markers including Nestin and Sox2 (Kriegstein and Alvarez-Buylla, 2009; Kriegstein and Götz, 2003). Also, the embryonic radial glia and the adult NSCs share the morphological trait of radial fibre extension (Elkabetz et al., 2008; Kriegstein and Alvarez-Buylla, 2009; Kriegstein and Götz, 2003). The radial glia extend their cytoplasm radially and maintain contact with both the pial and the ventricular regions of the developing tissue, which is key in mediating the INM and INM dependent cell cycle of radial glia, which leads to production of new neurons (Kriegstein and Alvarez-Buylla, 2009; Kriegstein and Götz, 2003; Spear and Erickson, 2012a, 2012b). The adult SVZ and SGZ NSCs also possess radial extensions that contact the endothelium, which in turn modulates adult neurogenesis (however, it is unclear whether the adult NSCs partake in INM) (Kriegstein and Alvarez-Buylla, 2009). INM is also

observed in differentiating embryonic stem cells when they attain radial glial maturity (Elkabetz et al., 2008). However, although the radial extensions and INM have been proposed to be unique to radial glia, these biophysical properties are yet to be investigated as to if they are a reliable biomechanical marker of radial glial properties (including neurogenesis).

1.1.2. Adult neurogenesis in the mammalian brain

Active neurogenesis in the adult mammalian brain is restricted to the lateral ventricles (LV) of the sub-ventricular zone, (SVZ) and the dentate gyrus (DG) of the sub-granular zone (SGZ) of the hippocampus (reviewed in Braun and Jessberger, 2013) (Figure 1.1). The evidence for neurogenesis stems from the presence of actively dividing NSCs and the production of new neurons in the SVZ and the SGZ in animal models. In humans however, there is an ongoing debate of adult neurogenesis, in the SVZ and the SGZ (reviewed in Kempermann et al., 2018). Using a wide range of patient samples, and immunohistochemical techniques for detecting protein expression of NSCs and cell division, independent groups have come to contradictory conclusions regarding the presence of neurogenesis in the adult SVZ and SGZ of humans (Boldrini et al., 2018; Sanai et al., 2011; Sorrells et al., 2018). However, it is evident from both the studies that neurogenesis in adult human, if occurring, is only at relatively low levels *in vivo*, compared to rodent and primate animal models (reviewed in Kempermann et al., 2018). Nevertheless, both SVZ and SGZ derived NSCs can be isolated from rodents and humans, which

show self-renewal and differentiation abilities *in vitro* (Guo et al., 2012; Johansson et al., 1999). Given the therapeutic possibilities of adult NSCs in the brain, efforts have been made to understand the adult NSC niche, and to discover other places of possible neurogenesis in the adult brain.

In the SVZ, quiescent NSCs called the 'B' cells give rise to actively proliferating type 'C' cells called transient amplifying cells, which then give rise to type 'A' cells called neuroblasts (Doetsch et al., 1999). Neuroblasts then migrate away from the SVZ, through the rostral migratory stream, and reach the olfactory bulb where they integrate into the local network by differentiating into mature GABAergic or glutamatergic neurons (Braun and Jessberger, 2013; Lois and Alvarez-Buylla, 1994). In the SGZ, quiescent NSCs can divide symmetrically to produce two radial NSCs (named as 'type 1' or 'radial' NSCs), or asymmetrically to give rise to either an NSC and a progenitor or two progenitors (reviewed in Braun and Jessberger, 2013). The progenitors are called 'type 2' cells which give rise to neuroblasts called 'type 3' cells (reviewed in Braun and Jessberger, 2013). The neuronally committed neuroblasts then migrate to the granule layer, branch out processes, and project out a large dendritic arbor into the molecular layer and an axon into the hilus that terminates in the CA3 (a region in the hippocampus responsible for memory) (reviewed in Braun and Jessberger, 2013). NSCs can also produce different types of glia including oligodendrocytes, as observed in response to injury or demyelination (Jablonska et al., 2010). All NSCs are characterised based on their ability to proliferate and make new neurons and glia. The characterisations are made using

techniques including *in vivo* lineage tracing by genetic engineering (including Cre-Lox systems), *in vivo* assessment of proliferative markers (BrdU and Ki67) (Kempermann et al., 2018), *in vitro* assessment of neurosphere forming ability in the presence of growth factors (epidermal growth factor (EGF) and basic fibroblast growth factor (bFGF)), and *in vitro* assessment of differentiation into neuroglia subtypes upon removal of growth factors (EGF, bFGF) and addition of differentiation factors (retinoic acid, brain derived growth factor (BDNF), serum) (Jiao et al., 2014; Tan et al., 2015).

Recently, it has been noticed that cells expressing the canonical NSC markers including Sox1, Sox2, Nestin and Glial fibrillary acidic protein (GFAP), may exist in other parts of the adult CNS but with low to undetectable levels of neurogenesis under normal physiology, and show *in vitro* NSC characteristics (Alcock and Sottile, 2009; Sottile et al., 2006; Su et al., 2014). Tanycytes (α-tanycytes) of the hypothalamus have shown to express multiple NSC markers including nestin, vimentin and GFAP *in vivo* and form neurospheres and differentiate into neuronal (Tuj1) and glial (GFAP, RIP) lineages *in vitro*, and significant but low neurogenesis *in vivo* compared to SVZ and SGZ sites of the adult brain (Arias-Carrion, 2011; Pellegrino et al., 2018; Robins et al., 2013) (Figure 1.1). Similarly, NSCs have been characterised and isolated from the cerebellum (will be discussed in section 1.2.3) of the adult rodent brain and have shown neurogenic properties of self-renewal and differentiation *in vitro*, but lacks evidence for active neurogenesis *in vivo* under normal conditions (Ahlfeld et al., 2017; Alcock and Sottile, 2009; Klein et al.,

2005) (Figure 1.1). Moreover, it is considered that NSCs represent a glial phenotype (Doetsch, 2003; Kriegstein and Alvarez-Buylla, 2009). NSCs share multiple markers including GFAP and Glutamate aspartate transporter (GLAST), with resident parenchymal astrocytes in the adult CNS (Doetsch, 2003; Kriegstein and Alvarez-Buylla, 2009). Additionally, it has been reported that resident glial cells including NG2 glia and astrocytes can become reactive upon injury, and show NSC properties (Götz et al., 2015). However, it is largely unclear why NSCs present in regions apart from SVZ and SGZ appear to be dormant (show little to no active neurogenesis under normal conditions) compared to NSCs from the SVZ and the SGZ (Figure 1.1). Nevertheless, these observations have increased the interest and research activities in harnessing the potential of NSCs in the CNS to provide therapeutic strategies for neurological disorders. Appendix pdf file 1 contains a diagram poster (Abcam Adult Neurogenesis, Dresden, 2018) summarizing the recent findings on active neurogenic sites in the adult mouse brain.

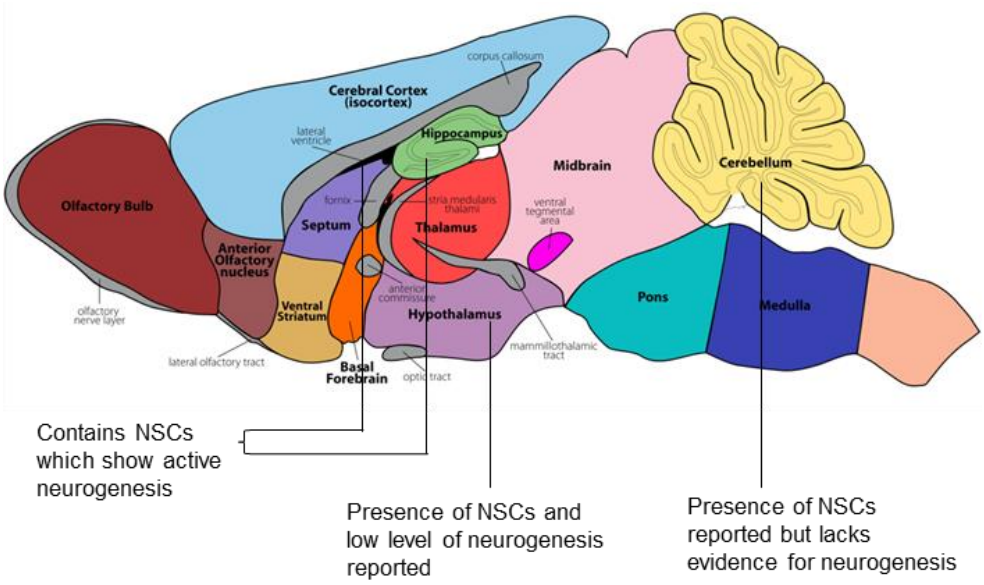


Figure 1.1: Neural stem cells are reported to be present in multiple sites of the adult mouse brain. Diagram adapted from Allen's Brain Atlas (Information adapted from Ahlfeld et al., 2017; Alcock and Sottile, 2009; Arias-Carrion, 2011; Braun and Jessberger, 2013; Robins et al., 2013)

1.1.3. Markers of neural cells

Markers of NSCs, and neuronal and glial subtypes have been widely established (Figure 1.2). Here, some of the prominently used neural markers will be discussed, which will be used in the study. More markers of NSCs and neural lineage have been extensively reviewed elsewhere (Zhang and Jiao, 2015).

1.1.3.1. NSC markers

Among the Sox (also known as sex determining region Y) family of genes, Sox1 and Sox2 are the most prominently known NSC markers (Graham et al., 2003; Venere et al., 2012). Sox2 encodes a highly conserved DNA-binding motif identified as high-mobility group box. Sox1 and Sox2 are known to be associated with NSCs in the neurogenic

niches of the adult mammalian brain and developmental NSCs (Graham et al., 2003; Venere et al., 2012), and are expressed by NSCs when isolated *in vitro* (Barraud et al., 2005; Zhao et al., 2004). Sox1 and Sox2 proteins are known to act as a transcription factors which play an important role in the development of CNS. Sox1 is the earliest known marker specific for neural lineage during development (Pevny et al., 1998; Wood and Episkopou, 1999). In the SGZ of adult mouse CNS, Sox1 has been reported to be restricted to a subset of NSCs which are GFAP+ve radial astrocytes and Sox2+ve non-radial progenitors; whereas Sox2 shows a broader expression profile across non-radial progenitors, radial astrocytes and mature astrocytes (Venere et al., 2012). Sox2 overexpression has been reported to reprogram resident glia into functional neurons in the adult brain, indicating its role in neural lineage potential (Heinrich et al., 2014; Niu et al., 2015). Recently, Sox9 has also been identified to be co-expressed in NSCs along with Sox1 and Sox2 (Alcock and Sottile, 2009). Nestin is a neuro-epithelial intermediate filament protein expressed specifically by self-renewing NSCs and neural progenitors (Hendrickson et al., 2011; Mignone et al., 2004). They are also expressed by reactive astrocytes upon injury (reviewed in Götz et al., 2015). Nestin expression is known to reduce upon differentiation of NSCs (Sunabori et al., 2008). Studies have suggested that Nestin plays a role in modulating cytoskeletal dynamics of a cell by cross-linking intermediate filaments, microfilaments and microtubules (Herrmann and Aebi, 2000; Michalczyk and Ziman, 2005).

1.1.3.2. Neuronal markers

β-Tubulins are known to play an important role in formation of microtubules in a cell and its subset, βIII-Tubulin (also known as Tuj1, neuron-specific class III β-tubulin) is a specific marker for neuronal lineage (Liu et al., 2007). It is expressed by immature neurons throughout development (Liu et al., 2007). It is also expressed by mature neurons including basket cells of SGZ and Purkinje cells (PCs) of the cerebellum (Katsetos et al., 1993; Seri et al., 2004). Doublecortin (DCX) is a microtubule-associated protein known to polymerize tubulin and is expressed by migrating neuroblasts and immature neurons (Gleeson et al., 1999). DCX can be co-expressed with the NSC marker Nestin, and the neuronal marker βIII-Tubulin, in the SGZ and SVZ (Ambrogini et al., 2004; Brown et al., 2003; Yang et al., 2004). Consequently, DCX has been regarded as a marker for neurogenesis in the adult brain. However, it is to be noted that not all new-born neurons express DCX. Calbindin is calcium-binding protein and is a mature neuronal marker expressed specifically by PCs in the cerebellum, and also granule cells (GCs) in the hippocampus (Abe et al., 1992). NeuN is neuron specific nuclear protein expressed by mature GCs in the cerebellum and the hippocampus (Gusel'nikova and Korzhevskiy, 2015). NeuN/Fox-3 are being suggested to be RNA-binding proteins involved in mRNA splicing in neuronal cells (Underwood et al., 2005).

1.1.3.3. Glial markers

GFAP is a marker primarily used for labelling astrocytes. GFAP is highly expressed by reactive astrocytes and radial glial NSCs (reviewed in Götz et al., 2015). Also, GFAP has been identified to be expressed by NSCs in the SVZ and SGZ (reviewed in Braun and Jessberger, 2013). S100b is a calcium binding protein anchored to the cytoplasm and/or nucleus of the cell (Deloulme et al., 2004; Heizmann et al., 2002). It is specifically expressed by astrocytes, particularly, to a subpopulation of GFAP+ve cells *in vivo* that have matured from their NSC state (Raponi et al., 2007). GLAST (also known as EAAT1) is expressed by mature astrocytes (co-expressing S100b) and radial glial NSCs (Namba et al., 2005; Sutherland et al., 1996). GLAST is also strongly expressed by the BG population in the adult CNS (Miyazaki et al., 2017). Aldehyde dehydrogenase 1 family, member L1 (Aldh1L1) has been reported to be a reliable astrocyte marker based on transcriptional studies of the mouse CNS (Cahoy et al., 2008). Aldh1L1 has been shown to be expressed in adult rat astrocytes and is able to label more astrocytes than GFAP, with widespread localisation in the CNS (Cahoy et al., 2008; Neymeyer et al., 1997). Markers for oligodendrocytes include myelin basic protein (MBP-mature marker), Olig1, Olig2 and Olig4 (immature mature markers), and NG2 (oligodendrocyte progenitor marker) (reviewed in Miron et al., 2011).

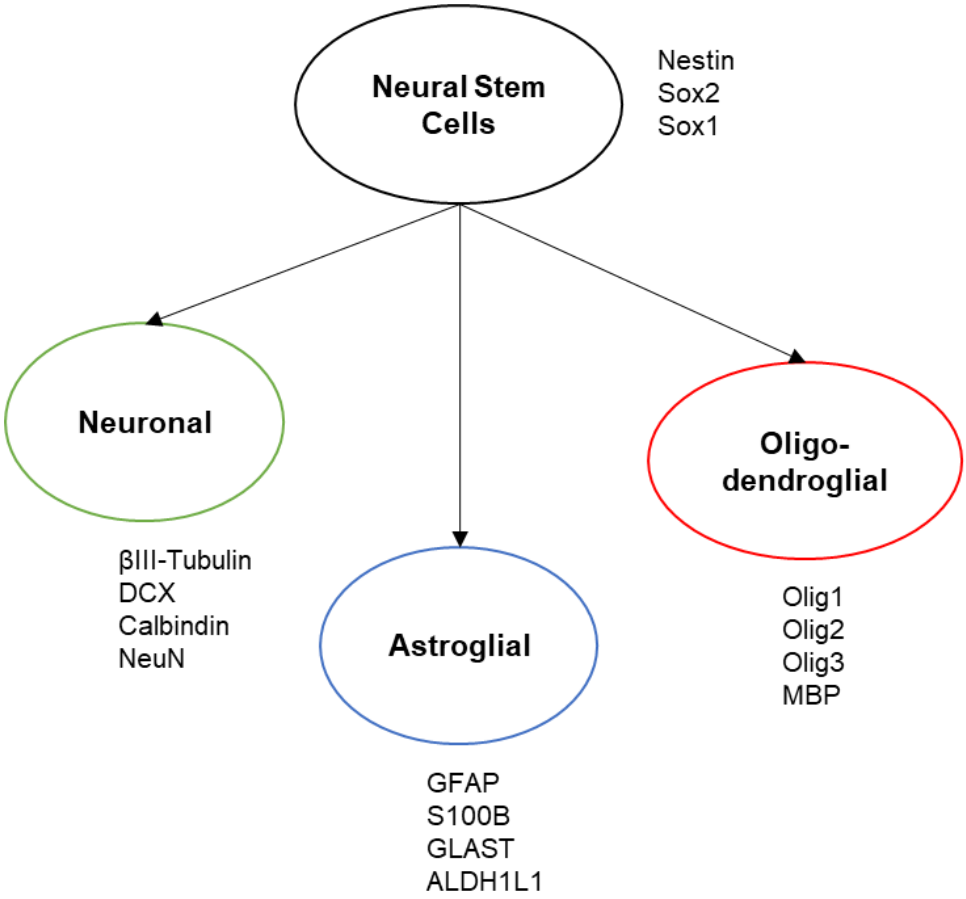


Figure 1.2: Candidate markers for neural and glial lineages (adapted from Zhang and Jiao, 2015).

1.1.4. Therapeutic properties of NSCs

Studies investigating the properties and potential of NSCs are vital for understanding development, disease progression and regeneration in the CNS.

Adult NSCs provide a source of cellular repair strategy in the CNS. It has been demonstrated that adult and postnatal NSCs can be isolated, expanded, and transplanted back into CNS, which can result in successful integration and differentiation of NSCs into the neural network of the brain (Klein et al., 2005). Interestingly, SVZ-derived and

cerebellum derived adult NSCs were able to produce distinct set of neural subtypes with respect to their regional identity (only SVZ-NSCs produced DRPP-32 positive cells while only cerebellum-NSCs produced TAG1 positive cells) (Klein et al., 2005). NSC transplantation of the established C17.2 neural progenitor cell line has shown functional benefits of improved neuronal survival in animal models of ataxia (nervous mouse) and Sandhoff disease (*Hexb*$^{-/-}$ *mouse)* (Jeyakumar et al., 2009; Li et al., 2006). NSCs generated from reprogramming of somatic cells (induced NSCs or iNSCs) have been reported to show functional recovery in a variety of animal models and are progressing into clinical trials for human patients. iNSCs transplanted in ischaemic stroke pig model has been demonstrated to improve symptoms by improving white matter integrity, improving brain metabolism, enhancing cerebral blood perfusion in the ipsilateral hemisphere, improving neuronal protection, neuroblasts activation (and migration to lesion site), reduced microglial activation, and differentiation into neurons and oligodendrocytes (Baker et al., 2017). Moreover, *in vivo* reprogramming has been recently established to target NSC and NSC-like cells in the brain and stimulate repair endogenously. Resident pericytes (expressing platelet-derived growth factor receptor-β) and glial cells (expressing NG2) in the brain have been demonstrated to have the ability to directly convert into functional neurons upon ectopic overexpression of neuronal genes (Aravantinou-Fatorou et al., 2015; Heinrich et al., 2011, 2014; Karow et al., 2012). Finally, NSCs can also promote their therapeutic effect in an acellular manner via extracellular vesicles, and this is growing

to be an attractive strategy for clinical therapy (discussed later in section 1.4.3.2).

Several reports have demonstrated that patient-derived induced pluripotent stem cells (iPSCs) can be used for disease modelling (Juopperi et al., 2011). Recently, a study demonstrated that iPSCs can be used to produce mini-cerebellar organoids in the lab, recapitulating development of the CNS including production of embryonic neurons (including PCs) (Muguruma et al., 2015). A following study demonstrated that PCs produced from iPSCs derived from Spinocerebellar ataxia type 6 (SCA6) patients can show diseased physiology including thyroid hormone depletion-dependent degeneration which can be supressed by drugs (thyroid releasing hormone and Riluzole) (Ishida et al., 2016). Taken together, adult NSCs (in the CNS or from iPSCs) provide an attractive treatment strategy for neurological disorders, and an efficient source for disease modelling and drug testing.

1.1.5. Astroglia

Glial cells were long known as supporting cells of neurons or ‘glue’ material of the brain. But now it has been well established that glial cells are much more complex with important roles in development and disease progression in the mammalian CNS. Glia are classically subdivided into three subtypes namely astroglia, oligodendroglia and microglia. With respect to the scope of the current study, this section will only cover astroglia.

Morphologically, mature astroglia can be divided into two major subtypes namely protoplasmic and fibrous astrocytes (Tabata, 2015) (radial glia has been discussed earlier). Protoplasmic astroglia are structurally more complex than fibrous astroglia as they contain comparatively more branching and multiple fine processes (Tabata, 2015). In addition to these, recent studies have discovered regional heterogeneity of astrocytes with distinct phenotypes which include tanycytes of the hypothalamus, Muller glia of the retina and BG of the cerebellum (Arias-Carrion, 2011; Pellegrino et al., 2018; Robins et al., 2013, Alcock and Sottile, 2009; Bernardos et al., 2007). Astroglia have been studies using various protein markers during immunohistochemistry including GFAP, GLAST and S100b (Heizmann et al., 2002, Tabata, 2015). However, no universal marker for astroglia exist. As mentioned earlier, NSCs and astroglia can share similar protein expression patterns.

Interactions between the cerebellar BG and its surrounding neurons including Purkinje cells (PCs) and Granule cells have been well established and provide as a good model for studying astrocyte function. Using in vivo and in vitro slice culture experiments, it was reported that BG can modulate PC cell output from the cerebellum by controlling Ca2+ dependent K+ uptake (Wang et al., 2012). By using a transgenic mouse model to selectively stimulate Ca+ in BG, this study reported that BG can evoke a transient reduction of extracellular K+ in cerebellar slices and cerebellum in live adult mice (Wang et al., 2012). Because the concentration of extracellular K+ is a critical determinant of PC-membrane potential, these observations suggest the modulation of PC

membrane bistability by BG in the adult mouse cerebellum. Astroglia including BG are known to play a crucial role in the synaptogenesis of surrounding neurons. Using a combination of biolistic labelling of BG ex vivo cerebellar slices and adenoviral labelling of BG in vivo, a study revealed the dynamic modulation of synaptogenesis by BG fibres by dendritic spine ensheathment during development (Lippman et al., 2008). BG also plays an intricate role in the development and differentiation of cerebellum neurons (discussed in detail in section 1.2.2). Taken together, astroglia play an important role in regulating neuronal activity, supporting neuronal development and maintaining CNS homeostasis (De Zeeuw and Hoogland, 2015).

1.2. The Cerebellum

The cerebellum is a highly conserved structure in the mammalian brain and is involved in vital functions of the body including motor coordination, learning, speech, memory and cognition (Buckner, 2013; Manto et al., 2012). This section focuses on the structure and development of the cerebellum, and the current knowledge of stem cells in the adult cerebellum.

1.2.1. Structure of the adult cerebellum

The structure of cerebellum is well studied and established since the late nineteenth century. Mature mammalian cerebellum is characterised by developed fissures, lobules and hemispheres (Figure 1.3).

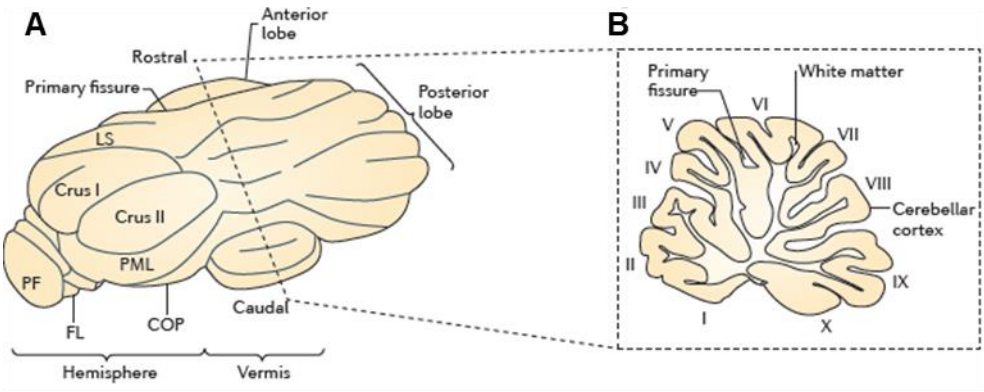


Figure 1.3: Anatomy of adult rat cerebellum showing the fissures, lobules and hemispheres. The flocculundar and vestibular lobules are not shown in this representation. (A) Dorso–posterior view. The anatomical midline (dashed line) divides the cerebellar vermis into two halves and a hemisphere on each side. (B) Zoomed in section is a midsagittal cross-section, showing cerebellar lobular organization, with each lobe demarcated by a Roman numeral. COP, copula pyramidis; FL, flocculus; LS, lobulus simplex; PF, paraflocculus; PML, paramedian lobule. (Adapted from Cerminara et al., 2015).

Figure 1.4 depicts a graphical representation of the cellular organisation in the cerebellar cortex. PCs found in the PC layer (PCL) are the largest neurons in the cerebellum (Herndon, 1963). PCs are GABAergic inhibitory neurons; their fibres extend towards the pial surface contacting the parallel fibres and their axons have direct contact with the deep cerebellar nuclei (Purves et al., 2001). The distinct cellular organisation of PCs accurately reveal their function as the sole output and a developmental central orchestrator of the cerebellum (Cerminara et al., 2015; Fleming and Chiang, 2015). Stellate, basket, lugaro and unipolar brush cells, along with the parallel fibres of excitatory glutamatergic GCs, are located in the molecular layer (ML), while the cellular body of GCs are found in the GC Layer (GCL) below the ML (Cerminara et al., 2015; Herndon, 1963). The PCs receive direct excitatory inputs from the climbing fibres that arise from the inferior olive (Cerminara et al., 2015; White and Sillitoe, 2013). The MF arise from the regions of the

precerebellar nuclei, and indirectly contact the PCs via the extensions of GC's parallel fibres (Cerminara et al., 2015; White and Sillitoe, 2013). Apart from these excitatory inputs, the PCs receive inhibitory signals from the stellate, basket and lugaro cells (Cerminara et al., 2015; White and Sillitoe, 2013). The deep cerebellar nuclei modulates multiple connections; it receives output signals from PCs and input signals from inferior olive and mossy fibres, which are then transmitted to the motor cortex of the cerebrum (Cerminara et al., 2015; White and Sillitoe, 2013). Among glial cells, the BG are the most abundant type in the cerebellum. They are situated in the PCL, with their fibres extending to the pial end of the cortex where they contact the granule cell fibres, and their soma situated very close to PCs (Yamada and Watanabe, 2002). A single PC is surrounded by approximately 8 BGs, with their fibres encapsulating the PC soma and dendrites, regulating the maturation and stability of PCs by providing fibres for neural migration and modulating Ca^{+} signalling (Bellamy, 2006; Reichenbach et al., 1995; Yamada and Watanabe, 2002). Other cerebellar glial cells include fibrous, vellate and protoplasmic astrocytes along with oligodendrocytes (Buffo and Rossi, 2013).

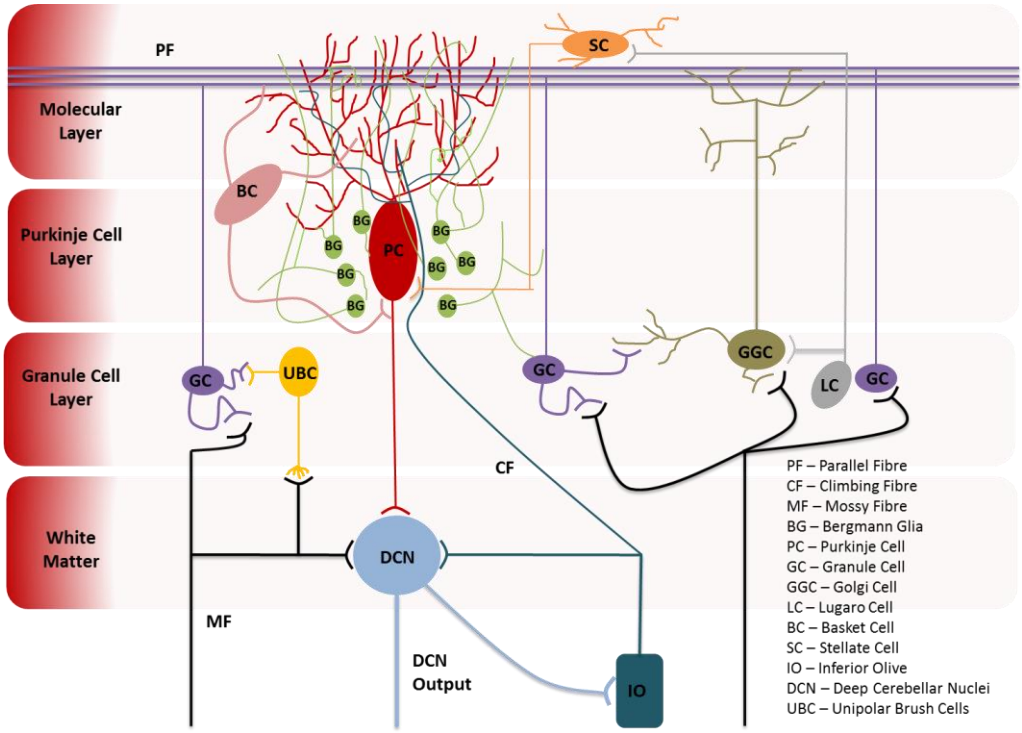


Figure 1.4: Simplified representation of cellular organisation in the adult mammalian cerebellum. MFs arise from the precerebellar nuclei and CFs arise from IO. PCs receive excitatory input via MFs and CFs. CFs directly contact PCs while MFs contact PCs through PF extensions of GCs. SCs and BCs provide inhibitory signals on PCs. BCs, SC, and GGCs contact the PFs, and GGCs provide inhibitory input to MFs. UBCs (only type 1 shown in the image) contact the MFs and the GCs. Glia other than BG are not shown here. (Adapted and re-made from Cerminara et al., 2015).

1.2.2. Cerebellar Development: Interaction of Purkinje neuron and Bergmann glia

In mice, PCs and BGs are born at early embryonic stages, establishing the primordial cerebellar developmental signalling pathways (Yamada and Watanabe, 2002). Both of these cell populations originate from the ventricular neuroepithelium, and migrate radially towards the pial surface to establish the PCL, which persists throughout adulthood (Yamada and Watanabe, 2002). They are interdependent and drive the maturation of each other, and regulate the proliferation and differentiation of GCs and other interneurons; therefore, their development pathways indicate key

aspects of cerebellar maturation (Leto et al., 2016; Yamada and Watanabe, 2002). This sub-section covers the developmental stages of BG and PC in mouse cerebellum.

The development of the cerebellum starts at the isthmic organizer (IO) near the midbrain-hindbrain boundary (MHB) around embryonic day 8. (E8). At E8.5 in mice, Fgf8 expression between the Otx2 expressing mid-brain and Gbx2 expressing hind-brain (in mice) becomes the central orchestrator of MHB and induces cerebellar differentiation by activating Irx2 expression via Ras-ERK pathway (Nakamura et al., 2005) (Figure 1.5).

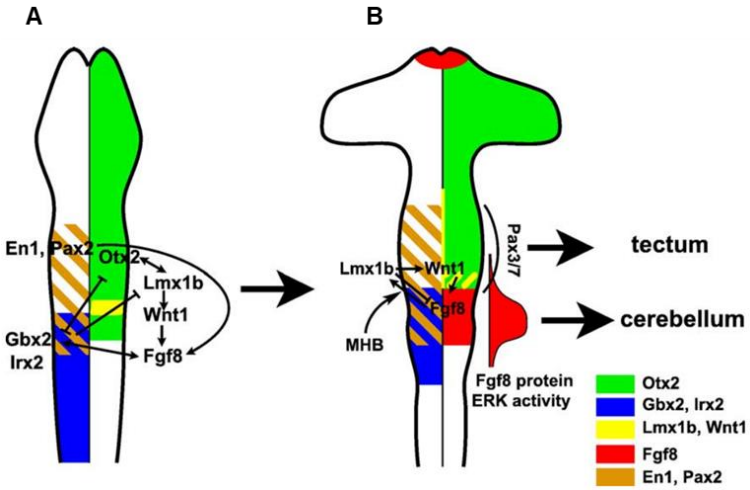


Figure 1.5: Isthmus related genes and organizing activity. Expression of Otx2 and Gbx2 in the rostral neural tube and in the posterior neural tube, respectively, from very early stages of development. Although (A) at first their expression overlaps near the isthmus, (B) later, due to the repressive interaction between Otx2 and Gbx2, their expression domains separate and abut at the isthmus and set the mid–hindbrain boundary (MHB) (as adapted from Nakamura et al., 2005).

The neural tube closes by E9, and from E10 to E14, the production of cerebellar progenitors begins; where the ventricular zone (VZ) and the rhombic lip (RL) gives rise to Ptf1a+ve GABAergic neurons including PCs

and Math1+ve glutamatergic neurons including GCs, respectively (Leto et al., 2016). Figure 1.6 shows the approximate birth date of cerebellar neurons.

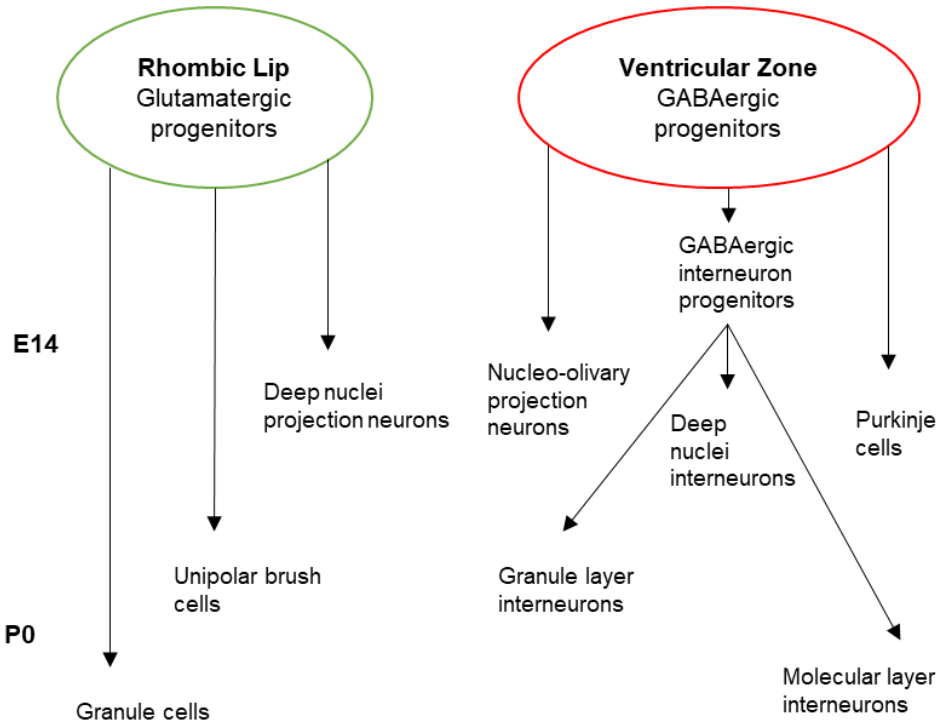


Figure 1.6: Birthdate of cerebellar neurons from rhombic lip and the ventricular zone (adapted from Leto et al., 2006).

PCs have a very distinct developmental pattern and are dependent upon BG migration. Two distinct progenitors derive all GABAergic neurons in the cerebellum – PC progenitors (PCPs) and Pax2+ve interneuron (IN) progenitors (Leto et al., 2016). The PCPs can be divided into two categories. The early born (~E10 to E11.5) posterior cohort of PCPs later become Zebrin II (ZII)+ve PCs while the late born (~E11.5 to E13) posterior cohort of PCPs become Zebrin II (ZII)-ve PCs (Chung et al., 2008; Leto et al., 2016; Sillitoe et al., 2009). At this time, the BGs, expressing the radial glial marker GLAST, arise from the VZ (from

approximately E14), following PC migration (E10.5 to E13) dorsally along the radial glial fibres (Yamada and Watanabe, 2002; Yuasa, 1996). Radial glial fibres may act as scaffolds for migration and maturation of both BGs and PCs. By E14.5, PCPs are depleted and are replaced by Pax2+ve interneuron (IN) progenitors (Seto et al., 2014) (Figure 1.7). Around this time, the migrating radial glia immediately form BG progenitors and begin to interact with PCs (Leto et al., 2016). On the other hand, GCs arise from the RL at E13.5 and proliferate tangentially along the dorsal end of PCL (Hatten and Heintz, 1995; Leto et al., 2016).

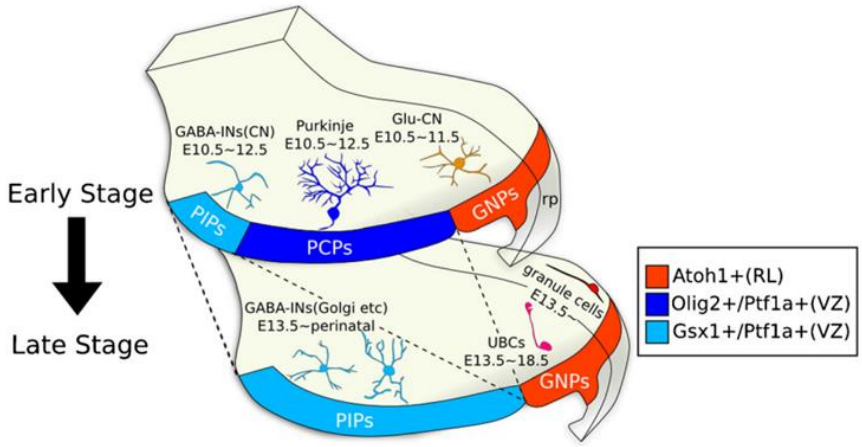


Figure 1.7: Progenitors and neurons in the cerebellum. Right is dorsal, left is ventral. GNPs-glutamatergic neuron progenitors, PIPs Pax-2+-IN progenitors, PCPs- Purkinje cell progenitors, rp-roof plate, GABA-INs (CN)-GABAergic interneurons in the cerebellar nuclei, Glu-CN-glutamatergic neurons in the cerebellar nuclei (adapted from Leto et al., 2016)

PCs and BG take part in cerebellar development by controlling proliferation of cerebellar niche. During postnatal development, PCs generate Sonic hedgehog (Shh) in a bidirectional axis that results in proliferation of GCs in EGL, and of a population of progenitors in the prospective white matter – the only two neurogenic sites in the cerebellum at this stage (Figure 1.8) (De Luca et al., 2015, 2016; Fleming

and Chiang, 2015). Following clonal expansion, GCs switch from tangential to radial migration downwards via the BG fibres to form the GCL (Figure 1.8) (Kerjan et al., 2005). During this time, BG undergo unique transformation of their fibres which extend to the pial layer and contact developing PC dendrites. The rod like domain of BGC fibre supports directional growth while the reticular fibre promotes glial covering and structural maturation of PCs (Bellamy, 2006). By the end of second postnatal week, the BG form sprouting fibres with multiple projections (a feature different from radial glial projections), towards the pial layer, facilitating the migration and maturation of GCs towards the future GCL (Leto et al., 2016). Simultaneously, the activation of Notch signalling in BG by establishing intricate synaptogenesis with PC dendrites, that binds the Delta/Notch-like EGF-related receptor (DNER), drives BG maturation (Eiraku et al., 2005). While other late-astroglial progenitors found in the prospective white matter below the GCL give rise to other cerebellar glial and IN population in response to extra-cerebellar as well as PCs' Shh signals, PCs and BGCs are involved in development and maturation of topographic zones and foliation of the adult cerebellum (Cerminara et al., 2015; De Luca et al., 2016; Fleming et al., 2013; Leto et al., 2016; Reeber et al., 2018; Yamada and Watanabe, 2002).

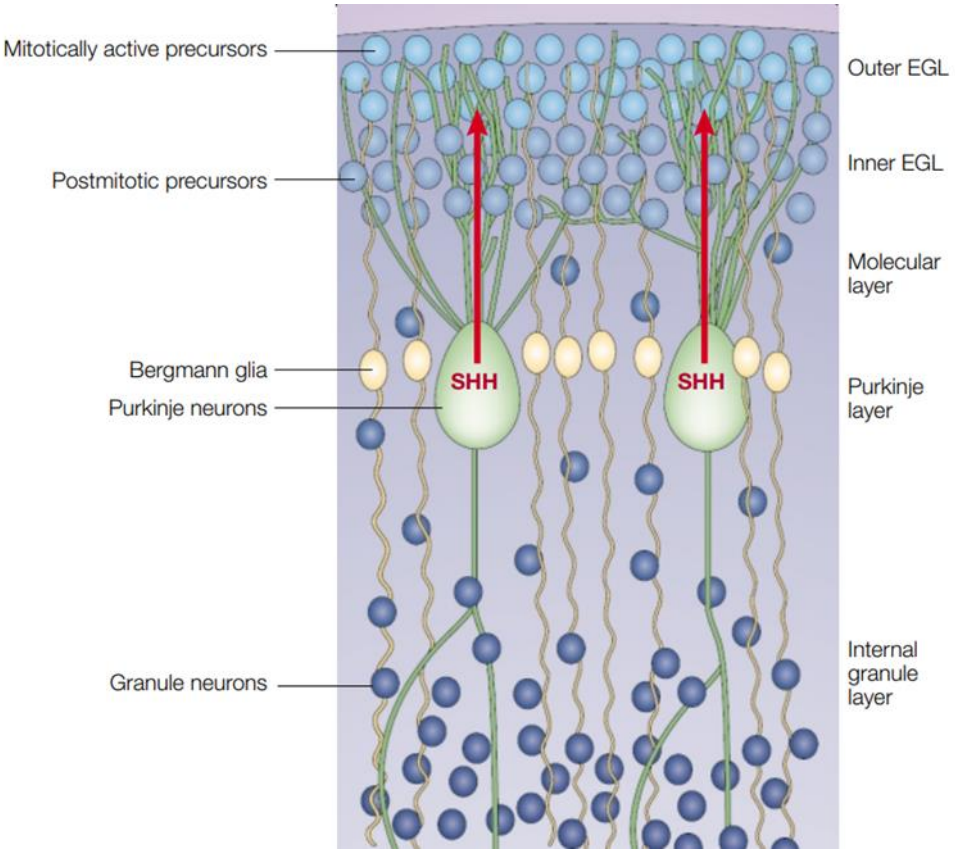


Figure 1.8: Migration of granule cells to granule cell layer via Bergmann fibres during the first postnatal week of cerebellar development. SHH (sonic hedgehog) modulation by PCs drive the granule cell migration from external granular layer (EGL) to internal granular layer (IGL) (adapted from Ruiz i Altaba et al., 2002).

1.2.3. Adult cerebellum stem cells: NSC characteristics of Bergmann glia

The adult cerebellum has been reported to show poor regenerative capacity after saponin induced PC death, as seen in rat models (Altman and Das, 1966; Grimaldi and Rossi, 2006). Unlike the active neurogenic niches, including the SVZ and the SGZ, there is a lack of evidence for stem cell activity in the cerebellar cortex of the adult mammalian brain. However, there has been increasing speculation over the years for the presence of dormant NSC population in the cerebellum to exist within the

BG in the adult mammalian brain (Alcock and Sottile, 2009; Alcock et al., 2009; Sottile et al., 2006).

Over a decade ago, a study demonstrated that NSCs exist in the cerebellum of postnatal day 7 (P7) mice, and these NSCs are CD133+ve and lineage -ve (did not express markers of neurons/astrocytes/oligodendrocytes) (Lee et al., 2005). A parallel study demonstrated that NSCs existed in adult mouse cerebellum as well, and that these NSCs show neurosphere forming ability and subsequent differentiation into cerebellum specific neuroglia including Tag1+ve GCs, Calbindin+ve PCs, and GFAP+ve BGs *in vitro* (Klein et al., 2005). A subsequent study proposed the identity of the above mentioned cerebellar NSCs to be BG (Alcock and Sottile, 2009). BG expressed the NSC markers Sox1, Sox2 and Sox9 in the cerebellum of adult mice (Sottile et al., 2006). The Sox1/2/9 expression pattern of BG was shown to be conserved in the adult human cerebellum as well (Alcock et al., 2009). Further analysis showed that Sox1+ve cells represented 90.1% of the CD133+ve cells in the P7 mice cerebellum, indicating BG to be the source of NSCs in the previous study (Alcock and Sottile, 2009; Lee et al., 2005). Upon puromycin-based selection of Sox1-GFP cells from the adult mice cerebellum, BG showed the ability to form neurospheres and differentiate into neural lineages, consistent with the observations of previous reports (Alcock and Sottile, 2009; Klein et al., 2005; Lee et al., 2005). The above-mentioned findings are outlined in Figure 1.9.

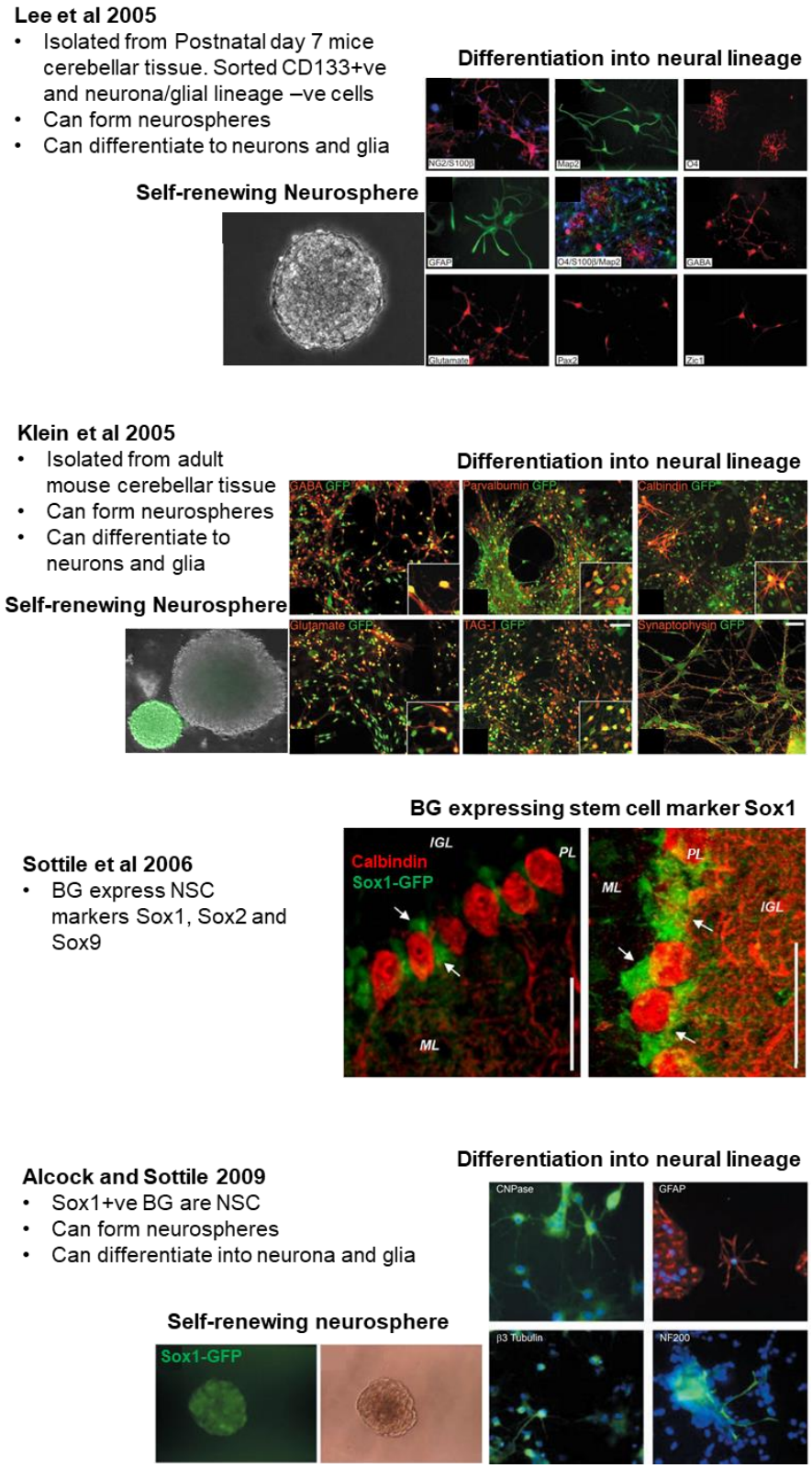


Figure 1.9: Key discoveries supporting BG as NSCs of adult cerebellum. Figures are adapted from published materials (Alcock and Sottile, 2009; Klein et al., 2005; Lee et al., 2005; Sottile et al., 2006) (Studies from Sottile lab were conducted on adult mice). Annotations are hidden here to avoid confusion. BG-Bergmann glia, PC-Purkinje cell, PL-Purkinje layer, ML- Molecular layer, IGL-Internal granular layer.

Although, BG show potential for proliferation and differentiation *in vitro*, their neurogenic potential *in vivo* is under debate. BG generally appear to be dormant in the adult brain under normal physiology. Using a combination of immunohistochemistry for labelling NSCs and neural cells, and BrdU (Bromodeozyuridine) and EGFP-retroviral injections for labelling proliferating cells, a study has demonstrated that most cerebellar NSCs in the adult mice brain are quiescent and do not give rise to new neuroglia under normal physiological conditions (Su et al., 2014). In contrast, a recent study has shown that BG harbour a discrete Sox2+ve population which express the proliferation marker of Ki67 (Ahlfeld et al., 2017) (Figure 1.10). Interestingly, BG have been reported to respond to external stimuli. BG fibres are shown to re-express the NSC marker Nestin in response to transplantation of embryonic PCs into the cerebellar cortex (Sotelo et al., 1994). Moreover, physical exercise has shown to increase the proliferative and differentiation ability of Sox2+ve cells in the adult mice cerebellum, showing BG response to stimuli (Ahlfeld et al., 2017) (Figure 1.10).

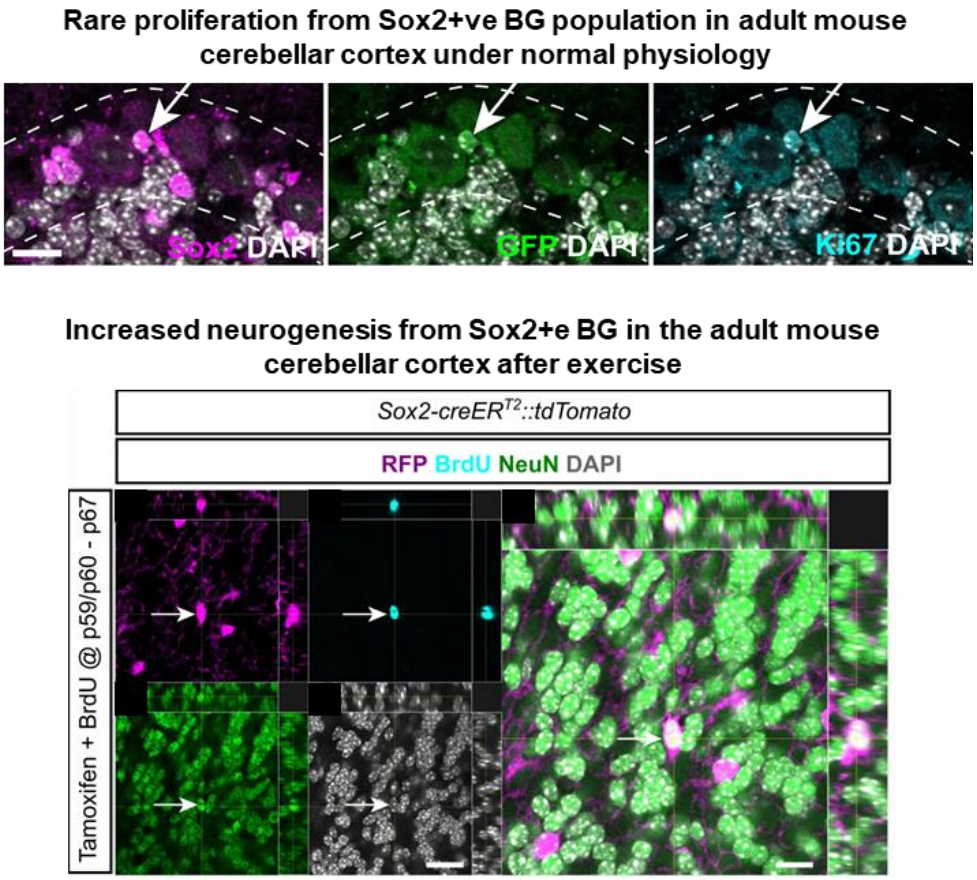


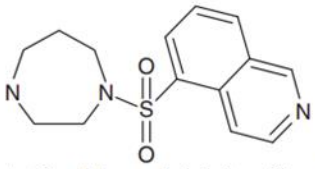
Figure 1.10: Evidence for BG (Bergmann glia) neurogenesis in the cerebellar cortex of adult mice. Top image shows proliferation of BG under normal physiology; colocalisation of BG marker Sox2, active NSC marker Nestin (GFP), and proliferation marker Ki67. Bottom image shows neurogenesis by BG. RFP (red fluorescent protein) marks cells derived from Sox2, BrdU marks divided cell and NEUN marks mature granule neurons. Here, mice that underwent rotarod tests showed 3-fold increase in NeuN cells generated by Sox2 cells. Figure adapted from published material (Ahlfeld et al., 2017).

These observations indicate the potential of BG as a source of neurogenesis in the adult cerebellum. However, further research is necessary to understand the extent of neurogenic potential of BG in the adult cerebellum, and in the future, identify pathways to stimulate stem cell-based repair in cerebellar degenerative disorders.

1.3. Neurogenic effect of ROCK inhibitor - fasudil

Fasudil (also known as HA-1077) is an isoquinoline sulfonamide derivative, and the only clinically available Rho-associated protein kinase (ROCK) inhibitor in use for patients with neurological disorders (Figure 1.11). Fasudil promotes its effect by inhibiting ROCK1 and ROCK2 of the Rho-ROCK cascade. This section will introduce the role of Rho-ROCK cascade in CNS and the properties of fasudil as a neuroprotective drug.

Drug summary.

Drug name	Fasudil
Phase	Phase II/III clinical trials
Indication	CNS disorders
Pharmacology description	Protein kinase inhibitor
Route of administration	Inhaled, injectable
Chemical structure	
Pivotal trial(s)	A Rho-kinase inhibitor (fasudil) in the treatment of Raynaud's phenomenon The effects of fasudil on vascular function in humans Rho-kinase (ROCK) inhibition in carotid atherosclerosis Antihypertensive agent [angiotensin-converting enzyme inhibitors (ACEi)] and heart function improvement in association with ROCK activity changes in humans

Pharmaprojects – copyright to Citeline Drug Intelligence (an Informa business). Readers are referred to Pipeline (http://informa-pipeline.citeline.com) and Citeline (http://informa.citeline.com).

Figure 1.11: Summary of fasudil (Adapted from Chen et al., 2013).

1.3.1. Rho-ROCK cascade in central nervous system

Accumulation of ROCK has been involved in a variety of neuronal functions including inhibition of axonal regeneration, inhibition of neuronal differentiation and proliferation of tumor cells (Chen et al., 2013; Compagnucci et al., 2016; Liu et al., 2015b; Ying et al., 2006). ROCK is a direct downstream effector of Rho (a member of the Rho-GTPases belonging to the Ras superfamily) (reviewed in Fujita and Yamashita, 2014; Kubo et al., 2008; Liu et al., 2015b). There are two isoforms of ROCK – ROCK1 and ROCK2, of which the latter is mainly expressed in the CNS.

Myelin-associated inhibitory factors such as myelin associated glycoprotein, oligodendrocyte myelin glycoprotein and Nogo-A can activate the Rho-ROCK signalling pathway by binding to the Nogo receptor (NgR1/2/3)/Lingo-1/p75 receptor complex present in the cell membrane (reviewed in Fujita and Yamashita, 2014; Liu et al., 2015b) (Figure 1.12). Rho-ROCK signalling can also be activated by the binding of repulsive guidance molecule to neogenin receptor, or by the binding of Nogo-A to G protein-coupled receptor, sphingosine-1-phosphate receptor 2, or by the binding of chondroitin sulfate proteoglycans (released from reactive astrocytes) to protein tyrosine phosphatase, leukocyte common antigen phosphatase (LAR), or the NgR1/3 receptors (reviewed in Fujita and Yamashita, 2014) (Figure 1.12). This is followed by conversion of Rho guanosine diphosphate (GDP) to guanosine triphosphate (GTP) which will activate ROCK (Figure 1.12).

ROCK can then inhibit axonal regeneration by multiple pathways. ROCK can phosphorylate Lin-11, Isl-1, and Mec-3 kinase, which will in turn phosphorylate cofilin, resulting in stabilization of actin filaments in the growth cone, which will prevent growth (reviewed in Fujita and Yamashita, 2014; Liu et al., 2015b) (Figure 1.12). ROCK can also prevent neurite outgrowth by inhibiting tubulin polymerization, by phosphorylating collapsin response mediated protein 2 (CRMP-2) which leads to disrupted tubulin polymerization (reviewed in Fujita and Yamashita, 2014; Liu et al., 2015b) (Figure 1.12). ROCK can also phosphorylate the myosin light chain (MLC) which leads to a series of events that causes neurite retraction and collapse of the growth cone in the CNS (reviewed in Fujita and Yamashita, 2014; Liu et al., 2015b) (Figure 1.12). ROCK activation can take place alternatively via the PIR-B receptor (Figure 1.12). Overall, the result is a lack of nerve growth, neural support and axon regeneration. Therefore, inhibitors for Rho-ROCK pathway are being targeted for their potential to treat neurological disorders including stroke, ischaemia, Alzheimer's Disease and Parkinson's Disease (reviewed in Chen et al., 2013).

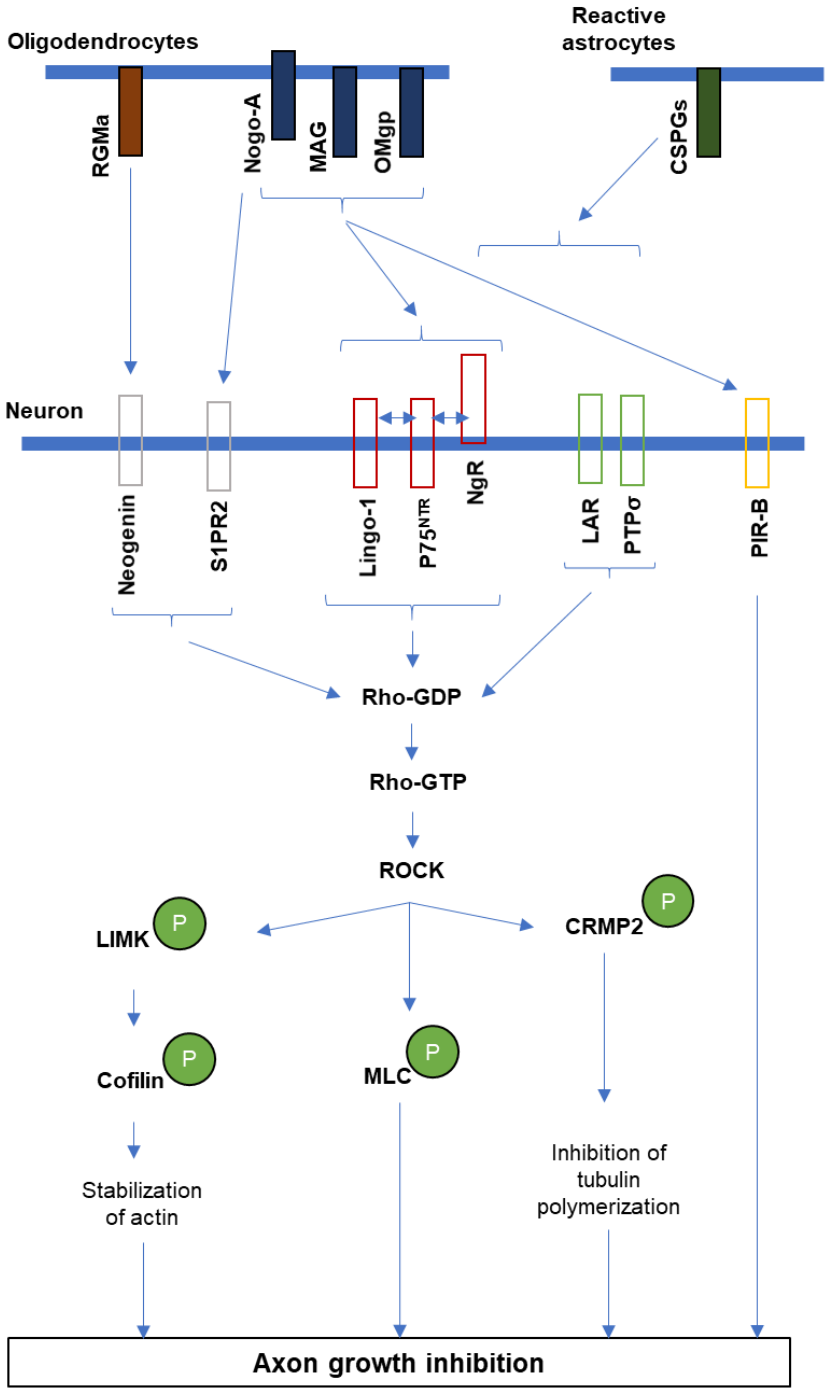


Figure 1.12: Graphical overview of Rho-ROCK cascade in axonal growth inhibition of neurons. RGMa (repulsive guidance molecule), MAG (myelin associated glycoprotein), OMgp (oligodendrocyte-myelin associated glycoprotein), CSPGs (chondroitin sulfate proteoglycans), S1PR2 (sphingosine-1-phosphate receptor 2), NgR (Nogo receptor), LAR (leukocyte common antigen phosphatase), PTPσ (protein tyrosine phosphatase), GDP (guanosine diphosphate), GTP (guanosine triphosphate), ROCK (Rho-associated protein kinase), LIMK (Lin-11, Isl-1, and Mec-3 kinase), MLC (myosin light chain), CRMP2 (collapsin response mediator protein 2), Upper case letter 'P' in green circle – Phosphorylation. (Adapted and re-made from Fujita and Yamashita, 2014; Liu et al., 2015b).

1.3.2. Fasudil as a clinical drug for neurological disorders

The inhibition of ROCK by fasudil is known to improve axon regeneration and neurite outgrowth, and multiple studies in animal models have shown that fasudil can be effective in promoting neuronal protection. The beneficial effects of fasudil has been suggested to be associated with its modulation of ROCK, MLC phosphorylation, nitric oxide (NO) production, blood flow viscosity and intracellular calcium (reviewed in Chen et al., 2013). Fasudil has been reported to improve stroke protection and blood flow after cerebral ischaemia by increasing NO production and eNOS (endothelium-derived NO synthase) expression (Rikitake et al., 2005). In experimental autoimmune encephalomyelitis, fasudil has been shown to delay the onset and severity of the disease by shifting microglia to an anti-inflammatory M2 phenotype that promotes tissue repair (Hou et al., 2012). Moreover, studies have suggested that fasudil can protect neurons and mobilize NSCs in *in vitro* ischaemic models by activating astrocyte secretion of granulocyte-colony stimulating factor (G-CSF) and inhibiting glutamate induced neurotoxicity (Ding et al., 2010; Huang et al., 2009; Yamashita et al., 2007). Table 1.1 provides an overview of the use of fasudil in clinical as well as animal models for multiple neurological disorders.

Table 1.1: The effects of fasudil against CNS disorders in clinic or animal models: potential mechanism(s) and the delivery and dosage used. EAE: Experimental autoimmune encephalomyelitis; EBI: Early brain injury; eNOS: Endothelial nitric oxide synthase; IFN: Interferon; IL: Interleukin; i.p.: Intraperitoneal injection; i.v.: Intravenous injection; i.c.v.: Intra-cerebroventricular injection; MLCP: Myosin light chain phosphatase; NF-kB: Nuclear factor-kappa B; SCI: Spinal cord injury; TLR-4: Toll-like receptor. (Adapted from Chen et al., 2013).

Disorders	Pathophysiological conditions	Mechanism of action	Delivery and dosage
SAH	Vasospasm; EBI	Blockade of ROCK and MLCP; decreasing myosin phosphorylation; dilating smooth muscle; reduction of blood viscosity; inhibition of glutamate-induced excitotoxicity; release of intracellular Ca2+; upregulating eNOS expression	Orally 10 mg/d in human
Stroke	Excitotoxicity; calcium dysregulation; oxidative and nitrosative stress; inflammation	Inhibiting ROCK; increasing expression of carbon monoxide synthase and cerebral blood flow; preventing neuron death; preserving endothelial function; attenuating leukocyte trafficking in the microcirculation	Orally 60 mg twice per day in human
SCI	Initial mechanical trauma; axons injury; excitotoxicity	Reducing the number of infiltrating cells; prolonging the expression of eNOS; enhancing nerve-fiber growth; decreasing tissue damage and cavity formation	i.p. 10 mg/kg in rat; infused into arteries 0.1 mg/kg in rabbit
AD	Neurodegeneration; chronic low grade; systemic inflammation; oxidative stress	Decreasing Aβ42 level; promoting the regeneration of neuron; repairing the neural circuits; lessening branching of the dendrite; enhancing learning ability; decreasing phosphorylated tau levels	i.c.v. 0.6 mg/kg/d in mice; i.p. 10 mg/kg in rat
PD	Loss of dopaminergic neurons in the substantia nigra pars compacta; presence of lewy body; axonal degeneration	Attenuating dopaminergic cell loss; preserving doparminergic terminals	Orally 30 mg/kg in mice
Neuropathic pain	Inflammation; peripheral sensitization; central sensitization	Inhibiting ROCK; anti-inflammation	i.v. 30 mg/kg in rat
EAE	Activation of T cells and macrophages; release of cytokines and inflammatory mediators	Downregulation of interleukin-17 and IFN; inhibiting T-cell proliferation; preventing the inflammatory cells into the CNS; inhibiting TLR-4, p-NF-kB/p65, and inflammatory cytokines (IL-1b, IL-6, and TNF-a); enhancing IL-10 production	i.p. 5 mg/kg in rat
Epilepsy	Epileptic seizures; excessive enhancement of excitatory neurotransmission; reduction of inhibitory pathways	Reducing the average seizure levels; suppressing the percentage of tonic convulsion index and recovery latency	i.p. 25 mg/kg in mice

1.4. Extracellular vesicles

Extracellular vesicles (EVs) are lipid membraned nanostructures secreted by cells either directly from the plasma membrane or via the endosomal pathway (reviewed in van Niel et al., 2018). EVs contain and transport miRNAs (Valadi et al., 2007), mRNAs (Valadi et al., 2007) and active proteins (Katsuda et al., 2013) reported to modulate inter-cellular communication, with increased prevalence in a range of biological processes linked to cancer (reviewed in Wu et al., 2017), neuroscience (reviewed in Chivet et al., 2012), and stem cell biology (reviewed in Chen et al., 2017). Stem cells have been reported to secrete paracrine factors largely via EVs, with relevance to immune modulation (reviewed in Zhang et al., 2014) and tissue repair (reviewed in Chen et al., 2017). Mesenchymal stem cells (MSCs) are known to be a rich source of EVs suggested to promote healing in cutaneous wounds (Hu et al., 2016), bone fractures (Furuta et al., 2016) and liver injury (Tan et al., 2014). NSC derived EVs have shown specific properties including modulating downstream signalling pathways in recipient cells, mediate viral entry, act as independent metabolic units, promote neuronal recovery, slow aging process and protect neurons after stroke (reviewed in Vogel et al., 2018). These observations indicate stem cells may provide a source of therapeutically useful EVs that could offer possible cell-free treatment strategies for regenerative therapy.

1.4.1. Classification of EVs

EVs are highly heterogeneous and contain multiple subtypes which are yet to be identified and understood. However, EVs can be broadly classified into two groups based on their biogenesis and size distribution, namely- exosomes and microvesicles (reviewed in van Niel et al., 2018). Exosomes are considered to be 30 nm to 100 nm EVs which are intraluminal vesicles (ILVs) formed by the inward budding of endosomal membrane during maturation of multi-vesicular endosomes, which are intermediates within the endosomal system, and secreted upon fusion of multi-vesicular endosomes with the cell surface (reviewed in van Niel et al., 2018). On the other hand, microvesicles are considered to be 50 nm to over 1 µm in diameter and are generated by the outward budding and fission of the plasma membrane and the subsequent release of vesicles into the extracellular space (reviewed in van Niel et al., 2018). In addition, the extracellular niche will contain other types of particles which are yet to be confirmed to be classified as EVs or not; for example, lipoproteins (Karimi et al., 2018). Novel technical developments for isolation and characterisation of EVs are constantly being made to further the understanding of EV biology. Figure 1.13 shows the current knowledge on classification of EVs as exosomes and microvesicles.

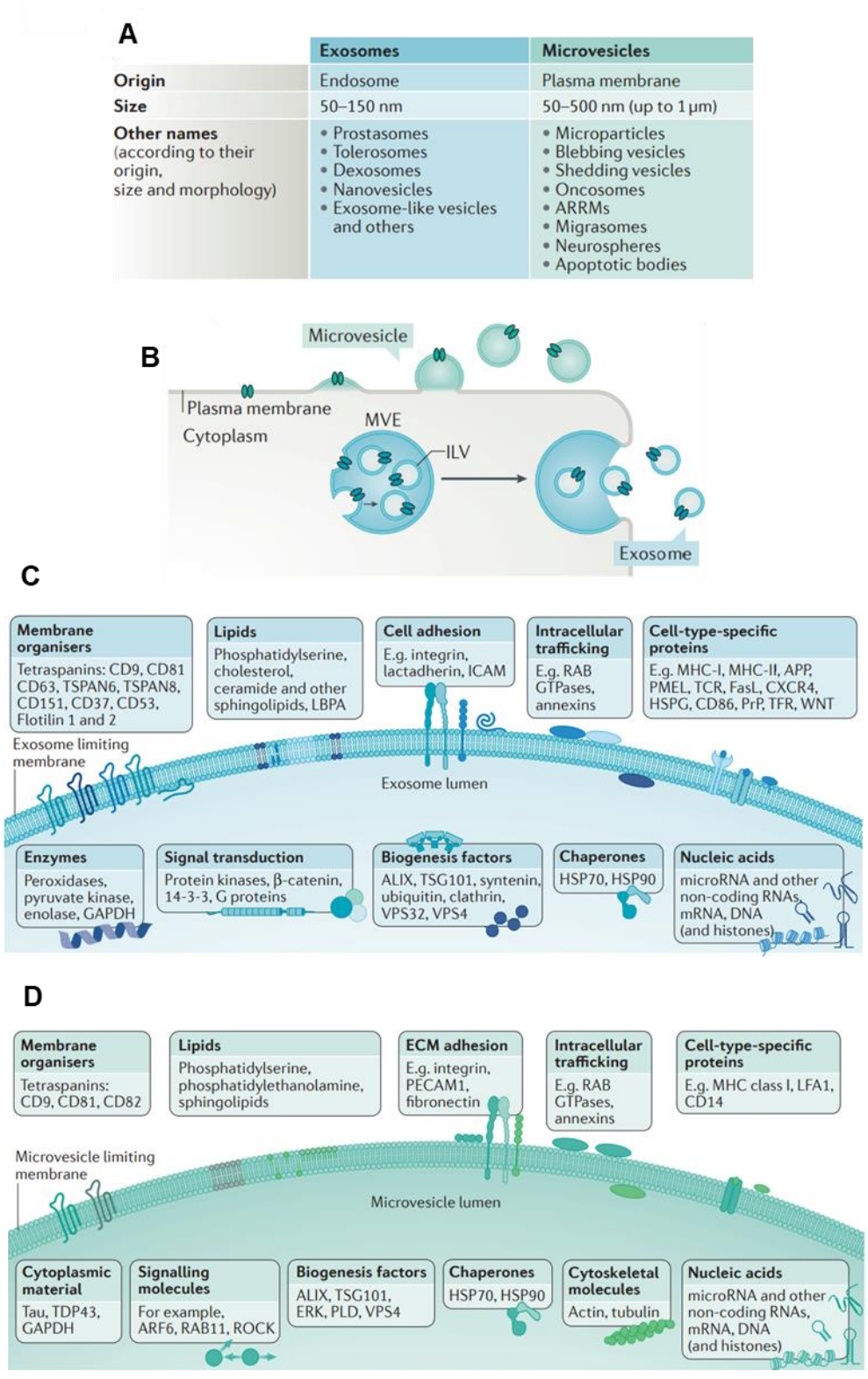


Figure 1.13: Classification of EVs as exosomes and microvesicles. (A) Size range and nomenclature of exosomes and microvesicles. (B) Graphical representation of the differences in the biogenesis of exosomes vs microvesicles. Biological composition of (C) exosomes and (D) microvesicles. ILV, intraluminal vesicles; MVE, multivesicular endosomes; ALIX, ALG-2 interacting protein X; APP, amyloid precursor protein; ARF6, ADP-ribosylation factor 6; ARMMs, arrestin-domain-containing protein 1-mediated microvesicles; CXCR4, CXC-chemokine receptor

4; GAPDH, glyceraldehyde-3-phosphate dehydrogenase; HSP70, heat shock 70 kDa protein; HSPG, heparan sulfate proteoglycan; ICAM, intercellular adhesion molecule; LBPA, lyso-bis-phosphatidyl acid; LFA1, lymphocyte function-associated antigen 1; MHC, major histocompatibility complex; PECAM1, platelet endothelial cell adhesion molecule; PLD, phospholipase D; PrP, prion protein; ROCK, RHO-associated protein kinase; TCR, T cell receptor; TDP43, TAR DNA-binding protein 43; TFR, transferrin receptor; TSG101, tumour susceptibility gene 101 protein; TSPAN, tetraspanin; VPS, vacuolar protein sorting-associated protein. (Adapted from van Niel et al., 2018).

1.4.2. Biogenesis and secretion of EVs

1.4.2.1. Formation of EVs

To investigate the function of EVs, it is necessary to understand the biogenesis and fate of EVs in the cell biology. Specific machineries are involved in EV biogenesis. However, exosome and microvesicle biogenesis may share multiple components of the same EV machinery. For exosomes, the biogenesis begins by segregating cargo (proteins or nucleotides) on microdomains of the limiting membrane (the membrane that is going to form ILVs) with subsequent inward budding and fission forming small vesicles with sequestered cytosol components (reviewed in van Niel et al., 2018) (Figure 1.14). Exosome biogenesis can be broadly classified by two machineries, namely- the endosomal sorting complex required for transport (ESCRT)-dependent and the ESCRT-independent machineries (reviewed in van Niel et al., 2018). In the ESCRT dependent machinery, the ESCRT components (ESCRT-0, I, II and III) work in a step-wise manner to produce ILVs, which can additionally be intersected by syntenin and ALG2 interacting protein X (ALIX) and vacuolar protein sorting-associated protein 32 to sort specific cargoes (Baietti et al., 2012; Hurley, 2008; Tamai et al., 2010) (Figure 1.14). Via the ESCRT independent machinery, exosomes can be

produced by either ceramide or tetraspanins (eg: CD63, CD9 and CD81) (reviewed in van Niel et al., 2018) (Figure 1.14). On the basis of cargo sorting, protein molecules are known to be recruited either via lipid-based affinity, ubiquitylation, or co-sorting with other proteins such as heat shock 70kDa protein, and nucleotides are known to be sorted based on motif recognition by sub-complexes of ESCRT-II, tetraspanin microdomains, and the KRAS–MEK signalling pathway (reviewed in van Niel et al., 2018). Microvesicles biogenesis is known to be modulated by change in Ca^{+} levels. Ca^{+} dependent machineries including aminophospholipid translocases (flippases and floppases), scramblases and calpain, are known to modulate plasma membrane symmetry and underlying actin cytoskeleton, resulting in microvesicle formation (reviewed in van Niel et al., 2018). Also, the Rho-ROCK cascade mediated cytoskeletal changes via actin and myosin have been proposed to module microvesicle formation (Li et al., 2012). Microvesicle cargo are sorted via lipid affinity-based molecules and/or plasma membrane anchors (palmitoylation, prenylation, myristoylation) (reviewed in van Niel et al., 2018).

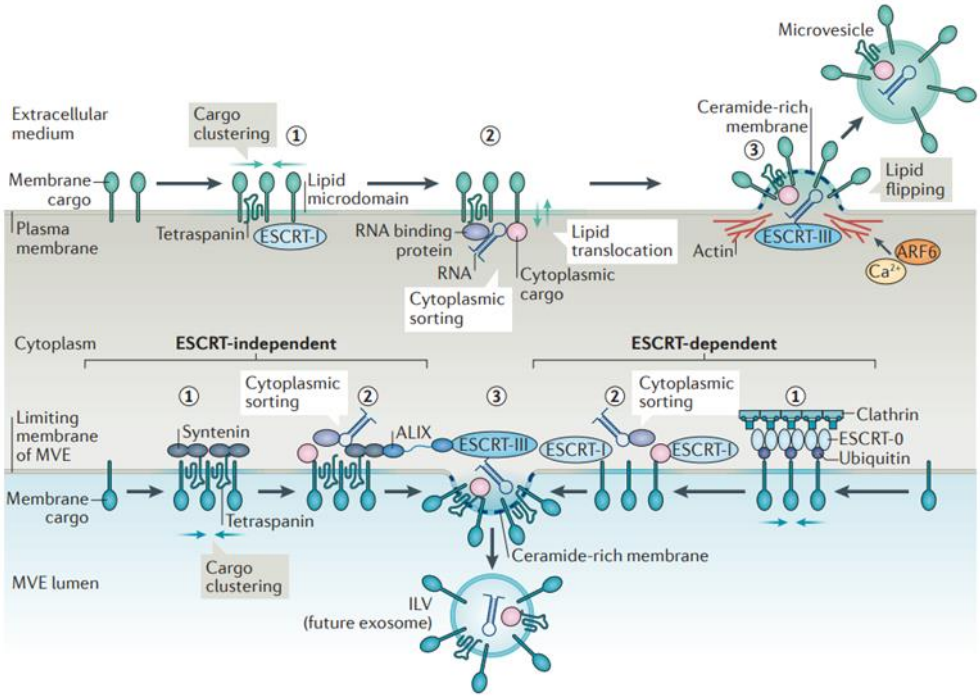


Figure 1.14: Formation of EVs in cells via ESCRT- dependent and ESCRT independent machineries. ILV, intraluminal vesicles; MVE, multivesicular endosomes; ALIX, ALG-2 interacting protein X; ARF6, ADP-ribosylation factor 6; ESCRT, endosomal sorting complex required for transport. (Adapted from van Niel et al., 2018).

1.4.2.2. Transport and/or release of EVs

After formation, vesicles are known to be destined for either of the three routes, namely- lysosome degradation, autophagosome digestion, or vesicle release (reviewed in van Niel et al., 2018) (Figure 1.15). Some evidences supported the syntenin-syndecan-ALIX pathway to be secretion specific (Baietti et al., 2012), while ESCRT pathway is destined for both secretion and lysosome degradation (reviewed in van Niel et al., 2018). Vesicles are transported using the cytoskeletal components (actin and microtubules), molecular motors (dynein,kinesin and myosin), and molecular switches (GTPases) (Bonifacino and Glick, 2004; Cai et al., 2007) (Figure 1.15). Ras related protein 7 (RAB7) has been proposed to be involved in transporting ILVs either to lysosomes or to plasma

membrane based on its ubiquitylation status (Figure 1.15). Additionally, the RAB27 isoforms (a and b), RAB11 and RAB37 have been considered recently as essential components for directing ILVs for exosome secretion (van Niel et al., 2018; Ostrowski et al., 2010) (Figure 1.15). Soluble NSF attachment protein receptor complex of proteins have been proposed to be associated with fusion of ILVs with the plasma membrane (Cai et al., 2007; van Niel et al., 2018) (Figure 1.15). The release of microvesicles has been shown to be dependent on interaction and changes in actin and myosin with a subsequent ATP-dependent contraction, such as the activation of small GTP-binding proteins leading to the phosphorylation of MLC and actomyosin contraction, which allows vesicle budding in cancer cells (reviewed in van Niel et al., 2018). Importantly, in biogenesis as well as for the release of vesicles, Ca^{+} concentration has been observed to play a controlling role (reviewed in van Niel et al., 2018).

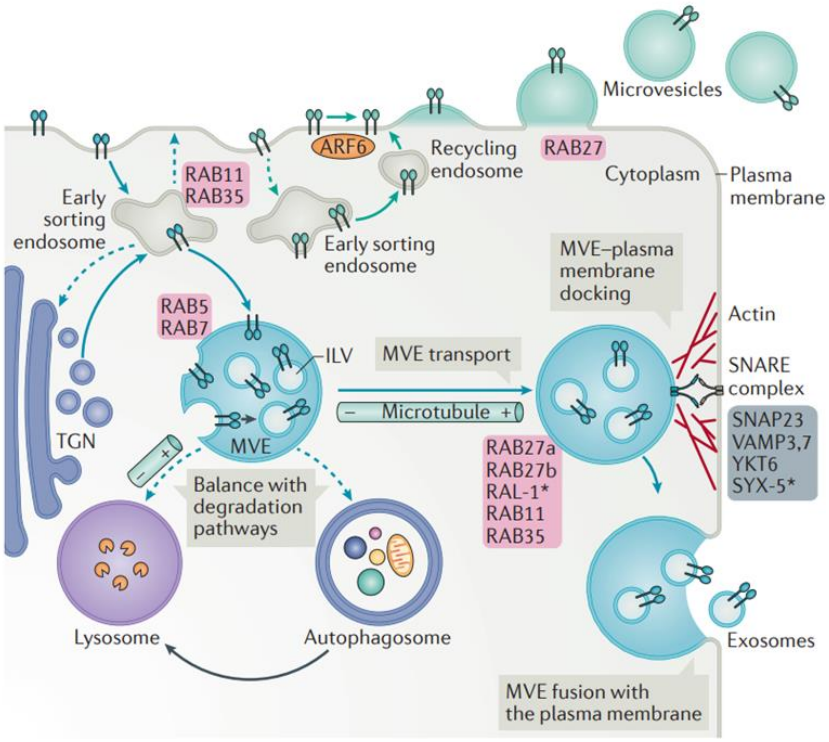


Figure 1.15: Release of EVs and major components proposed to be associated with the EV release. ILV, intraluminal vesicles; MVE, multivesicular endosomes; TGN, trans-Golgi network; RAB, Ras related protein; SNARE, Soluble NSF attachment protein receptor; ARF6, ADP-ribosylation factor 6; RAL-1, RAL (Ras-related GTPase) homolog; SNAP23, synaptosomal-associated protein 23; SYX-5, syntaxin 5; VAMP3, vesicle-associated membrane protein 3. *Denotes Caenorhabditis elegans proteins. (Adapted from van Niel et al., 2018).

1.4.2.3. Internalisation of EVs in recipient cells

After their release, EVs can target a wide range of cells or specific cells depending on its membrane composition and become internalised. Target cell-EV interaction and specificity can be mediated by integrin extracellular matrix (ECM), tetraspanins, lipids, lectins and heparan sulfate proteoglycans; help in docking, internalisation, and/or membrane fusion of EVs on plasma membrane (reviewed in van Niel et al., 2018) (Figure 1.16). EVs may stay at the plasma membrane or get internalised via endocytosis (clathrin-dependent/independent, caveolae, or lipid rafts) (reviewed in van Niel et al., 2018) (Figure 1.16). Once docked at the

plasma membrane, EVs can enter the endocytic pathway where majority the EVs are transported to lysosomes and some escape to release contents into the cytoplasm, or activate downstream signalling pathways to modulate cell behaviour (reviewed in van Niel et al., 2018) (Figure 1.16).

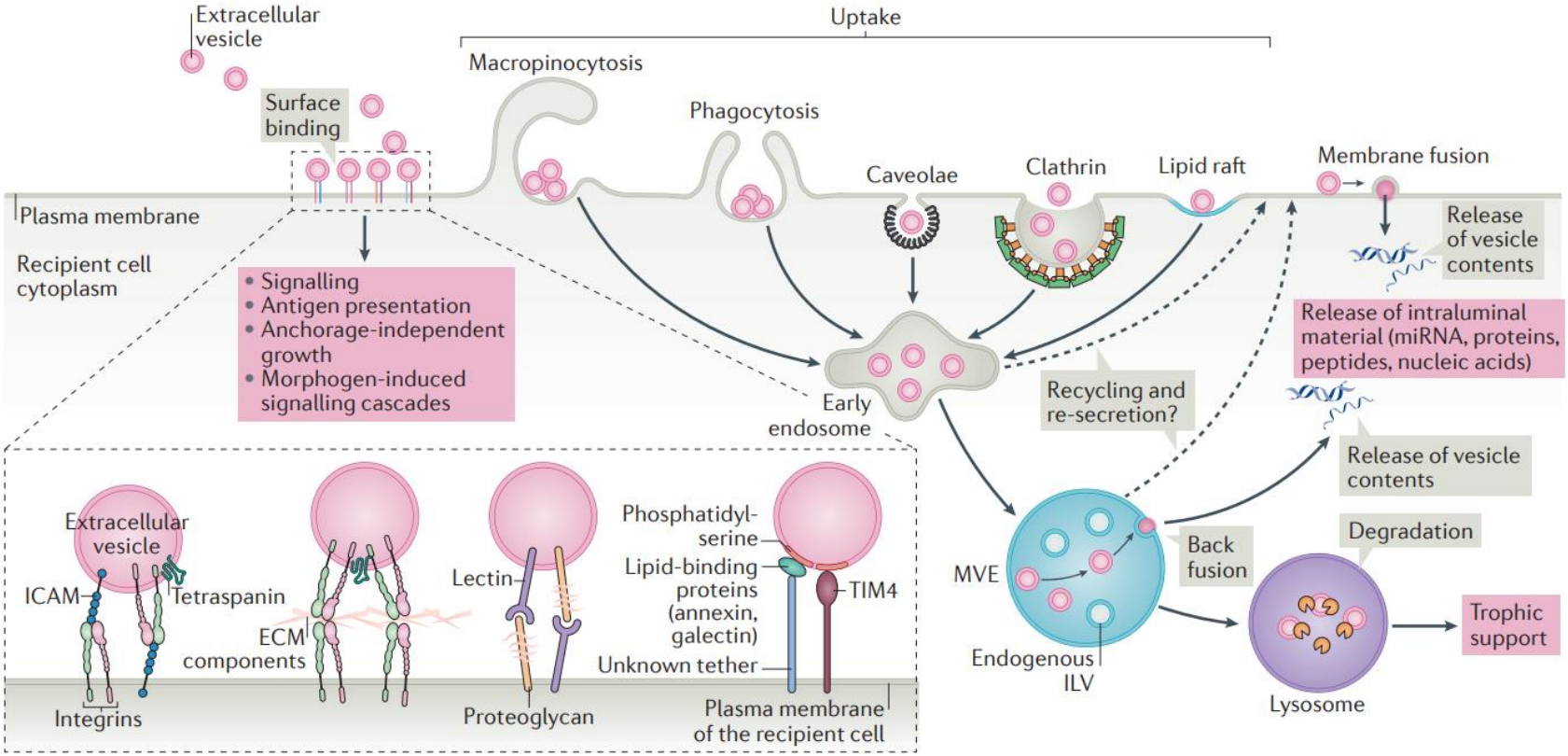


Figure 1.16: Mechanisms of EV uptake into recipient cells. Of note, there is no evidence so far to exclude potential recycling to the plasma membrane of endocytosed vesicles (dashed arrows). ILV, intraluminal vesicles; MVE, multivesicular endosomes; ECM, extracellular matrix; ICAM, intercellular adhesion molecule; TIM4, T cell immunoglobulin mucin receptor 4. (Adapted from van Niel et al., 2018)

1.4.3. EVs in the CNS

1.4.3.1. EVs in healthy and injured CNS

EVs have been reported to play crucial roles in the cellular communication, disease progression and neural repair of the CNS (reviewed in Holm et al., 2018).

In the healthy CNS, EVs have been reported to play a vital role in maintaining physiology. However, the mechanisms of the overall EV based-communication systems are still largely unknown. Several studies have suggested that neurons secrete miRNA containing EVs with specific functions. It has been reported that neuronal EVs can be associated with modulation of synaptic activity by transferring miR-124a into astrocytes (Morel et al., 2013), increase microglial phagocytosis and synaptic pruning by increasing microglial expression of complement component 3 (Bahrini et al., 2015), and modulate brain vascular integrity by transferring miR-132 into vascular endothelial cells and increase their expression of the adherent junction protein- cadherin 5 (Xu et al., 2017). On the other hand, glial EVs are also known to play independent as well as synergic roles in brain homeostasis. Oligodendroglia-derived EVs have shown to increase neuronal firing, modulate the expression of neuronal plasticity genes (VGF nerve growth factor inducible and brain-derived neurotrophic factor (Bdnf)) (Fröhlich Dominik et al., 2014; Frühbeis et al., 2013), and auto-inhibit myelin membrane expansion *in vitro* via ROCK activation (Bakhti et al., 2011). Microglial EVs been

reported to play a role in modulating excitatory neurotransmission followed by presynaptic release of neurotransmitters, such as decreased release of GABA in response to cannabinoid receptor binding (Gabrielli et al., 2015).

In the injured CNS, EVs play a vital role in regulating neuro-inflammation, neuro-protection and regeneration. Adenosine tri-phosphate (ATP) released from astrocytes and/or injured brain tissues are known to promote release of pro-inflammatory cytokine IL-1β containing EVs by astrocytes and microglia (Bianco et al., 2005). It was recently shown that microglial cultures treated with ATP and pro-inflammatory cytokines can release EVs containing miR-146a-5p, which results in decrease in synaptic proteins (Neuroligin 1 and Synaptotagmin 1), synaptic stability and strength of hippocampal neurons (Prada et al., 2018). Oligodendroglia-derived EVs have been reported to promote neuronal survival in a stroke model of oxygen-glucose deprivation by activating pro-survival pathways including PKB (AKT) and extracellular signal-regulated protein kinases (ERK1d ERK 2) (Fröhlich Dominik et al., 2014; Frühbeis et al., 2013). Also, astrocyte-derived EVs have been reported to promote neuronal outgrowth in an oxygen-glucose deprivation model by releasing synapsin 1 (Wang et al., 2011). Figure 1.17 summarises the key roles of EVs in the CNS.

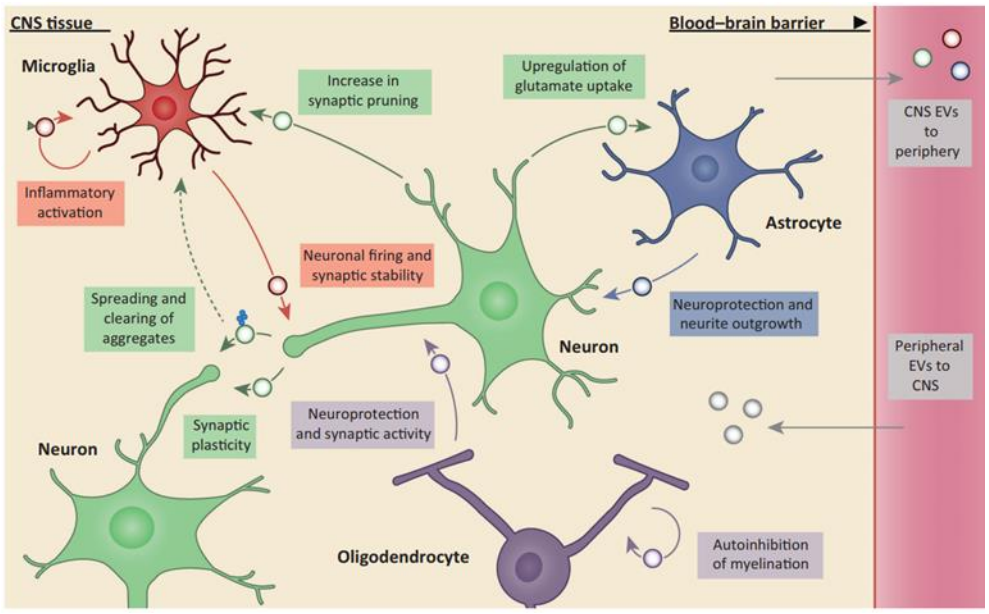


Figure 1.17: Graphical representation of the role of EVs in the CNS. (Adapted from Holm et al., 2018)

1.4.3.2. Therapeutic potential of NSC-derived EVs

Recently, NSC derived EVs have been considered to provide therapeutic benefits in multiple neurological disorders including stroke and AD, and provide as an alternative to cellular therapy and other invasive procedures (reviewed in Vogel et al., 2018). NSC-EVs are known to be responsive and communicative with the microenvironment. A study has reported that NSCs respond to pro-inflammatory environment (Th1-like cytokine cocktail media) and specifically pack and release components of interferon gamma-Stat1 pathway, which results in activation of Stat-1 pathway in recipient NIH 3T3 cells (Cossetti et al., 2014). Recent report has demonstrated that NSC-EVs show L-asparaginase activity, and therefore acting as independent metabolic units with the ability to modulate critical nutrients in the extracellular space and influence cell physiology (Iraci et al., 2017). NSC-EVs have also been considered as

modulators of ageing, where a study has demonstrated that EVs derived from postnatal hypothalamic NSCs can reduce age-related neurological symptoms of a middle aged mutant mouse model (Zhang et al., 2017). NSC-EVs have recently been considered as microglial morphogen, where SVZ-derived EVs have shown to specifically target and the microglia and modify their morphology. Here, CD9 SVZ-EVs are shown to target CD11b microglia and shift their appearance to a rounded and non-stellate morphology, a process thought to be influenced by miRNA transfer (Let7) (Morton et al., 2018). NSC-EVs have also shown great promise is animal models of stroke. Human NSC-EVs have been demonstrated to improve motor function (assessed by beam walk and hanging wire tests), improve episodic memory and alleviated chronic inflammation (by modulating microglia phenotype). A follow-up study using a porcine model of permanent middle cerebral artery occlusion demonstrated that NSC-EVs can eliminate intracranial haemorrhage in ischemic lesions, decreased cerebral lesion volume and brain swelling, promote neuroprotection and preserve motor coordination functions after stroke (Webb et al., 2018). These recent observations demonstrate the wide potential of NSC-EVs in for treating neurological disorders.

Aims of the project

This project focuses on investigating the neurogenic potential of BG-NSCs by studying 1) the differentiation of BG-NSCs and 2) the response of neuronal cells to BG-NSC derived EVs. To summarise, this project has three aims.

The first aim was to develop and optimise protocol to aid the investigation of cellular and acellular properties of BG-NSCs. This is covered in Chapters 4 and 5. Chapter 4 focuses on optimising a differentiation protocol for primary NSCs using fasudil. Chapter 5 focuses on developing an innovative approach to characterise size distribution and concentration of EVs derived from stem cells using a super resolution imaging technique.

The second aim was to investigate the stem cell and differentiation properties of BG-derived NSCs. This will be covered in Chapter 6 and will utilize the protocol developed in Chapter 4.

The third aim was to investigate the effect of BG-NSC derived EVs on a neuronal culture system. This is covered in Chapters 6 and 7. Chapter 6 will utilize the approach developed in Chapter 5 to characterise EVs derived from BG-derived NSCs. Chapter 7 focuses on investigating the effect of low-power sonication on isolated EVs and whether it modulates EV mediated neuronal response.

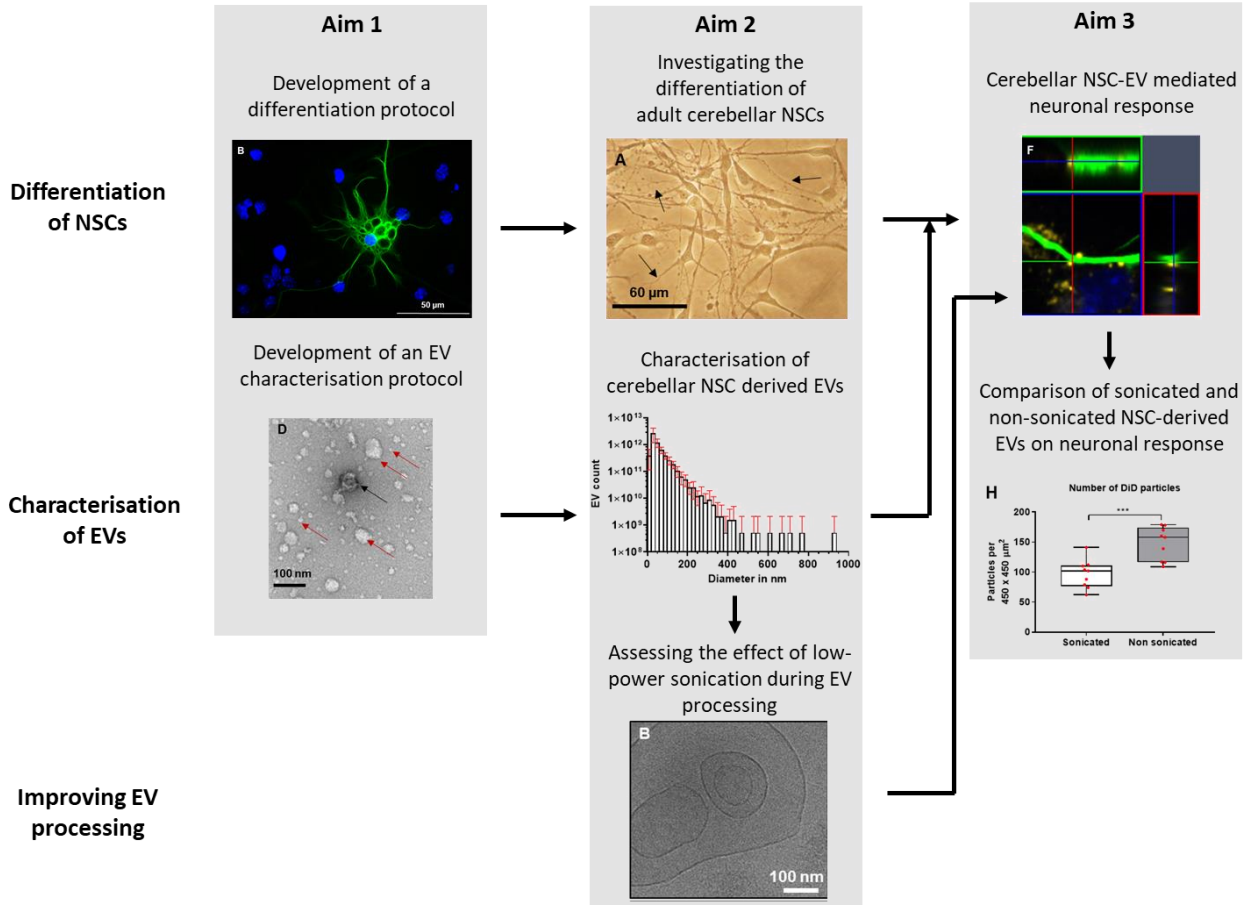


Figure 0.1: Diagrammatic representation of thesis project plan.

2. Materials and methods

All materials and reagents are from Thermofisher unless mentioned otherwise.

2.1. Cell Culture

In Chapter 3, NSCs isolated from postnatal and adult mouse brains and neural progenitor cells of C17.2 cell line were used. LV-NSCs provided as a well-established primary NSC population to study the effect of fasudil. In our lab, LV-NSCs from Sox1±GFP mouse brain were routinely isolated and provided as a reliable mouse strain to identify Sox1-GFP+ve NSCs in vitro (during early passages of neurosphere forming stage). For unclear reasons, establishment of a healthy population of primary adult LV-NSCs was unsuccessful during the initial stages of this project. Troubleshooting involved setting up primary cultures from of LV-NSCs from postnatal mouse brain tissues. During trials, postnatal day 21 mice established a healthy culture which was used for further experimentation. Later, healthy adult LV-NSCs (over 3-month-old) were established and compared with postnatal day 21 with respect to their response to fasudil. Healthy adult LV-NSCs were then established from wildtype C57BL6/N mouse brain (3-month-old). These cells resulted in a culture with significantly higher neuronal differentiation and also avoided GFP fluorescence in the nucleus of cells in contrast to Sox1+ve cells and was therefore used for further experiments. C17.2 cells provided as a positive

control for fasudil mediated differentiation with respect to published sources.

MSCs are an established source of EVs and MSC-D1 cells were routinely cultured in the lab during this project. Therefore, they provided as a good source to optimise EV isolation and characterisation in Chapter 4, while LV-NSC cultures were being optimised. CB-NSCs from C57BL6/N took much longer to establish (Chapter 5) during which fasudil differentiation and EV characterisation technique were optimised.

Cell counting of brightfield images was done using Image J manual counting tool from respective regions of interest. For immunostained images, DAPI count or total area covered by DAPI fluorescence was used to normalise to cell count. For passaging, doubling time and EV isolation experiments, cells were counted using Countess II automated cell counter as per manufacturer's instructions.

2.1.1. Primary mouse neural stem cells

Heterozygous Sox1-GFP+/− mice, which carry a knocked in GFP reporter (Aubert et al., 2003) (supplied in Nottingham animal house unit) and C57BL6/N mice (3 months old; Charles River UK Ltd) were sacrificed by cervical dislocation (in accordance with the UK Animals (Scientific Procedures) Act 1986). Primary NSCs were isolated and cultured as previously described (Nizamudeen et al., 2018b). For primary NSC isolation, lateral ventricle tissues from postnatal day 21 (referred to as 'postnatal NSCs') and adult (referred to as 'NSCs') mice brain, and the

cerebellum tissue were isolated, minced using scalpel, and incubated in Accumax (Sigma-Aldrich, UK) for 30 minutes at 37°C with mild agitation every ten minutes. The digested tissue was then washed with phosphate buffered saline (PBS) and centrifuged at 200G for 5 minutes. The cell pellet was re-suspended in NSC medium (made from DMEM (Dulbecco's modified Eagle's medium) F12/Neurobasal (1:1) medium containing 0.5% penicillin/streptomycin and 0.01% heparin, with B27 and N2 supplements, and added growth factors basic fibroblast growth factor (bFGF) and epidermal growth factor (EGF) (20 ng/µl)). The mouse strains used in this study are Sox1 ± GFP mice (Alcock and Sottile, 2009) and C57BL6/N mice. Accordingly, the NSCs were labelled as follows: NSCs from Sox1 ± GFP mice were labelled as Cell_(LV or BG)sg, and NSCs from C57BL6/N mice were labelled as Cell_(LV or BG)wt (Refer Table 2.1). For expansion of primary NSCs, cells were cultured in NSC medium, refreshed every 2 to 3 days, split using Accutase (Sigma-Aldrich, UK) and used within 10 passages. For cryopreservation, NSCs were mixed with NSC medium with added growth factors and 10% DMSO (Dimethyl sulfoxide) and stored in liquid nitrogen (cryopreservation allowed in a reduction in animal sacrifices). For differentiation of NSCs, cells were seeded on either 0.1% gelatin coated coverslips or Geltrex coated dishes at 50,000 to 100,000 cells/ml. Upon reaching confluency, the medium was changed to differentiation medium (identical to NSC medium but without growth factors denoted by STD (standard) medium). For fasudil differentiation, the differentiation medium was supplemented with 0.5% or 0.05% fetal bovine serum

(FBS), with 100 µM Fasudil (FAS, Tocris) as indicated. For neuronal differentiation, the differentiation medium was supplemented with the retinoic acid analogue 1 µM EC23 (Tocris), 10 ng/µl BDNF (Source Bioscience) and 0.05% FBS which was referred to as retinoid-based medium (RET). The medium was refreshed every 48 hours. Treated samples were labelled as follows: Cell_(LV or BG)(sg or wt)_(FAS or RET) (Refer Table 2.1).

Table 2.1: Cell and EV sample nomenclature used in this study

Nomenclature	Full form
Cell_C17.2	C17.2 cell line
Cell_C17.2_FAS	C17.2 cells treated with fasudil
Cell_C17.2_RET	C17.2 cells treated with retinoic acid
Cell_C17.2_D0	C17.2 cells at day 0 (untreated)
Cell_LVsg	LV-NSCs from Sox1 ± GFP mice
Cell_LVsg_FAS	LV-NSCs from Sox1 ± GFP mice treated with fasudil
Cell_LVsg_RET	LV-NSCs from Sox1 ± GFP mice treated with retinoic acid
Cell_LVsg_D0	LV-NSCs from Sox1 ± GFP mice at day 0 (untreated)
Cell_LVwt	LV-NSCs from C57BL6/N mice
Cell_LVwt_FAS	LV-NSCs from C57BL6/N mice treated with fasudil
Cell_LVwt_RET	LV-NSCs from C57BL6/N mice treated with retinoic acid
Cell_LVwt_D0	LV-NSCs from C57BL6/N mice at day 0 (untreated)
Cell_BGwt	BG-NSCs from C57BL6/N mice
Cell_BGwt_FAS	BG-NSCs from C57BL6/N mice treated with fasudil
Cell_BGwt_RET	BG-NSCs from C57BL6/N mice treated with retinoic acid
Cell_BGwt_D0	BG-NSCs from C57BL6/N mice at day 0 (untreated)
EV_LVsg	EVs derived from Cell_LVsg
EV_LVsg_FAS	EVs derived from fasudil treated Cell_LVsg
EV_LVsg_RET	EVs deived from retinoic acid treated Cell_LVsg
EV_LVsg_D0	EVs derived from untreated Cell_LVsg (day 0)
EV_LVwt	EVs derived from Cell_LVwt
EV_LVwt_FAS	EVs derived from fasudil treated Cell_LVwt
EV_LVwt_RET	EVs derived from retinoic acid treated Cell_LVwt
EV_LVwt_D0	EVs derived from untreated Cell_LVwt (day 0)
EV_BGwt	EVs derived from Cell_BGwt
EV_BGwt_FAS	EVs derived from fasudil treated Cell_BGwt
EV_BGwt_RET	EVs derived from retinoic acid treated Cell_BGwt
EV_BGwt_D0	EVs derived from untreated Cell_BGwt (day 0)

2.1.2. C17.2 cerebellar progenitor cell line

C17.2 immortalised mouse cerebellar cells (European Collection of Authenticated Cell Cultures (ECACC) 07062902) were cultured in DMEM high glucose medium supplemented with 10% FBS and 0.5% penicillin/streptomycin, 0.25% trypsin-EDTA was used for splitting the cells. For cryopreservation, C17.2 cells were mixed with 10% DMSO and 25% FBS in their culture medium and stored in liquid nitrogen. This cell line was used as a positive control for fasudil mediated neural differentiation *in vitro* (Chen et al., 2015). For differentiation, C17.2 cells (passage 20) were seeded onto coverslips placed onto 24-well plates at 20,000 cells per well. After 24 hours, cells were checked for attachment onto coverslips, and then refreshed with C17.2-FAS medium (added 100 µM fasudil). Differentiating cells were refreshed with FAS medium every 48 hours.

2.1.3. Mouse D1 mesenchymal stem cell line

Mouse mesenchymal D1 cells (MSCs, ATCC CRL-12424) were cultured in low-glucose DMEM supplemented with 10% FBS, 1%, penicillin/streptomycin, 1% L-glutamine and 1% non-essential amino acids (named as MSC medium). 0.25% trypsin-EDTA was used for splitting the cells. For cryopreservation, cells were mixed with 10% DMSO and 25% FBS in their culture medium and stored in liquid nitrogen. For differentiation, MSCs cells (passage 20) were seeded onto coverslips placed onto 24-well plates at 20,000 cells per well. After 24 hours, cells were checked for attachment onto coverslips, and then

refreshed with MSC-FAS medium (MSC medium supplemented with 100 µM fasudil). Differentiating cells were refreshed with FAS medium every 48 hours.

2.2. Neurite outgrowth analysis

Images of undifferentiated and FAS-treated cultures were captured using Nikon microscope and images processed using ImageJ software (www.imagej.nih.gov/ij/). Images were captured from 3 independent biological replicates, and from each replicate 3 image sections were selected for neurite outgrowth measurements (technical replicates). Only the neurite lengths longer than the diameter of the cell body were considered for analysis. Total neurite length was normalised to the number of cells visualized in each image. Briefly, images were taken at 10x magnification and from each image, 3 sections of 999x999 μm^2 dimensions (regions of interest- ROI) chosen for cell counting. Location of these ROI were constant in relation to the field of view. Number of cells were manually counted using image J manual counting tool within each region of interest and then averaged. This was repeated for 3 independent images from the same well as technical replicates, and for 3 different wells as biological replicates.

2.3. Pico Green assay

Pico green dye binds specifically to DNA and is widely used as a surrogate measure to quantify the number of cells. Pico green DNA quantification dye was used according to manufacturer's instructions.

Standard curve was produced using DNA standard provided by the kit to test the sensitivity and accuracy of the kit prior to cell proliferation analysis. Cells cultured in 24 well plates were washed with PBS, and frozen with 1 ml SDW (sterile distilled water) in each well. The samples were subjected to three freeze-thaw cycles prior to sample collection. From each sample, 0.5 ml of solution was transferred to a new 24-well plate. The collected samples were subjected to pico green dye incubation, which was diluted in reagent buffer following manufacturer's instructions. Samples were then analysed for fluorescence at 480 nm (excitation) and 520 nm (emission).

2.4. Presto Blue assay

Presto Blue is cell-permeable dye (resazurin) which gets changed to a fluorescent compound (resorufin) in the presence of cellular metabolic environment (such as the mitochondria) and provides as a surrogate measure for viability and as a metabolic assay. Presto Blue kit (Invitrogen) was used to analyse the metabolic activity of cells according to manufacturer's instructions. Dilutions and incubation timings were optimised according to manufacturer's instructions. Cells were cultured in 24 or 96 well plates. Cells were imaged (brightfield) using Nikon microscope, followed by incubation with Presto Blue containing medium for 60 or 30 minutes at 37°C. 50 µl of Presto Blue incubated media from each sample were transferred to 96 well plates and analysed for fluorescence at 560 nm (excitation) and 590 nm (emission) wavelength using Tecan M200 plate reader. For normalisation: cell count for Presto

Blue normalisation was performed using either ImageJ software or pico green assay (section 2.4). ImageJ cell count was done as described in section 2.3. Day 0 undifferentiated samples were taken as controls to normalise cell count and metabolic activity of treated samples. Cell count normalised PB analysis provided metabolic activity per cell.

2.5. Immunohistochemistry

2.5.1. Paraffin embedding and dewaxing of brain tissues

Paraffin embedding allows for thin sectioning of tissues for immunohistochemistry. In this study, paraffin brain sections were used for optimising antibody concentration of immunostaining procedures and were used to investigate the BG population in adult cerebellum tissues. Isolated brain tissues were fixed in 4% ice-cold paraformaldehyde (PFA) for 48 hours and transferred to wax embedding cassettes. The tissue cassettes were then subjected to a series of dehydration steps in ethanol concentrations of 25%, 50%, 75%, 96% and (2x) 100% (each for 1 hour). After dehydration, the tissues were cleared using xylene (1 hour) before infiltrating them with wax (58˚C for 1 hour) and embedding them in wax blocks. The wax blocks were processed using a Leica microtome to make 10 µm thick slices which were later fixed onto an adhesive glass slide (superfrost). Sections were then dewaxed and rehydrated. Briefly, tissue embedded slides were incubated in Histoclear (Sigma) (15 minutes x2) followed by 100% methanol (1 minute x2), 75% methanol (1 minute x1), 50% methanol (1 minute x1), 25% methanol (1 minute x1)

and then washed twice for 5 min in PBT (PBS + 0.1% Tween 20 (Sigma)). Sodium citrate buffer was prepared by mixing 2.94 g of Tri-sodium citrate (dihydrate) in 1 L distilled water and adjusted to pH 6.0 using 1 N Hydrochloric acid (HCL) followed by addition of 0.5ml Tween 20. Tissue embedded slides were then subjected to heat induced antigen retrieval step using sodium citrate buffer for 20 minutes at 95˚C. The samples were then washed with PBT and used for immunostaining. Note: Paraffin wax embedding and dewaxing of brain tissues for Sox positive cell counting was performed by SS.

2.5.2. Standard immunostaining protocol

Note: Immunostaining of brain tissues for Sox positive cell counting was performed by SS. After antigen retrieval step, endogenous peroxidase activity was blocked by incubating the sections in 3% H202 for 10-20 minutes followed by 3 washed with PBS for 5 minutes each. Slides were then blocked in 0.1% FBS containing PBS for 1 hour at room temperature. Subsequently, the slides were incubated with primary antibody diluted in blocking solution overnight at 4°C, followed by extensive PBS washes for 1 hour, and then incubated with secondary antibodies for 1 hour at room temperature, and then washed 3 times for 15 minutes each. For single immunostaining, slides were treated with DAB (3,3'-Diaminobenzidine) peroxidase substrate kit (Vector Laboratories) according to the manufacturer’s instructions until brown colour developed for 2-10mins (time was optimized for each primary antibody), followed by two 5min PBS washes and then mounted with

(4',6-Diamidino-2-Phenylindole) DAPI-containing Vectashield (Vector Laboratories). For double immunostaining, 2 different substrates were used for the detection of each of the antigens analysed. Slides were first incubated with DAB until brown colour developed for the first antigen detection. The sections were washed 3 times with PBT and then incubated with alkaline phosphatase substrate kit (Vector Labs) in the dark for 20-40 min until blue colour was developed for detection of the second antigen. Finally, the slides were washed with PBT 3 times, each for 5 min, and mounted with Dapi mounting medium. Primary and secondary antibodies used in this study and their respective dilutions are listed in Appendix document Table 10.1. The imaging of the immunostained samples and sox-positive cell counting was performed by ZN. This experiment did not focus on quantifying sox-positive cells in a specific lobule of the cerebellar cortex. Lobules were chosen where the ones whose sections had at least 700 µm of length of PCL showing good quality sectioning and staining of cells. All other immunostaining experiments in this project was performed by ZN. Cells were fixed in 4% PFA, washed with PBS, then incubated in 0.1% Triton-X (Sigma-Aldrich), followed by a PBS wash. Samples were then washed briefly in PBT and blocked using 5% goat serum (Sigma-Aldrich) in PBS. Samples were incubated overnight in primary antibodies diluted in blocking solution. Samples were then briefly washed in PBT and incubated for 1 h in secondary antibodies diluted in blocking solution. Details of antibodies used are mentioned in Appendix document Table 1. Samples were then mounted using DAPI-containing Vectashield mounting solution (Vector

Laboratories, UK) or incubated in 4′,6-diamidino-2-phenylindole (DAPI) solution (Sigma) and imaged with a Nikon Eclipse 90i fluorescent microscope or Operetta High-Content Imaging System (Perkin Elmer, UK), using the ImageJ software (https://imagej.net) and Harmony Image Analysis system respectively (http://www.perkinelmer.com). Note: Immunostaining of brain tissues for Sox positive cell counting was performed by SS.

2.6. Immunofluorescence imaging

In this study, immunofluorescence images were captured using either the Nikon Eclipse 90i fluorescent microscope or the operetta high content imaging system. Images acquired from Nikon were processed using ImageJ software while images acquired from operetta were processed using Harmony software. This section provides details of how image acquisition to analysis was performed to determine and interpret results from fluorescence labelled cells.

2.6.1. Considerations while imaging using Nikon 90i Eclipse

For fluorescence imaging using Nikon 90i Eclipse (Nikon), cells were seeded on coverslips, fixed, stained and mounted onto glass slides. Volocity software was used for image acquisition. Gain, exposure and offset settings (GEO) were set according to secondary antibody only negative control threshold. GEO settings were set constant for each antibody and cell type for standardisation. For double and triple

immunofluorescent images, the images were taken separately with optimal focus for each antibody and then manually merged. Exported images were then processed for further analysis using ImageJ software (https://imagej.net). Note: Low magnification (≤10x) used in chapter 3 for immunofluorescence quantification were primarily focused on absolute quantitation of fluorescence intensity and were not aimed at representation of immunofluorescence observation at single cell level.

2.6.2. Immunofluorescence quantification using ImageJ software

For ImageJ, immunostaining was quantified by determining the area of intensity of antibody fluorescence over the area covered by DAPI fluorescence for each image or the number of nuclei per each image (https://imagej.net). Immunofluorescent quantification of samples for antibodies were then normalised to their respective day 0 samples. To do this, the images were first subjected to the following settings – 'image type': 16-bit, 'brightness and contrast': standard values for each experiment and 'threshold': standard values for each experiment. For counting the number of cells in an image, DAPI image was chosen and after thresholding, 'watershed' setting was applied to distinguish single nuclei from clusters. Cell count and total intensity of DAPI was then determined using tools from 'Analyse' tab. For manual counting neurons and thresholding neurons and glia, images were converted to 8-bit format and thresholding was done appropriately. Figure 2.1 shows an example of manual thresholding to detect neurons and glia.

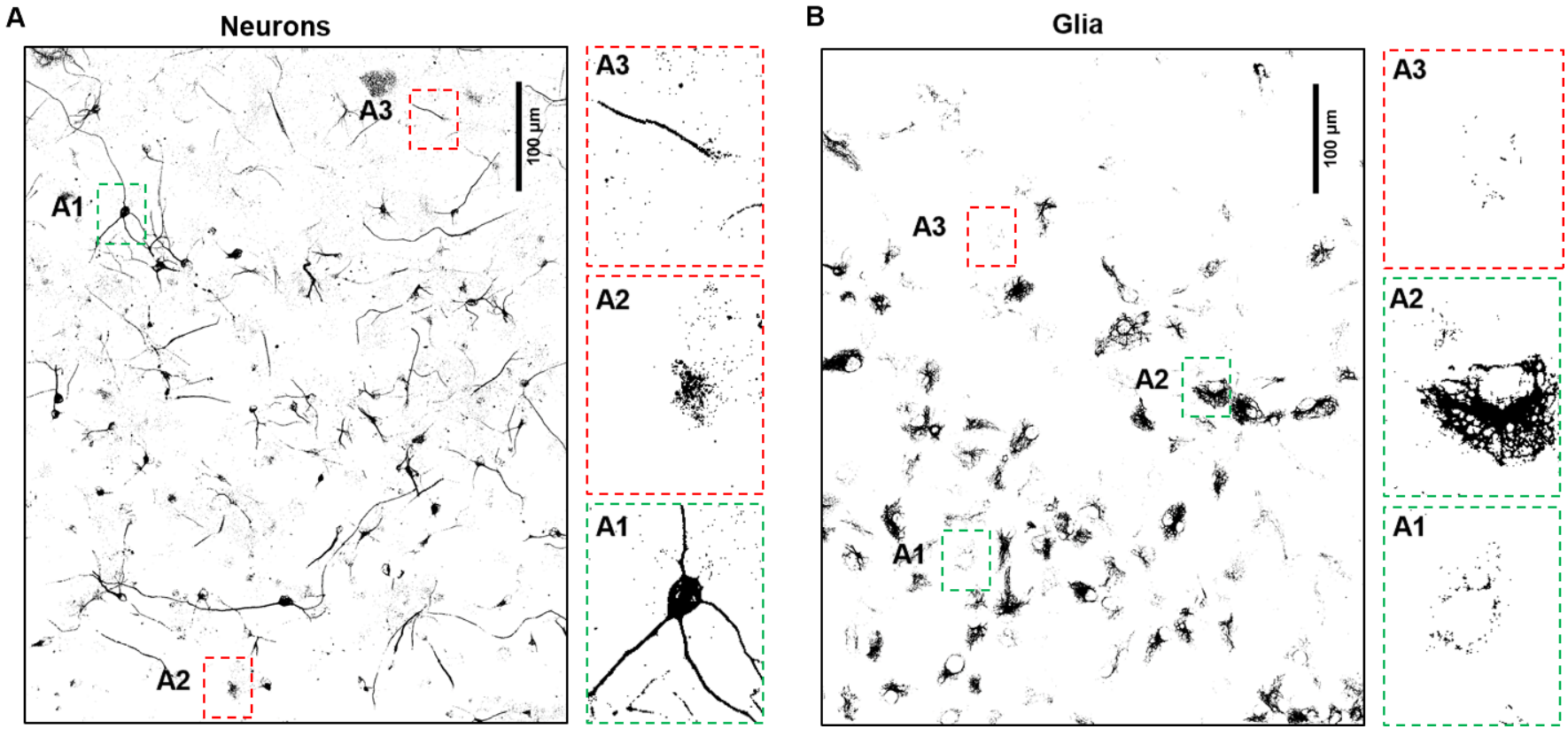


Figure 2.1: ImageJ manual thresholding of (A) neurons and (B) glia. Sub boxes 1, 2 and 3 refer to zoomed in versions. Examples of cells counted as positive are in green boxes and examples of cells which are not counted positive are in red boxes. In neurons, cells are counted positive only if neurites and cell body are visible together.

2.6.3. Operetta high throughput imaging

The Operetta imaging system (Perkin Elmer) allows for high throughput imaging and quantification of fluorescent samples in a much quicker fashion compared to manual imaging. For imaging, samples were produced in a 96 well plate format. Prior to imaging, samples were checked for ideal focal distance by capturing multiple images in z-stacks with 1 to 3 µm distance intervals between each shot using 10x and 20x objective lens for DAPI, AF488 and DRAQ5 channels for blue, green and red fluorescence, respectively. Then the wells and their area of interest were selected. The system automatically acquired images for the mentioned settings which could later be processed for quantification and morphological analysis using Harmony software.

2.6.4. Immunofluorescence quantification using Harmony software

For quantification using the Harmony software, a standard set of modules were used which can be further optimised depending on the antibody of interest (http://www.perkinelmer.com). The modules are as follows – 'Find Nuclei' – 'Find Cytoplasm' – 'Calculate Morphology Properties' – 'Calculate Intensity Properties' – 'Select Population' – Define Results'. The number of each modules depends on the number of channels to be imaged. Each module block has subsections that allows for modifying parameters specific for every image. 'Find Nuclei' module was used to identify cells with respect to DAPI or any other nuclear marker. In the

‘Find Cytoplasm’ block, appropriate ‘method’ was selected to cover the antibody specific region in all samples. The ‘Calculate Morphology Properties’ block was used to determine the area, length of width ratio and circularity of nuclear as well as cytoplasmic region of fluorescence region of cells. The ‘Calculate Intensity Properties’ block was used to determine fluorescence intensity of antibodies used on cells. ‘Select population’ block was used to set threshold minimum and maximum nucleus size and fluorescent intensity according to negative controls. In the module block ‘Define Results’, ‘mean’ or ‘sum’ of intensity or number of cells were selected as per analysis. For images processed by Harmony Software, total fluorescence was calculated from 9 fields of view of each well. All quantifications were analysed above the negative threshold set calculated from negative control fluorescence.

2.6.5. Immunofluorescence neurite quantification using MetaXpress

In MetaXpress, ‘Neurite Outgrowth’ module was chosen and customised to appropriate ‘Intensity over background’ for ‘Cells’ and ‘Outgrowth’. From the analysed data, only ‘total number of processes was chosen as the neurite mapping was not reliable for the other datasets including ‘total outgrowth, ‘total branching’, and ‘length of outgrowth’, as evidently seen in Figure 2.2.

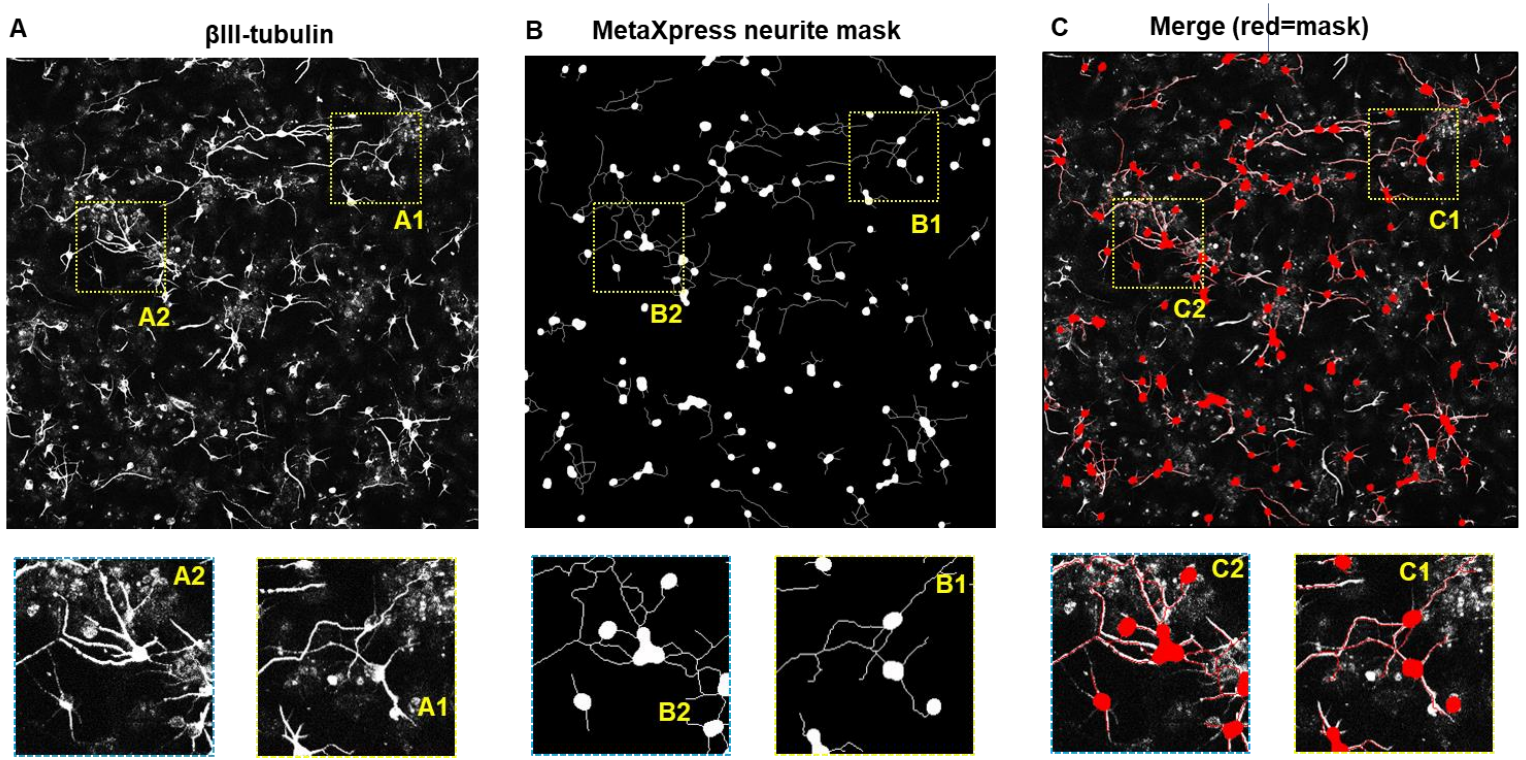


Figure 2.2: Masking of neurites for counting total neurite processes in an image using Neurite outgrowth module in MetaXpress. (A) Original image with βIII-tubulin positive neurons (white), (B) Neurite masking (white) and (C) Merge image of βIII-tubulin (white) and neuronal mask by MetaXpress (red). Zoomed in boxes are depicted as 1 and 2 of respective images.

2.7. Real-time analysis of 2-D neural migration

In order to analyse the properties of migration of neural cells, the operetta system was used to monitor cellular movement in real-time. In brief, cells grown in 6-well plate were imaged at regular intervals in digital phase contrast mode, which allows segmentation and tracking of cells. Tracking options allowed studying the cells that migrate, divide, and also disappear from start to the end of tracking. Given below are the settings used to calculate migration properties of cells in this study.

2.7.1. Live imaging settings for neural stem cells using Operetta system

Live imaging of cells was performed using Operetta High-Content Imaging system and the analysis was performed using Harmony software. Prior to imaging, samples were checked for ideal focal distance by capturing multiple images in z-stacks with 1 to 3 µm distance intervals between each shot using 10x and 20x objective lens. Live images were taken every 3 seconds (every time-point was 3 seconds apart) for 2 hours and 45 minutes from one field of view in each well in brightfield and digital phase contrast modes at 37°C, 5% CO_2. Digital phase contrast images allowed segmentation and tracking of cells, while brightfield images were used for better user visualisation.

2.7.2. Module construction in Harmony software for migratory cell selection

The building blocks for analysis were as follows: Input Image - Filter Image – Find Cells – Track Objects – Calculate Kinetic Properties – Calculate Properties – Calculate Track Properties – Define Results. Only digital phase contrast images were used for tracking analysis and they allowed filtering using the sliding parabola option under ‘Filter Image’ block. Under ‘Find Cells’ block, the channel digital phase contrast was selected in common for all samples, but the ‘Method’ option differed between samples depending on the size, shape and clustering of cells in culture, so that maximum number of cells were tracked from each sample. Method for all the other modules was chosen to be ‘Standard’. ‘Track Properties’ module was used to determine ‘Accumulated Distance’ (normalised to track count), ‘Start/End Type’, ‘Number of Time-points’, ‘Displacement’, and ‘Speed’ of the tracked cells. Raw data was exported in an excel format and used for further analysis.

2.7.3. Quantification of neural migration using Harmony software

Before interpreting ‘Accumulated Distance’ of the cells tracked from each sample as a surrogate measure for neural migration/motility, the percentage of cells tracked from ‘BEGIN’ to ‘END’ (B-E) type in each sample was determined (Figure 2.3 A and B). This track population represents the cells that allowed themselves to be tracked throughout all

timepoints without division/fusion or any imaging hinderance (cosmos/border). The percentage of cells tracked from 'SPLIT' to 'SPLIT' (S-S) type was calculated to determine the change in actively dividing cells (Figure 2.3 A and B). This tracked population represents actively dividing cells as they undergo division at least twice while being tracked. Captured videos of live cells in culture were observed to study the phenotypical mechanism of neuronal migration adopted in response to treatment. Finally, averaged accumulated distance (normalised to track count) of B-E type tracks was calculated to determine change in cellular migration.

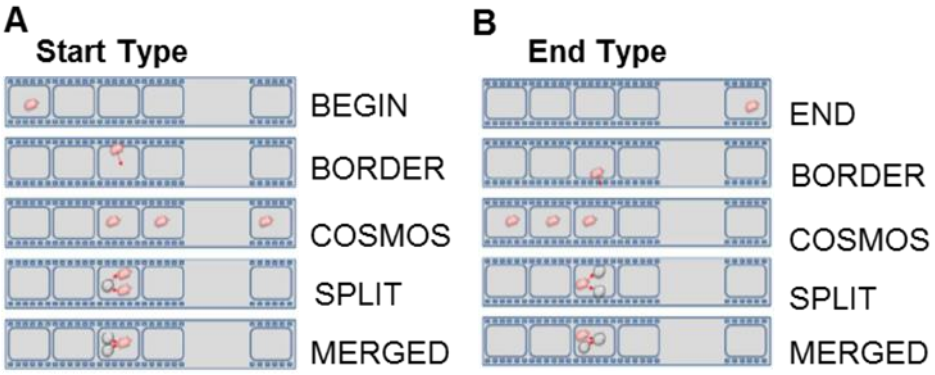


Figure 2.3: Graphical representation of the parameters used for cell-track types. Cells were tracked during the time-lapse analysis of Start (A) and End (B) stages using the Harmony High-Content Imaging Software.

2.8. PCR

Polymerase chain reaction (PCR) allows the amplification of a given sequence of nucleotides. This technique allows the validation and quantification of gene expression changes in cells and tissues. This section will describe the methodology used in this study for RNA (Ribonucleic acid) extraction, cDNA (complementary DNA

Deoxyribonucleic acid) synthesis and PCR to investigate the change in gene expression of neural stem cells during differentiation and maturation.

2.8.1. RNA extraction

Cultures were extracted from T25 flasks using TRI Reagent (Sigma) according to manufacturer's protocol. Total RNA was extracted using RNA Clean and Concentrator (Zymo Research) following manufacturer's protocols. Briefly, cells in TRI reagent mixture were subjected to chloroform incubation for 15 minutes at room temperature followed by centrifugation at 12000G at 4˚C for 15 minutes. The aqueous phase containing RNA was then isolated and mixed with RNA binding buffer followed by 100% ethanol at volumes recommended by the manufacturer's protocol. The samples were then subjected to column centrifugation with RNA Prep buffer and RNA Wash buffer sequentially followed by elution of RNA using 30 µl of DNAse/RNAase free water. RNA concentration and purity were determined using Nanodrop. Samples were then stored in -80˚C until use.

2.8.2. cDNA synthesis

cDNA synthesis is the process by which RNA is used to create a complementary DNA strand via reverse transcription (RT) which can be then used for amplification by PCR reaction. 1 µg of RNA was used for each reaction. DNAse 1 (Invitrogen) treatment was performed to avoid genomic contamination. Tubes containing no RNA and no enzyme

controls were used in parallel reactions to confirm the absence of contamination. RT was performed either using the Superscript III RT enzyme kit or the High Capacity RNA-to-cDNA™ Kit, on 1ug of RNA from each sample to produce cDNA following manufacturer's protocol.

2.8.3. RT-PCR

After reverse transcription, PCR was performed using the Platinum Taq DNA polymerase kit (according to manufacturer's instructions), cDNA samples and specific primers (Appendix document Table 2). All primers were designed to span intra-exonic regions and were blasted for specificity using NCBI's primer blast (https://www.ncbi.nlm.nih.gov/tools/primer-blast/) or UCSC genome browser's In-Silico PCR (https://genome.ucsc.edu/cgi-bin/hgPcr). Primers were designed for Nestin, Sox2 (NSC markers), GFAP (glial lineage marker) and βIII-tub (neuronal marker) (refer to section 1.1.2 for more information). Tubes containing no RNA and no enzyme controls were used in parallel reactions to confirm the absence of contamination. PCR products were detected by gel electrophoresis.

2.8.4. Gel electrophoresis

Briefly, PCR products (mixed with loading dye) were run on 2% agarose gel with 0.01% ethidium bromide (Sigma). Gel was run for 1 hr at 90V and 400mA. Gel images were captured using LAS4000 imaging instrument. Aida image analysis software's 2-D densitometry (Elysia Raytest, Belgium, http://www.elysia.be/en/) or ImageJ software's plot

lanes option (https://imagej.net) was used to calculate band intensities from gel and normalise to Clathrin6k (housekeeping gene) (Alcock and Sottile, 2009) to provide semi-quantification of gene expression.

2.8.5. Quantitative real-time PCR

qPCR, also known as real-time or quantitative PCR uses fluorescent probes to detect amplification of PCR products in real-time and therefore provides a highly sensitive and quantitative analysis of gene expression. For qPCR, Power SYBR Green and Power Up SYBR Green PCR Master Mix products (Applied Biosystems) was used. Gene expression was normalised against expression of Clathrin6k, 18s or GAPDH. Gene expression fold changes were determined using 2-ΔΔCt method of quantification (Livak and Schmittgen, 2001) (Appendix excel file 1). The sequence for primers used for qPCR reactions are listed below (Appendix document Table 3). All primers were designed to span intra-exonic regions and were blasted for specificity using National centre for biotechnology information's (NCBI's) primer blast (https://www.ncbi.nlm.nih.gov/tools/primer-blast/) or UCSC genome browser's In-Silico PCR (https://genome.ucsc.edu/cgi-bin/hgPcr). Primers were validated using mouse brain tissue as positive control, and mouse liver tissue as negative control. Mean gene expression (2-ΔΔCt) was calculated between three independent experiments with three internal replicates and graphed with standard deviation (SD).

2.9. EV isolation

Prior to EV isolation, cells were washed with PBS and then incubated in with EV enrichment (Exo-E) medium – appropriate culture medium containing Exo-free FBS (System Biosciences) instead of conventional FBS, with added DiD Vybrant Cell labelling solution according to manufacturer's instructions (5 µl/ml). After 6 hours, the medium was collected and filtered using 0.45 µm syringe filters (SLS). For EV isolation, exoEasy Maxi Kit (Qiagen) was used according to manufacturer's instructions. For negative controls, freshly prepared [DiD in PBS], [DiD in Exo-E medium] and [DiD in serum-free Exo-E medium], were processed in the same way. Eluted EVs were either immediately diluted and used for size distribution and particle count analysis or stored at -80˚C. Samples were sonicated prior to use using Bioruptor (Diagenode) at low power three times for 10 seconds. For studying the effect of sonication in the experiments, freshly eluted EVs were split into two groups – 'non-sonicated' (nsEVs) and 'sonicated' (sEVs). nsEVs were subjected to gentle manual tapping and pipetting up and down 3 times prior to analysis. sEVs were subjected to sonication using Bioruptor (Diagenode) 230V/2.1A (EU) 50/60Hz 'Low-power' option, 10 second on-off cycle for 3 times. EVs were either immediately used or stored at -80°C for future use.

2.10. EV characterisation using conventional methods

2.10.1. Transmission electron microscopy (TEM) and cryo-TEM

For TEM, samples were prepared according to previously published protocol with slight modifications (Théry et al., 2006). Briefly, samples were fixed with 4% PFA and added (5 µl/grid) to glow discharged (10 seconds at 5 mA using an Agar turbo coater aux power unit and dedicated glow discharge head) Formvar-carbon coated EM grids (EM resolutions) and adsorbed for 20 minutes. Samples grids were then washed with PBS and then incubated with 1% glutaraldehyde for 5 minutes. Grids were then washed with sterile distilled water and incubated with 3% uranyl-acetate for 15 minutes for negative staining. TEM was carried out using a Tecnai Biotwin-12 with an accelerating voltage of 100 kV. For cryo-TEM, glow discharged Holey carbon copper TEM grids were used (EM resolutions). Samples were let to adsorb onto the grids (5 µl/grid) for 20 before the excess solution was removed using filter paper and the grids allowed to dry under ambient conditions. Samples were then frozen using a Gatan CP3 plunge freezing unit, blotting for 1 second and freezing in liquid ethane. Samples were transferred to cryo-TEM storage boxes and then loaded into a Gatan 626 cryo-TEM holder on a JEOL 2100+ TEM. Images were acquired for 2-4 seconds at a dose of below 10 e/A2, using a US1000 CCD camera and

Digital Micrograph GSM 3. Note: The TEM images were captured by Dr RL and ZN. The cryo-TEM images were captured by CP.

2.10.2. Nanoparticle tracking analysis (NTA)

An LM10/14 Nanosight (Nanosight, Malvern) instrument was used to analyse EVs. Prior to analysis, 1:10 dilution of CPC100 (IZON) and 1:1000 dilution of 200 nm polystyrene (Malvern) nanoparticles were used to test the sensitivity of the instrument. EV samples were used at a dilution that allowed less than 200 particles to be tracked at each frame. Automatic settings were applied for the minimum expected particle size, minimum track length and blur settings. For capture settings, screen gain was set at 1 and camera level was set at 10 (shutter 1500; gain 680). For analysis settings, screen gain was set at 10 and detection threshold was set at 10. For NTA experiments in chapter 6, capture settings, screen gain was set at 1 and camera level was set at 150 (shutter 1500; gain 574680); for analysis settings, screen gain was set at 10 and detection threshold was set at 7. Five movies of 60 seconds were captured at 30 frames per second for each sample. Data processing and analysis of particle size distribution and concentration were performed using NTA Software (https://www.malvern.com). NTA concentration estimation is dependent on the refractive index of particles under analysis according to the Rayleigh approximation $\sigma_s = \frac{2\pi^5}{3}\frac{d^6}{\lambda^4}\left(\frac{n^2-1}{n^2+2}\right)^2$ (where d is the particle diameter, λ is the wavelength, and n is the ratio of particle refractive index to solvent refractive index (Dragovic et al., 2011)), which is known to vary in EV samples due to heterogenic size and content (Willms et al., 2016).

Therefore, NTA analysis was used only to determine particle size distribution (PSD) and not EV concentration.

2.10.3. Tunable resistive pulse sensing (TRPS)

TRPS was performed using the qNano system (IZON Sciences, New Zealand) with the IZON Control Suite software (V3.1.2.53). NP100, NP200 or NP300 elastomeric tuneable nanopores were used, suitable for analysing beads between 85 and 600 nm (as stated by the manufacturer). Carboxylated polystyrene beads, denoted as CPC200 (Bangs Laboratories, USA), with a mean nominal diameter of 210 nm and stock concentration of 1×10^{12} particles/mL, were used as a concentration calibrant at 2 x 10^{9}/ml. Prior to use, the beads were vortexed for 30 seconds and sonicated for 1 minute to ensure mono-dispersity. An appropriate stretch and a voltage was applied throughout so that the blockades of CPC200s in PBS were at least 0.5 nA above the background noise. The qNano was operated as previously described (Billinge et al., 2014). Briefly, the lower fluid cell was filled with 75 µL of PBS, ensuring no air bubbles are present and the upper fluid cell contained 40 µL sample. After each measurement, the sample was removed from the upper fluid cell and replaced with PBS. This was repeated several times, applying varying amounts of pressure and vacuum, until visible blockades were observed. Note: The qNano was performed by MP.

2.10.4. Dynamic light scattering (DLS)

A Zetasizer Nano ZS (Malvern, UK) was used to determine particle hydrodynamic size. Measurements were taken at 173° backscatter with auto attenuation. 3 measurements were taken per sample. DLS was performed by RX and assisted by ZN.

2.11. Direct stochastic reconstruction microscopy (d-STORM) based EV characterisation

For d-STORM imaging, a 1 in 1000 dilution of DiD-labelled EVs in PBS was seeded onto poly-L-lysine (Sigma) coated 4-well glass bottom petridishes (Greiner-Bio). Imaging was performed using a Zeiss Elyra PS1 super resolution microscope, with α-Plan Apo 100x/1.46 oil immersion objective in total internal reflection microscopy (TIRF) mode. Before imaging, 30˚C oil (Zeiss, Immersol™ 518F/30°) droplet was placed on 100x objectives. The LP 650filter was used to visualise EVs. TIRF was used to visualize and scan the EVs bound to the cover glass, automatic focusing (definite focus) maintained the desired focal plane during the experiment. Before the STORM experiment, a wide-field snapshot was captured using the '16 Avg' option at 0.5% (0.02kW/cm^2) laser power in TIRF mode. '16Avg' is a built-in option in Zeiss and uses average intensity projection of 16 frames to reduce noise. This feature was off when running d-STORM. Then d-STORM was run for 5000 frames at 8% (0.31kW/cm^2) laser power, with 35 ms exposure, and 200

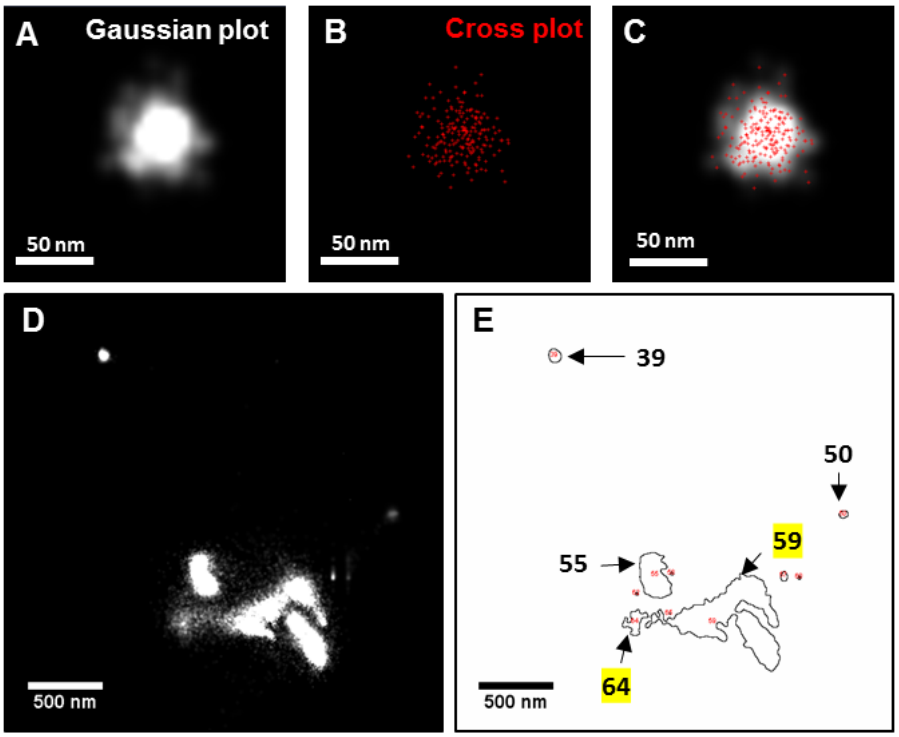
gain on the EM-CCD (Andor EM-CCD camera iXon Du 897). Test runs with higher power laser and longer scans did not provide extra information for this experiment (data not shown). It might be important to note that at higher laser power, the smallest of vesicles might be damaged in addition to losing the dye quickly which in turn does not allow sufficient multiple reads necessary for a reliable STORM experiment in this case. Therefore, low laser power could be more suitable for small and fragile vesicular structures which are not fixed so that their structure can be maintained while imaging. An 80 second video showing the photo-switching property of DiD-labelled EVs in TIRF mode during d-STORM imaging was recorded (25 frames per second) (Appendix video file 1).

Images were processed using the PALM module of the Zeiss Zen Black software. Data were filtered as follows: number of photons threshold was adjusted to 200 according to measurements made on the negative controls -PBS only and medium only (no FBS). Localisation point centroids were blurred with a Gaussian filter, whose diameter equals the localisation precision for each localised molecule. The accuracy of the rendered image can be adjusted using the expansion factor slider in Zen (PSF). Lower values than 1 PSF will render higher precision to gaussian representation of the localised molecules. A value of 0.25 PSF expansion factor was used. This resulted in a rendering of the vesicles so that the cluster of localisations matched the rendered image (checked using cross plots), therefore sizes of vesicles were not over estimated (Figure 2.4 A-C). To export, image resolution was set at 5 nm/pixel with Render

auto dynamic range of 90%. For line profiling, EV fluorescence intensity was measured on 16-bit tiff files exported as raw data from the czi files. For comparison of resolution, images were exported as tiff files and merged with reconstructed standard wide field (rSWF, for further info please see Zeiss Zen 2012, Palm Module, Help menu) of corresponding counterparts. Calibration experiments for this workflow was done using 100 and 190 nm beads.

An ImageJ macro was developed to identify and measure vesicles from exported 16-bit tiff files (Appendix document Macro 1). The processing and analysis was carried out following the steps: (i) raw tiff images exported from Zen were imported into FIJI, (ii) a Gaussian blur filter (3 pixel) was applied to the image to smooth the edges of the vesicles, (iii) the default thresholding method was used to distinguish the vesicles from the background- thresholding will set a minimum and maximum pixel intensity range on the selected image that will group all pixels that fall within this range and exclude the background, (iv) Once the vesicles were identified using the thresholding tool, particle analysis was carried out to generate size, intensity, shape measurements including the area, perimeter and circularity of the particle, (v) Outline of the identified vesicles was automatically exported as tiff so that it can be compared to the original images, (vi) Results were automatically exported as a text file. Result files generated from ImageJ macro were open in Microsoft Excel software for further analysis as follows- (i) the diameter of objects was calculated by averaging the diameter calculated from the measured area and the measured perimeter of the object, (ii) then the objects were

sorted according to their circularity. Objects below a circularity of 0.5 were discarded from the dataset as they largely corresponded to aggregate or tubular like structures (Figure 2.4 D-F). (iii) The resulting data set from each sample was used to create a histogram frequency set in Excel. (iv) the concentration of particles was calculated using the following equation: Concentration=n*dA*df, where n is the number of vesicles observed per imaged area, dA is the area of the dish where sample is loaded and df is the dilution factor of loaded sample, (v) Mean ± SEM was plotted using GraphPad Prism Software (https://www.graphpad.com). Note: The d-STORM experiments and the macro were developed and performed by RM and ZN.



F

Count number	Area	Perimeter	Circularity	Diameter from Perimeter	Dimeter from Area	Average diameter
39	5950	282.63	0.94	89.96392313	87.03892975	88.50142644
50	2300	176.07	0.93	56.04482166	54.1151638	55.07999273
55	47600	986.19	0.62	313.9140267	246.1832698	280.0486482
59	202575	4267.51	0.14	1358.390622	507.8646481	933.1276352
64	13450	704.77	0.34	224.3352585	130.8627979	177.5990282

Figure 2.4: Image analysis of EVs captured using d-STORM super resolution microscopy. (A-C) Snapshots describing the precision of d-STORM gaussian plot. (A) Gaussian rendered image of a vesicular structure (white). (B) Cross plot (red) of localised molecules used to render gaussian image. (C) Merged image of gaussian and cross plot. (D-F) Snapshots describing the ImageJ analysis of exported d-STORM images. (D) Exported d-STORM image. (E) ImageJ macro mapping of vesicle shape and size. (F) ImageJ export of particle analysis. Yellow highlights point out the structures with circularity below 0.5.

2.12. Analysis of EV uptake

2.12.1. Seeding of labelled EVs onto cells

Vybrant DiO was used to stain adherent cells in culture according to manufacturer's protocol. Cells were then incubated with DiD-labelled EVs of concentration that did not affect the viability of cells, as calculated by d-STORM concentration analysis and Presto Blue (procedure and

rationale for seeding of labelled EVs for NSC response experiments are discussed in section 4.3.5). Nuclei were labelled with Hoescht 33258 according to manufacturer's instructions. Samples were imaged at different time points as required per experiment.

2.12.2. Confocal, real-time wide-field and structured illumination microscopy (SIM) imaging for EVs

NSCs were seeded at $1x10^5$ cells/cm^2 and left to grow for 24 hours. Vybrant DiO was used to stain NSCs in culture according to manufacturer's protocol. NSCs were then incubated with $6x10^9$ EVs DiD-labelled MSC derived-EVs (as calculated by d-STORM). Nuclei were labelled with Hoescht 33258 according to manufacturer's instructions. Samples were imaged within 30 minutes. For confocal microscopy, real-time wide-field imaging and SIM, Zeiss Elyra PS.1 microscope equipped with C-Apochromat 63x/1.2 W Korr M27 objective was used. Lasers 633 (10%), 488 (0.2%) and 405 (2%) were used for confocal imaging. A pinhole of 1.06 Airy unit was used to image the full field of view to have an optical slice equivalent of 1 µm thickness. For real-time wide-field imaging, the lasers 642 (1%), 488 (0.02%) and 405 (2%) were used with multi-bandpass filter BP 420-480 + BP 495-550 + LP 650 at exposure time of 40 ms and 200 camera gain on EMCCD camera (25 frames per second). The microscope had access to 'internal' hardware switch option which was used for fast imaging. For SIM, the following settings were used: multi-bandpass filter set BP 420-480 + BP 495-550 + LP 650,

camera exposure time 35.0 ms, lasers 642 (20%), 488 (8%), 405 (8%), grating period 51 µm. Prior to sample imaging for datasets, the DAPI, AF488 and AF594 channels were checked for cross-leakage of fluorescence into the DiD channel (to avoid artefacts; none was found) (Figure 2.5). Within DAPI, AF488 and AF594 channels, some leakage was found and was optimised using excitation-emission adjustments and laser settings in Zeiss platform.

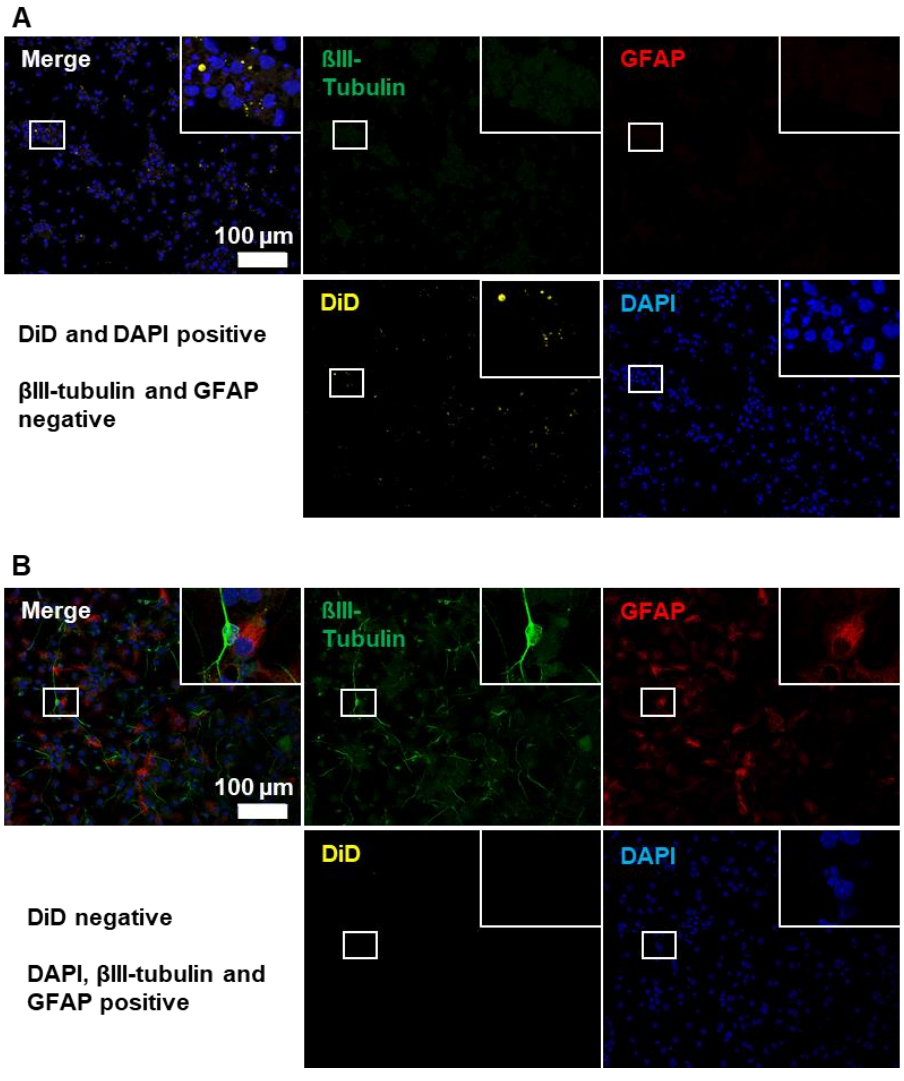


Figure 2.5: Testing for fluorescence channel leakage into the far-red (DiD) channel. (A) Samples negative for AF488 and AF594, and positive for DiD. (B) Samples positive for AF488 and AF594, and negative for DiD. DAPI (blue) was used as nuclei counterstain.

2.12.3. Flow cytometry

DiD-labelled EVs (sonicated or non-sonicated) were added to MSCs at an equal volume (0.5 µl of EVs/cm2) or at an equal particle count (1 x 109 particles/cm2) for a 6-hour incubation followed by a gentle PBS wash and trypsinisation to detach the cells from the tissue culture plastic. The cells were pelleted at 200G for 5 minutes and the resuspended in 1 ml PBS solution before analysis on a Cytomics FC 500 (Beckman Coulter, USA) using FL4 channel at 20mW target laser power (a minimum of 5000 events were recorded) and data processing using FlowJo V10.5 software. Flow cytometry was performed by DO, analysed by ZN.

2.13. Dot blot

Cell and EV extracts were lysed using RIPA Lysis and Extraction Buffer with added proteinase inhibitor and phosphatase inhibitor cocktails (Sigma). Protein concentration was measured using a Bradford assay (Sigma). For dot blot analysis (Gallagher et al., 2008), 10 µg of protein from each sample were added onto nitrocellulose membranes and dried for 10 minutes. The membranes were blocked using 1% skimmed milk in TBS-T (0.1% Tween20 (Sigma) in Tris buffer) and incubated with primary antibodies (Table 2.4) against CD63, TSG101, or GM130 (Santa Cruz) for 30 minutes. Membranes were then washed with TBS-T, incubated with peroxidase conjugated secondary antibody (Vector Laboratories) (Appendix document Table 4) for 30 minutes, and then washed with TBS-

T, before a 1-minute incubation with ECL detection reagent. Membranes were immediately imaged using LAS-4000 (Fujifilm).

2.14. Statistical analysis

All experiments were run in triplicates. For cell culture (neurite outgrowth, metabolic activity, cell count and migration) and differentiation experiments of Cell_LVsg, biological replicates were used, n=3 is samples from 3 independent mouse brains. For cell culture and differentiation experiments of C17.2 cell line, 3 separate culture plates were used, i.e, technical replicates. For cell culture and differentiation experiments of Cell_LVwt and Cell_BGwt, 3 separate culture plates were used, i.e, technical replicates. For EV characterisation, EVs from 3 separate culture conditions were isolated, i.e, biological replicates. For EV response studies, EVs were added to three independent culture wells, i.e, technical replicates. For immuhistochemistry of mouse brain sections, samples from 3 independent mice were use, i.e, biological replicates. All statistical graphs and analysis was performed using Prism (GraphPad Software, lnc., San Diego,CA, http://www.graphpad.com). One-way ANOVA with multiple comparison tests or Student's t-test was run to determine the statistical significance for all analysis (mentioned in the figure legends accordingly). All data represented as Mean ± SD or Mean ± SEM and are mentioned in the figure legends accordingly. Statistical significance level was set for *$p<0.05$, **$p<0.01$, ***$p<0.001$, ****$p<0.0001$.

3. *In vitro* differentiation of primary LV-NSCs to radial-like glia using fasudil

3.1. Introduction

Fasudil is a ROCK inhibitor that has been shown to alleviate symptoms from a range of CNS disorders including subarachnoid haemorrhage (SAH), spinal cord injuries, cerebral stroke, Parkinson's Disease neuropathic pain and epilepsy (Chen et al., 2013). Although other ROCK inhibitors including C3 transferase and Y27632 have shown similar neurogenic effects on animal models *in vivo* and *in vitro*, fasudil is the only clinically approved ROCK inhibitor currently in use for patients suffering from CNS disorders (Jia, et al., 2016, Gu, et al., 2013).

An *in vivo* study has shown that intra peritoneal administration of fasudil in a hypoxia/reoxygenation mouse model can mobilise endogenous progenitors from the SVZ, suggesting that NSCs may be responsive to fasudil (Ding, et al., 2010). Moreover, a recent study reported that fasudil could differentiate the C17.2 neural progenitor cell line into neurons and glia *in vitro* (Chen et al., 2015). However, the cellular effects of this drug on primary neuro-progenitor cell populations remain unclear. Here, the effect of fasudil on primary NSC culture and differentiation *in vitro* was analysed using cells isolated from the lateral ventricles of early postnatal and adult mouse brain tissue.

3.2. Aims

This Chapter has 2 aims.

The first aim was to investigate the response of primary early postnatal LV-NSCs to FAS by monitoring morphological changes, metabolic activity, migratory changes and differentiation potential (Sections 3.3.1 – 3.3.3).

The second aim was to assess the responsiveness of primary adult LV-NSCs to FAS by monitoring morphological changes, metabolic activity and differentiation potential (Sections 3.3.4 – 3.3.6).

3.3. Results

Note: Please refer to Table 2.1 for nomenclature

3.3.1.1. Changes in metabolic and morphological properties of postnatal Cell_LVsg and Cell_C17.2 on exposure to fasudil

The effect of fasudil treatment on postnatal Cell_LVsg was first analysed by monitoring changes in cell morphology at day 0, day 2 and day 4 (Figure 3.1 A-C). Particularly, morphological analysis of neural outgrowth *in vitro* have been widely used to assess the differentiation and maturation ability of neural cells (Gaub et al., 2010; Jia et al., 2016; Lodish et al., 2000; Roloff et al., 2015; Wang et al., 2015a; Zaim and Isik, 2018). C17.2 cells (Cell_C17.2) were used as a positive control for FAS mediated neural differentiation according to a recently published study (Chen et al., 2015). Brightfield images of FAS-treated samples at day 2 and day 4 showed cytoskeletal changes with increased cytoplasmic outgrowth (from here referred to as ‘neural outgrowth’ or ‘neurite length’) in both postnatal Cell_LVsg and C17.2 cells, compared to day 0 controls (Figure 3.1 A-C). Total neurite length increased significantly from day 2 to day 4 of FAS treatment for both cell types, and this increase was more pronounced in Cell_C17.2 (Figure 3.1 A-C). It was noticed that postnatal Cell_LVsg under FAS treatment (Cell_LVsg_FAS) showed smooth radial-like elongated neural outgrowth with less or no branching

compared to Cell_C17.2 under FAS-treatment (Cell_C17.2_FAS) (Figure 3.1 A).

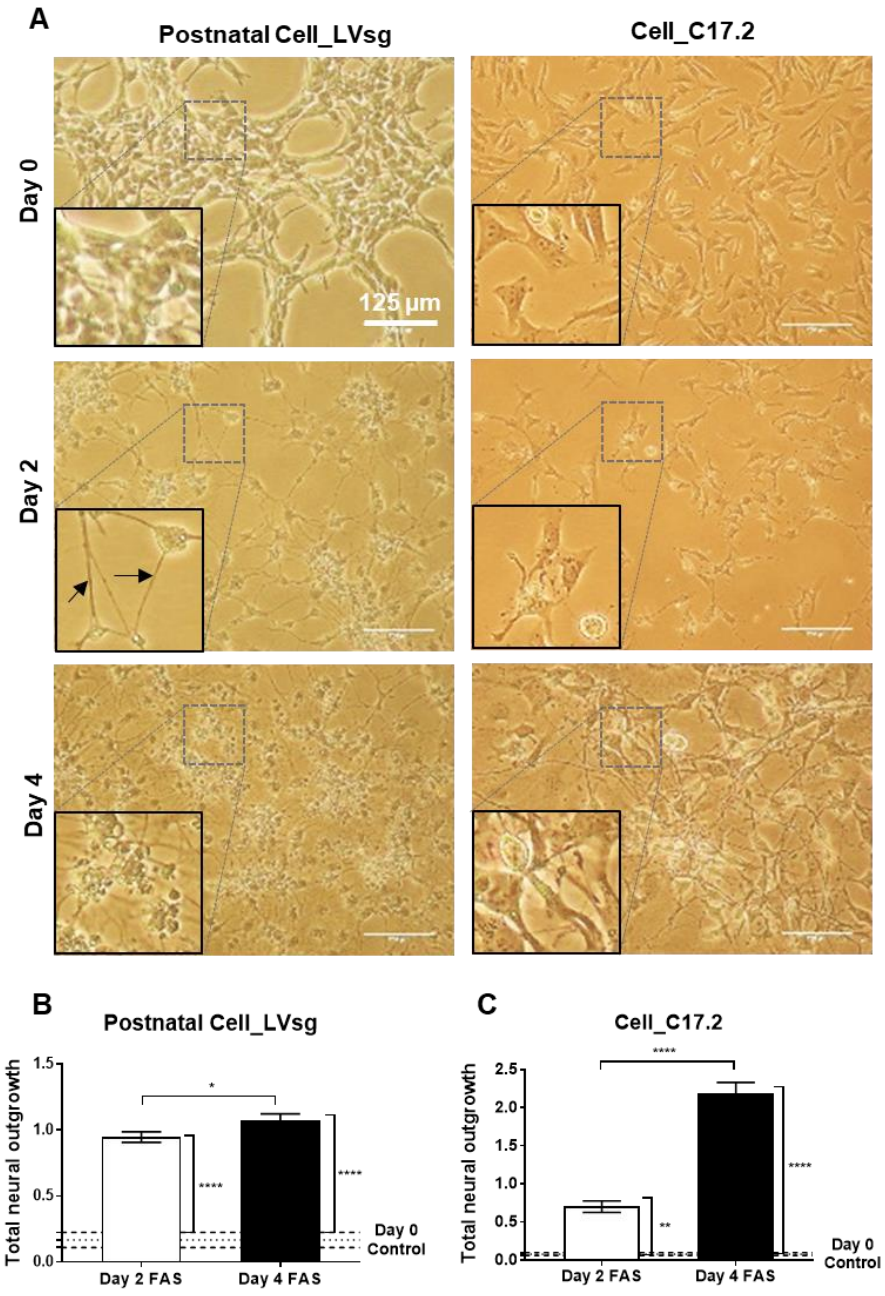


Figure 3.1: Morphological changes of Cell_LVsg_FAS and Cell_C17.2_FAS at day 2 and day 4 compared to day 0. (A) Brightfield images showing cytoskeletal changes of cells under FAS treatment. (B-C) Quantitation of neural outgrowth of (B) Cell_LVsg_FAS (C) Cell_C17.2_FAS. One-way ANOVA Tukey's multiple comparison test, Mean ± SD, n=3, (*) p<0.05.

To further investigate whether the radial-like unbranched neural extensions observed in Cell_LVsg_FAS were of neuronal origin, βIII-tubulin immunostaining was performed. (Figure 3.2 A and B). βIII-tubulin detection showed a moderate increase in postnatal Cell_LVsg_FAS neurite outgrowth by day 4 (Figure 3.2 A and B). However, it was observed that βIII-tubulin expression in postnatal Cell_LVsg_FAS was very low (0.9 ± 0.7% at day 2 and 1.5 ± 0.9% at day 4), suggesting that postnatal Cell_LVsg_FAS did not produce neuronal-like outgrowth but rather radial-like projections. Comparison with undifferentiated controls at day 2 and day 4 confirmed that increased βIII-tubulin neuronal outgrowth was due to FAS-treatment and not spontaneous differentiation (Figure 3.2 A and B).

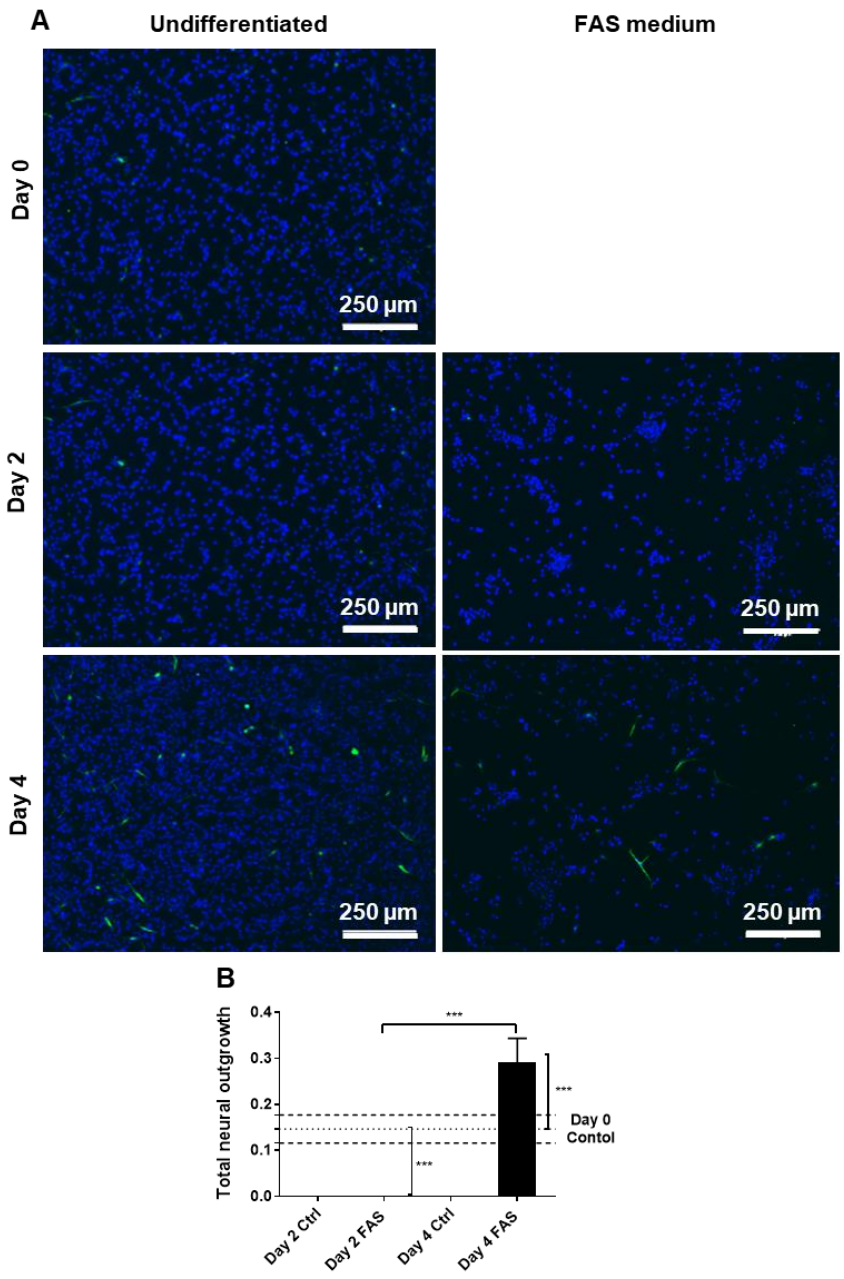


Figure 3.2: βIII-tubulin staining of Cell_LVsg_FAS. (A) Immunohistochemistry of undifferentiated and FAS-treated Cell_LVsg for βIII-tubulin (green) at day 2 and day 4. Nuclei counterstain DAPI (blue) was used. (B) Quantitation of total neural outgrowth of undifferentiated and FAS-treated Cell_LVsg. One-way ANOVA Tukey's multiple comparison test, Mean ± SD, n=3, (*) p<0.05.

By contrast, Cell_C17.2_FAS showed stronger βIII-tubulin immunoreactivity with significant increase on day 2 (10 ± 1.3%) and day 4 (18.75 ± 3.1%) (Figure 3.3 A and B) compared to postnatal Cell_LVsg_FAS (Figure 3.2 A and B). It was also observed that the

neuronal outgrowth induced was FAS specific as the βIII-tubulin neuronal outgrowth was significantly higher in FAS-treated controls than undifferentiated controls at day 2 and day 4. Taken together, the results from neural outgrowth analysis indicated that FAS-treatment induced non-neuronal radial-like outgrowth in postnatal Cell_LVsg and neuronal neurite-like outgrowth in Cell_C17.2.

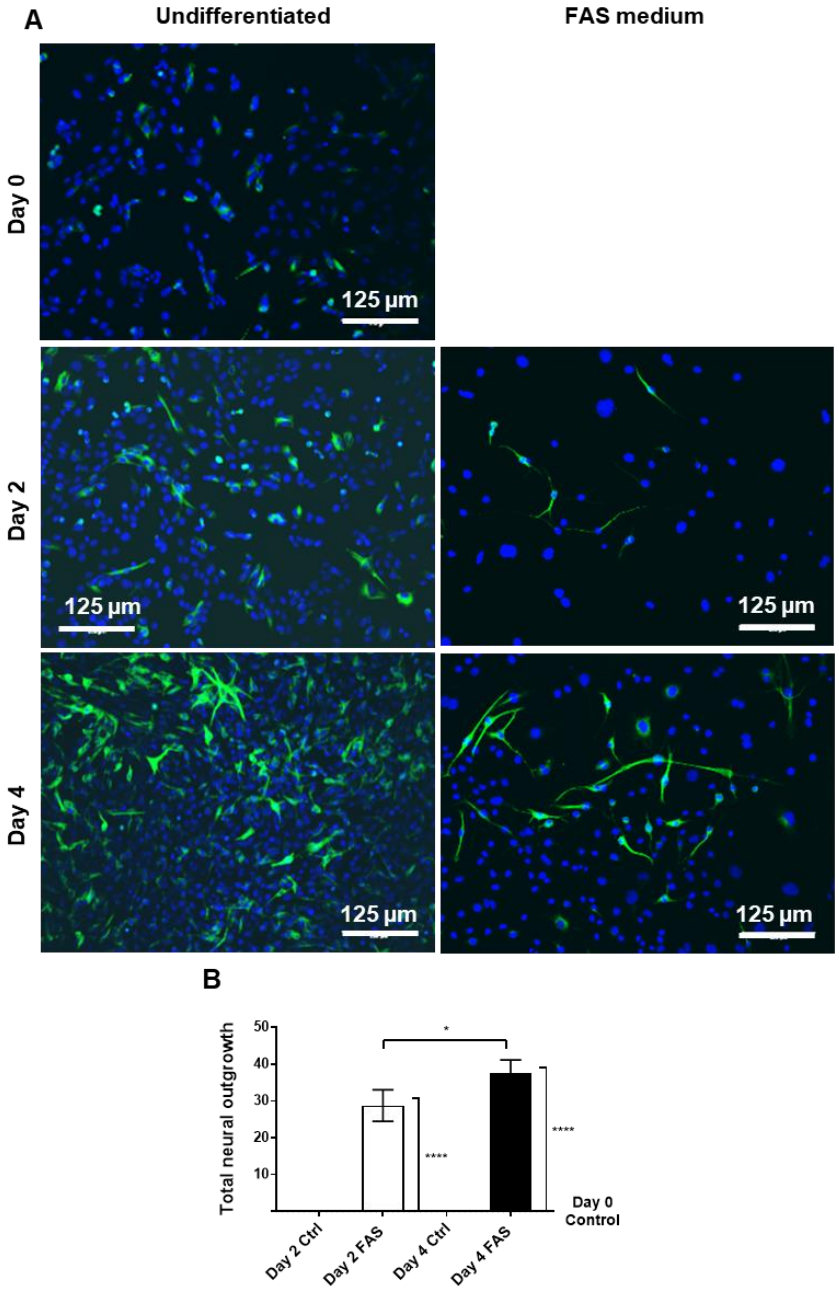


Figure 3.3: βIII-tubulin staining of Cell_C17.2_FAS. (A) Immunohistochemistry of undifferentiated and FAS-treated Cell_C17.2 for βIII-tubulin (green) at day 2 and day 4. Nuclei counterstain DAPI (blue) was used. (B) Quantitation of total neural outgrowth of undifferentiated and FAS-treated Cell_C17.2. One-way ANOVA Tukey's multiple comparison test, Mean ± SD, n=3, (*) p<0.05.

To investigate the toxic effect of FAS treatment, cell count was performed using brightfield images. There was a significant reduction of cell number in both cell types after FAS-treatment at day 2 and day 4 compared to their undifferentiated controls (Figure 3.4 A and B). It

was also observed that there was no significant change in the cell count of postnatal Cell_LVsg from day 2 to day 4 of FAS-treatment (Figure 3.4 C). A significant increase in cell number from day 2 to day 4 of FAS-treatment was observed for Cell_C17.2 (Figure 3.4 C). These results indicated that FAS-treatment might be involved in a selection process of differentiating cells, causing loss of cell initially but was non-toxic as it did not promote steady decline of cells in culture.

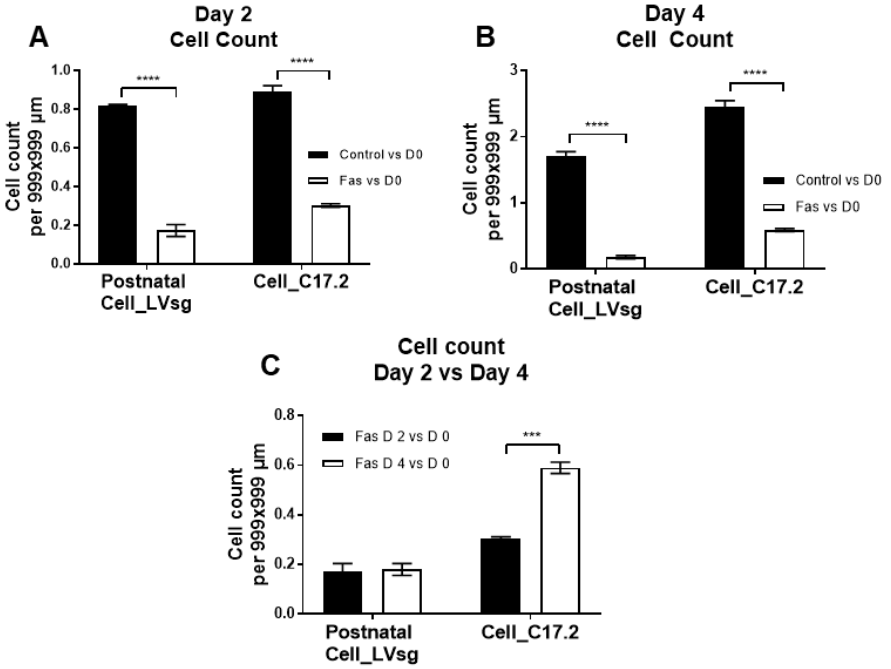


Figure 3.4: Brightfield cell count analysis of Cell_LVsg_FAS and Cell_C17.2_FAS. (A-B) Cell count at (A) day 2 and (B) day 4 of FAS-treatment compared to undifferentiated controls. (C) Cell count of FAS-treated samples at day 2 compared to day 4. Student's t-test, Mean ± SD, n=3, (*) p<0.05.

Next, the change in metabolic state of the FAS-treated cells in culture was assessed. Metabolic analysis revealed that FAS-treatment significantly increased the metabolic activity of postnatal Cell_LVsg at day 2 and day 4 compared to their day 0 and their undifferentiated

controls (Figure 3.5 A). Cell_C17.2 also showed an increase in metabolic activity, but it was statistically significant only at day 2 of FAS-treatment (Figure 3.5 B). Taken together, these results suggested that postnatal Cell_LVsg were responsive to FAS-treatment with immediate increase in radial-like neural outgrowth and metabolic activity.

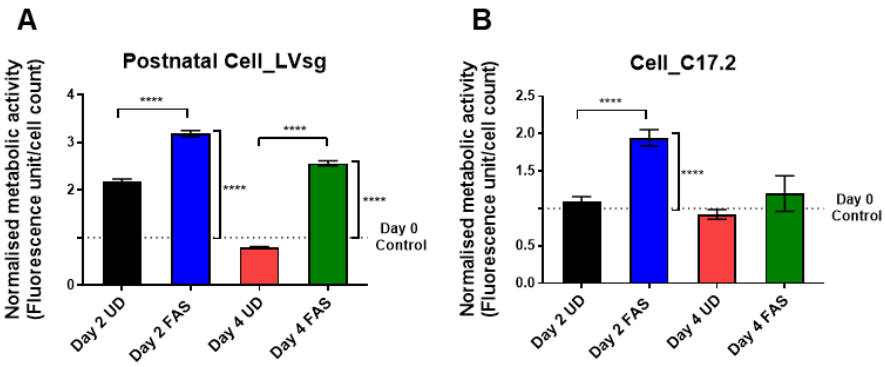


Figure 3.5: Change in metabolic activity of (A) postnatal LV-NSCs and (B) C17.2 cells after FAS-treatment at day 2 and day 4 compared to day 0 and undifferentiated (UD) controls. One-way ANOVA Tukey's multiple comparison test, Mean ± SD, n=3, (*) p<0.05.

3.3.2. GFAP and βIII-Tubulin expression of fasudil treated postnatal LV-NSCs and C17.2 cells

To further investigate changes observed *in vitro* in response to FAS-treatment, expression of NSC markers Nestin and Sox2, glial marker GFAP, and neuronal marker βIII-Tubulin were analysed over the 4-day FAS treatment by immunostaining (Figure 3.6 A). Undifferentiated day 0 postnatal Cell_LVsg (postnatal Cell_LVsg_D0) showed moderate Nestin, strong Sox2 signal, and were rare of GFAP or βIII-Tubulin expression (Figure 3.6 A). Upon FAS-treatment, there was a striking loss of Nestin

signal, and a significant increase in Sox2 detection in day 2 and day 4 (all compared to day 0 control) (Figure 3.6 A-C). Postnatal Cell_LVsg_FAS also displayed significantly higher levels of GFAP expression on day 2 and day 4 compared to untreated control (Figure 3.6 A, D), while βIII-Tubulin signal, which was generally low, was reduced on day 2 but significantly increased by day 4 FAS-treatment (Figure 3.6 A, E).

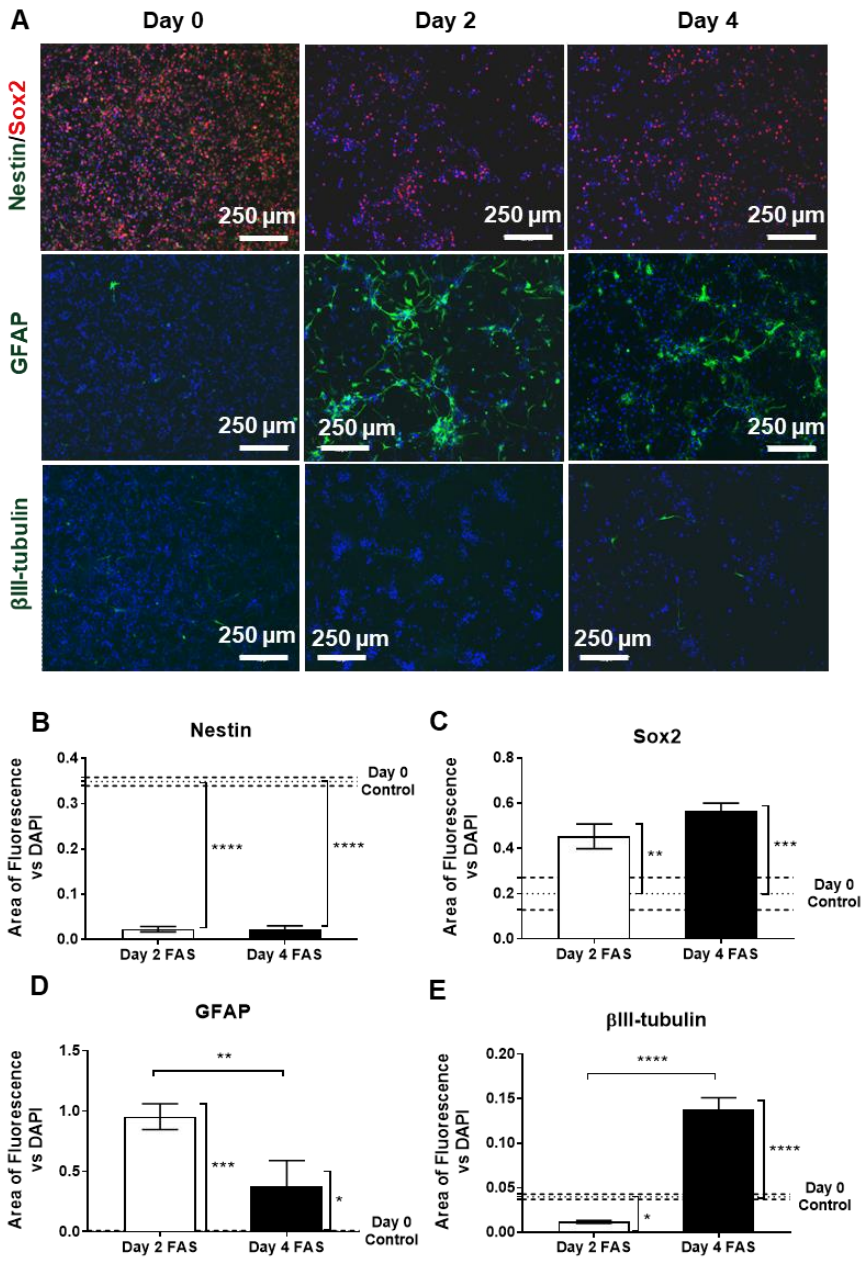


Figure 3.6: Marker expression analysis in postnatal Cell_LVsg exposed to FAS-treatment. (A) Immunofluorescence images showing the expression of Nestin (green), Sox2 (red), GFAP (green) and βIII-tubulin (green) in undifferentiated day 0 and FAS-treated cells at day 2 and day 4. DAPI used as nuclear counterstain (blue). (B-E) Signal quantitation using image analysis for (B) Nestin, (C) Sox2, (D) GFAP and (E) βIII-tubulin. One-way ANOVA Tukey's multiple comparison test, Mean ± SD, n=3, (*) p<0.05.

RT-PCR was then performed to compare the expression pattern at mRNA level during differentiation of postnatal Cell_LVsg (Figure 3.7 A). No significant changes were observed for *nestin* at mRNA level over the

4-day FAS-treatment (Figure 3.7 A, B) suggesting that the change in nestin expression is predominantly post-translational. However, a significant increase in *sox2* (Figure 3.7 A, C) and *GFAP* (Figure 3.7 A, D) at day 2 and day 4, and increase in *βIII-Tub* (Figure 3.7 A, E) at day 4 was observed which complemented the results from immunostaining. Taken together these results hinted that fasudil promoted gliogenesis of Cell_LVsg by increasing the expression of GFAP and Sox2 (markers of proliferating NSCs and reactive astrocytes) with concomitant reduction in Nestin and low βIII-Tubulin expression (markers of neuronal progenitors and early neural lineage, respectively).

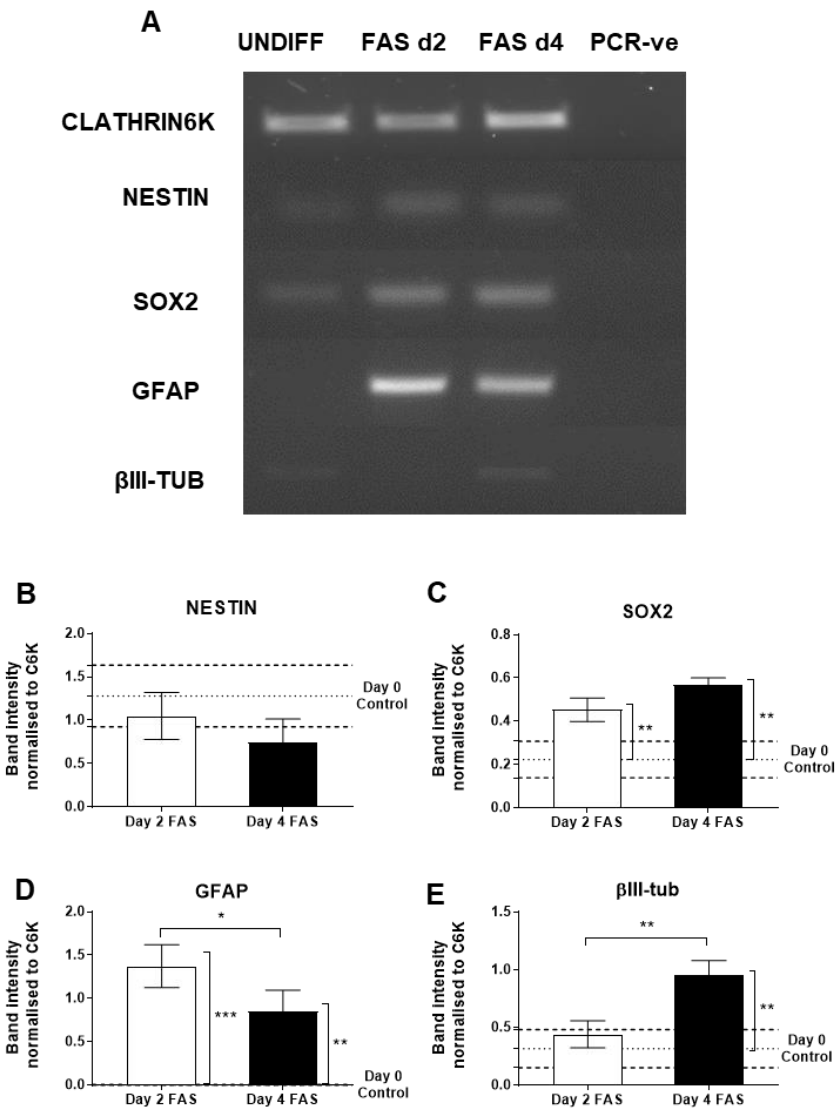


Figure 3.7: RT-PCR analysis of postnatal Cell_LVsg treated with FAS-medium. (A) Gel electrophoresis images showing band intensity of amplified cDNA from undifferentiated day 0 (UNDIFF), day 2 FAS-treated (FAS d2) and day 4 FAS-treated (FAS d4). (B-E) Corresponding quantitation of RT-PCR band intensity samples for (B) Nestin, (C) Sox2, (D) GFAP and (E) βIII-tubulin. PCR-ve represents the no template control for PCR. Clathrin6K was used as the housekeeping gene. One-way ANOVA Tukey's multiple comparison test, Mean ± SD, n=3, (*) p<0.05.

In contrast to its effect on postnatal Cell_LVsg, fasudil promoted the appearance of βIII-Tubulin-positive cells from Cell_C17.2 (Figure 3.8 A-E). Nestin signal was low in these cells at day 0 but showed a significant increase at day 2 and day 4 of FAS-treatment (Figure 3.8 A, B); this was accompanied by a moderate decrease in Sox2 detection on day 4 (Figure

3.8 A, C). GFAP expression was observed to be weak throughout the FAS-treatment course for Cell_C17.2 (Figure 3.8 A, D).

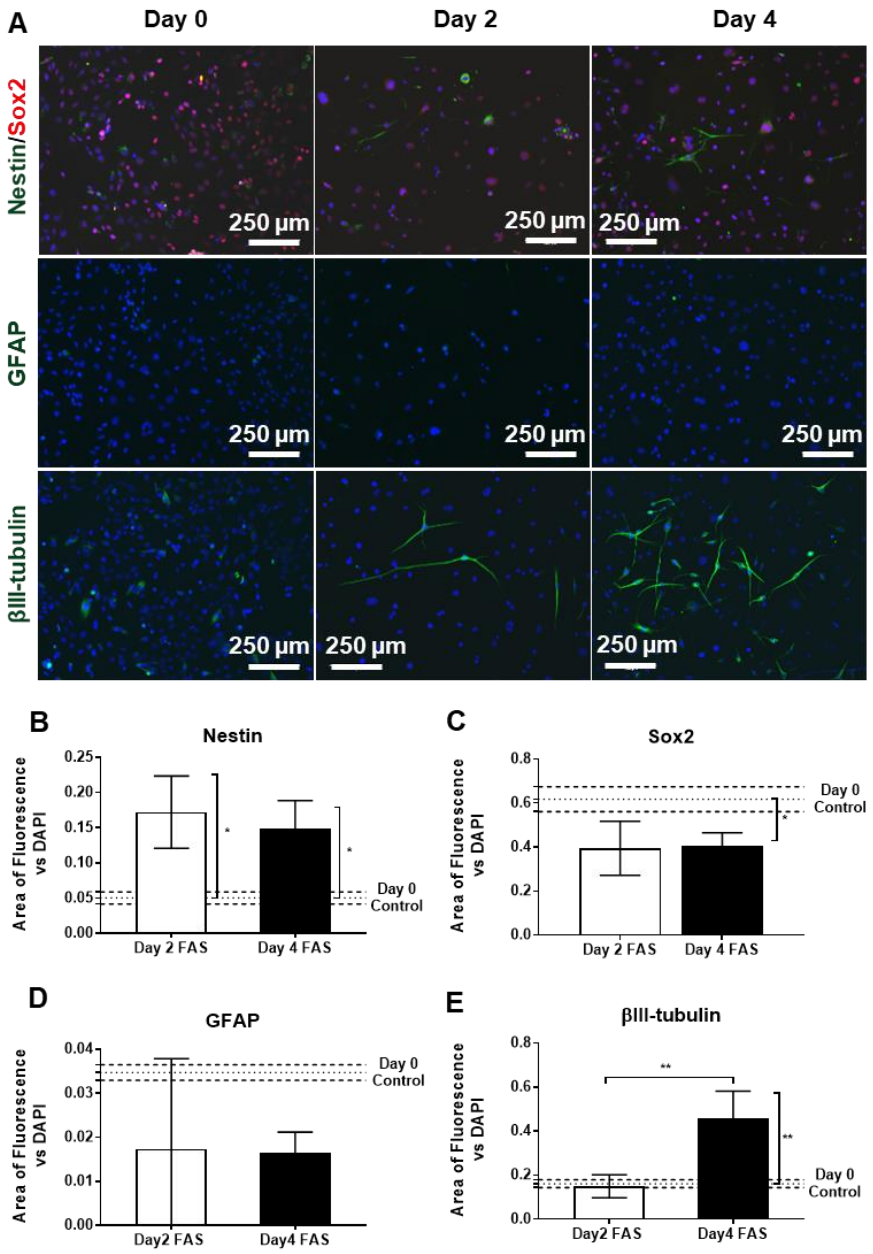


Figure 3.8: Marker expression analysis in Cell_C17.2 exposed to FAS-treatment. (A) Immunofluorescence images showing the expression of Nestin (green), Sox2 (red), GFAP (green) and βIII-tubulin (green) in undifferentiated day 0 and FAS-treated cells at day 2 and day 4. DAPI used as nuclear counterstain (blue). (B-E) Signal quantitation using image analysis for (B) Nestin, (C) Sox2, (D) GFAP and (E) βIII-tubulin. One-way ANOVA Tukey's multiple comparison test, Mean ± SD, n=3, (*) p<0.05.

RT-PCR analysis showed no difference in *nestin* detection over the time course of FAS-treatment (Figure 3.9 A, B), decrease in *sox2* at day 4 (Figure 3.9 A, C), poor detection of *GFAP* at both day 2 and day 4 (Figure 3.9 A, D), and significant increase in *βIII-Tub* at day 2 and day 4 (Figure 3.9 A, E), thereby complementing the results from immunostaining, for Cell_C17.2. These results suggested that fasudil promoted neuronal rather than glial lineage differentiation in C17.2 cells.

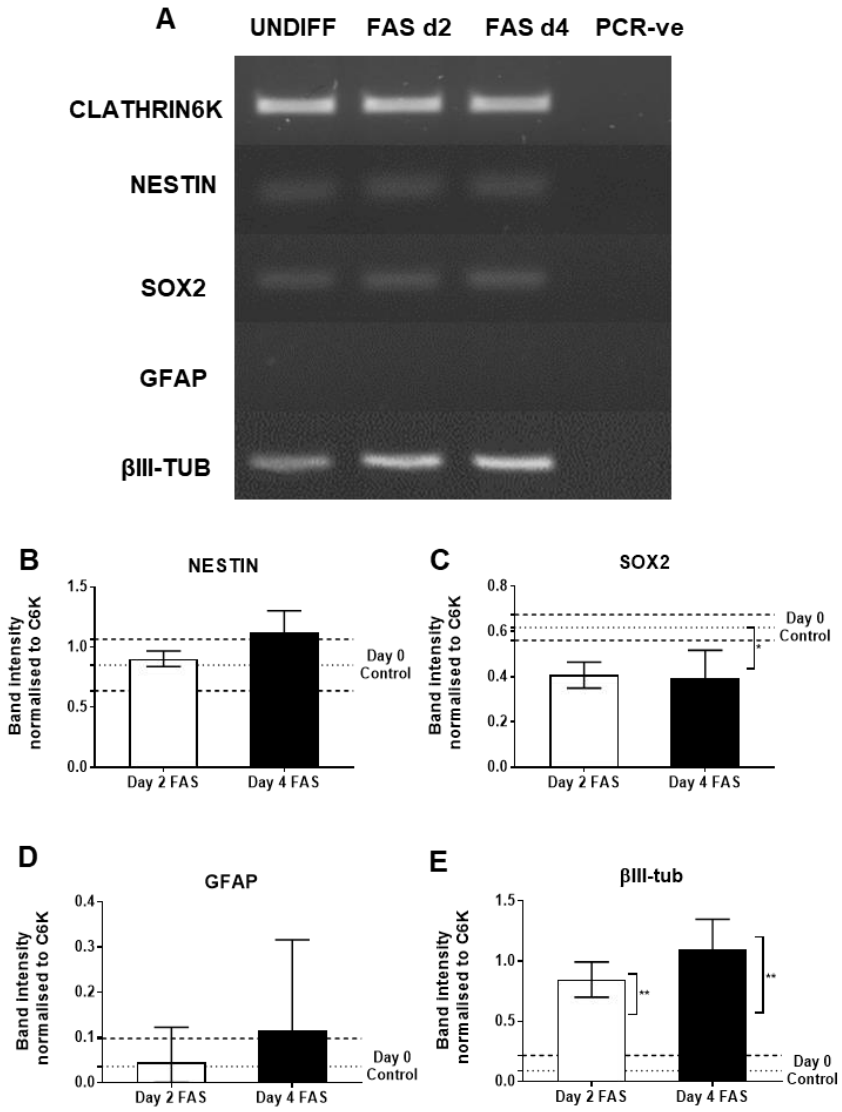


Figure 3.9: RT-PCR analysis of Cell_C17.2 treated with FAS-medium. (A) Gel electrophoresis images showing band intensity of amplified cDNA from undifferentiated day 0 (UNDIFF), day 2 FAS-treated (FAS d2) and day 4 FAS-treated (FAS d4). (B-E) Corresponding quantitation of RT-PCR band intensity samples for (B) Nestin, (C) Sox2, (D) GFAP and (E) βIII-tubulin. PCR-ve represents the no template control for PCR. Clathrin6K was used as the housekeeping gene. One-way ANOVA Tukey's multiple comparison test, Mean ± SD, n=3, (*) p<0.05.

Next, FAS-treated samples were compared with undifferentiated controls of day 2 and day 4 (Figure 3.10 and Figure 3.11). Postnatal Cell_LVsg_FAS showed lower levels of Nestin and higher levels of Sox2 and GFAP signals compared to all untreated controls, while βIII-Tubulin was always detected at low levels (Figure 3.10 A-E). In contrast,

Cell_C17.2_FAS showed higher levels of Nestin and βIII-Tubulin, and lower of GFAP signal when compared to day 2 untreated controls. Also, it was noticed that day 4 undifferentiated controls showed increased detection of GFAP (significantly more than all other samples) and βIII-Tubulin (with no significant difference compared to day 4 FAS-treated samples) (Figure 3.11 A, D and E). These results not only show that FAS-treated samples differentiated in a unique manner different from that of spontaneous differentiation of overconfluent cultures and *in vitro*, but also that FAS-mediated differentiation of NSCs can depend on cell source.

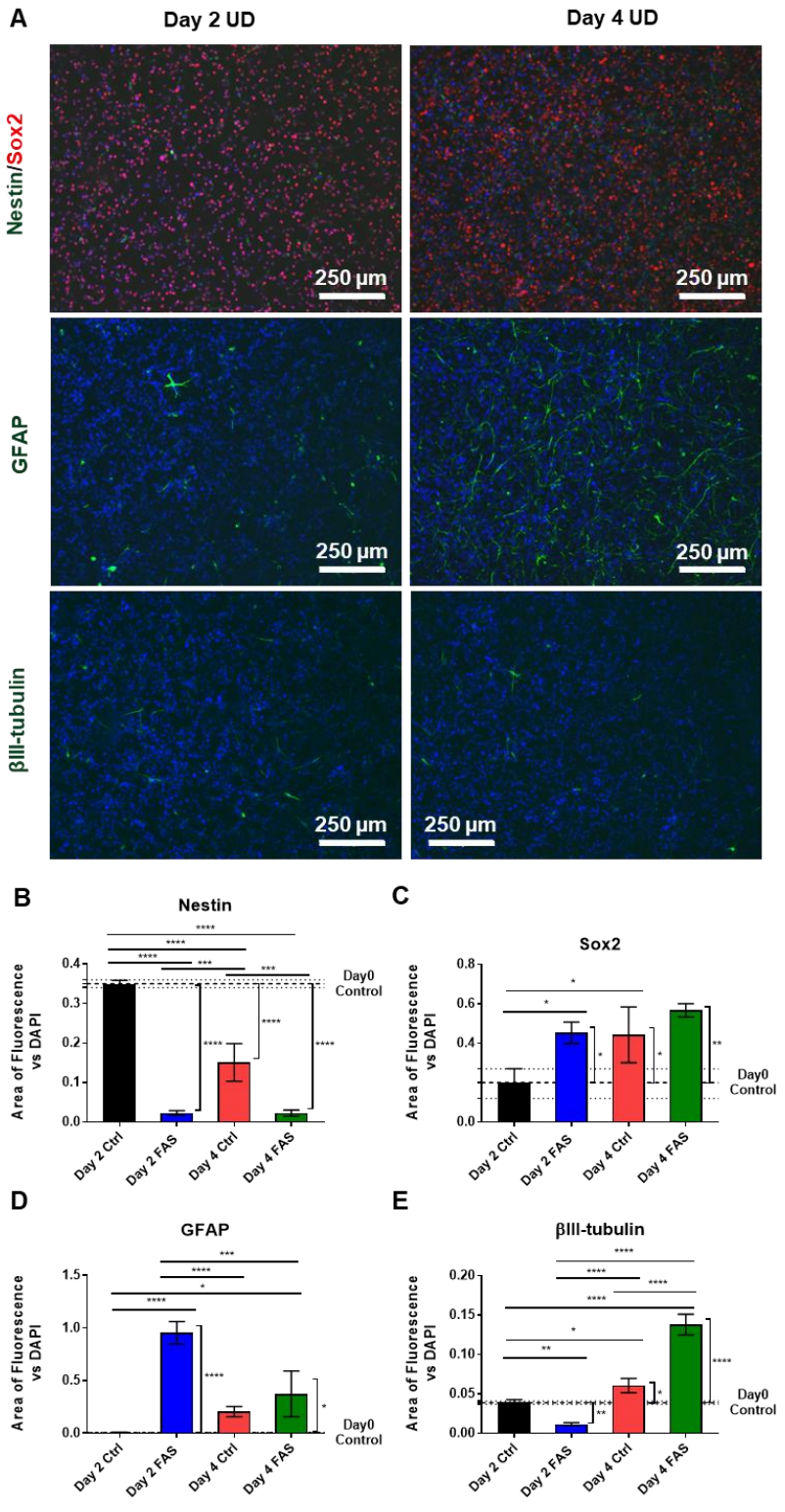


Figure 3.10: Marker expression analysis in overgrown cultures of postnatal Cell_LVsg compared to FAS-treated cultures. (A) Immunofluorescence images showing the expression of Nestin (green), Sox2 (red), GFAP (green) and βIII-tubulin (green) in undifferentiated day 2 and day 4. DAPI used as nuclear counterstain (blue). (B-E) Corresponding signal quantitation using image analysis for (B) Nestin, (C) Sox2, (D) GFAP and (E) βIII-tubulin. One-way ANOVA Tukey's multiple comparison test, Mean ± SD, n=3, (*) p<0.05.

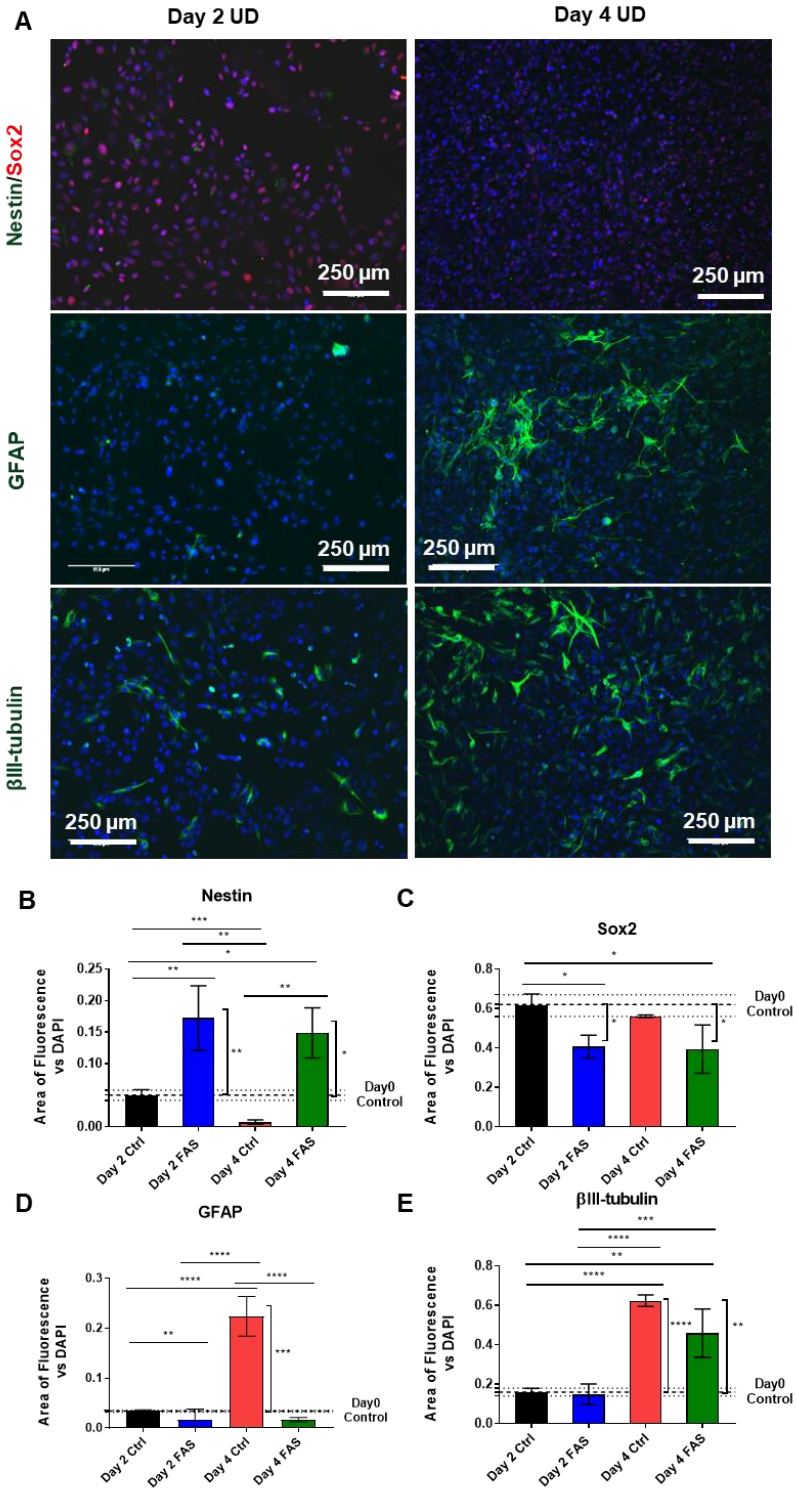


Figure 3.11: Marker expression analysis in overgrown cultures of Cell_C17.2 compared to FAS-treated cultures. (A) Immunofluorescence images showing the expression of Nestin (green), Sox2 (red), GFAP (green) and βIII-tubulin (green) in undifferentiated day 2 and day 4. DAPI used as nuclear counterstain (blue). (B-E) Corresponding signal quantitation using image analysis for (B) Nestin, (C) Sox2, (D) GFAP and (E) βIII-tubulin. One-way ANOVA Tukey's multiple comparison test, Mean ± SD, n=3, (*) p<0.05.

3.3.3. Migratory properties of fasudil treated postnatal Cell_LVsg and Cell_C17.2

In order to further analyse the phenotypic changes in postnatal Cell_LVsg treated with FAS, the dynamics and migratory properties of the cells in culture were monitored by time-lapse microscopy. In the mammalian brain, migrating NSCs are known to express GFAP and show radial-like morphology (Del Bene, 2011; Doetsch et al., 1999; Kulikova et al., 2011; Malatesta et al., 2008; Spear and Erickson, 2012a). Radial glia populations display INM, a distinct migration pattern of the cell body along the radial-bidirectional cytoplasmic elongation, between the basal and apical layer of ventricular zone (Spear and Erickson, 2012b, 2012a).

When postnatal Cell_LVsg cultures were monitored under FAS-treatment, cultures were observed to form dense colonies at day 2 from which cells exhibited a radial-like migratory pattern suggestive of INM (Figure 3.12 A). Notably, there was a significant increase in trackable migratory cells (B-E type) by day 4 (Figure 3.12 B) (refer to section 2.9 for more information on B-E type cells). Video file 2 shows the chain migration of postnatal Cell_LVsg and video file 3 shows their radial-like movement after FAS-treatment at day 2 (Appendix video files 2 and 3).

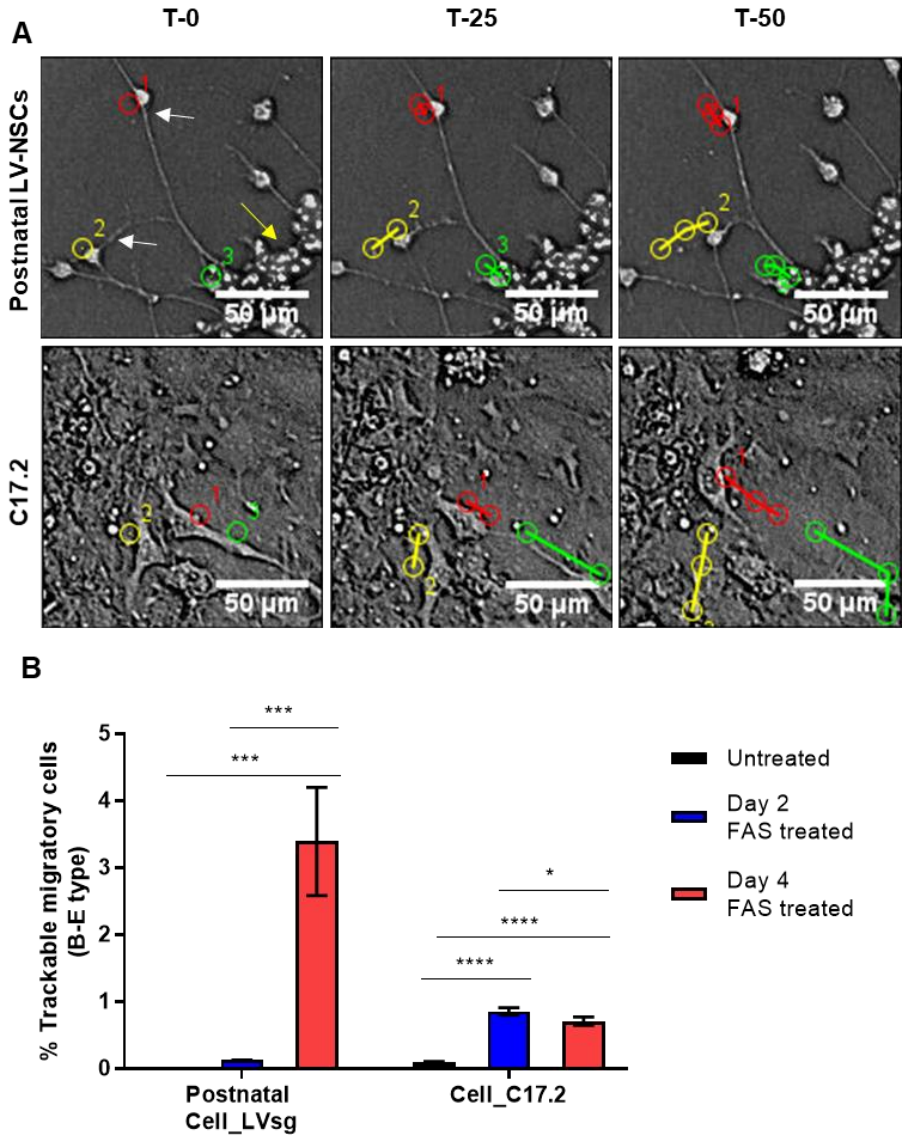


Figure 3.12: Comparative time-lapse analysis of postnatal Cell_LVsg and Cell_C17.2 during FAS-treatment. (A) Morphological changes of postnatal Cell_LVsg and Cell_C17.2 *in vitro*. Example of INM-like movement of postnatal Cell_LVsg and tangential movement of Cell_C17.2 under FAS-treatment at day 2. T0, T25, T50 represent sequential time-points in minutes. Red, green and yellow markings represent the tracking of three independent cells in the images. White arrows show the radial-like morphology of cells. Yellow arrow shows a dense colony formed during FAS differentiation of postnatal Cell_LVsg at day 2. (B) Percentage of trackable migratory cells (B-E type) in postnatal Cell_LVsg and Cell_C17.2. INM- interkinetic nuclear movement. One-way ANOVA Tukey's multiple comparison test, Mean ± SD, n=3, (*) p<0.05.

It was noted that the percentage of trackable migratory postnatal Cell_LVsg after FAS-treatment at day 2 was much lower (0.13 ± 0.002%) compared to day 4 of treatment (3.4 ± 0.81%) (Figure 3.12 B), although

radial-like migration was observed predominantly at day 2 (Appendix video file 3). Moreover, although the proportion of cells undergoing division (S-S type) significantly decreased in all FAS-treated Cell_LVsg samples compared to their day 0 counterparts (Figure 3.13) (refer to section 2.9 for more information on S-S type cells) (indicating FAS medium reduced the percentage of dividing cells or delayed the cell division), it was also noted that there was no significant difference in the percentage of S-S type cells (dividing postnatal LV-NSCs) between day 2 (4.95 ± 0.09%) and day 4 (5.21 ± 0.22%) (Figure 3.13). This suggested that the low number of postnatal Cell_LVsg tracked during day 2 of FAS-treatment was due to the dense colonies of cells formed during this stage that could have hindered cell tracking and not due to high number of dividing cells which were excluded from the cell tracking module (refer to section 2.9 for more information of cell selection module during live imaging).

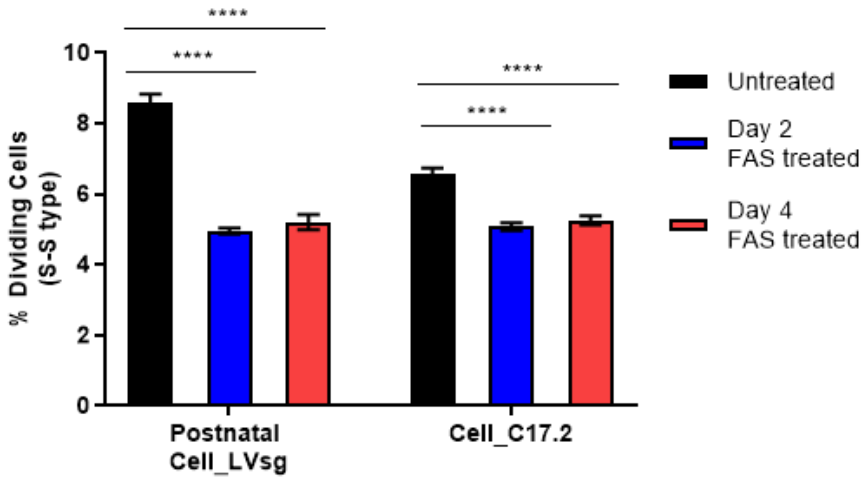


Figure 3.13: Percentage of dividing cells (S-S type) tracked in postnatal Cell_LVsg and Cell_C17.2 samples. One-way ANOVA Tukey's multiple comparison test, Mean ± SD, n=3, (*) p<0.05.

Cell_C17.2 showed a significant increase in trackable migratory cells both day 2 and day 4, however most cells showed a tangential migratory pattern on day 2 of FAS treatment (Figure 3.12 A, B), displaying a ‘crawling’ behaviour with short extensions. Video file 4 shows the tangential migratory behaviour of Cell_C17.2 at day 2 of FAS-treatment respectively (Appendix video file 4). These results suggested that, exposure to FAS promoted a radial-like migratory phenotype in postnatal Cell_LVsg, different from the predominantly tangential-like migratory phenotype observed in Cell_C17.2_FAS.

Finally, the total accumulated distance travelled by the non-dividing migratory cells in postnatal Cell_LVsg under FAS medium on both day 2 and day 4 was found to rise sharply compared to day 0 control (Figure 3.14). Particularly, it was noted that migratory distance of postnatal Cell_LVsg was higher at day 2 compared to day 4 of FAS-treatment (Figure 3.14). In contrast, for Cell_C17.2, the distance travelled under FAS medium was significantly lower than its day 0 control (Figure 3.14). Taken together, FAS-treatment promoted and increased INM-like migration of postnatal Cell_LVsg in contrast to its effect on Cell_C17.2.

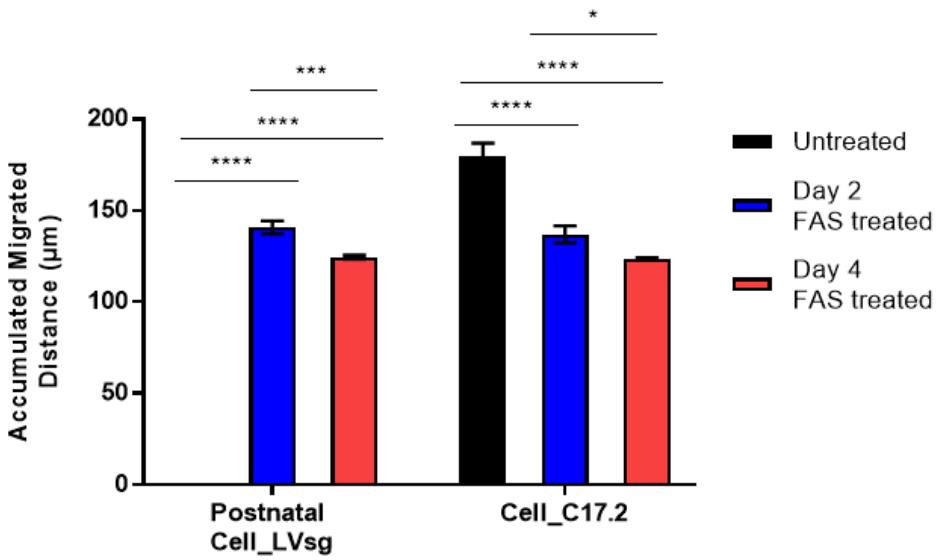


Figure 3.14: Quantitative analysis showing the total distance migrated by postnatal Cell_LVsg and Cell_C17.2 cells treated with FAS medium vs. undifferentiated cells. One-way ANOVA Tukey's multiple comparison test, Mean ± SD, n=3, (*) p<0.05.

3.3.4. Changes in morphology, metabolic activity and NSC marker expression during FAS-differentiation compared to RET-differentiation of adult Cell_LVsg

Adult NSCs are more restricted in terms of differentiation and migration than embryonic and early postnatal NSCs (Obernier et al., 2014). In order to determine how FAS-treatment may affect adult LV-NSCs in culture and to compare its efficiency to that of conventional neuronal differentiating protocols involving a retinoic acid analogue (RET), adult LV-NSCs (Cell_LVsg) were isolated and treated with both FAS and RET for 10 days and monitored for morphological and metabolic changes.

Both differentiation conditions were associated with rapid changes in cell morphology (Figure 3.15). By day 10, Cell_LVsg showed mature neuronal morphologies with branched dendrites during RET-treatment, and flat morphological properties with radial-like extensions and less branching during FAS-treatment (Figure 3.15).

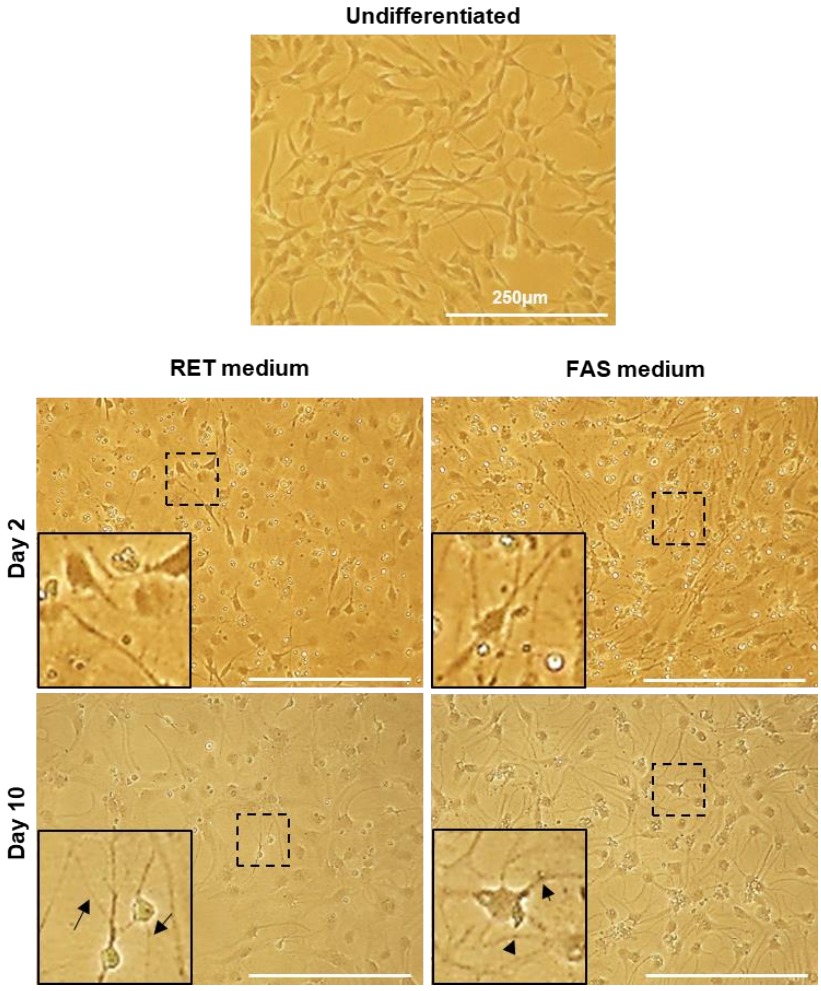


Figure 3.15: Brightfield images showing morphological response of adult LV-NSCs during RET- and FAS-differentiation on day 2 and day 10. Arrows show the branching neurites in RET-treated adult NSCs vs flattened radial-like outgrowth in FAS-treated adult LV-NSCs at day 10.

To determine the differences in metabolic activity of Cell_LVsg cultured in RET and FAS medium, Metabolic analysis assay normalised to cell count determined by pico green assay was performed. There was no

significant difference in cellular metabolic activity between the FAS-based and the RET-based conditions at day 2 and day 10 (Figure 3.16 A, B). No decrease in metabolic activity was observed during FAS or RET differentiation compared to day 0 controls (Figure 3.16 A, B).

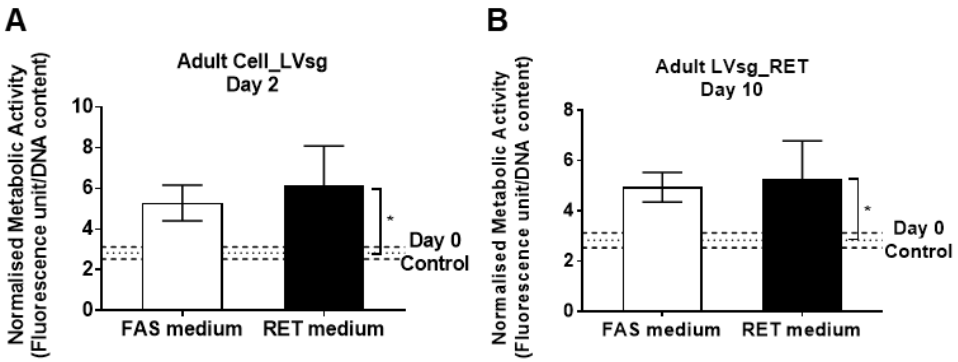


Figure 3.16: Metabolic response (normalised to DNA content) of adult LV-NSCs during RET- and FAS-differentiation on (A) day 2 and (B) day 10. One-way ANOVA Tukey's multiple comparison test, Mean ± SD, n=3, (*) p<0.05.

To determine if lower concentrations of FAS decreased cell loss while maintaining radial-like neural outgrowth in Cell_LVsg, increasing concentrations (0 µM, 25µM, 50 µM, 75 µM and 100 µM) of FAS containing medium were prepared and added to Cell_LVsg and compared with RET- and STD- (STD – Standard medium which is NSC media without growth factors or serum) treatment (Figure 3.17 A and B). Pico green assay showed that all treatments resulted lower amount of total DNA on day 2 and day 10 compared to day 0 but no significant decrease between day 2 and day 10 (Figure 3.17 A). 50 µM and 25 µM FAS resulted in significantly higher number of cells at day 10 of differentiation compared to RET-treated cells (Figure 3.17 A). Presto blue per pico green analysis showed that the increase in cellular metabolic activity on all treatments at day 2 and day 10 between the different

concentrations of FAS-treatment was not statistically different (Figure 3.17 B).

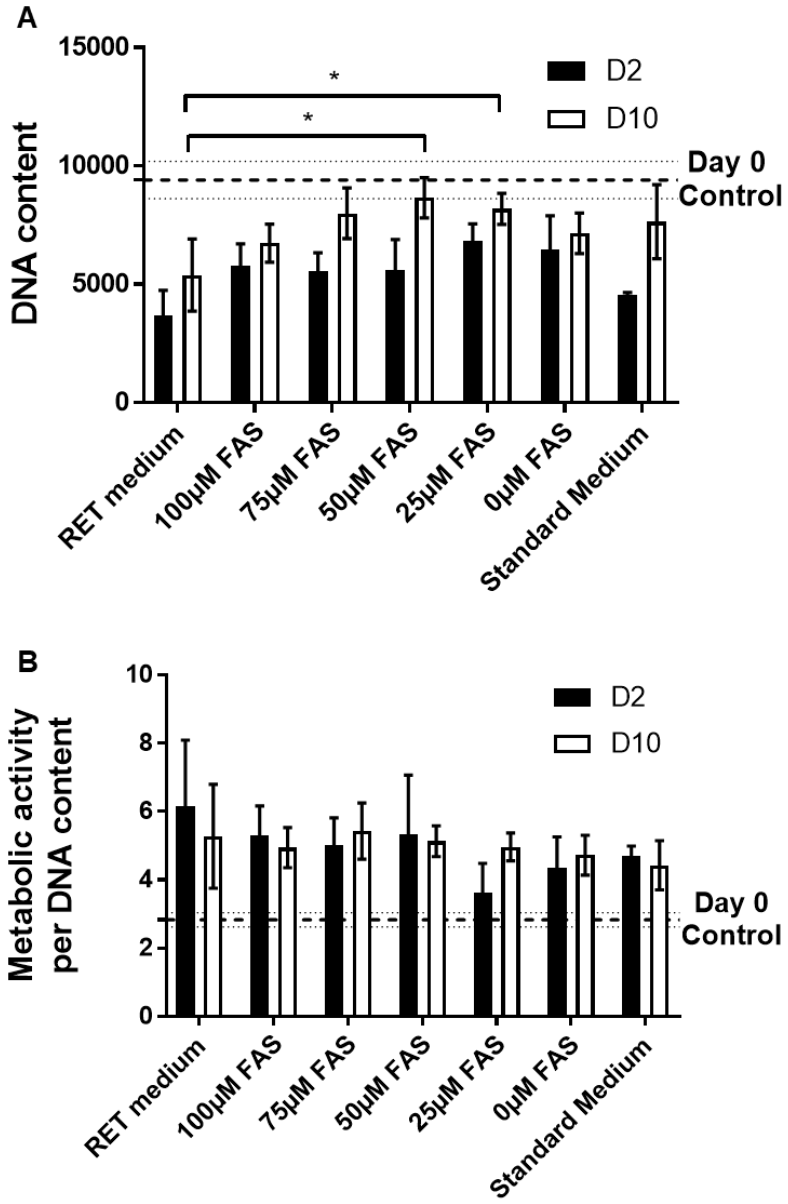


Figure 3.17: Cell count and metabolic profiling of adult LV-NSCs in response to different concentrations of FAS. (A) Pico green DNA quantification assay. (B) Presto blue per pico green quantification assay to determine cellular metabolic activity. One-way ANOVA Tukey's multiple comparison test, Mean ± SD, n=3, (*) p<0.05.

Brightfield imaging analysis showed that the radial-like neural growth Cell_LVsg was most evident when 100 µM FAS concentration was used

(Figure 3.18 A-G). Decrease in FAS concentration to even 75 µM decreased the visibility of radial-like outgrowth (Figure 3.18 A-G). These results indicated that 100 µM FAS treatment promoted efficient radial-like neural outgrowth of adult Cell_LVsg without toxicity.

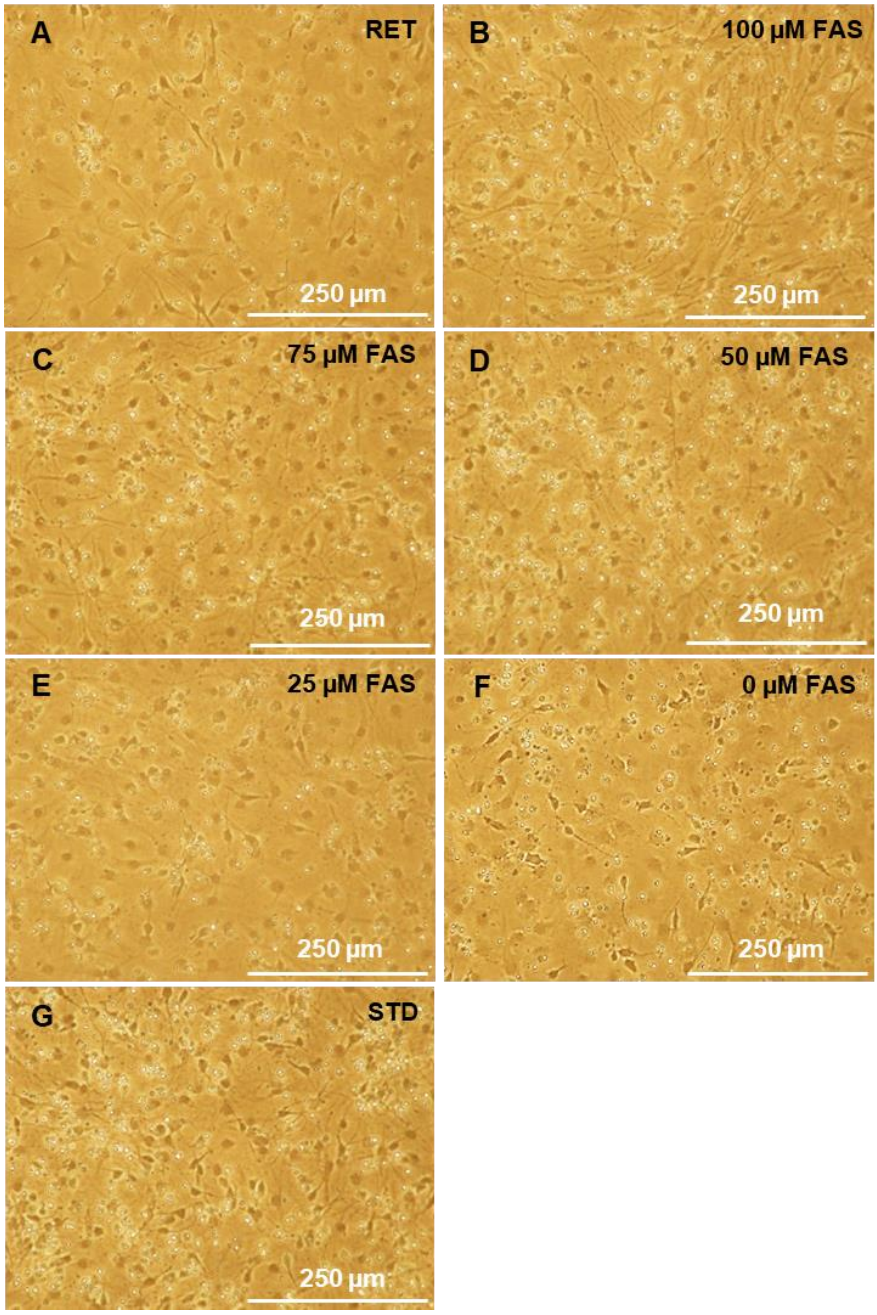


Figure 3.18: Morphological assessment of radial-like outgrowth of adult LV-NSCs in response to different concentrations of FAS. (A) RET medium, (B) 100 µM FAS, (C) 75 µM FAS, (D) 50 µM FAS, (E) 25 µM FAS, (F) 0 µM FAS and (G) Standard medium.

Based on these observations, NSC marker analysis for Nestin and Sox2 was performed to evaluate potential phenotypic differences under the two differentiation regimes *in vitro*. Both protocols equally reduced the expression of Nestin at day 2 and day 10 (Figure 3.19 and 3.20 A, B). Moreover, both protocols increased the expression of Sox2 by day 2 (Figure 3.19 and 3.20 C). By day 10, RET medium produced a marked reduction of Sox2 expression, while FAS medium maintained the increased expression of Sox2 (Figure 3.19 and 3.20 D). qPCR analysis complemented the above immunohistochemical analysis and showed reduction in *nestin* by both protocols at day 2 and day 10 (Figure 3.20 E, F), and higher detection of *sox2* in FAS-treated samples compared to RET-treated Cell_LVsg on day 10 (Figure 3.20 G, H). These results indicated that FAS-treatment increased Sox2 during differentiation of adult Cell_LVsg in contrast to RET-treatment.

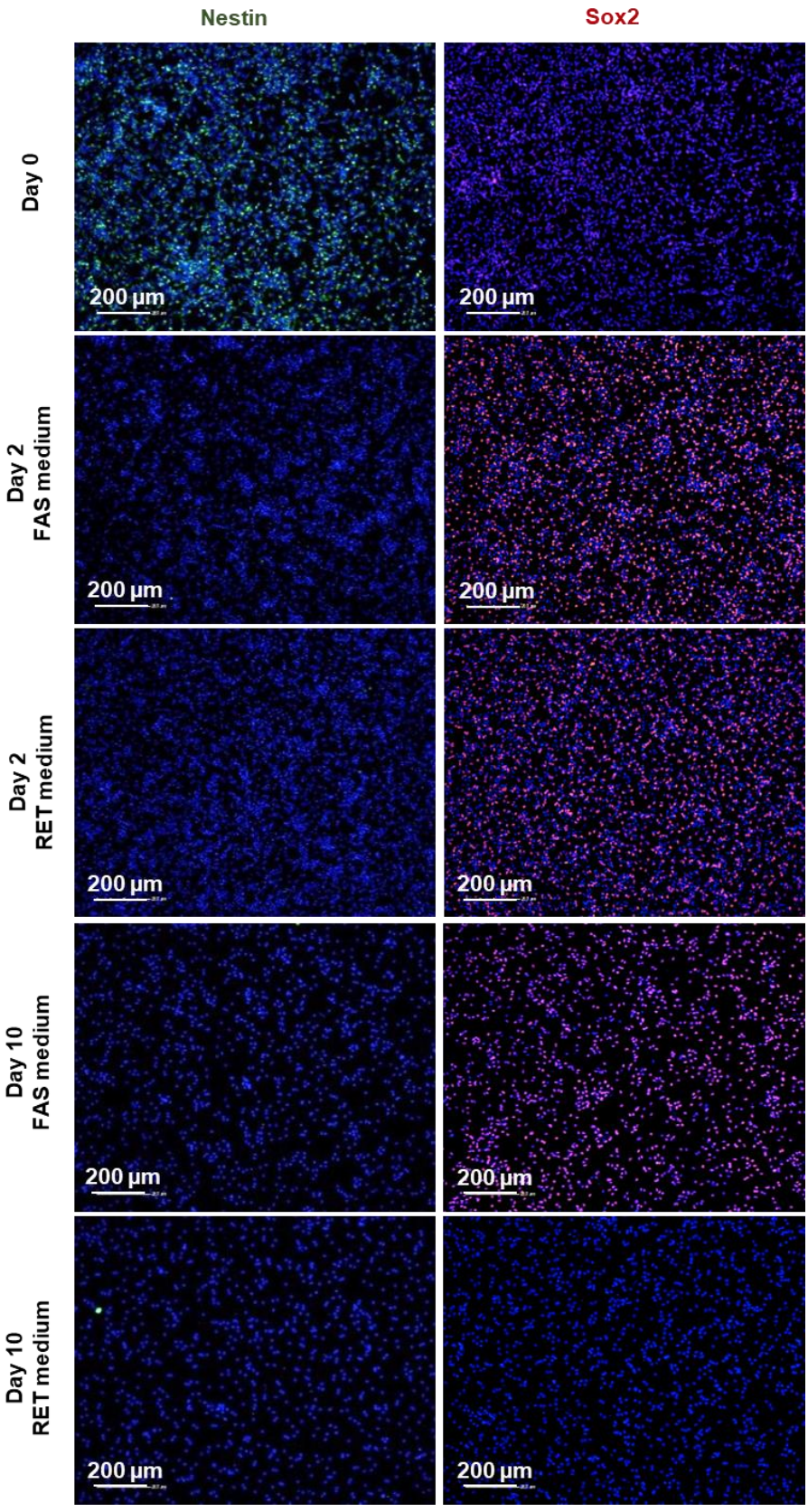


Figure 3.19: Nestin and Sox2 expression in adult LV-NSCs under FAS- and RET-differentiation protocols. Nestin (green) and Sox2 (red) immunostaining at day 0, day 2 and day 10 of treatment. DAPI (blue) nuclei counter stain was used.

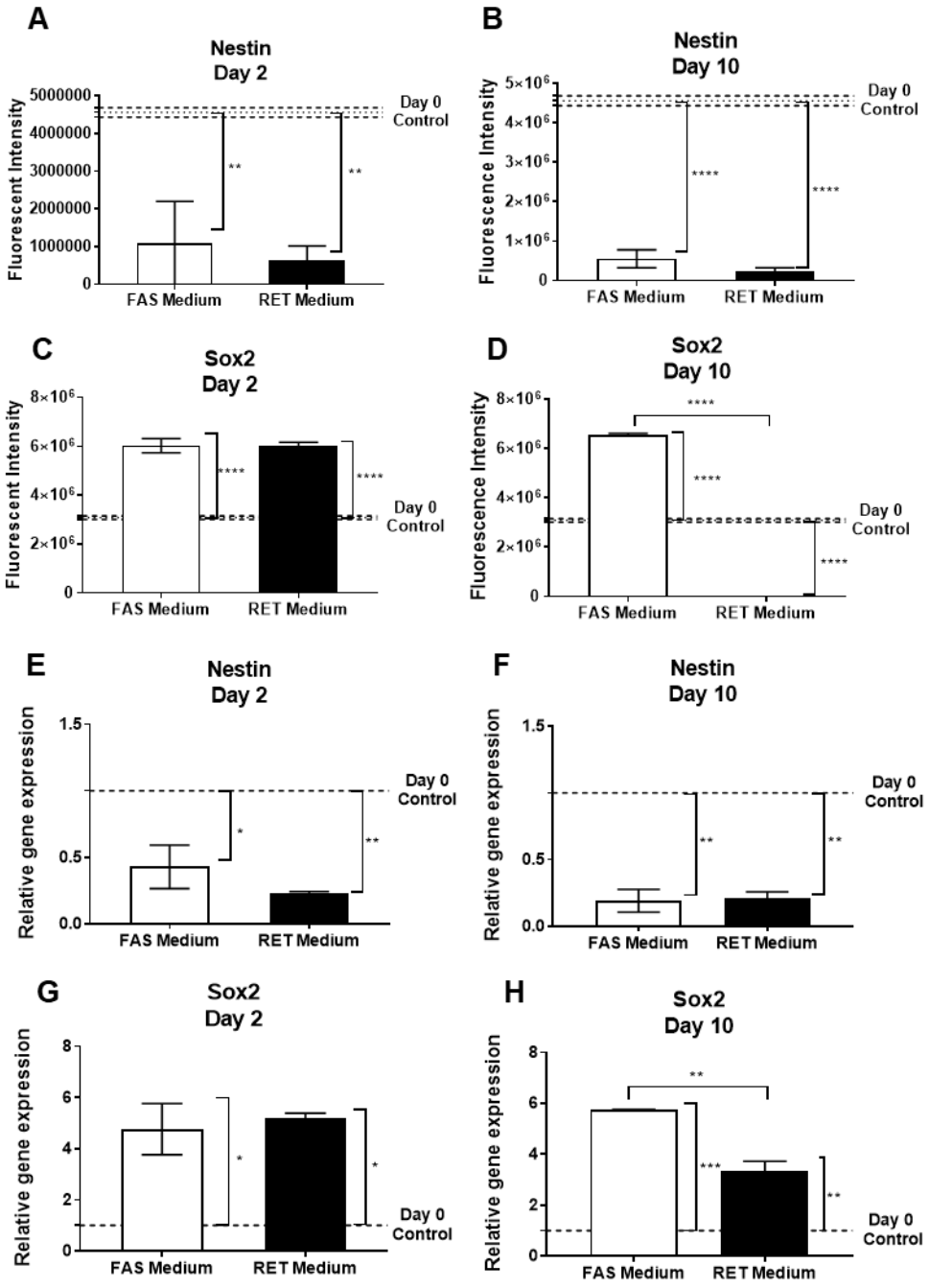


Figure 3.20: (A-D) Quantitation of immunofluorescence images of (A and B) Nestin and (C and D) Sox2 detection in adult LV-NSCs under FAS- and RET-differentiation protocols at day 2 (A and C) and day 10 (B and D) of treatment compared to day 0 controls. (E-F) qPCR analysis of (E and F) Nestin and (G and H) Sox2 detection in adult LV-NSCs under FAS- and RET-differentiation protocols at day 2 (E and G) and day 10 (F and H) of treatment compared to day 0 controls. One-way ANOVA Tukey's multiple comparison test, Mean ± SD, n=3, (*) $p<0.05$.

3.3.5. Divergent differentiation responses of adult Cell_LVsg under FAS- and RET-based conditions

Further analysis of lineage markers GFAP, βIII-Tubulin, S100b and DCX immunodetection was carried out to refine the phenotypic differences between the two treated adult Cell_LVsg populations. While GFAP expression increased in both FAS- and RET-treatments, cells under FAS-medium displayed significantly higher expression at day 2 and on day 10, with an elongated radial-like morphology in contrast to cells grown in RET-medium (Figure 3.21 and 3.22 A and B). At day 10, expression of the neuronal marker βIII-Tubulin in Cell_LVsg showed significant reduction during FAS-treatment, in contrast to the RET-treatment where multiple βIII-Tubulin positive neurons were observed (Day 10 FAS-treatment- 0.56 ± 1.3 %, Day 10 RET-treatment 8.32 ± 1.9%) (Figure 3.21 and 3.22 C, D).

qPCR analysis complemented the immunohistochemistry analysis above (Figure 3.22 E-F). *GFAP* gene expression was increased in both FAS- and RET-treated samples on both time-points while *βIII-Tub* gene expression was observed to be lower in FAS-treated samples compared to RET-treated samples at both day 2 and day 10 although only statistically significant on day 2 (Figure 3.22 E-F).

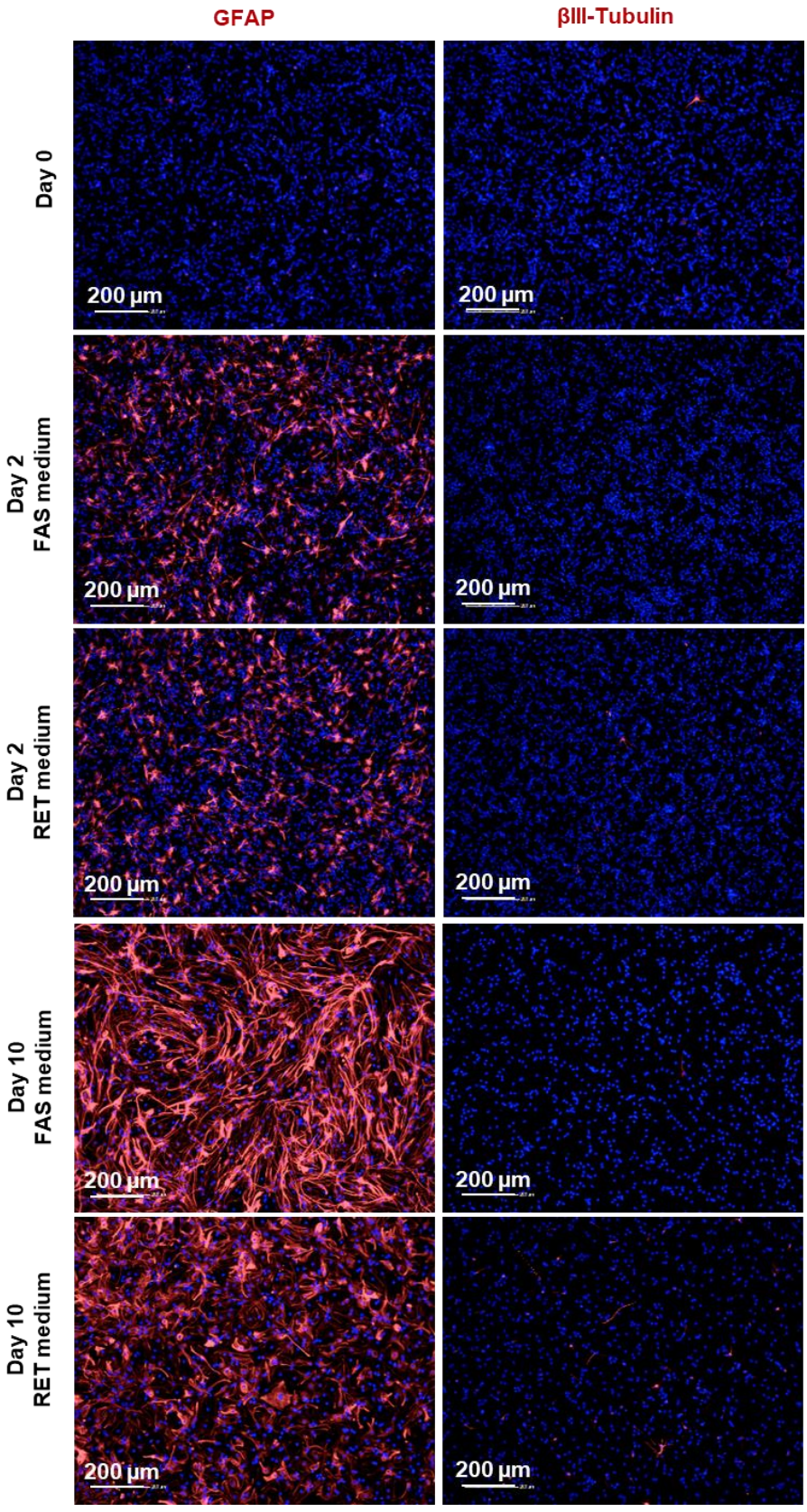


Figure 3.21: GFAP and βIII-tubulin expression (red) in Cell_LVsg under FAS- and RET-differentiation protocols. Immunofluorescence images at day 0, day 2 and day 10 of treatment. DAPI (blue) nuclei counter stain was used.

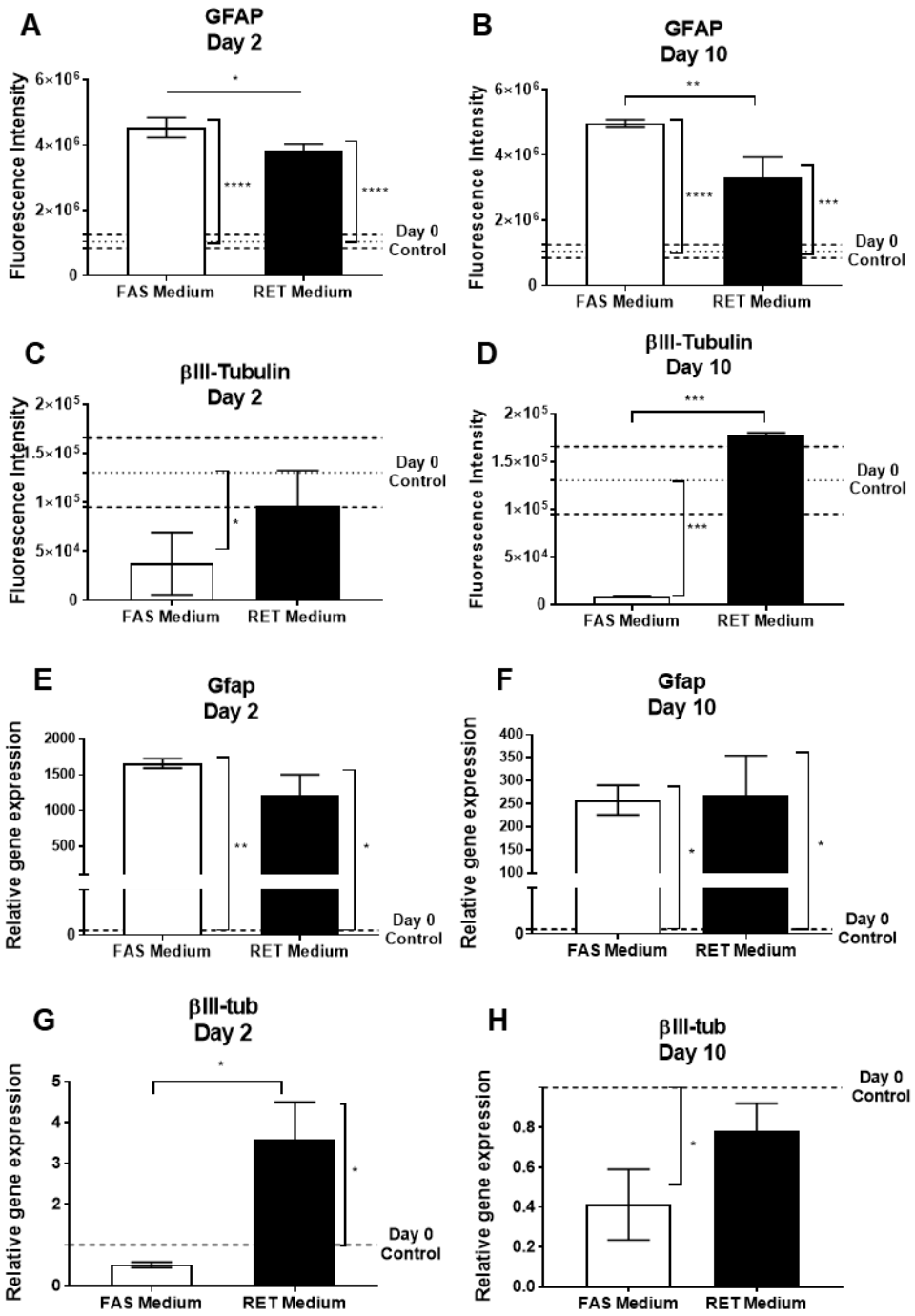


Figure 3.22: (A-D) Quantitation of immunofluorescence images of (A and B) GFAP and (C and D) βIII-tubulin detection in adult Cell_LVsg under FAS- and RET-differentiation protocols at day 2 (A and C) and day 10 (B and D) of treatment compared to day 0 controls. (E-F) qPCR analysis of (E and F) GFAP and (G and H) βIII-tubulin detection in Cell_LVsg under FAS- and RET-differentiation protocols at day 2 (E and G) and day 10 (F and H) of treatment compared to day 0 controls. One-way ANOVA Tukey's multiple comparison test, Mean ± SD, n=3, (*) $p<0.05$.

At day 10 of differentiation, Cell_LVsg were further stained for S100b and DCX, markers for mature astrocytes and migrating neuroblasts, respectively. While S100b expression was increased to comparable levels in both treatments, expression of the neuronal marker DCX was only detected in RET-treatment (Figure 3.23 A-C).

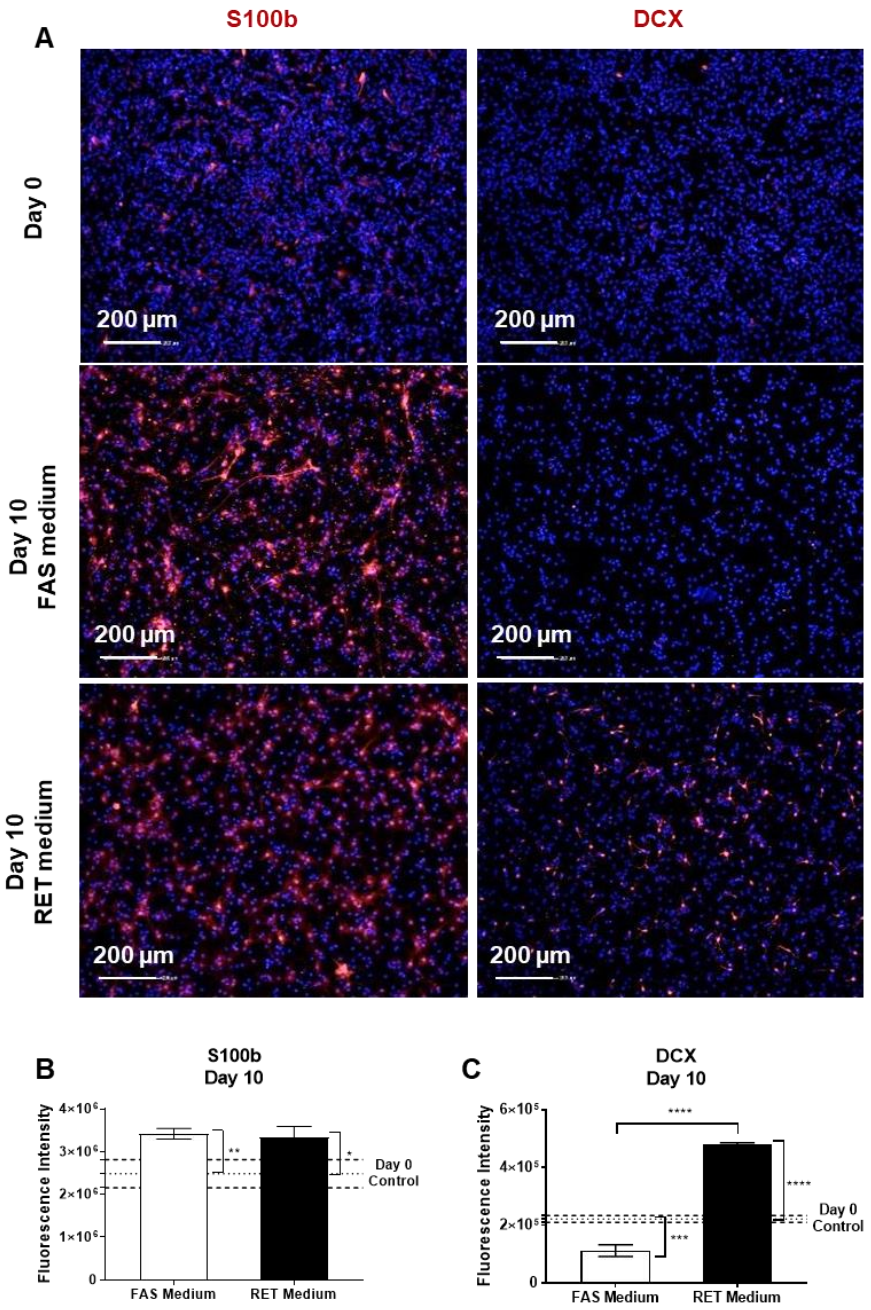


Figure 3.23: S100b and DCX expression in Cell_LVsg under FAS- and RET-differentiation protocols (day 10). (A) Immunofluorescence images of s100b and DCX (red) at day 0 and day 10 of treatment. DAPI (blue) nuclei counter stain was used. (B and C) Quantitation of immunofluorescence images of (B) s100B and (C) DCX expression in Cell_LVsg under FAS- and RET-differentiation protocols at day 2 and day 10 of treatment compared to day 0 controls. One-way ANOVA Tukey's multiple comparison test, Mean ± SD, n=3, (*) $p<0.05$.

3.3.6. Effect of changes in substrate coating, serum concentration and source of LV-NSCs on fasudil mediated radial-like glial differentiation

Astroglia have been routinely cultured in high serum concentrations such as 10% to 20% FCS in growth media (Foo et al., 2011). In this study, only a low serum concentration of 0.05% was used to support differentiation and therefore was unclear whether if any increase in serum concentration would hinder the radial-like differentiation effect mediated by fasudil on primary NSCs. On the other hand, the differences in surface coating substrates may also play a prevalent role in cytoskeletal properties of cells. Therefore, to investigate the effect of changes in surface coating and serum concentration during FAS-treatment with respect to radial-like glial differentiation of LV-NSCs, Cell_LVsg were differentiated in 0.1% gelatin or geltrex coated coverslips, with FAS-medium containing 0.5% FBS or 0.05% FBS. Geltrex coated coverslips provided single-cell distribution of GFAP positive cells in contrast to 0.1% gelatin coated coverslips where majority of GFAP detection was observed in dense colonies of cells (Figure 3.24 A). Moreover, increase in serum concentration to 0.5% resulted in an increase in GFAP fluorescence detection in 0.1% gelatin coated dishes and reduced βIII-Tubulin detection (which was generally rare in FAS-treated LV-NSCs) in 0.1% gelatin as well as geltrex coated coverslips, compared to 0.05% serum concentration (Figure 3.24 A-C). Nevertheless, all samples showed GFAP cells with radial-like outgrowth suggesting that FAS-

mediated radial-like differentiation of LV-NSCs is not affected by changes in serum concentration or surface coating (Figure 3.24 A).

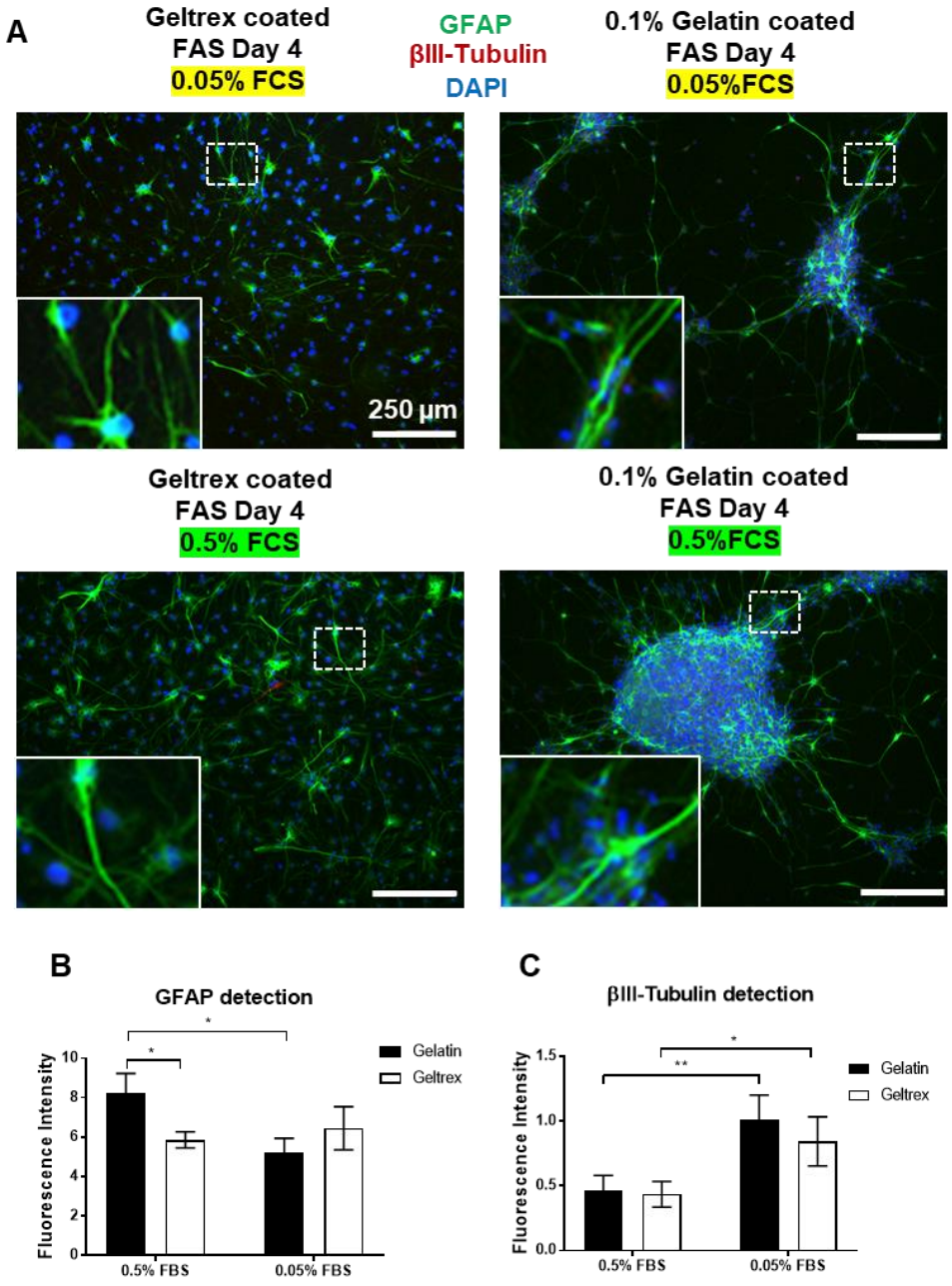


Figure 3.24: Effect of change in serum concentration and surface coating during FAS-treatment of Cell_LVsg. (A) Immunohistochemistry of GFAP (green) and βIII-Tubulin (red) of FAS-treated Cell_LVsg in 0.05 or 0.5% FBS on 0.1% gelatin or geltrex. (*) p<0.05. DAPI (blue) nuclei counter stain was used. Zoomed in boxes show radial-like neural extensions (B) Quantitation of the corresponding immunofluorescence detection of (B) GFAP and (C) βIII-Tubulin of Cell_LVsg cultures in 0.05 or 0.5% FBS on 0.1% gelatin or geltrex. One-way ANOVA Tukey's multiple comparison test, Mean ± SD, n=3, (*) p<0.05.

Here, Cell_LVsg_FAS showed vacuolation which could be clearly seen when cultured under geltrex. Vacuolation in astrocytes have been related to astroglial reactivity, astroglial differentiation and disease phenotype of astrocytes in Huntington's Disease (Juopperi et al., 2012). The single cell distribution of Cell_LVsg due to geltrex coating allowed for better visibility of the cytoplasmic architecture of cells (Figure 3.25 A-C). Brightfield images of Cell_LVsg in geltrex coated coverslips showed that FAS-treatment generated cells with multiple vacuoles in the cytoplasm of cells at day 10 (Figure 3.25 A). Immunohistochemistry analysis for GFAP showed 2 types of GFAP positive vacuolar cells - 1) cells with multiple short radial extensions and multiple multi-sized vacuoles (1 µm to 10 µm) (Figure 3.25 B) and 2) cells with 1 or 2 long radial fibres with fewer vacuoles (Figure 3.25 C). Although further analysis on vacuoles in cells was not done here, it would be interesting to investigate the vacuolisation properties of FAS differentiated glia; this can be explored by immunohistochemical confirmation for vacuoles involved in lysosomal degradation, autophagy, phagocytosis and lipid accumulation.

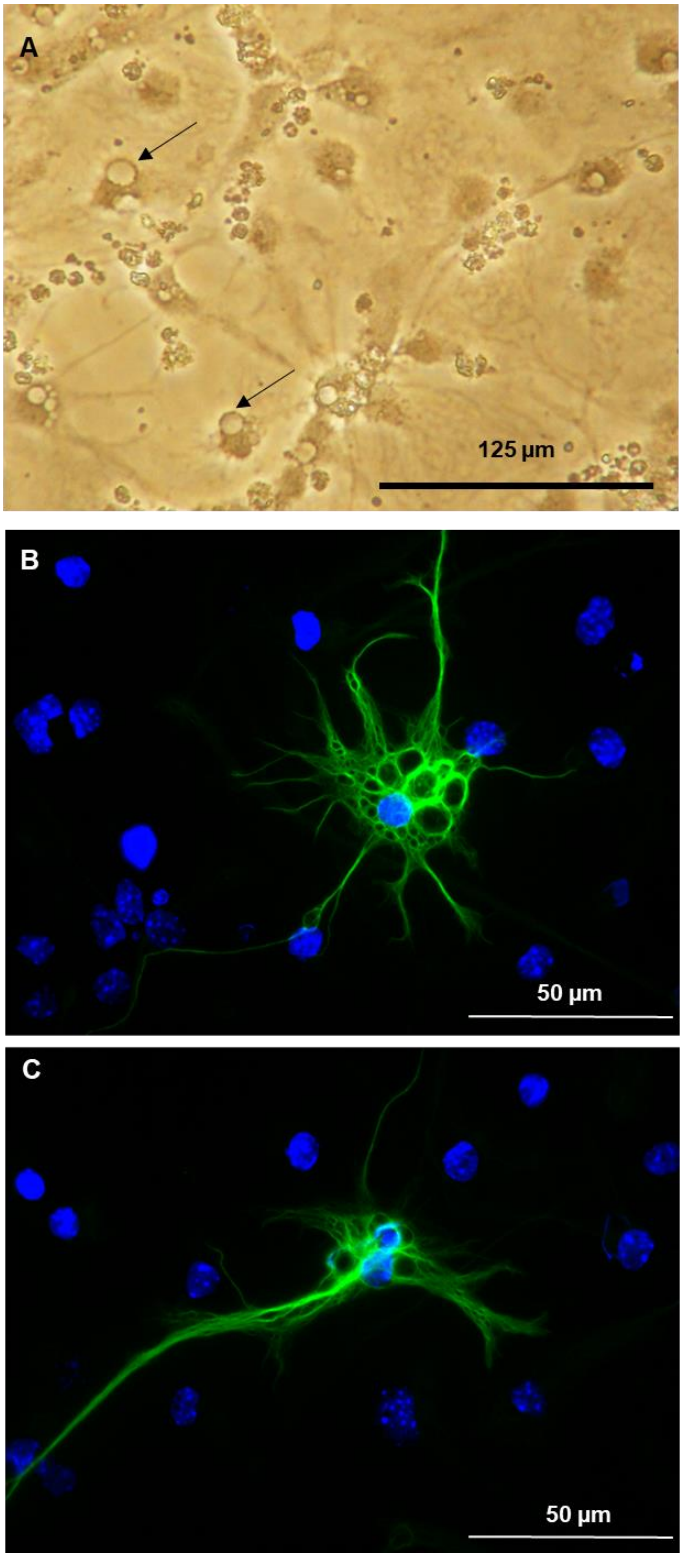


Figure 3.25: Vacuolar formation in FAS-treated Cell_LVsg. (A) Brightfield image showing multiple vacuoles in Cell_LVsg at day 10 of FAS-treatment. Arrows show vacuoles. (B-C) Immunohistochemistry showing 2 types of vacuolar GFAP (green) positive cells produced after FAS-treatment (A) a cell with multiple short radial extensions containing multiple multi-sized vacuoles, and (B) a cell with a long radial fibre containing fewer vacuolar structures. DAPI (blue) nuclei counter stain was used.

To investigate the reproducibility of FAS-mediated radial-like differentiation, a fresh preparation of adult LV-NSCs were isolated from C57BL6/N mice (referred to as Cell_LVwt) and compared with Cell_LVsg. Brightfield images showed that Cell_LVwt resulted in a significantly higher number of neuronal bodies during RET-treatment compared to Cell_LVsg at day 10 (Figure 3.26 A and B), and immunohistochemistry results showed that Cell_LVwt consisted of radial-like GFAP positive neural growth at day 0 in contrast to Cell_LVsg observed earlier (Figure 3.27 A), suggesting that the two LV-NSC populations are not identical and that Cell_LVwt produce more neuronal cells in culture compared to Cell_LVsg. However, similar to adult Cell_LVsg, FAS-treated adult Cell_LVwt showed radial-like GFAP positive cells in contrast to majority of GFAP positive cells found in their RET-treated counterparts (Figure 3.27 B-D). This suggested that fasudil treatment promoted radial-like differentiation of independent preparations of LV-NSCs.

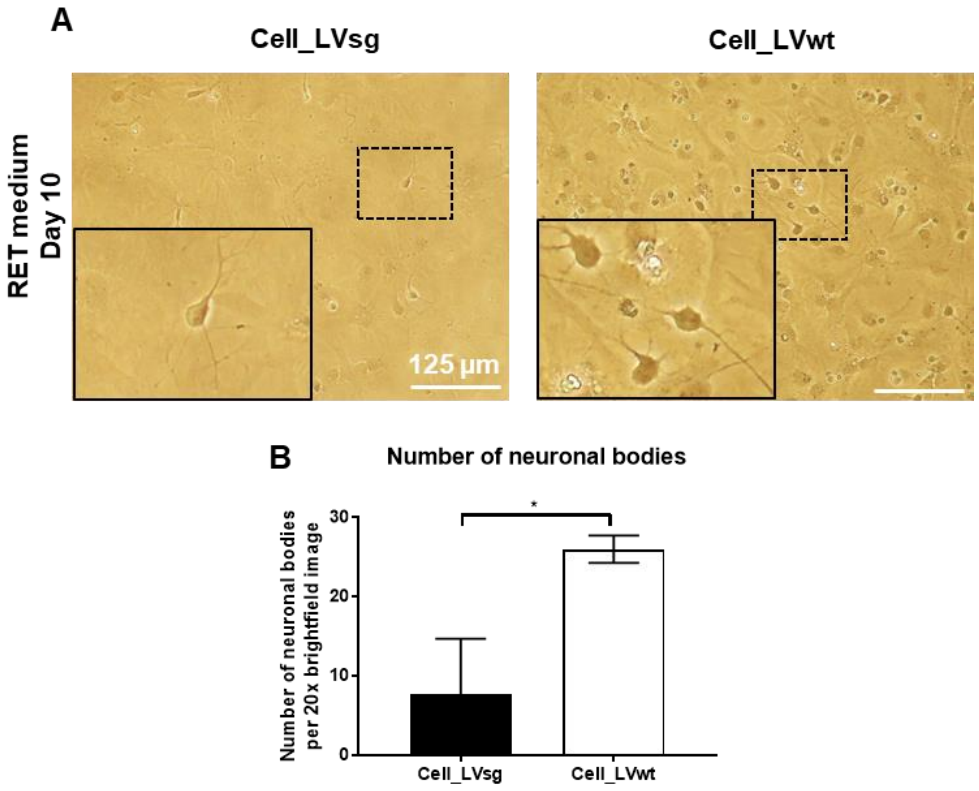


Figure 3.26: Number of neuronal bodies produced by adult Cell_LVsg (Sox1+/-GFP) and Cell_LVwt (Wildtype C57BL6/N) after day 10 RET-treatment. (A) Brightfield images showing number of neuronal bodies produced. Zoomed in boxes show neuronal bodies (B) Quantitation of number of neuronal bodies produced. Student's t-test, Mean ± SD, n=3, (*) p<0.05.

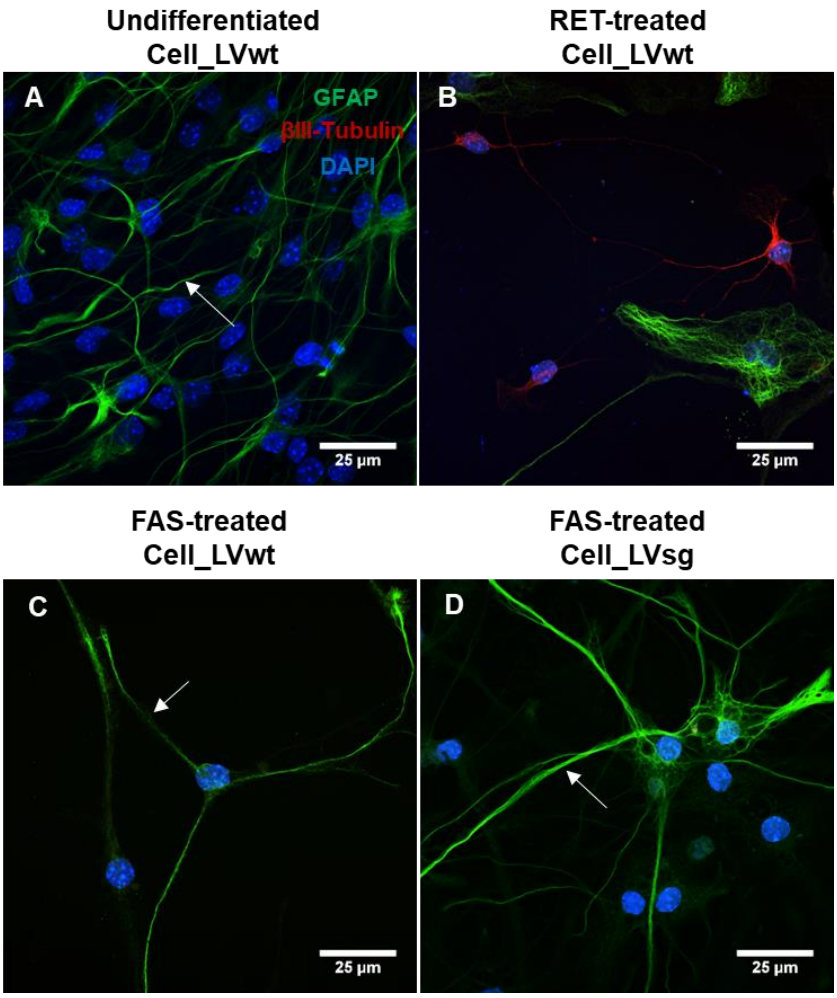


Figure 3.27: (A-D) Immunohistochemistry for GFAP (green) and βIII-Tubulin (red) during (A) day 0, (B) day 10 RET- and (C) day 10 FAS-treatment of (A-C) adult Cell_LVwt. (D) Day 10 FAS-treated adult Cell_LVsg. DAPI (blue) nuclei counter stain was used. Arrows show radial-like neural extensions (B) Corresponding quantitation of percentage of cells.

It was also noted that Cell_LVwt showed higher detection of βIII-Tubulin compared to Cell_LVsg used earlier (Figure 3.28 A and B). However, compared to RET-treatment, FAS-treated Cell_LVwt resulted in significantly lower detection of βIII-Tubulin (Figure 3.28 C and D).

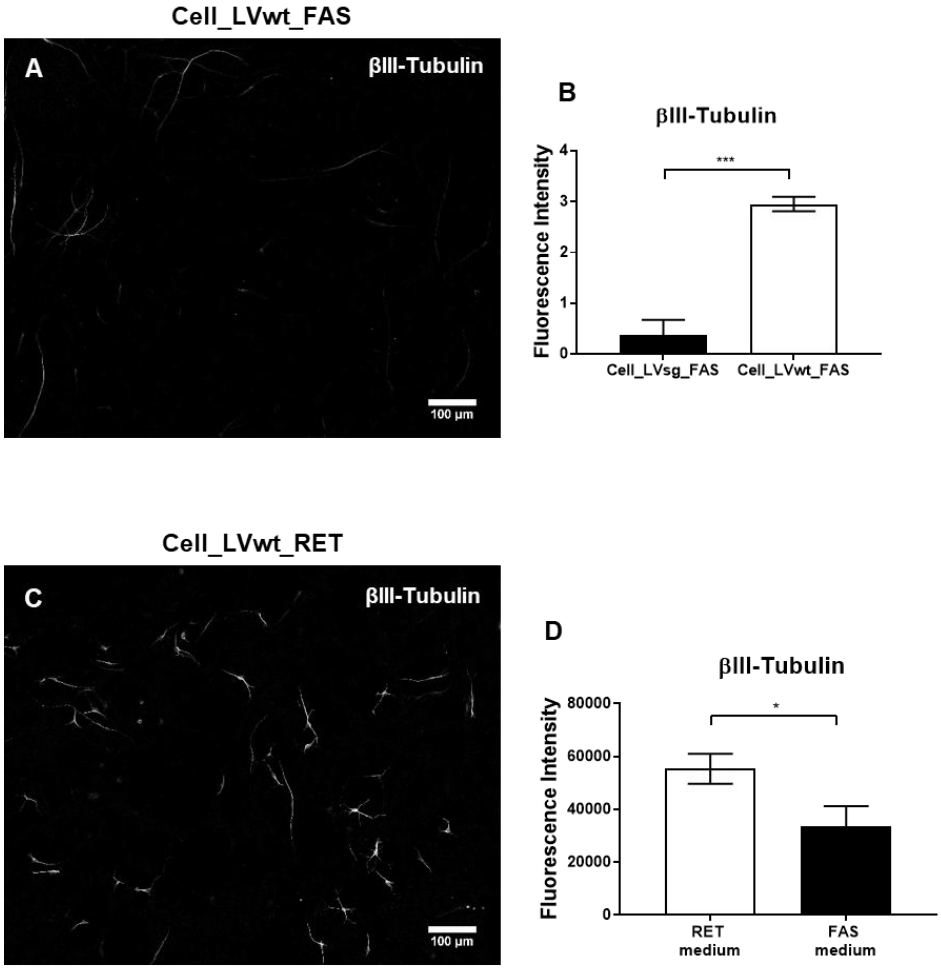


Figure 3.28: βIII-Tubulin immunostaining detection in FAS- and RET treated Cell_LVwt (day 10). (A and B) Immunohistochemistry for (day 10) βIII-Tubulin for (A) Cell_LVwt_FAS and (B) Quantitation of βIII-Tubulin intensity in Cell_LVsg and Cell_LVwt after FAS-treatment. (C and D) Immunohistochemistry for (day 10) βIII-Tubulin for (C) Cell_LVwt_RET and (D) Quantitation of βIII-Tubulin intensity in Cell_LVwt_RET and Cell_LVwt_FAS. DAPI (blue) nuclei counter stain was used. Student's t-test, n=3, (*) p<0.05.

3.4. Discussion

This chapter investigated the effects of the clinically approved ROCK-inhibitor-fasudil on primary LV-NSCs *in vitro*.

3.4.1. 100 µM fasudil concentration is non-toxic to primary LV-NSC derived neural cells.

The use of fasudil has been reported in a variety of established neural and tumour cell lines at different concentrations (Chen et al., 2015; Compagnucci et al., 2016; Deng et al., 2010; Ding et al., 2010; Huang et al., 2009; Lingor et al., 2007; Roloff et al., 2015; Takata et al., 2013; Tatenhorst et al., 2016; Tilson et al., 2015; Tonges et al., 2012; Yamashita et al., 2007). A recent study has reported that 100 µM concentration of fasudil can stimulate rapid differentiation of C17.2 cerebellar progenitor cells, resulting in the production of neuronal cells expressing DCX (Chen et al., 2015). In the current study, 100 µM fasudil was shown to differentiate C17.2 cells into βIII-tubulin neuronal cells, thereby confirming its effect. Interestingly, the differentiation effect of fasudil on primary NSCs has not yet been investigated. A previous study reported that 100 µM FAS can be toxic to primary midbrain neurons (by reducing their cell number) (Tonges et al., 2012), suggesting that primary neural cells may be sensitive to this concentration of fasudil. In the current study, loss of Cell_LVsg (postnatal and adult) in culture was noted only from day 0 to day 2 during RET- as well as FAS-treatment, which could relate to the natural death of a proportion of LV-derived new

born neurons based on observations *in vivo* (Pfisterer and Khodosevich, 2017). Also, it has been reported that differentiating and maturing neural cells tend to increase their mitochondrial mass and respiratory capacity compared to undifferentiated NSCs (Agostini et al., 2016; Wang et al., 2010), which could be measured using presto blue metabolic activity assay (Al-Nasiry et al., 2007; Boncler et al., 2014). In the current study, 100 µM FAS treatment of postnatal and adult Cell_LVsg showed the most distinct radial-morphology with increased metabolic activity and no significant cell loss after day 2, indicating the concentration of 100 µM FAS promoted neural differentiation without compromising the integrity of differentiating primary Cell_LVsg.

3.4.2. Fasudil promotes radial-like gliogenesis of primary LV-NSCs

Radial glial NSCs present during development and radial glia-like NSCs present in the adult mammalian brain have shown potential to form neurons *in vivo* that can integrate within the surrounding brain tissue and provide functional support during development, and tissue repair during adult neurogenesis, respectively (Bignami and Dahl, 1974; Campbell and Götz, 2002; Doetsch et al., 1999; Faiz et al., 2015; Götz et al., 2015; Hutton and Pevny, 2011). In this study, fasudil treatment was observed to push the primary LV-NSCs towards a radial glial-like phenotype. FAS-treatment of Cell_LVsg (postnatal and adult) lead to a loss of Nestin expression and an increase in Sox2 and GFAP expression *in vitro*, similar to proliferating radial-like NSCs during development prior to

differentiation *in vivo*. FAS-treatment also promoted INM-like characteristics of postnatal LV-NSCs *in vitro*, which is a migratory phenotype shown by developmental radial glia where the cell soma moves along the radial extensions and is known to modulate various stages of neural development including epithelial remodelling, maintenance of epithelial structure and polarity, and neural proliferation and differentiation (Glaser and Brüstle, 2005; Spear and Erickson, 2012b, 2012a). Additionally, FAS-treatment significantly reduced the expression of the neuronal marker βIII-tubulin during differentiation of LV-NSCs. Finally, FAS-treatment promoted consistent radial-like characteristics in differentiating LV-NSCs - 1) in both geltrex as well as gelatin coated coverslips, 2) when cultured in 0.05% and 0.5% serum concentration, 3) and reproducibly generated radial-like GFAP positive cells in Cell_LVwt, which predominantly produced neurons in culture. These observations indicated the potential of fasudil as a pro-neuroglial agent for radial-like differentiation of LV-NSCs. However, NSCs are known to produce a variety of glial subtypes including oligodendrocytes in addition to astrocytes and neurons. Therefore, future studies are necessary to understand the complete differentiation of NSCs in response to fasudil.

3.4.3. Sox2 expression is maintained in LV-NSCs during FAS-treatment

In this study, an increase in Sox2 expression by day 10 of Cell_LVsg_FAS was observed, which contrasted with their response to

RET-treatment. Sox2 plays a vital role in NSC proliferation and regulation (Cimadamore et al., 2013; Episkopou, 2005; Hutton and Pevny, 2011), and has been reported to inhibit neuronal differentiation in the mouse neocortex, unless the Notch pathway is blocked (Bani-Yaghoub et al., 2006). A recent study has shown that overexpression of Sox2 can reduce the number of MAP2 positive neurons in human pluripotent NT2/D1 cells *in vitro* (Klajn et al., 2014), while astrocytes retained Sox2 expression along with GFAP. It is thus possible to speculate that fasudil may promote gliogenesis in NSCs by increasing Sox2 expression. Also, fasudil has been suggested to be involved in modulating major NSC signalling pathways including Notch and NF-kB (Chen et al., 2015; Okamoto et al., 2010). Notch signalling acts as a molecular switch in regulating neural stem cell (NSC) lineage determination *in vivo* and *in vitro*, by promoting gliogenesis, self-renewal of NSCs, and inhibiting neuronal differentiation (Zhou et al., 2010). Fasudil has also been known to modulate NFκB by inhibiting IL-1–induced activation of NFκB in a rat model of rheumatoid arthritis (Okamoto et al., 2010; Sato et al., 1998). In NSCs, inhibition of NF-kB has been shown to increase expression of NSC markers Nestin and Sox2 while inhibiting neuronal differentiation *in vitro* (Zhang et al., 2012). It will thus be of interest to determine whether fasudil's effect on Sox2 expression in primary LV-NSCs may be mediated through its effects on the Notch and/or NFκB pathways.

3.4.4. Serum concentration and substrate coating can improve FAS-mediated glial differentiation of LV-NSCs.

Although FAS-treatment consistently promoted a radial-like morphology in GFAP positive cells, this study also shows that the efficiency of FAS-medium based-glial differentiation might vary significantly depending on the media components and the cell source. Serum concentrations of 10 to 20% have been reported to be used for astrocyte maturation *in vitro* (Foo et al., 2011). Here, a change in concentration of FBS from 0.05% to 0.5% significantly increased GFAP detection in during the FAS-mediated differentiation of Cell_LVsg, indicating that optimisation of serum concentration may improve the efficiency of glial differentiation promoted by FAS-based medium. Also, there is a clear difference of cellular organisation between geltrex- and gelatin- coated dishes during FAS-treatment of LV-NSCs. Geltrex contains many essential components of the *in vivo* NSC nice including laminins, entactins, collagen IV and heparin-sulphate proteoglycans (manufacturer's catalogue) and therefore promoted better distribution and attachment of primary LV-NSCs (Kazanis and ffrench-Constant, 2011). In contrast, gelatin- (which is derived from collagen (Liu et al., 2015a)) coated coverslips promoted the formation of GFAP positive-dense colony of cells, from whose borders, single cells started to show INM-like movement. This is similar to INM observed *in vivo* where radial glia are known to migrate between multicellular apical and basal end-linings *in vivo*, a process which tightly

controls the cell cycle progression, resulting in the development of the CNS (Del Bene, 2011; Kulikova et al., 2011; Spear and Erickson, 2012b, 2012a). Although geltrex-coating allowed single cell visibility of LV-NSCs *in vitro* for better structural and count analysis of cells, gelatin-coating avoided structural change of cells and resembled *in vivo* characteristics of neural development, making it would be important to consider the differences of impact that coating substrates might infer to stem cell culture and differentiation (Saha et al., 2008). Therefore, further investigation and careful selection of substrate coating for LV-NSC culture would be necessary to improve and investigate FAS-mediated LV-NSC differentiation.

3.4.5. Source of NSCs and the state of LV-NSCs can significantly impact FAS-mediated glial differentiation

It was also observed that FAS-mediated glial differentiation was dependent on the source and state of NSCs. For postnatal Cell_LVsg, FAS-treatment promoted INM-like migration pattern and differentiation the cells into radial-like GFAP positive with increase in Sox2 expression. But for C17.2 cells, it promoted tangential-like migration pattern and differentiated the cells into βIII-Tubulin positive cells with increase in Nestin. One possible explanation could be that C17.2 cells are predominantly neurogenic, as they are known to differentiate into a neuronal phenotype rather than a astroglial phenotype *in vitro* (Ryder et al., 1990; Snyder et al., 1992). Also, C17.2 cells are derived from the

external germinal layer of the postnatal day 4 mice cerebellum, which are known to predominantly produce neurons *in vivo* (Leto et al., 2016; Ryder et al., 1990; Snyder et al., 1992). Although C17.2 cells were initially used as a control for fasudil mediated differentiation of NSCs as per published study, here it is shown that they show a different response to fasudil compared to primary LV-NSCs. On a parallel note, Cell_LVwt produced a significantly higher number of neuronal bodies compared to Cell_LVsg, showing variability between similar cell sources. One possible explanation for this could be due to the variability of primary NSCs between culture preparations. LV-NSCs have been reported to not only comprise a heterogeneous population *in vivo* (Ihrie and Alvarez-Buylla, 2011), but also generate distinct neurosphere forming cells *in vitro* which can be treated as separate colonies with significantly varied differentiation potential *in vitro* (Suslov et al., 2002). Future studies can use fluorescence activated cell sorting (FACS) to isolate pure population of NSCs to avoid variability (Maric and Barker, 2005). Nevertheless, FAS-treatment consistently generated radial-like GFAP cells and reduced the number of βIII-tubulin cells in both LV-NSCs, indicating its unique effect as a LV-NSC differentiation factor.

3.5. Conclusion

The results from this chapter show that primary LV-NSCs are not only responsive to the ROCK-inhibitor-fasudil, but also that the FAS-treatment efficiently increased radial-like neural outgrowth and metabolic activity of differentiating neural cells. FAS-treatment promoted immediate INM-like movement of postnatal Cell_LVsg with increased expression of glial markers GFAP and Sox2. The radial-like differentiation was shown to be reproducible with independent preparations of primary LV-NSCs. These results provide the first evidence that fasudil can be used for the treatment of primary LV-NSCs in culture with no toxicity, and can promote differentiation towards a gliogenic phenotype, thus contributing to the development of *in vitro* models of neural differentiation, which will be used in the following Chapters.

4. Development of a reliable EV characterisation technique using d-STORM super resolution imaging and subsequent EV uptake analysis using real-time wide-field and confocal imaging

4.1. Introduction

Cell-secreted EVs show a high degree of heterogeneity in size with apoptotic bodies and microvesicles ranging from 50 to 1000 nm, and exosomes ranging from 30 to 100 nm (van Niel et al., 2018). Exosomes can be separated into different size groups, with distinct mRNA and protein composition, and different effects on the gene expression of recipient cells (Willms et al., 2016). It has been reported that smaller EVs (43.3 ± 11.7 nm) are more readily taken up by cells resulting in increased cellular uptake, compared to larger EVs (81.1 ± 3.9 nm) (data presented as Mean ± SD) (Caponnetto et al., 2017). These recent reports highlight the importance of size as a differentiating factor for EV populations, underlining the analysis of particle size distribution (PSD) as a crucial parameter to characterise the structural and functional properties of EVs in cell biology.

Electron microscopy (EM), including scanning EM (SEM) and TEM, have emerged as standard techniques for EV characterisation, allowing high

resolution imaging for the acquisition of size and morphology information (Momen-Heravi et al., 2012), and immuno-labelling of samples to detect protein content (Szatanek et al., 2017; Théry et al., 2006). Although the development of cryo-TEM has improved the preservation of sample structure and morphology (Yuana et al., 2013), the uneven and inconsistent distribution of EVs onto EM grids makes it technically challenging to accurately measure concentrations. Two common alternatives to EM used to characterise EVs include nanoparticle tracking analysis (NTA) (Dragovic et al., 2011), and tuneable resistive pulse sensing (TRPS) (Maas et al., 2014). However, the highly polydispersed nature of EVs make them challenging to measure using these techniques. For NTA and TRPS the minimal size range for EV detection is on average 70 nm to 150 nm, which excludes most exosomes (van der Pol et al., 2014). The ability of NTA to accurately resolve two EVs, which depends on the light scattered by particles in Brownian motion (Gardiner et al., 2013), requires a 1.5 fold difference in their size (Erdbrügger and Lannigan, 2016; Filipe et al., 2010), while its Raleigh approximation-based concentration estimation is strictly dependant on their refractive index, which varies with size and cargo (Dragovic et al., 2011; Gardiner et al., 2013). By contrast, TRPS can provide more accurate size and concentration measurements by detecting current blockage from particles passing through a nanopore (Maas et al., 2017), but the detection of EVs <100 nm is problematic due to nanopore blockage by larger EVs (Anderson et al., 2015). Therefore, these techniques have significant limitations including the need for several detection settings

and calibration beads for NTA (Gardiner et al., 2013), and the application of multiple nanopore sizes to minimise blockage in TRPS (Coumans et al., 2014).

Immunoblotting (e.g. western or dot blot) is generally performed alongside these analyses to confirm the presence of EVs based on their protein content (Théry et al., 2006; Wu et al., 2015). However, the high heterogeneity in cargos exposes protein-based quantification of EVs to inaccuracy. For instance, CD63 has been observed to be inconsistently expressed in EVs isolated from different human prostate and breast cell lines (Yoshioka et al., 2013), while other EV markers have been found to be unevenly enriched in different proportions depending on PSD (Willms et al., 2016). This implies that in the absence of ubiquitous EV protein markers, immunodetection approaches are inaccurate and likely to misestimate the concentration of EVs present in cell samples.

Stochastic optical reconstruction microscopy (STORM) and direct-STORM (d-STORM- a widely used STORM technique using spectrally distinct reporter dyes without the use of activating dyes) are emergent single-molecule super-resolution imaging techniques with a practical resolution limit of 20 nm (Rust et al., 2006). STORM exploits the photo-switchable property (single molecule blinking events, i.e, shifting laser on and off) of certain fluorescent probes to localise events with high precision and reconstruct the acquired image at a high spatial resolution (Heilemann et al., 2008). As a result, STORM has been used extensively to image and characterise subcellular structures with regards to their

anatomy (Stone et al., 2017), organisation (Dudok et al., 2015), and biomechanical (van der Zwaag et al., 2016) properties at the nanoscale. Recently, cancer cell-derived EVs labelled using Alexa Fluor 647-conjugated anti-CD63 antibodies have been imaged at high resolution using STORM (Chen et al., 2016). Since all EVs are lipid membraned structures (Villarroya-Beltri et al., 2014), lipophilic dyes can provide a helpful alternative to label EVs (Tian et al., 2013), irrespective of the variability in their protein content. Highly lipophilic dyes such as DiI and its derivatives exhibit photo-switching behaviour, shifting between brightly fluorescent (light) and dark states, which enables STORM imaging of lipid-based cellular structures including the plasma membrane and lysosomes (Shim et al., 2012). Building on this, the present investigation sought to exploit d-STORM imaging using a variant of DiI to explore the possible labelling and direct characterisation of EVs released by stem cells as a powerful alternative to existing approaches for the study of EV trafficking.

4.2. Aims

This Chapter has 2 aims.

The first aim was to develop an accurate and high throughput EV characterisation technique based on d-STORM imaging, and compare its efficiency with conventional techniques including EM, NTA and TRPS. (Sections 4.3.1 to 4.3.3)

The second aim was to assess the downstream applicability of the approach to perform live-imaging of EVs in NSCs, analyse EV response in neurons, and assess the EV secretion rate of NSCs (Sections 4.3.4 to 4.3.6).

4.3. Results

4.3.1. Sample analysis of MSC-derived EVs by TEM, cryo-TEM and immuno-dot blot

In addition to producing a variety of paracrine factors involved in tissue regeneration, MSCs produce a large number of EVs that can be collected *in vitro*. To identify the structure and morphology of EVs released from undifferentiated MSCs, TEM (Figure 4.1) and cryo-TEM (Figure 4.2) were performed. TEM images confirmed the presence of polydispersed EV structures from 20 to 250 nm in size (Figure 4.1 A-D). The identified EVs showed cup shaped morphology (Figure 4.1 A) and membrane folds (Figure 4.1 B) similar to previously published reports (Wu et al., 2015). Smaller EVs from 20 to 50 nm in size were also identified (Figure 4.1 C and D). Spherical structures from 5 to 100 nm in sizes were also identified that lacked a cup shaped morphology and contrast (Figure 4.1 A, D) which could correspond to the presence of lipoprotein vesicles as suggested by previously published reports (Karimi et al., 2018). This suggested that the sample contained EVs of 20 to 250 nm in size along with other lipid vesicular structures of 5 to 100 nm in size. Note: Negative control grids with no EV added were also imaged to confirm the absence of artefacts (Appendix Figure 10.1)

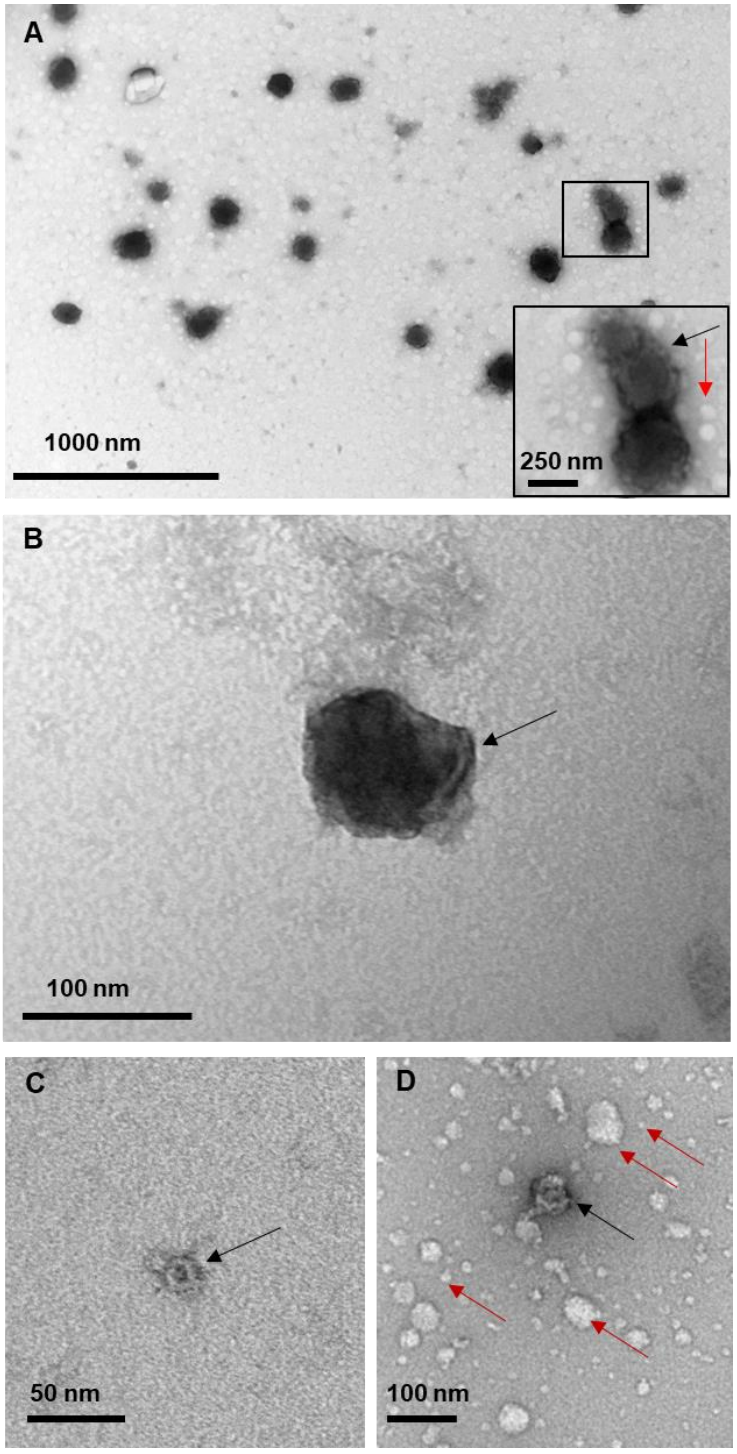


Figure 4.1: TEM images of MSC-derived EVs. (A) TEM showing EV structures of 100 to 250 nm in size. Zoomed-in box shows cup-shaped morphology of a vesicle (black arrow) and non-cup-shaped white vesicular structures below 50 nm in size (red arrow). (B) 100 nm vesicle, black arrow showing membrane fold. (C) 20 nm cup-shaped EV (black arrow). (D) 50 nm cup-shaped EV structure (black arrow) along with other white, non-cup-shaped vesicular structures of 5 to 100 nm in size (red arrows). Staining performed and images captured by RL and ZN.

As cryo-TEM avoids fixation and dehydration used for conventional TEM procedures, fresh samples were analysed by cryo-TEM to visualise EVs with minimal damage (Figure 4.2 A and B). This revealed EVs from 20 to 250 nm in size presenting round morphologies (Figure 4.2 A and B). Larger EVs of 150 to 250 nm in sizes with clear membrane borders with some of them having elongated membranes (Figure 4.2 A) similar to previously published reports (Yuana et al., 2013), were observed in low numbers. 20 to 50 nm structures were found in higher numbers with better overall contrast suggesting the presence of electron-dense cargo associated with them (Figure 4.2 B). Many structures with spherical shape but undefined borders were also found (Figure 4.2 B) which could suggest presence of lipoprotein structures and other contaminating proteins (Yuana et al., 2013). However, cryo-TEM images tended to provide poor contrast, and uneven vesicle distribution on EM grids resulted in lengthier imaging time and inconsistent particle counts for both TEM techniques.

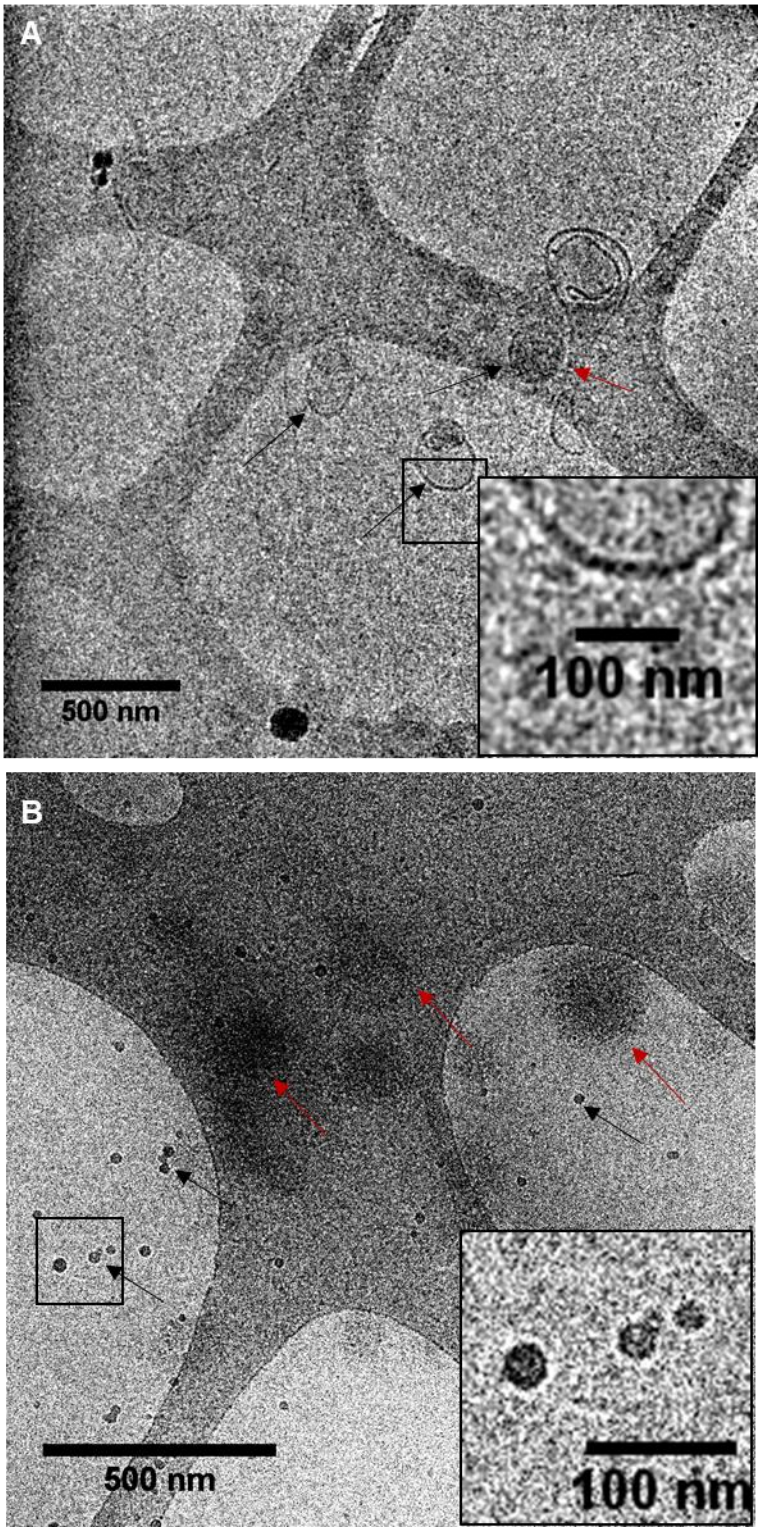


Figure 4.2: Cryo-TEM images of MSC-derived EVs. (A) Image showing spherical (black arrows) and elongated (red arrow) EV structure with a clear membrane (zoomed-in box). (B) Images showing 20 nm EVs with defined borders (black arrows and zoomed-in box) and larger EVs with undefined borders (red arrows). Cryo-TEM performed and images captured by CP (assisted by ZN).

To confirm the nature of the material in the samples, immunodetection was used to test for the presence of markers known to be enriched in exosomes (Figure 4.3 A and B) such as TSG101, ESCRT-related proteins, and the tetraspanin CD63 (Lötvall et al., 2014). Dot plots prepared from EV samples showed positive signal for TSG101 but not CD63 (Figure 4.3 A), suggesting that MSC-derived EV isolates may lack CD63 protein. The absence of signal for the Golgi protein GM130 (Figure 4.3 A and B), found in cells but not in exosomes, confirmed the purity of the EV sample.

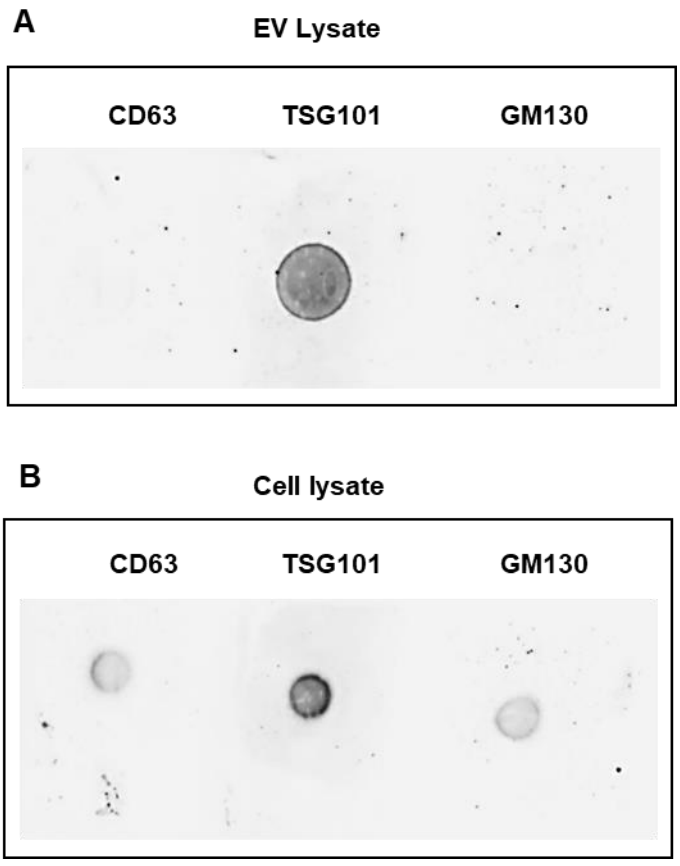


Figure 4.3: Dot blot immunodetection of CD63, TSG101 and GM130 proteins in (A) EV lysate and (B) cell lysate samples isolated from MSCs.

4.3.2. d-STORM imaging of MSC-derived EVs

Super-resolution fluorescence microscopy techniques have become widely used to visualise cellular nanostructures (Shim et al., 2012). d-STORM imaging in particular is known to resolve subcellular structures up to 20 nm in size (Tam and Merino, 2015), and would therefore theoretically allow resolution of EVs. To test this point, cultures of undifferentiated MSCs were incubated with Exo-E medium containing vybrant-DiD to label all lipid structures including EVs; these were then isolated from the medium and seeded onto poly-L-lysine coated dishes. The positively charged coating was used to promote the settlement of negatively charged EVs and thus decrease their mobility in order to facilitate d-STORM imaging (Chen et al., 2016).

DiD-labelled EVs showed a high frequency of single molecule blinking events (Figure 4.4 and Appendix video file 1), which confirmed the photo-switchable property of the DiD dye to light and dark states.

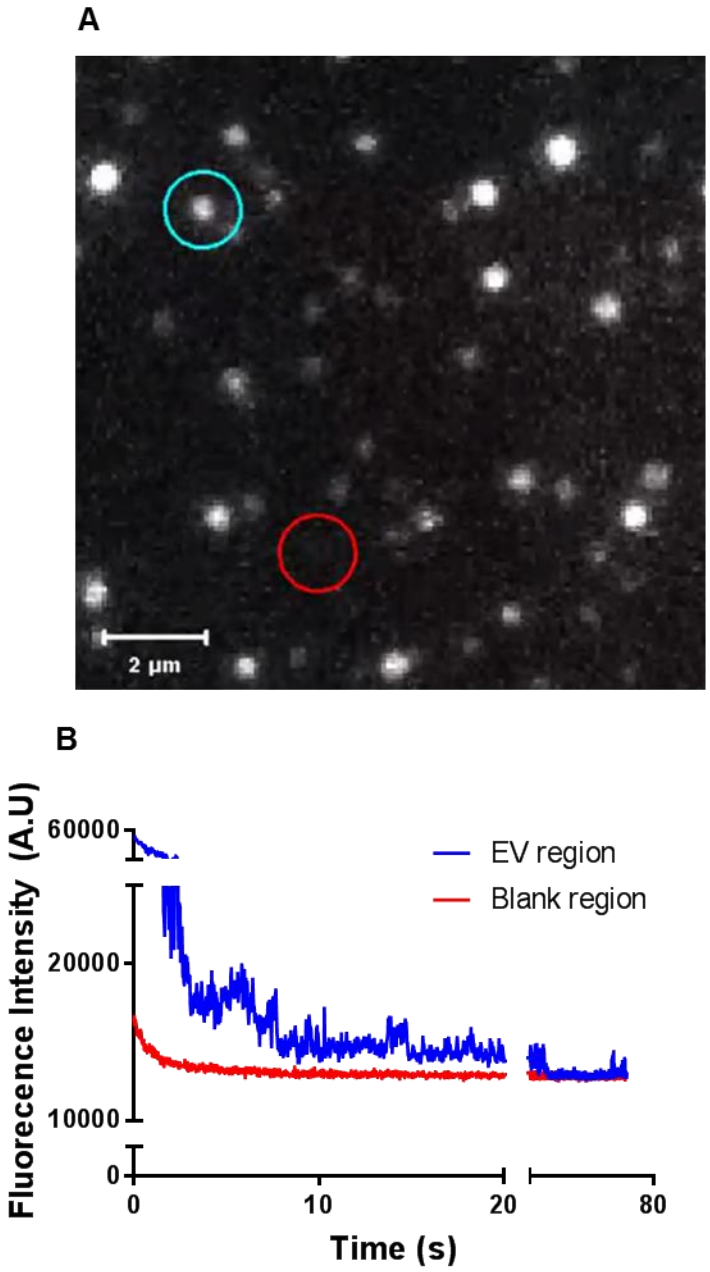


Figure 4.4: Photo-blinking frequency of DiD-labelled EVs isolated from MSCs during d-STORM imaging. (A) Screenshot from the video used to calculate the photo-blinking frequency of DiD-labelled EVs during STORM imaging, showing a positive blinking region with EVs (blue circle) and a background region for blank reading (red circle). (B) Graphical representation of the photo-blinking frequency of DiD-labelled EVs (blue) against blank region (red).

Contrary to EM observations, EVs were distributed evenly throughout the dish, allowing for rapid imaging of multiple vesicles in every field of view (Figure 4.5).

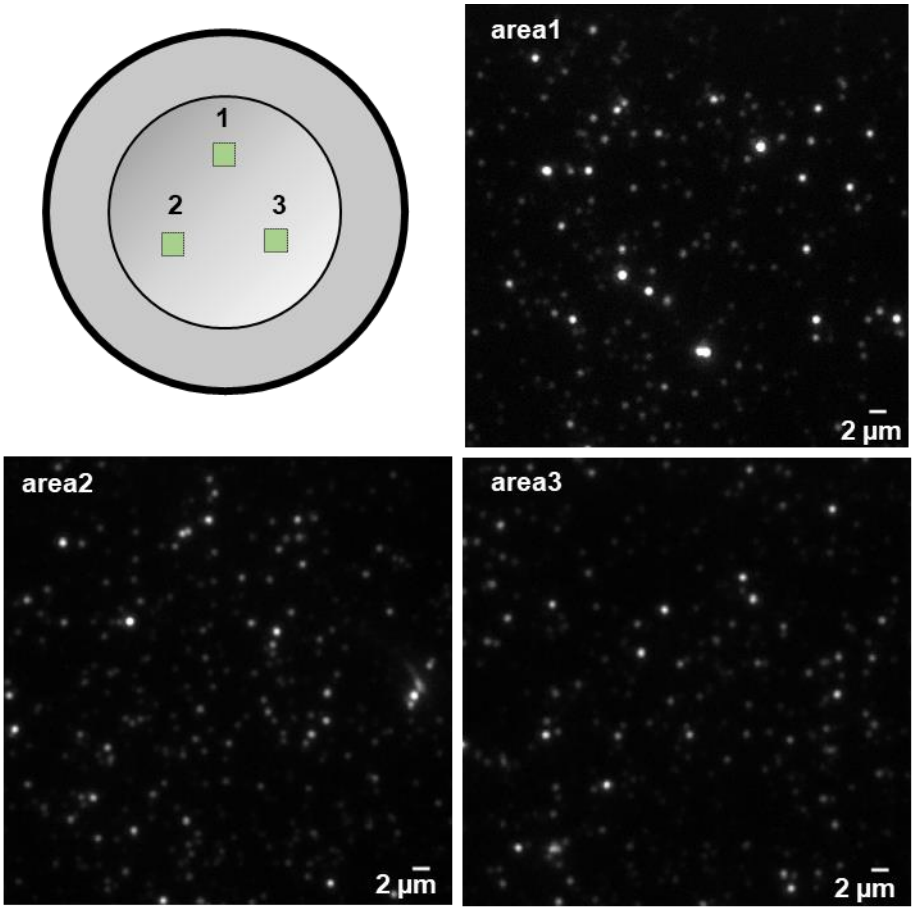


Figure 4.5: Graphical representation of EV sample scanning pattern with snapshots of areas 1, 2 and 3 recorded in TIRF.

d-STORM imaging was able to resolve structures <200 nm apart and detect EVs of 20 nm to 30 nm in size (Figure 4.6 A-E), which was comparable to earlier results from TEM in terms of spatial resolution. Moreover, EVs larger than 250 nm in size were rarely observed in MSC-derived samples, which was consistent with the cryo-TEM observations.

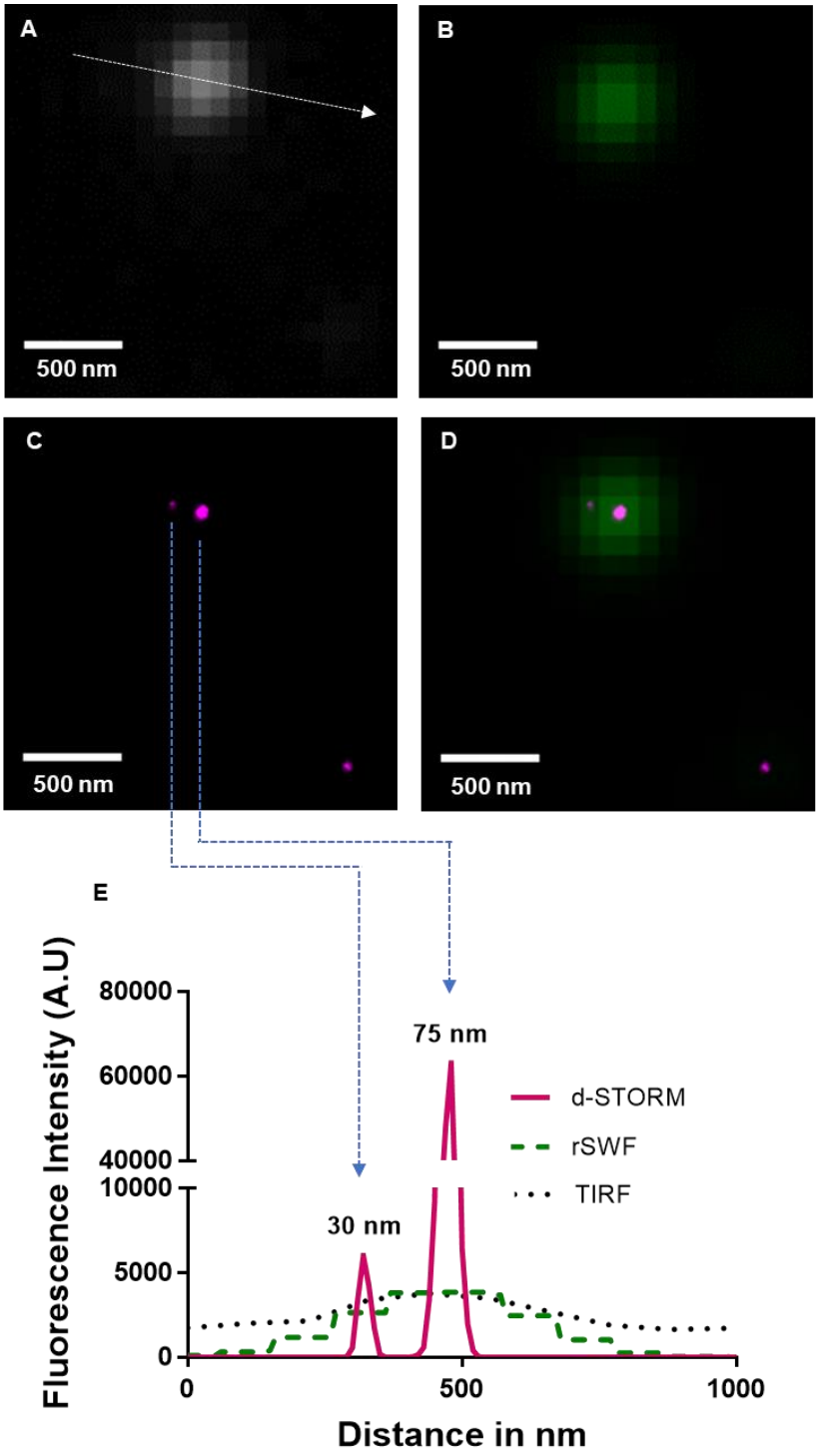


Figure 4.6: d-STORM images of MSC-derived EVs showing (A) TIRF (white), (B) rSWF (sum of wide field frames over the experiment) (green 75), (C) d-STORM (magenta) and (D) merge of rSWF and d-STORM. (E) Cross-sectional line-profiling of two EVs imaged in TIRF, rSWF and d-STORM as shown in (A) to (D), measured across the line indicated as dotted arrow in (A). Images captured by RM and ZN.

To confirm the d-STORM imaging results and exclude possible artefacts, EV-free samples ([DiD in PBS], [DiD in Exo-E medium] and [DiD in

serum-free Exo-E medium]) were analysed in parallel to evaluate non-specific fluorescence in the far-red channel (Figure 4.7). [DiD in PBS] used as control showed no photo-blinking events in the far-red channel, suggesting the absence of non-specific fluorescence from unbound dye. [DiD in Exo-E medium] produced rare single molecule events at a photon count which was 100 times lower than the experimental samples (Figure 4.7), while d-STORM imaging using [DiD in serum-free Exo-E medium] showed no detectable photo-blinking events (Figure 4.7), indicating that the weak signal observed with [DiD in Exo-E medium] was likely due to residual EVs from the serum. Collectively, the d-STORM approach generated direct and reproducible datasets of EVs released from MSC cultures observed to be in the 20 nm to 250 nm range, with no sample processing post EV isolation, resulting in minimal artefactual modification of morphological features.

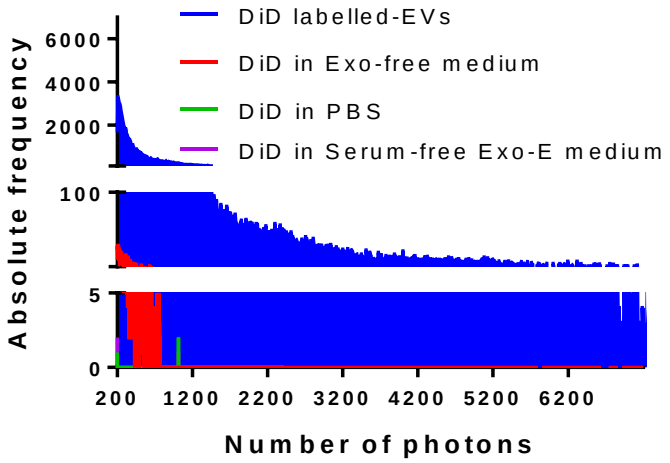


Figure 4.7: Absolute frequency of photon number recorded in [DiD in PBS] (green), [DiD in Exo-E medium] (red), [DiD in serum-free Exo-E medium] (purple) and DiD-labelled EV sample (blue).

4.3.3. Size and concentration characterisation of stem cell-derived EVs using d-STORM vs NTA and TRPS

NTA (Dragovic et al., 2011) and TRPS (Maas et al., 2017) are the most commonly used alternative approaches to EM for the analysis of EVs, due to their requirement for comparatively limited sample processing steps and speed of analysis (Szatanek et al., 2017). To analyse the size distribution of MSC-derived EVs, measurements using LM10/14 (NTA) and qNano (TRPS) were performed alongside the new d-STORM approach (Figure 4.8 A-C), and sensitivity was compared. The size distribution obtained by d-STORM indicated a majority of EVs under 100 nm in size, with a significant proportion of EVs (ca. 41.6%) below 50 nm in size (Figure 4.8 A). By contrast, TRPS and NTA measurements did not detect EVs smaller than 50 nm in the samples (Figure 4.8 B and

C). The TRPS instrument failed to maintain consistent readings for the detection of particles below 100 nm in size (Figure 4.8 B), as it was observed that the specific nanopore NP100 used for smaller EVs experienced repeated blockages by larger particles during the analysis. On the other hand, NTA analysis indicated a majority of EVs in the size range of 100 nm and above (Figure 4.8 C), in line with its reported overestimation of larger particles in highly polydispersed samples (Tuoriniemi et al., 2014). Overall, the PSD results obtained by d-STORM for MSC-derived EVs presented less variability (Figure 4.8 A-C) compared to NTA and TRPS results and showed an increase in sensitivity to vesicles within the smaller size range below 50 nm.

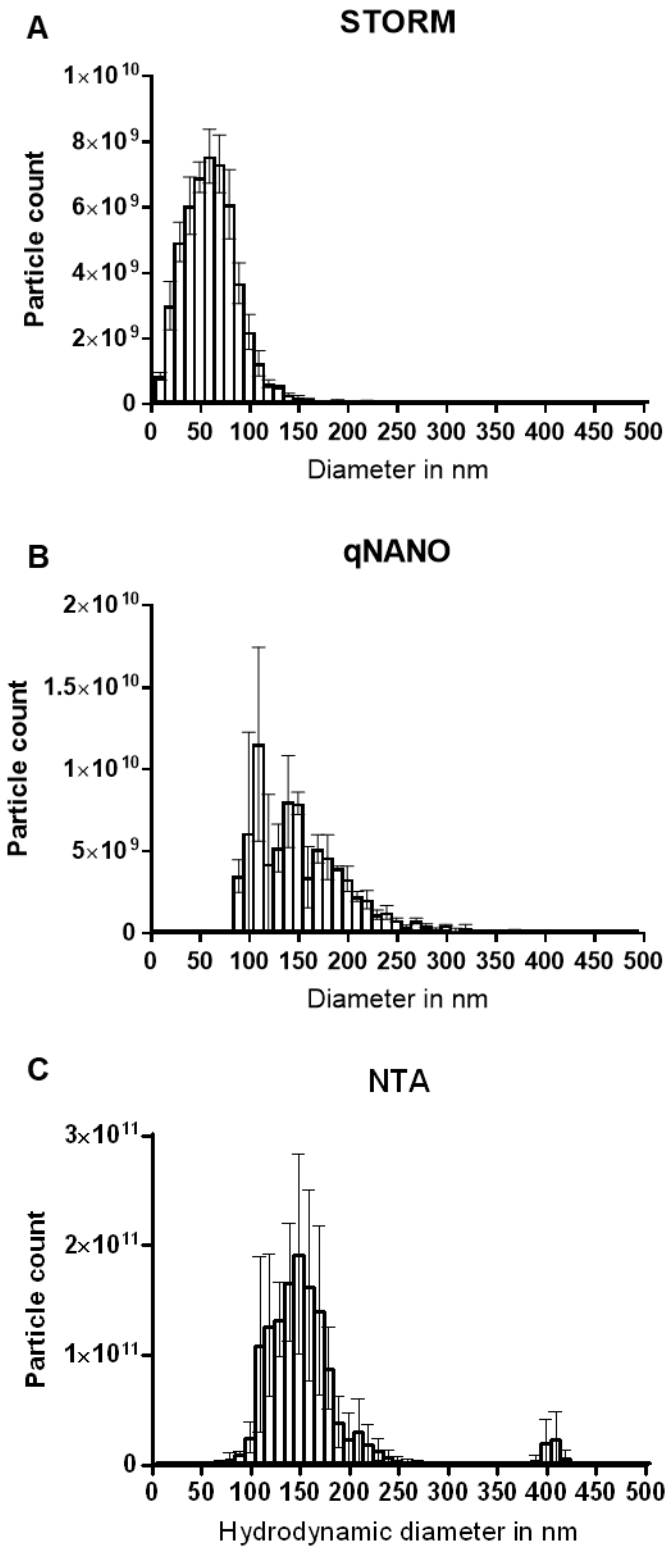


Figure 4.8: Particle size distribution of MSC-derived EVs analysed by (A) d-STORM imaging, (B) qNANO (TRPS; performed by MP) and (C) NTA. (Mean ± SEM; n=3).

The concentration of MSC-derived EVs was analysed as it is a critical parameter to standardise cell-based experiments based on EV uptake. While TRPS was used and provided a concentration of $7.86 \pm 2.11 \times 10^{10}$ particle/ml, NTA analysis was not suitable as it is dependent on the particle refractive index, which is known to vary in EV samples due to size and content heterogeneity (Dragovic et al., 2011; Gardiner et al., 2013). In order to extrapolate concentration values from the d-STORM measurements, serial dilutions of EVs were analysed to generate a standard curve, which produced a linear range between 1:100 to 1:10000 dilutions enabling the measurement of EV concentration in MSC-derived samples (Figure 4.9 A). d-STORM measured a EV concentration of $5.23 \pm 0.62 \times 10^{10}$ particle/ml, with 3.4 times less variability compared to the TRPS analysis obtained for the same sample (Figure 4.9 B). These results established that d-STORM could be used to provide simultaneous EV size and concentration measurements, with better accuracy compared to values obtained by standard nanopore-based TRPS.

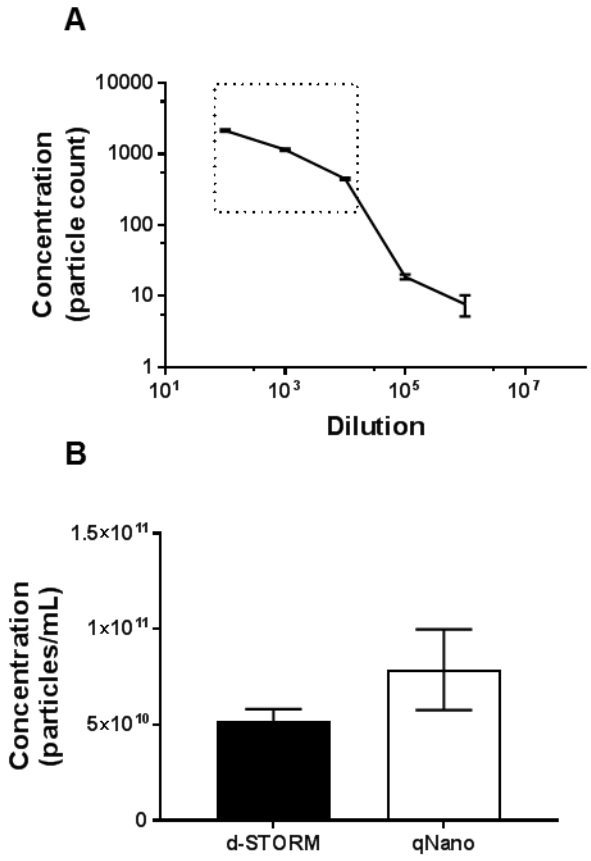


Figure 4.9: (A) Standard curve from DiD-labelled MSC-derived EV dilutions to determine the working range for d-STORM particle count, shown in the boxed area. (B) EV concentration measurements produced by d-STORM and TRPS based approaches. Data represented as Mean ± SEM, (*) $p < 0.05$, n=3.

4.3.4. Imaging of EV uptake in stem cell culture using confocal, SIM and live-epifluorescence microscopy

To determine whether the analytical approach developed for d-STORM characterisation could be used to directly examine whether MSC-derived EVs enter live cells, NSCs labelled with vybrant DiO (DiO-NSCs, green) were incubated in the presence or absence of DiD-labelled MSC-derived EVs (DiD-EVs, red). Live confocal microscopy within 30 min of incubation detected multiple DiD-EVs in the cytoplasm of DiO-NSCs exposed to

MSC-derived EVs (Figure 4.10 A), but not in control DiO-NSCs incubated in the absence of DiD-EVs (Figure 4.10 B), indicating the rapid uptake of MSC-derived EVs by NSCs.

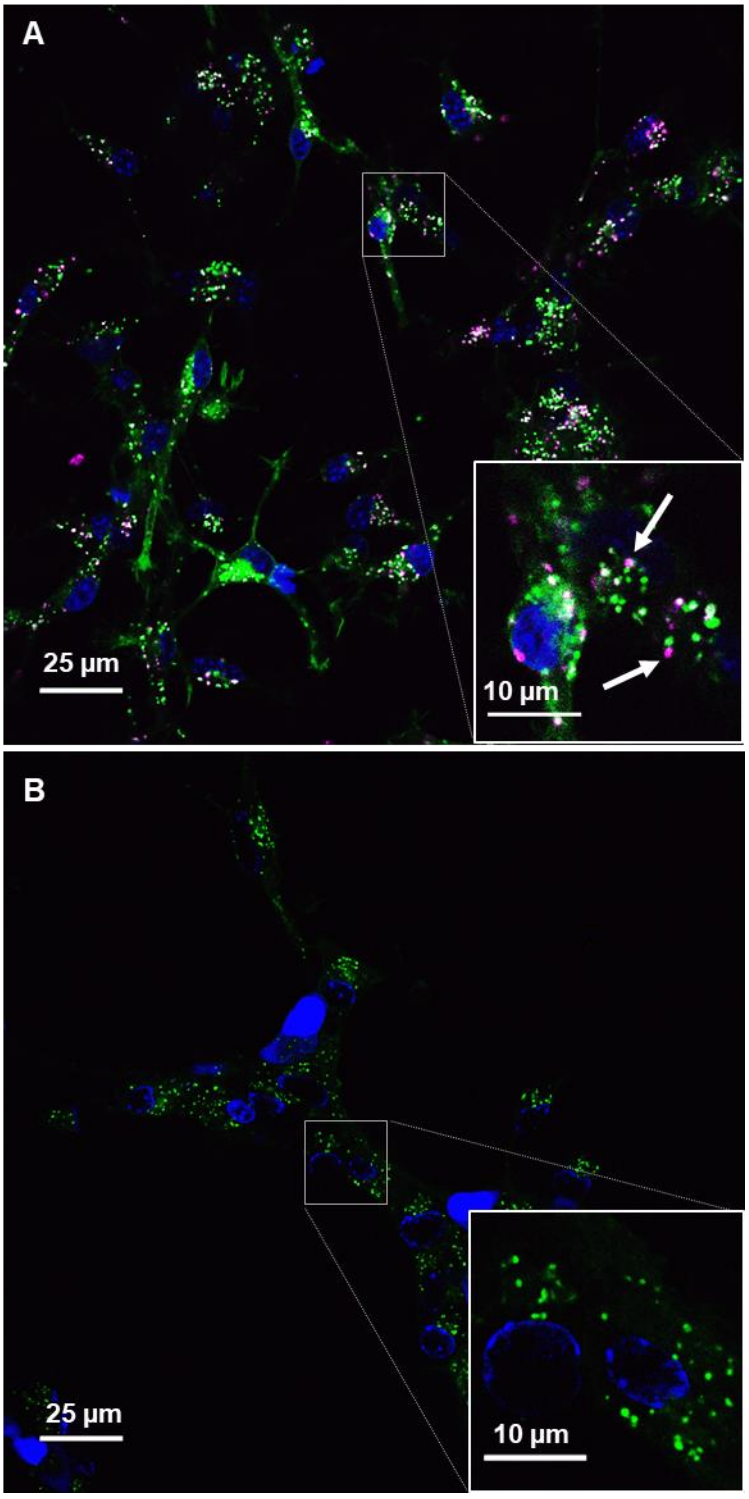


Figure 4.10: Confocal microscopy imaging of live DiO-labelled NSCs (green) with nuclear counterstain (blue), incubated in the (A) presence or (B) absence of DiD-labelled MSC-derived EVs (magenta). Arrows show DiD-labelled EVs in magnified view of boxed area.

Internalised DiD-EVs were examined using structured illumination microscopy (SIM), which provided a 2-fold increase in spatial resolution

compared to wide-field microscopy, allowing visualisation of cellular structures at 100 nm resolution (Wegel et al., 2016). SIM analysis established that internalised DiD-EVs had a mean size of 230 ± 59.67 nm (Figure 4.11), in line with d-STORM and TEM results indicating EVs were below 250 nm in size. These were significantly smaller than endogenous DiO-labelled structures seen in NSCs (mean size 765 ± 123.24 nm), which match recent reports that cells contain lipid vesicles ranging from 50 to 1000 nm in size (reviewed in van Niel et al., 2018).

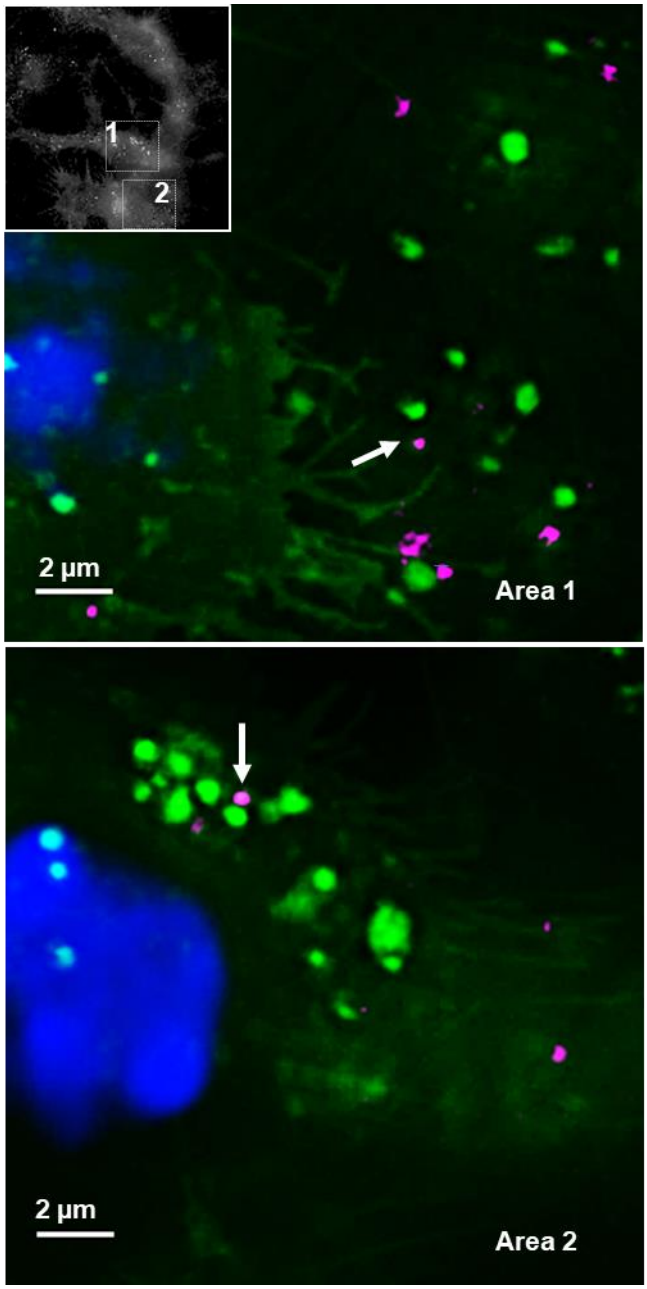


Figure 4.11: SIM imaging of DiD-labelled MSC-derived EVs (magenta) uptake by DiO-labelled NSCs (green), with magnified areas 1 and 2 showing intracellular DiD-labelled EVs (arrows). Images captured by RM and ZN.

Application of real-time wide-field fluorescence imaging further documented the movement of MSC-derived EVs present within recipient NSCs alongside endogenous intracellular DiO-labelled bodies (Figure 4.12, Appendix video file 5). Also, it was noted that an EV can cover approximately 13 µm of distance in 3 seconds within two connected cells.

This experiment established that EV exposure to the DiD labelling and storage steps employed for the d-STORM approach developed here did not interfere with their capacity for cellular uptake and trafficking in live cells.

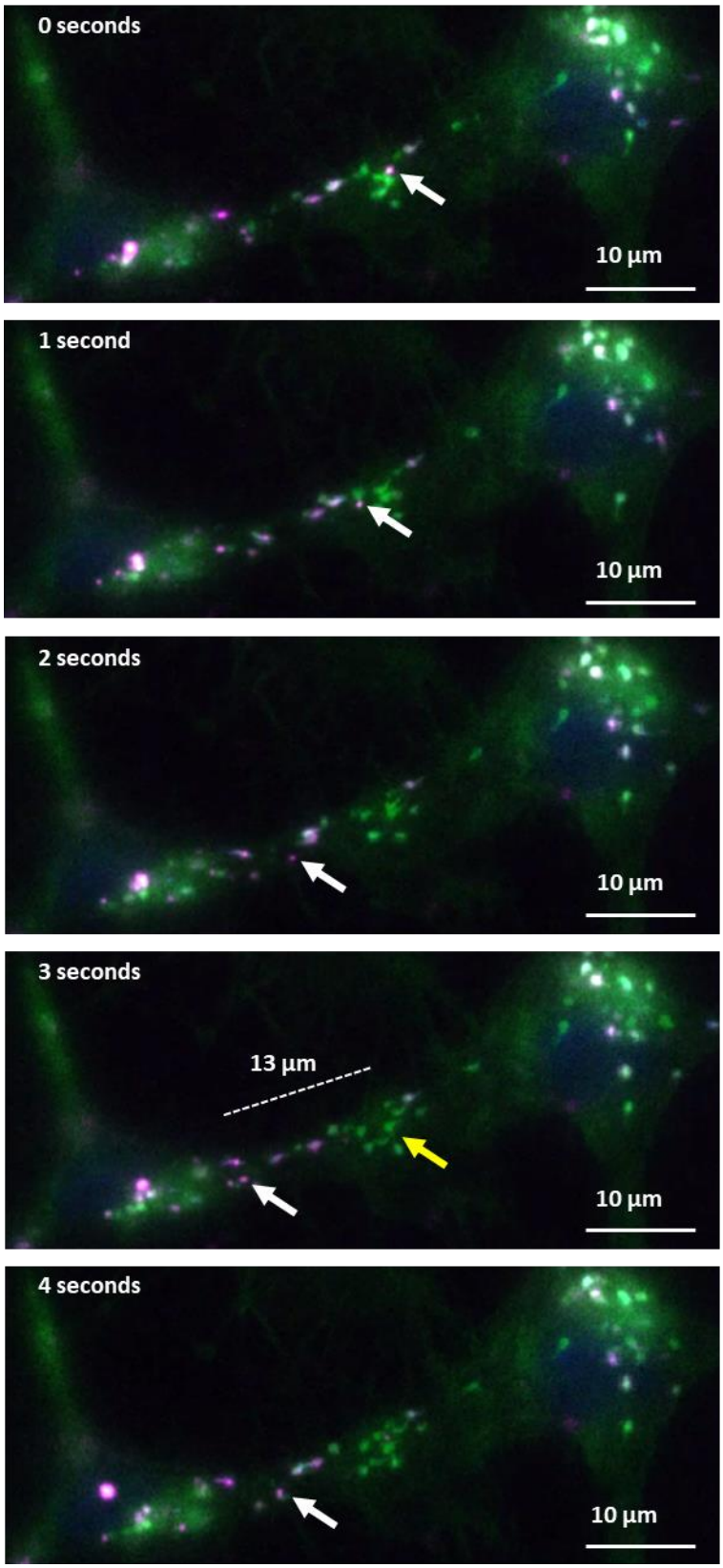


Figure 4.12: Real-time time-lapse snapshots of MSC-derived DiD-labelled EVs (magenta) inside DiO-labelled NSCs (green). White arrows show the position of the tracked EV at the respective time-point. In the image showing 3 seconds, yellow arrow denotes the starting point of tracked DiD-EV and dotted line denotes the distance travelled by the EV in 3 seconds.

4.3.5. Neuronal response, cellular uptake and localisation of Cell_LVwt derived EVs in neuronal culture system

The above developed approach based on DiD-labelling and d-STORM imaging was then used to investigate the acellular properties of LV-NSCs. To investigate the effect of NSC-derived EVs on neuronal maturation, EVs isolated from Cell_LVwt_D0 (EV_LVwt_D0 – EVs isolated from undifferentiated Cell_LVwt) were incubated with Cell_LVwt_RET (Cell_LVwt under RET treatment) (refer Table 2.1 for nomenclature). Because Cell_LVwt consistently produced more neurons in culture compared to Cell_LVsg during RET-treatment, and produced a mixture of neurons and glia, they were used as a 2-D neural culture model (2-DN) to study the EV mediated response in neurons in culture.

To determine the optimal concentration of EVs required for neuronal response study, EV_LVwt_D0 were added to 2-DN cultures from day 4 to day 10 of differentiation, every 48 hours with either undiluted (1x (no dilution)) or diluted (0.1x (1 in 10 dilution) and 0.01x (1 in 100 dilution)) amount of EVs (diluted from stock EV isolates). These dilutions will contain different number of EVs depending on the surface area of cell culture flask or plate (refer Table 4.1). Total EVs isolated from T75 flask is considered as 1x amount of EVs for cells cultured in 75 cm^2 tissue culture plastic. Therefore, based on the given surface area of tissue culture plastic, 1x, 0.1x and 0.01x amount of EVs can be calculated (refer Table 4.1). Theoretically, the addition of 1x amount of EV_LVwt_D0 to 2-

DN growing in 0.3 cm^2 tissue culture well corresponds to adding to these cells the amount of EVs that can be produced by Cell_LVwt_D0 in a 0.3 cm^2 well at 75 to 85% confluency (EVs are harvested only at this confluency). This assumption allows to choose the starting number of EVs to be tested for EV response study.

Table 4.1: Concentration of EVs from Cell_LVwt used for neuronal cell response study (Mean ± SEM; n=6)

1x stock concentration	**Total EVs from 75 cm^2**		**Total EVs from 2 cm^2**		**Total EVs from 0.3 cm^2**	
	Volume (µl)	**EV count**	**Volume (µl)**	**EV count**	**Volume (µl)**	**EV count**
EV_LVwt_D0	1000	$6.9 \pm 1.4 \times 10^{12}$	26.7	$1.9 \pm 0.3 \times 10^{11}$	4	$2.8 \pm 0.5 \times 10^{10}$

Metabolic measurements detected increased metabolic activity of 2-DN culture in response to added EV_LVwt_D0 of the dilutions 1x and 0.1x, but not of the dilution 0.01x (Figure 4.13 A). Brightfield images showed that neuronal bodies similar to 2-DN control (no added EVs) were observed only in 2-DN cultures where 0.1x and 0.01x dilution of EVs were added (Figure 4.13 B). Since increase in metabolic activity and presence of neurons, both were observed only when EVs of 0.1x dilution were added to neuronal cultures, this dilution was used for further analysis of neuronal response to EVs. The increase in metabolic activity was used as an indicator of change in functional activity of cells in culture as maturing neurons are reported to show increased mitochondrial biogenesis (Agostini et al., 2016). Further studies on neuronal metabolism was not done here as it was beyond the scope of this study.

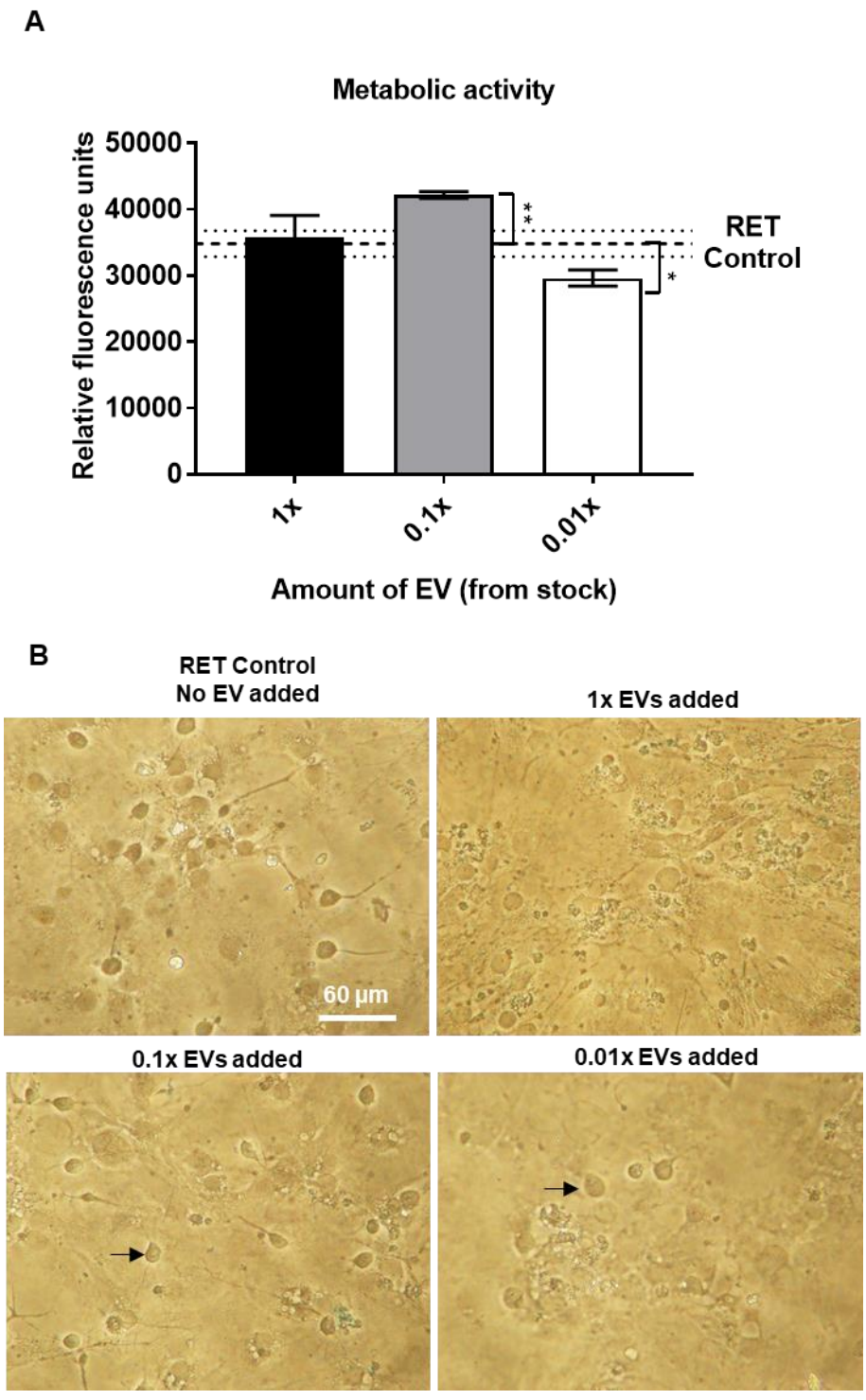


Figure 4.13: (A) Metabolic assay and (B) brightfield imaging of 2-DN cultures under different stock concentrations of EVs derived from Cell_LVwt_D0 on day 10. One-way ANOVA Tukey's multiple comparison test, (Mean ± SD) n=3, (*) p<0.05.

The metabolic analysis suggested that LV-NSC derived EVs might have a biological effect on maturing neurons in culture. Therefore, samples

were stained for βIII-Tubulin to assess the neuronal changes in cultures in response to added EVs. Qualitative analysis using MetaXpress neuronal outgrowth analysis module of immunofluorescence images suggested an increase in total neuronal processes per image for 2-DN cultures incubated with EV_LVwt_D0 compared to control wells with no added EVs (Figure 4.14 A-E).

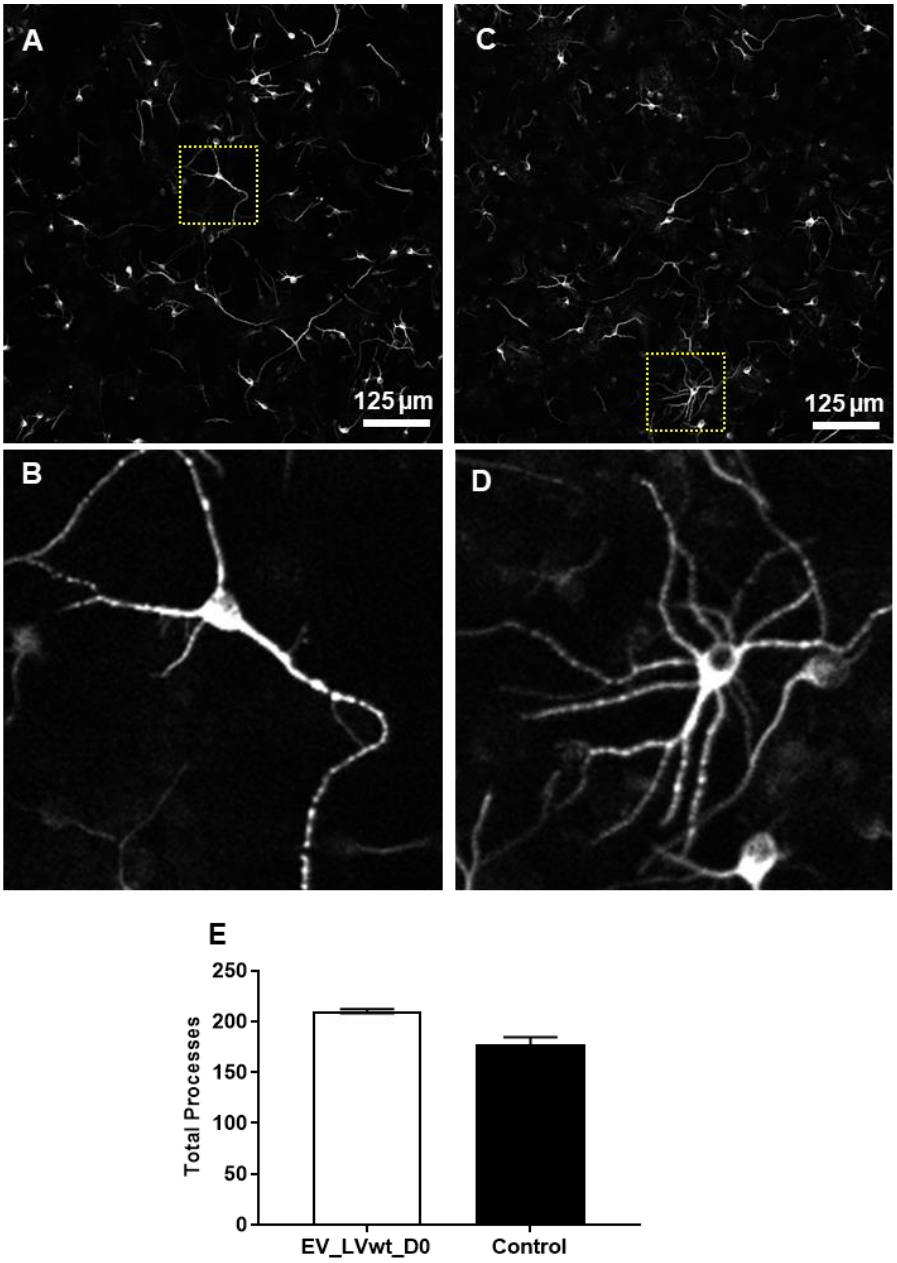


Figure 4.14: Changes in number of neuronal processes upon addition of EV_LVwt_D0 (day 10). Immunofluorescence images of βIII-Tubulin positive cells in (A) no EV added controls ((B) showing zoomed in image of a neuron in (A)) and (C) EV_LVwt_D0 added cells ((D) shows zoomed in image of neuron in (C)) of 2-DN cultures. (E) Quantitation of total neuronal processes per image. Mean ± SD, n=2.

To confirm if the increase in neuronal outgrowth was associated with cellular uptake of EVs in culture, samples were stained with βIII-Tubulin and GFAP and analysed for colocalization of DiD-labelled EVs within cells. Immunofluorescence images confirmed the colocalization of DiD

with cells in EV treated samples but no DiD signal from control cultures, confirming the uptake of DiD-labelled EVs (Figure 4.15 A-D). It was noted that majority of cells (71.61 ± 8.42% of DAPI nuclei and their perinuclear region) were associated with DiD detection; 16.06 ± 5.42% and 10.91 ± 2.49% of total cells were positive for GFAP and βIII-Tubulin, respectively and most them (94.67 ± 9.24% of total GFAP cells and 75.19 ± 6.54% of total βIII-Tubulin cells) colocalized with DiD detection (Figure 4.15 C and E). Also, it was noted that the majority of DiD positive cells did not express GFAP or βIII-Tubulin (68.05 ± 3.08%) (Figure 4.15 C and E). These observations suggested that EV uptake was associated with more processed neuronal cells in 2DN culture system.

It is worth noting that EVs were added to cultures every 48 hours in this experiment and therefore, it is possible that DiD-labelled lipids can be used by the endosome complex and related pathways for degradation and/or recycling, where they could get stored in large vacuoles (McKelvey et al., 2015). This could also explain the large detection sizes of DiD positive regions in cells although the majority of added EVs were confirmed to be below 50 nm in sizes. Nevertheless, these results confirmed that EV_LVwt_D0 were actively taken up by 2-DN cultures during neuronal differentiation and this was associated with an increase in total neuronal processes.

Next, 3D localisation of DiD detection was analysed to investigate if the added EVs showed axonal or intracellular association with βIII-Tubulin neurons in culture, promoting changes in neuronal morphology in a direct

manner. Confocal z-stack images showed detected DiD to be associated with axonal regions of neurons (Figure 4.15 F). 3-D reconstruction by Zen image analysis platform confirmed the partial detection of DiD within axons (Figure 4.15 F and G) and intracellular localisation of DiD within the soma of some neurons (Figure 4.16 A-E). Taken together these results suggested that EVs derived from LV-NSCs were actively taken in by cells in 2-DN and can promote neuronal outgrowth of neurons in culture. From these experiments however, it is not possible to confirm the precise subcellular localisation of added EVs in the 2DN. Also, it is not known if DiD dye confers additional electron contrast to be distinguished from endogenous EVs via TEM. Future super resolution fluorescence imaging and correlative light-electron microscopy techniques can be used to investigate further about the fate of EVs.

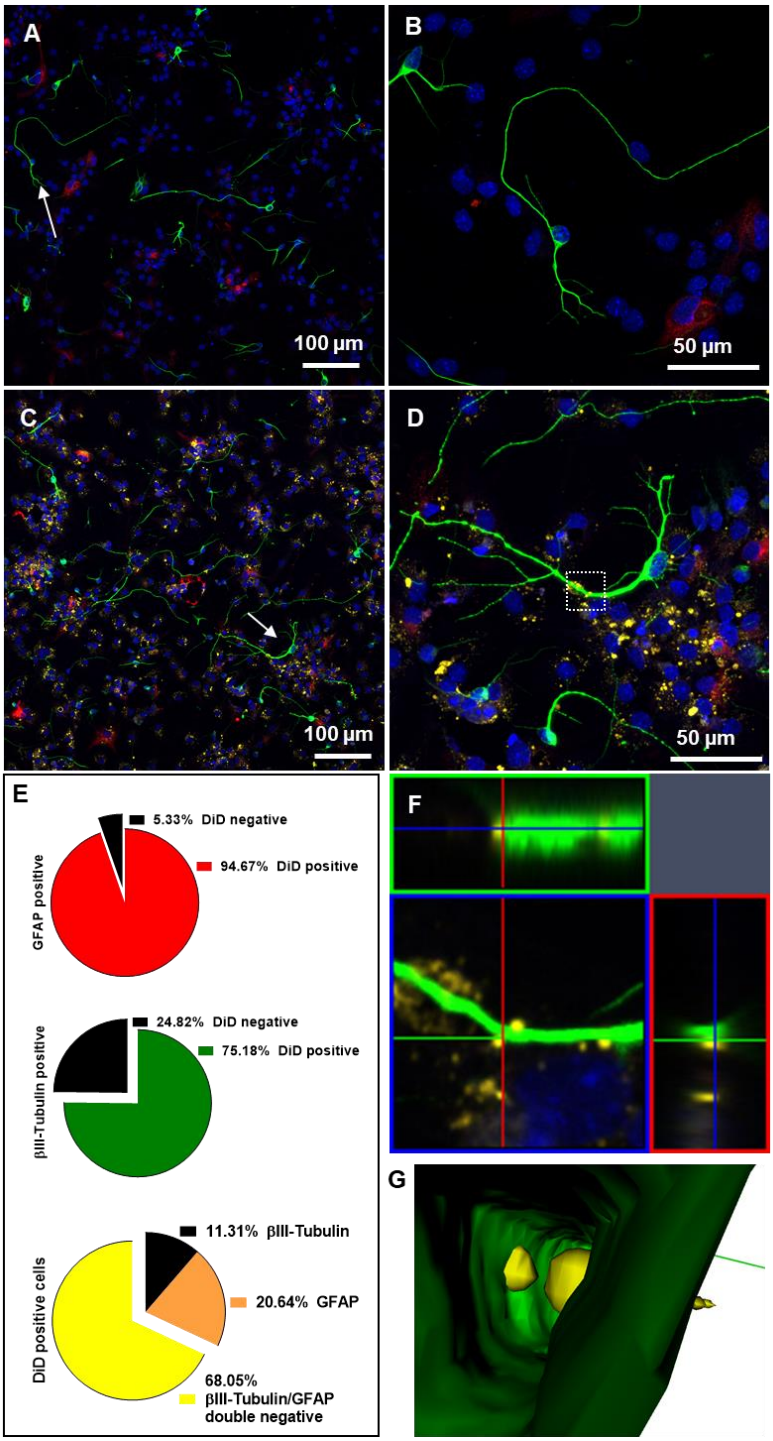


Figure 4.15: Immunofluorescence and subsequent 3-D reconstruction imaging of EV_LVwt_D0 uptake by 2-DN cultures (day 10). Immunofluorescence images of βIII-Tubulin (green), GFAP (red) and DiD (yellow) in (A) no added EV control cells and ((B) zoomed in image of neurons marked by white arrow in (A)) and (C) EV_LVwt_D0 added cells ((D) shows zoomed in image of neuron in (C)) of 2-DN cultures. (E) Population estimation of DiD localised cells from (C). Cells with DiD detection within the perinuclear (radius = 5 µm; for DAPI-only cells) and/or cytoplasmic regions (for green or red cells) were confirmed as DiD+ve cells. Vacuolar region (for GFAP+ve cells) and axonal. (F) Orthogonal view of the boxed region shown in (D) to localise DiD detection near axons. (G) Snapshot from reconstructed 3-D movie of DiD detection associated with the axon image of (F).

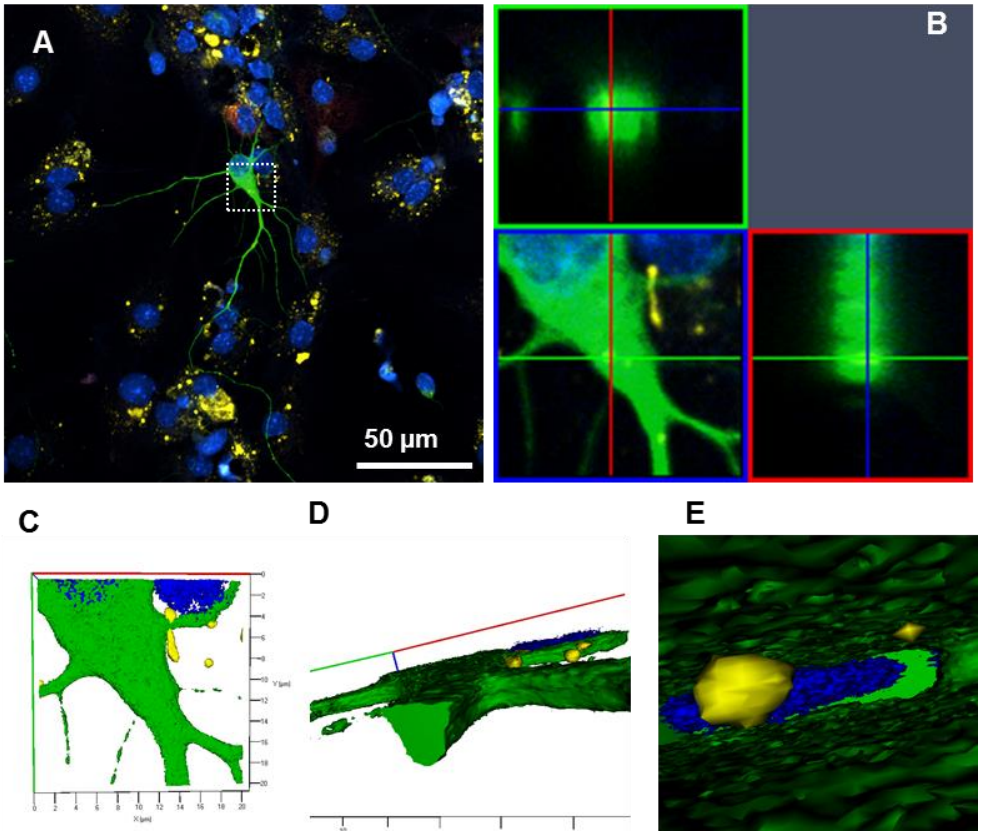


Figure 4.16: Immunofluorescence and subsequent 3-D reconstruction imaging of the soma of neurons after addition of EV_LVwt_D0 in 2-DN cultures (day 10). Immunofluorescence images of βIII-Tubulin (green), GFAP (red) and DiD (yellow) in (A) EV_LVwt_D0 added 2-DN cultures. (B) Orthogonal view of the boxed region shown in (A) to localise DiD detection in neuronal soma. (C-E) Snapshots from reconstructed 3-D movie of DiD detection associated with the axon image of (B).

4.3.6. Particle size distribution, concentration and changes in secretion rate of EVs derived from differentiating LV-NSCs

In order to characterise the EVs secreted by LV-NSCs, EVs from undifferentiated and differentiated Cell_LVsg and Cell_LVwt were isolated and analysed using the new d-STORM approach. PSD analysis confirmed that the vast majority of EVs secreted by all cell samples were below 400 nm in size (Figure 4.17 A-F). Note: Please refer to Table 2.1 for nomenclature of cell and EV samples.

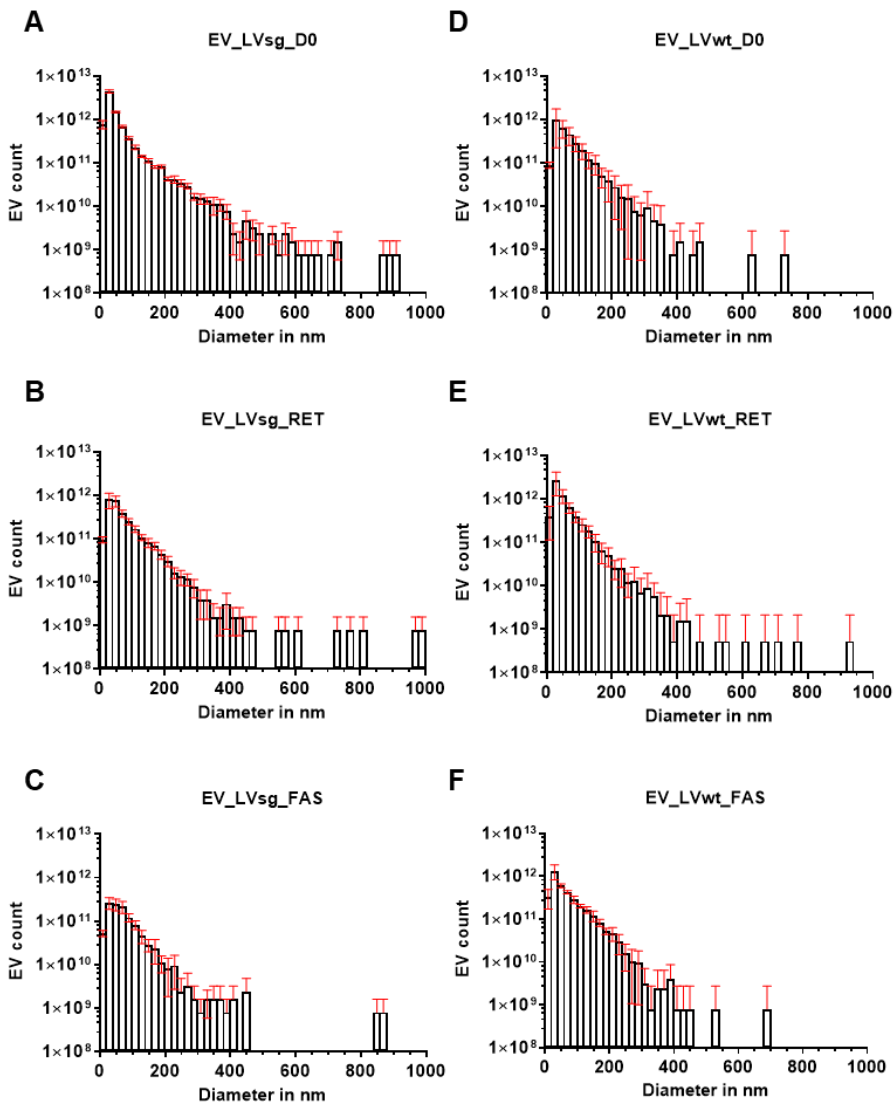


Figure 4.17: Particle size distribution of LV-NSC derived EVs. (A to C) EVs derived from (A) day 0, and day 4 (B) RET-treated and (C) FAS-treated LV-NSC_SG. (D to F) EVs derived from (A) day 0, and day 4 (E) RET-treated and (F) FAS-treated LV-NSC_WT. (Mean ± SD), n=6.

Further analysis revealed differences between the two LV-NSCs with respect to changes in total EVs collected from T75, average EVs secreted per cell, and average size of EVs during differentiation. Total amount of EVs isolated from Cell_LVsg was decreased at day 4 of differentiation in contrast to EVs isolated from Cell_LVwt (Figure 4.18 A and B). For Cell_LVsg, only Cell_LVsg_RET released significantly more

EVs/cell on average compared to its undifferentiated counterpart (Figure 4.18 C). In contrast, both RET- and FAS- treated Cell_LVwt released increased EVs/cell compared to their undifferentiated counterpart (Figure 4.18 D). Moreover, the increase in EVs/cell release by Cell_LVwt_RET compared to its undifferentiated counterpart was 5-fold higher than Cell_LVsg (EVs released/cell Mean ± SD by Cell_LVsg_RET = (1.7 ± 0.9) x 10^6; Cell_LVwt_RET = (9.2 ± 1.6) x 10^6) (Figure 4.18 C and D). Average size comparison showed an increase in EV size secreted by Cell_LVsg during RET- and FAS-treatment (Figure 4.18 E). In contrast, Cell_LVwt secreted EVs of smaller size after RET-treatment and no significant change in size during FAS-treatment. These observations suggested that neuronal differentiation of NSCs affects the release rate and size of secreted EVs. Moreover, the observed differences in EV release properties of the two LV-NSCs and complemented the previously observed cellular differences of two LV-NSCs.

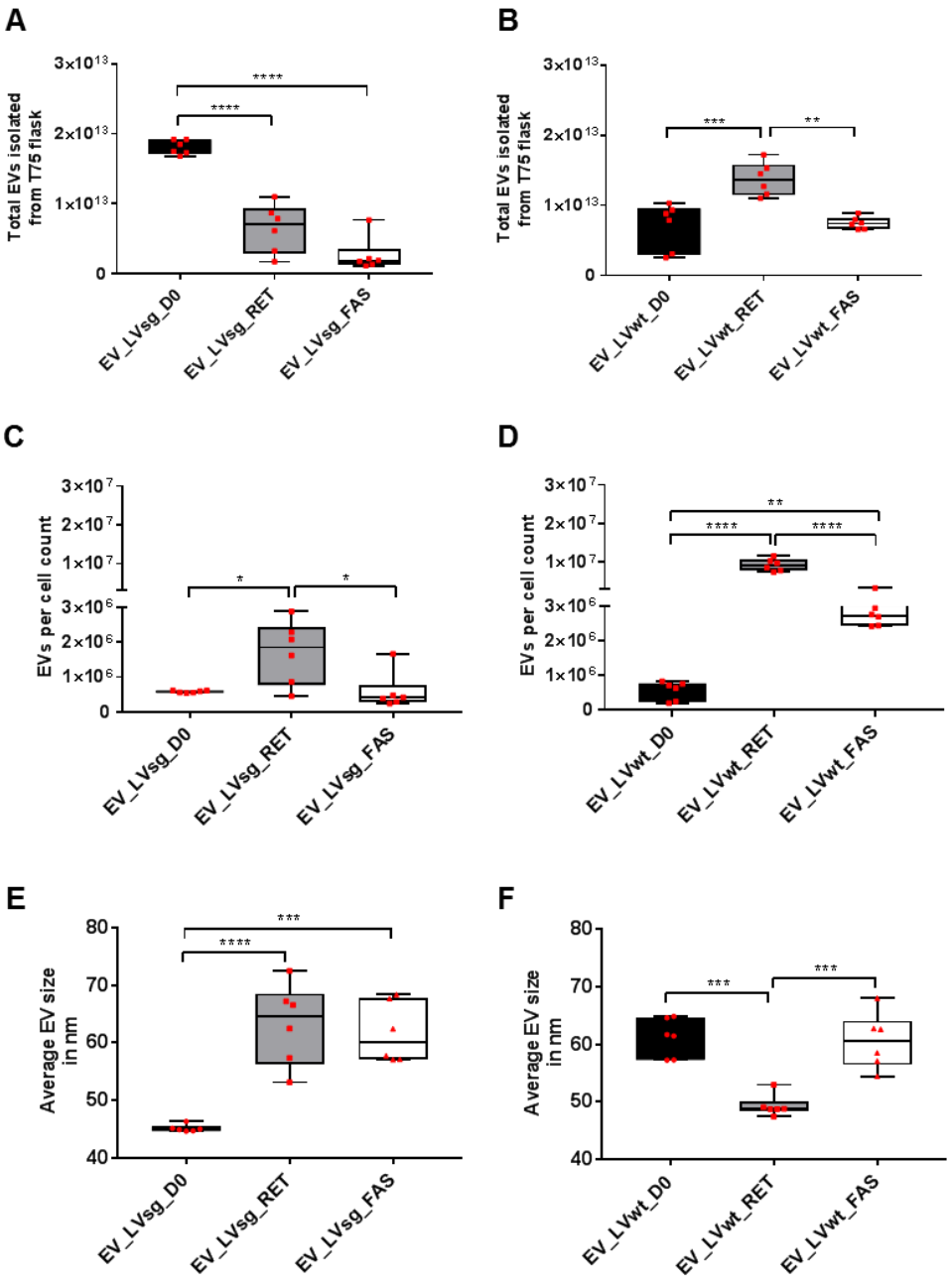


Figure 4.18: Average concentration and size determination of LV-NSC derived-EVs. Total EVs isolated from differentiating (A) Cell_LVsg and (B) Cell_LVwt. Average EVs secreted per (C) Cell_LVsg and (D) Cell_LVwt during differentiation. Average size of EVs isolated from differentiating (E) Cell_LVsg and (F) Cell_LVwt. One-way ANOVA tukey's multiple comparison test. (Mean ± SD), n=6, (*) p<0.05.

4.4. Discussion

This chapter focuses on the development of a characterisation approach based on d-STORM imaging to analyse stem cell-derived EVs collected in culture.

4.4.1. d-STORM is an efficient alternative to conventional EV characterisation techniques

Due to the limitations in reproducibility, sensitivity and time–consumption posed by conventional techniques, rapid and accurate characterisation of EVs has become increasingly important in the field of cancer and stem cell biology. Accordingly, developments in nano-sensing technologies including high sensitivity flow cytometry (Tian et al., 2018b), atomic force microscopy (Sharma et al., 2010), field emission scanning electron microscopy (Sharma et al., 2010), single molecule force spectroscopy (Sharma et al., 2011), asymmetrical-flow field-flow fractionation (Sitar et al., 2015), frequency-locked microtoroid optical resonators (Su, 2015) and evanescent light-scattering microscopy (Agnarsson et al., 2015) are constantly being developed for PSD and concentration analysis of EVs. Recently, d-STORM imaging has been used to visualise and track EVs *in vitro* (Chen et al., 2016, 2018). Here, in the current study, it was shown that d-STORM imaging can be used as a simple and rapid method to characterise the PSD and concentration of MSC- and NSC-derived EVs.

Previous studies have reported that MSC-derived EVs isolated via ultracentrifugation can range from 40 to 200 nm in size (Haga et al., 2017;

Katsuda et al., 2013; Mao et al., 2017; Nakamura et al., 2015; Tamura et al., 2016). Here, it is shown that MSC-derived EVs isolated from culture supernatants using membrane affinity columns were within 20 to 250 nm covering the size range of EVs reported in earlier studies. The d-STORM datasets showed MSC secreted EVs to include a majority of small-sized exosomes of 20 to 100 nm in size, in agreement with the literature (Lankford et al., 2018). These results compared favourably with those obtained from conventional EM, NTA and TRPS measurements with respect to reliability, sensitivity and efficiency of the EV analysis. Particularly, the d-STORM approach allowed simultaneous analysis of PSD with high sensitivity for EVs below 50 nm in size, and high-throughput particle concentration measurement.

d-STORM results reliably aligned with the particle size information from cryo-TEM, while the whole procedure from sample isolation to EV characterisation was completed in under 1 hour, establishing d-STORM super-resolution microscopy as an efficient and reliable alternative to EM, NTA and TRPS techniques. Further application of d-STORM approach in NSC-derived EVs provided as a useful tool to monitor EV release changes during neuronal differentiation.

4.4.2. Vybrant DiD is an efficient label for tracking EVs

The DiD labelling approach provided key advantages, as it avoided reliance on protein-based markers, known to be inconsistent due to the heterogeneity of exosomal expression (Baietti et al., 2012; Willms et al.,

2016; Yoshioka et al., 2013). This provided a simple and uniform labelling of all EVs irrespective of size or cargo, widening the detection range and avoiding demanding and/or damaging sample processing steps. Importantly, DiD labelling is stable (Shim et al., 2012), compatible with storage while preserving the integrity and bioactivity of samples, and could enable multiplexing to simultaneously label other EV components such as protein or nucleotides cargo using specific auxiliary fluorophores (Chen et al., 2018). Their multiplexing potential was shown here using confocal imaging with multiple fluorophores (GFAP-AF594, βIII-Tubulin-AF488, and DAPI). Moreover, d-STORM approach can be combined with other antibody-based microfluidics high-throughput systems to analyse the heterogeneity within EV populations (Contreras-Naranjo et al., 2017).

Also, here it was shown that the DiD molecule is photo-switchable and therefore allows for high resolution single-molecule localisation, in line with previous reports (Shim et al., 2012). DiD-labelled EVs switched to dark-state at a low laser power of 0.31kW/cm^2 which is particularly helpful as high laser power may damage EV membranes and can reduce the number of localised events in weakly fluorescent EVs of lower sizes (<50 nm) by bleaching them in a few frames. It has been reported that selection of optimal photo-switchable fluorophores and imaging buffers can improve STORM imaging (Dempsey et al., 2011). Accordingly, most red-adsorbing dyes including Alexa Fluor 647 showed improved photo-switching ability and increased number of switching cycles when an imaging buffer with both, an oxygen scavenging system and a primary thiol, was used (Dempsey et al., 2011). Therefore, optimisation of

imaging buffers can further improve the quality of the DiD-based d-STORM approach presented here to characterise EVs.

4.4.3. Investigation of EV trafficking using live-imaging

Live imaging using super-resolution microscopy techniques have emerged as powerful means to uncover and better understand the biomechanics of subcellular events including fast reorganisation of actin cytoskeleton in macrophages and complex dynamics of bacterial filopodium movement (Glogger et al., 2017; Godin et al., 2014; Jünger et al., 2016; Tian et al., 2013). However, due to long image acquisition periods, real-time super-resolution imaging of fast occurring subcellular events, including EV trafficking, have not yet been established (Godin et al., 2014). Particularly, the use of d-STORM for live imaging of EV intracellular trafficking can be technically challenging (Godin et al., 2014; MacDonald et al., 2015). The reliability of this imaging technology is based upon the precise localisation of a photo-switching event of a fluorescent molecule, which is impractical for mobile EVs in a living cell, especially if they move significantly between two localisation events. Interestingly, a recent study has reported the use of single molecule localisation microscopy to track EVs in live cells with a temporal resolution of 4 seconds (Chen et al., 2018). However, here it was shown that MSC-derived EVs can travel a significant distance of 13 µm in 3 seconds within NSCs after immediate incubation, which can hinder precise localisation of EVs during d-STORM imaging. Although EV

trafficking dynamics are still largely unclear, future adaptations of d-STORM imaging, along with other advanced live-microscopy techniques including high-speed camera wide-field microscopy, confocal and SIM imaging, might be able to address this issue, and allow full tracking of vesicle traffic and cargo transfer using *in vitro* culture models.

4.4.4. Further research to investigate *in vitro* neuronal differentiation using NSC-derived EVs

Here it is shown that NSC-derived EVs are actively taken up by cells in a 2-DN system and can influence neuronal outgrowth. A recent study has shown that EVs can be modified using bio-orthogonal conjugation (or 'click-chemistry') to carry tissue specific peptides that aid in tissue specific delivery of therapeutic cargo (curcumin) in the brain (Tian et al., 2018a). This strategy can be adapted in the future with the 2-DN system to further understand and manipulate neuronal differentiation. However, prior to this approach, the native targeting and functional ability of NSC-derived EVs must be identified.

Studies have suggested that NSC-derived EVs have a native targeting ability towards specific cells in the brain. A recent study has shown that H9 pluripotent stem cell-derived NSCs can secrete EVs, which when administered intravenously, are attracted to the infarcted hemisphere of the brain in a mouse stroke model, and can improve neurological symptoms (Webb et al., 2018). Another recent study has demonstrated that neonatal SVZ-NSC-derived EVs (labelled with CD9-GFP and Dil) can selectively target Iba1 positive microglia in the brain and change their

morphology from stellate to non-stellate type (Morton et al., 2018). Based on the above, it would be necessary to investigate the targeting ability of NSC-derived EVs used in this study by quantifying intercellular EV co-localisation with multiple neural cell markers for neuronal (MAP2, NEUN, DCX), glial (S100b, GLAST, BLBP) and oligodendrocyte (Olig1, Olig2, MBP) lineages. Another way is to characterise the surface proteins carried by EVs to find their potential targets.

Also, it is unknown whether the majority of EVs taken in by cells are producing a functional effect or directed to degradation and recycling via phagocytosis, micropinocytosis or receptor-/raft-mediated endocytosis (McKelvey et al., 2015). Future immunostaining experiments including co-localisation of EVs with endosomal markers such as ESCRT proteins, and lysosome markers such as LAMP-1 or Lysotracker kit will provide further information on the fate of added NSC-derived EVs in neuronal cultures.

NSCs-derived EVs can carry specific cargo mirroring their parent cells. A recent study demonstrated that NSCs incubated with pro-inflammatory cytokine cocktail can package EVs with components of interferon gamma-Stat1 pathway, and results in activation of Stat-1 pathway in recipient NIH 3T3 cells (Cossetti et al., 2014). Therefore, future experiments should include protein and nucleotide characterisation techniques for NSC-derived EVs including mass spectrometry based-proteomics (Lai et al., 2018) and RNA sequencing (Berardocco et al., 2017; Yagi et al., 2017), respectively, to identify native functional effect

of NSC-derived EVs prior to user defined modifications. Taken together, future research into EV biology couple with EV bio-engineering of NSC-derived EVs can be used to promote user defined influences in the recipient cells including neurons and glia in culture, to improve neuronal differentiation.

4.4.5. EV release characterisation can be used to monitor neuronal differentiation *in vitro*

It has been reported that different cells may secrete EVs of different size and cargo (Berardocco et al., 2017), but there is a lack of knowledge on EV secretion properties of NSCs during differentiation. Some studies have suggested the differential packaging of EVs during cell maturation of different cell types. A study reported that maturation of reticulocytes over a 7-day period showed distinct amount of ESCRT components in EVs over time (Carayon et al., 2011). Another study reported similar differential composition of EVs over maturation using dendritic cells where mature cells were enriched in major histocompatibility complex II (MHC class II), ICAM-1 (an adhesion molecule), and depleted in milk fat globule-EGF factor 8 (MFG-E8), as compared to immature exosomes; in functional T cell stimulation assays, exosomes secreted by mature DCs were 50- to 100-fold more potent than exosomes from immature DCs, both *in vitro* and *in vivo* (Segura et al., 2005). However, both these studies reported that there were no significant differences in EV PSD and EV morphology between the mature and immature cells of the respective studies. Here, in this project, it shown that NSCs show significant

changes in the PSD and release rate of EVs during differentiation, suggesting that such EV changes can be specific for NSCs. Particularly, increase in the presence in neuronal bodies in culture corresponded to an increase in EV release/cell and reduction in average EV size. Moreover, here it is shown that EVs are taken in by cells in cultures very rapidly (less than 15 minutes), and that DiD-labelled EVs can travel as quickly as 4 μm/sec within NSCs, thereby showing fast biomechanics at the macromolecular level. Further research should investigate whether EV biogenesis can be used to define the state of differentiation in a 2-DN culture, and to define the biological properties of a 2-DN in real-time.

4.5. Conclusion

The results from this chapter show that d-STORM provided a quicker and more reliable approach than conventional techniques to characterise stem cell-derived EVs in one step. Extension of this d-STORM approach to investigating EV biology offers significant potential, including future developments such as multiplexing with additional labels for concomitant cargo analysis and live intracellular EV imaging to analyse EV sorting and trafficking mechanisms. This could be exploited to analyse the release and functional contribution of EVs from distinct stem cell populations and could also be applied to the screening of EVs from cancer tissues, since EVs have been proposed as potential tumour biomarkers. This technique will be extensively used in the following chapters to characterise EV populations isolated from BG-NSCs.

5. Cellular and acellular properties of Bergmann glia (BG)-NSCs derived from adult mouse cerebellum

5.1. Introduction

Multiple studies have reported the lack of neurogenesis in the adult rodent cerebellum (Altman and Das, 1966; Grimaldi and Rossi, 2006). Active neurogenesis in the adult brain has been reported to be restricted to the SVZ and SGZ (Ming and Song, 2011). However, NSCs that have been isolated from the postnatal (P7) and adult (P>42) mouse cerebellum were shown to display properties of self-renewal and multipotency (Klein et al., 2005; Lee et al., 2005). A following study identified these NSCs as BG, situated in the PCL which express the NSC markers Sox1, Sox2 and Sox9 in the adult mouse cerebellum, and show NSC characteristics *in vitro* (Alcock and Sottile, 2009).

BG are one of the earliest born cells along with PCs during the embryonic development of the cerebellum and are suggested to be direct descendants of the radial glial NSCs of the ventricular zone (Leto et al., 2016; Yamada and Watanabe, 2002). BG are known to support the migration of GCs during postnatal development and the maturation of neurons including PCs and GCs throughout life (Yamada and Watanabe, 2002). PCs are closely associated with BG, and BG loss causes motor coordination dysfunctions such as ataxia (Lim et al., 2006). Although BG

express NSC markers, their potential to replace most of the cerebellar neurons including PCs *in vivo* are still unclear. A study has reported that NSCs in the adult rodent cerebellum are quiescent and do not generate neurons or astrocytes *in vivo* under physiological conditions (Su et al., 2014). In contrast, a recent study reported neurogenesis to occur from a subset of Sox2 expressing population intermingled within the BG of the adult mice cerebellum, but there has been no evidence of their PC differentiation (Ahlfeld et al., 2017). It would therefore be essential to investigate the properties of BG on neuroglial differentiation, particularly to PCs, and their response to PC damage, to uncover their possible neuroprotective potential in the injured adult cerebellum.

Given increasing evidence of BG as NSCs, this chapter will use the immunocytochemistry, differentiation and imaging protocols optimised from previous chapters, to study the cellular and acellular properties of BG-derived NSCs from the adult mouse cerebellum. The results will include neuronal/glial differentiation potential of BG-NSC in response to RET- and FAS-differentiation protocols *in vitro*. Next, the response of BG in a Purkinje cell degeneration (pcd) mouse model was analysed using the *pcd*^{5J} model, which carries an autosomal recessive mutation of the Nna1 gene causing the death of virtually all PCs by third to fourth postnatal (P) week (Chakrabarti et al., 2006*).* Image analysis of immunostained *pcd* mutant vs WT mouse cerebellum will provide information on BG-NSC response to neurodegeneration *in vivo*. Next, the properties of EVs secreted by BG-NSCs will be investigated based on their effect on neuronal outgrowth and cellular uptake in a 2DN culture to

study the acellular effects of BG-NSCs in neuronal maturation. Moreover, PSD and secretion rate of EV_BGwt will be determined to study the changes in EV release rate and investigate the differences in EV secretion properties of BG- and LV-NSCs.

5.2. Aims

This Chapter has 3 aims.

The first aim was to isolate BG-NSCs (Cell_BGwt) from adult mouse cerebellum and compare their cell growth properties and differentiation properties to adult LV-NSCs (Cell_LVwt) *in vitro* (Sections 5.3.2 and 5.3.2)

The second aim was to investigate the *in vivo* response of BG using a neurodegenerative mouse model (Section 5.3.3).

The third aim was to investigate the neurogenic effects of BG-derived EVs on neurons in culture and the changes in cellular secretion rate of EVs by BG during differentiation (Sections 5.3.4 and 5.3.5).

5.3. Results

5.3.1. Morphological and cell growth properties of Cell_BGwt *in vitro*

To study the *in vitro* stem cell properties of BG, adult cerebellum tissue from wildtype mice were minced, enzymatically digested and cultured in the presence of EGF and FGF. Within 3 weeks, neurospheres were observed. A brightfield image of passage 10 culture showed that BG-NSCs grew as an attached monolayer culture with radial-like morphology with some attached neurospheres as well (Figure 5.1 A), similar to LV-NSCs (Figure 5.1 B).

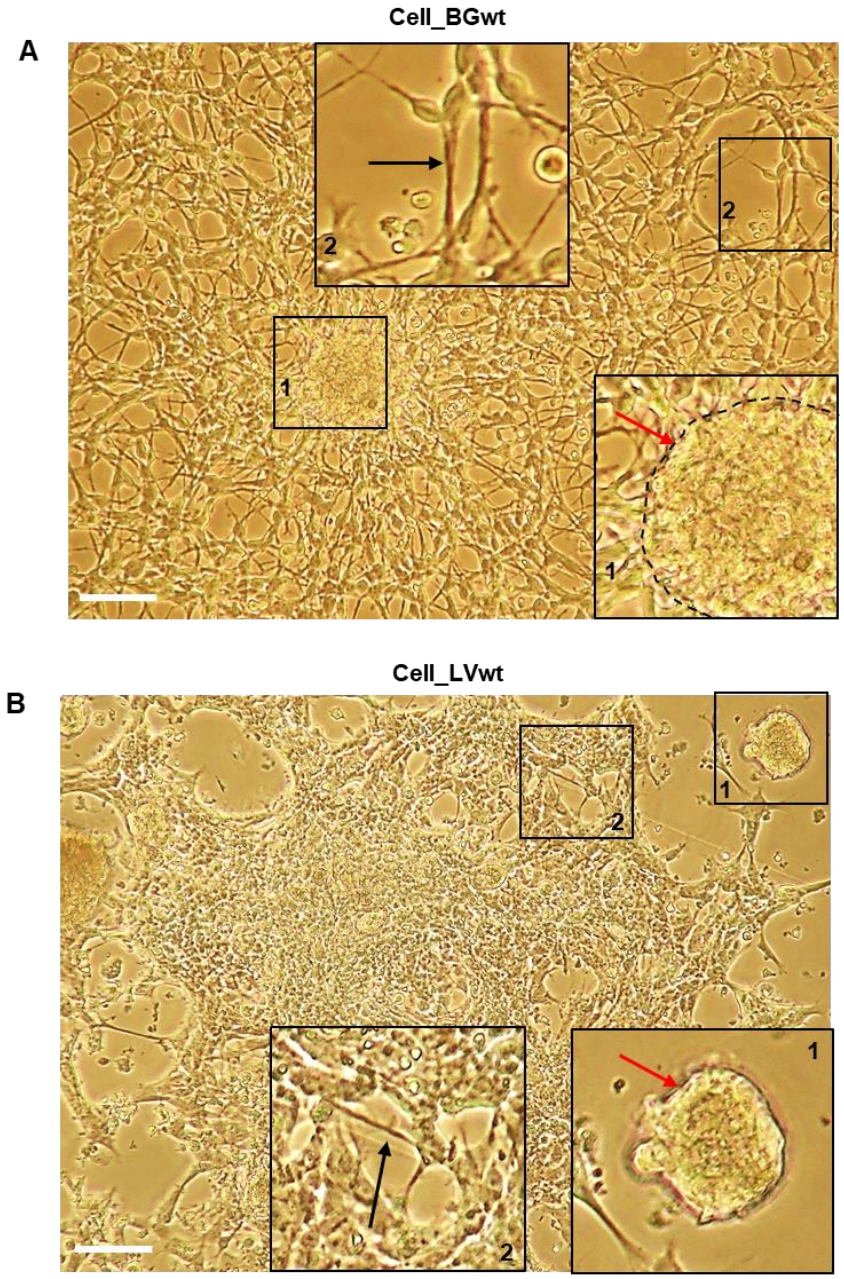


Figure 5.1: Brightfield images showing (A) Cell_BGwt-and (B) Cell_LVwt in culture. Zoomed in images show (1) neurospheres (red arrow shows neurosphere border) and (2) radial morphology (black arrow shows the radial extension) of NSCs.

To observe morphological differences, if any, a closer observation using x40 magnification images taken at early (passage 2) and late (passage 20) passages was done. As a monolayer, majority of cells in BG-NSCs did not grow in a chain-like formation but mostly separated from each

other at both passages (Figure 5.2 A and B). It was noted that Cell_BGwt showed fibrous radial morphology at passage 2 (Figure 5.2 A), which disappeared from passage 10 onwards (Figure 5.2 B). This contrasted with LV-NSCs, where cells were mostly found to be attached to each other in a chain-like formation at both passages 2 and 10 with not much visible fibres compared to Cell_BGwt even at passage 2 (Figure 5.2 C and D). One possible reason for the fibrous morphology of BG during early passages could be due to the intrinsic identity of BG with extensive fibres, as seen in *in vivo* studies (Yamada and Watanabe, 2002), which is distinct from LV-NSCs from the SVZ (Doetsch and Alvarez-Buylla, 1996). In the adult cerebellum, BG fibres are found to be intricately connected to PCs, extending towards to the pial layer through the ML, while during development, BG fibres are known to provide migrational support for GCs (Yamada and Watanabe, 2002). The disappearance of this morphology *in vitro* over time could be due to the adaptive ability of BG-NSCs to *in vitro* conditions.

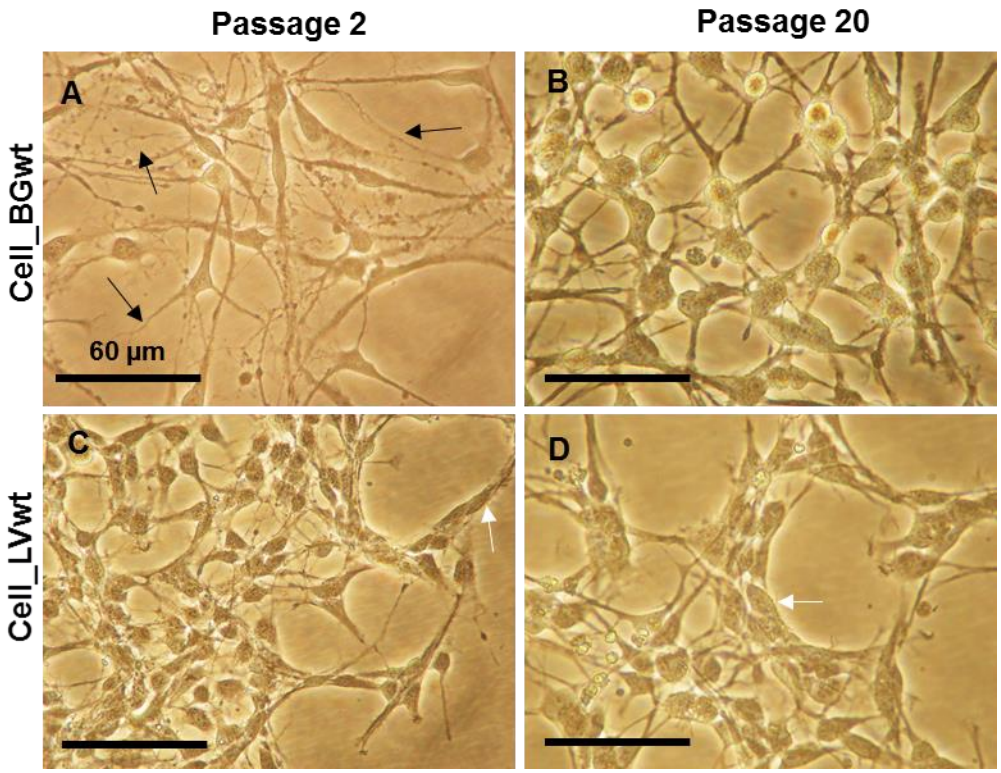


Figure 5.2: Brightfield images showing the morphological appearance of (A and B) Cell_BGwt, (C and D) Cell_LVwt at (A and C) passage 2 and (B and D) passage 20. Black arrows show fibrous extensions of Cell_BGwt in (B). White arrows show cells attached to each other in Cell_LVwt in (C) and (D).

It has been previously reported that neurosphere forming cells from the adult cerebellum are derived from Sox1 positive BG in the PCL (Alcock and Sottile, 2009). Consistent with previous observations, BG-NSCs displayed a slower doubling time (Cell_BGwt- 4.3 days; Cell_LVwt- 1.7 days) (Figure 5.3 A) along with better adhesion to tissue culture plastic compared to LV-NSCs (Alcock and Sottile, 2009). To assess the sensitivity of BG-NSCs due to Accutase treatment during passaging, trypan blue stained cell counting was performed using countess instrument. BG-NSCs showed significantly lower viability after Accutase treatment compared to LV-NSCs suggesting that they were more sensitive to splitting procedures (Figure 5.3 B).

Recent reports and reviews have indicated that new born neurons in the hippocampus, sub ventricular zone and the olfactory bulb undergo cell death as a controlling mechanism of adult neurogenesis in mice (Biebl et al., 2000; Petreanu and Alvarez-Buylla, 2002; Pfisterer and Khodosevich, 2017; Ryu et al., 2016; Winner et al., 2002). It has been reviewed that the time of death for new-born neurons differ between regions of the CNS, for instance, it has been suggested that migrating neuroblast from SVZ undergo cell death within 1 week of cell birth while granule cells from SGZ undergo cell death within 4 weeks of cell birth (Pfisterer and Khodosevich, 2017). To assess cell loss during differentiation, day 0 and day 4 RET- and FAS-treated cells were quantified using countess. Cell_LVwt showed significant cell loss during RET/FAS differentiation at day 4 (Figure 5.3 C), reflecting the cell death observed *in vivo* during SVZ neurogenesis (Pfisterer and Khodosevich, 2017). In contrast, the cell loss in Cell_BGwt cultures at day 4 of RET/FAS differentiation compared to day 0 was not statistically significant (Figure 5.3 C). It was also noted that Cell_BGwt produced less number of cells per a 75% confluent flask compared to Cell_LVwt (Figure 5.3 C). This could be since BG-NSCs have better attachment to the tissue culture plastic and take up more surface are per cell. Nevertheless, these results suggested that BG-NSCs did not follow a similar cell death program to LV-NSCs.

To investigate differences in neuronal bodies produced, if any, BG- and LV-NSCs were treated with RET-based medium for 7 days (longer time points were not used due to progressive loss of cells either by

detachment or death) from day 7 in contrast to LV-NSCs. Brightfield images showed that Cell_BGwt_RET produced neuronal-like bodies with larger perikaryon size (15.49 ± 1.79 µm) compared to neuronal bodies in Cell_LVwt_RET (11.79 ± 1.01 µm) at day 7 (Figure 5.3 D and E).

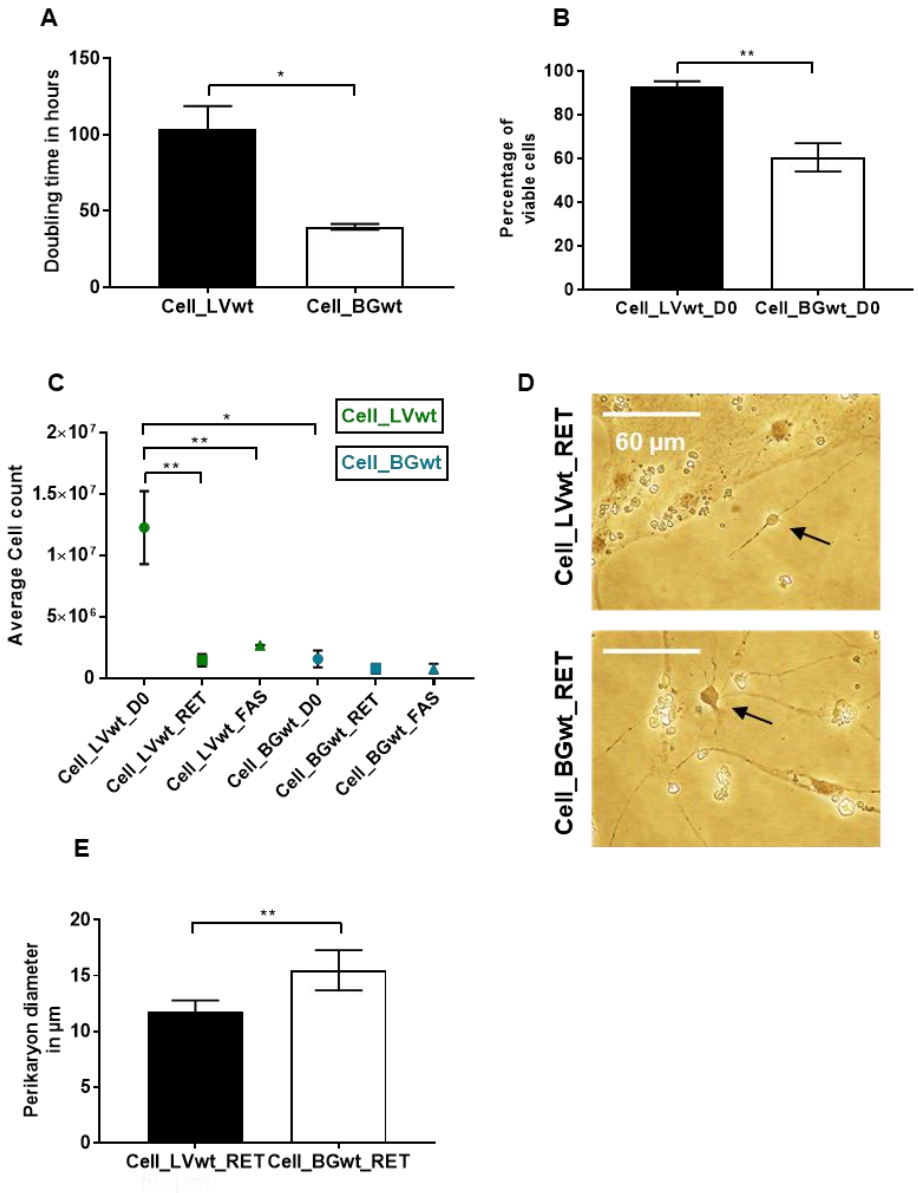


Figure 5.3: (A) Doubling time of Cell_BGwt and Cell_LVwt in culture. (B) Viability of NSCs after Accutase treatment. Student's t-test, n=3 (C) Change in cell count at day 4 of differentiation compared to day 0 in Cell_BGwt and Cell_LVwt. One-way ANOVA, Tukey's multiple comparison tests, n=3. (D) Brightfield images showing the size of neuronal bodies in Cell_BGwt_RET and Cell_LVwt_RET cultures. (E) Quantitation of neuronal perikaryon size in Cell_BGwt_RET and Cell_LVwt_RET cultures. Student's t-test, n=3, (Mean ± SD), (*) p<0.05

5.3.2. *In vitro* differentiation properties of Cell_BGwt

Immunocytochemistry results showed that at day 0, Nestin was detected in both, Cell_BGwt (Cell_BGwt_D0) (Figure 5.4 A) and Cell_LVwt (Figure 5.4 B). It was noted that Nestin detection was much brighter in Cell_BGwt_D0 (Figure 5.4 A) compared to Cell_LVwt_D0 (Figure 5.4 B). Also, Cell_BGwt retained Nestin detection at day 7 of RET-mediated differentiation (Figure 5.4 C) in contrast to Cell_LVwt (Figure 5.4 D). At day 7, Cell_BGwt_RET produced βIII-Tubulin positive neurons (Figure 5.4 G) similar to Cell_LVwt_RET (Figure 5.4 H).

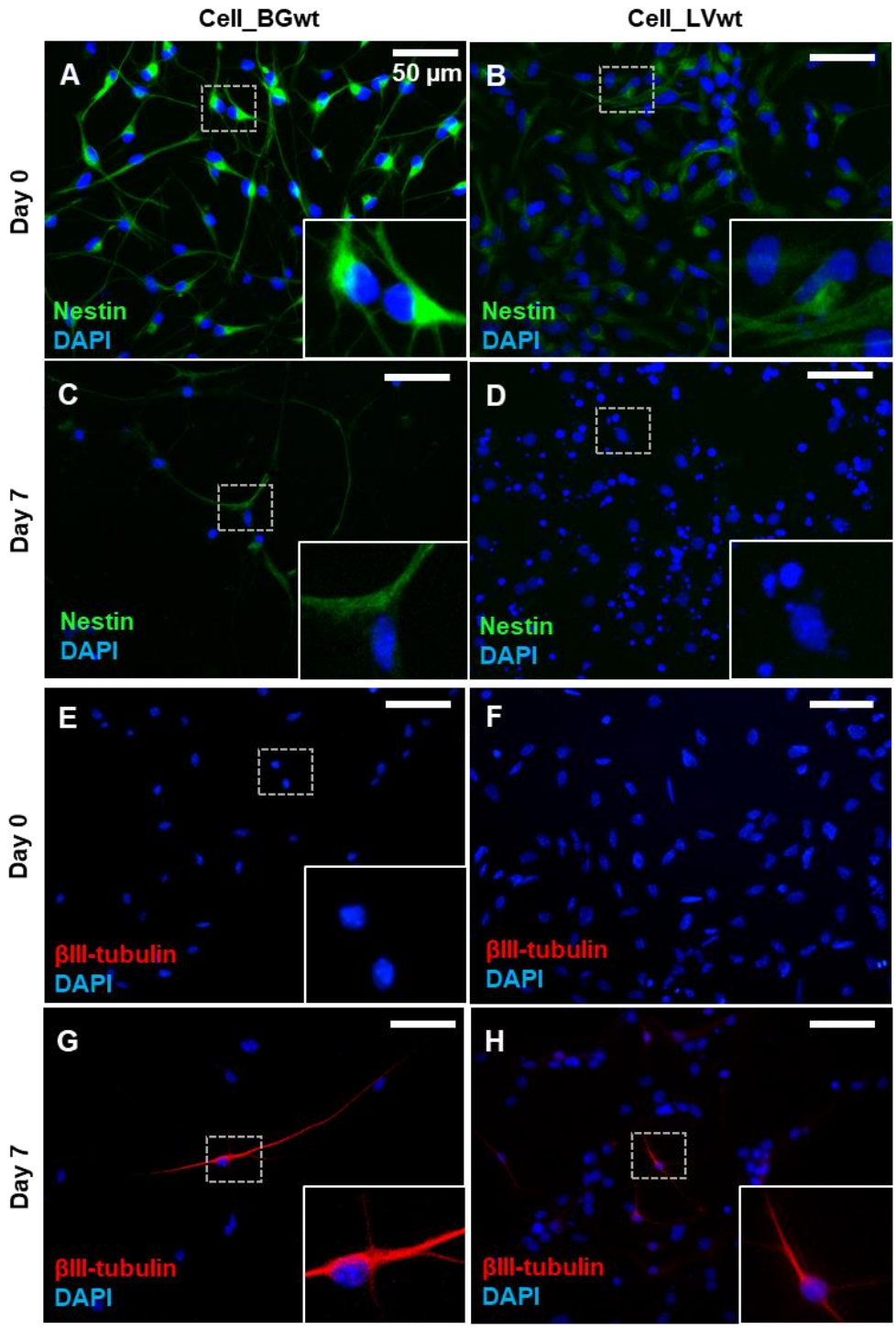


Figure 5.4: Immunofluorescence imaging of (A, C, E and G) Cell_BGwt and (B, D, F and H) Cell_LVwt during differentiation. (A-D) Nestin (green) and (E-H) βIII-tubulin (red) detection of NSCs from day 0 to day 7 of RET treatment. DAPI (blue) was used as nuclei counterstain.

To investigate the potential of BG-NSCs to generate PCs, Cell_BGwt_RET were immunostained for Calbindin (Barski et al., 2003;

Garcia-Segura et al., 1984). Calbindin positive cells were detected in day 7 RET-treated as well as in day 0 samples of both Cell_BGwt (Figure 5.5 A and B) and Cell_LVwt (Figure 5.5 C and D), implying spontaneous differentiation of a small proportion of cells (<1%) even in the presence of EGF and FGF. *In vivo*, Calbindin is detected throughout the large soma of PCs and along their dendrites and axons (Garcia-Segura et al., 1984). By comparing immunofluorescence images, here it was observed that Calbindin detection in Cell_BGwt at day 0 and at day 7 of RET-treatment was found along the elongated neural extensions of the cells (Figure 5.5 A and B). In contrast, Cell_LVwt did not show prominent detection of Calbindin in their neural extensions at day 0 nor at day 7 (Figure 5.5 C and D). Nevertheless, Calbindin detection was rare (<1%) in both Cell_BGwt and Cell_LVwt before and after differentiation, and no cells were found in either cell types resembling the *in vivo* PC morphology. Taken together these results indicate that BG express and maintain NSC marker Nestin during RET-mediated differentiation and has shown the potential to differentiate into βIII-Tubulin and Calbindin positive neurons. However, since this was found only at very low levels, further culture optimisation and differentiation should be done to improve neuronal growth and perform quantitative analysis on BG differentiation.

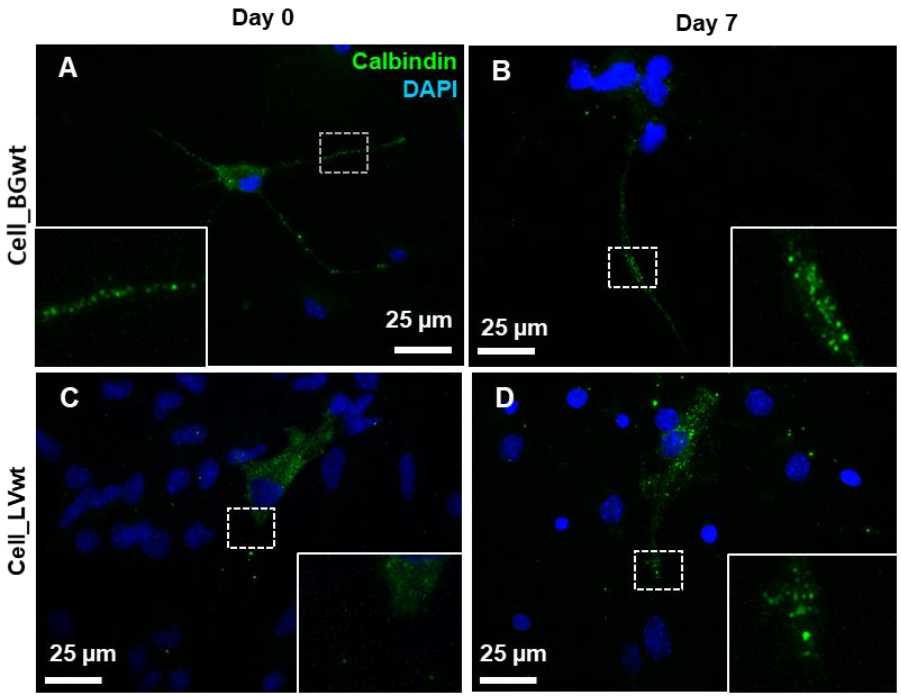


Figure 5.5: Immunofluorescence detection of calbindin (green) in (A and B) Cell_BGwt and (C an D) Cell_LVwt from day 0 to day 7 of RET treatment. DAPI (blue) was used as nuclei counterstain. n=3

To investigate the glial differentiation potential of BG-NSCs, Cell_BGwt were differentiated and stained for GFAP. Cell_BGwt_D0 showed no detection of GFAP (Figure 5.6 A) in contrast to Cell_LVwt_D0 (Figure 5.6 B). Upon RET treatment, Cell_BGwt showed rare detection of GFAP (Figure 5.6 C) (<1%) in contrast to Cell_LVwt_RET (12.8 ± 7.15%) (Figure 5.6 D). FAS mediated differentiation has been used earlier in this study for glial induction of LV-NSCs and was therefore used to test glial differentiation of BG-NSCs. FAS-treatment also produced only rare amount of GFAP positive cells (<1%) in Cell_BGwt (Figure 5.6 E), but also induced radial-like GFAP positive outgrowth similar to FAS-treated Cell_LVwt_FAS (Figure 5.6 E and F).

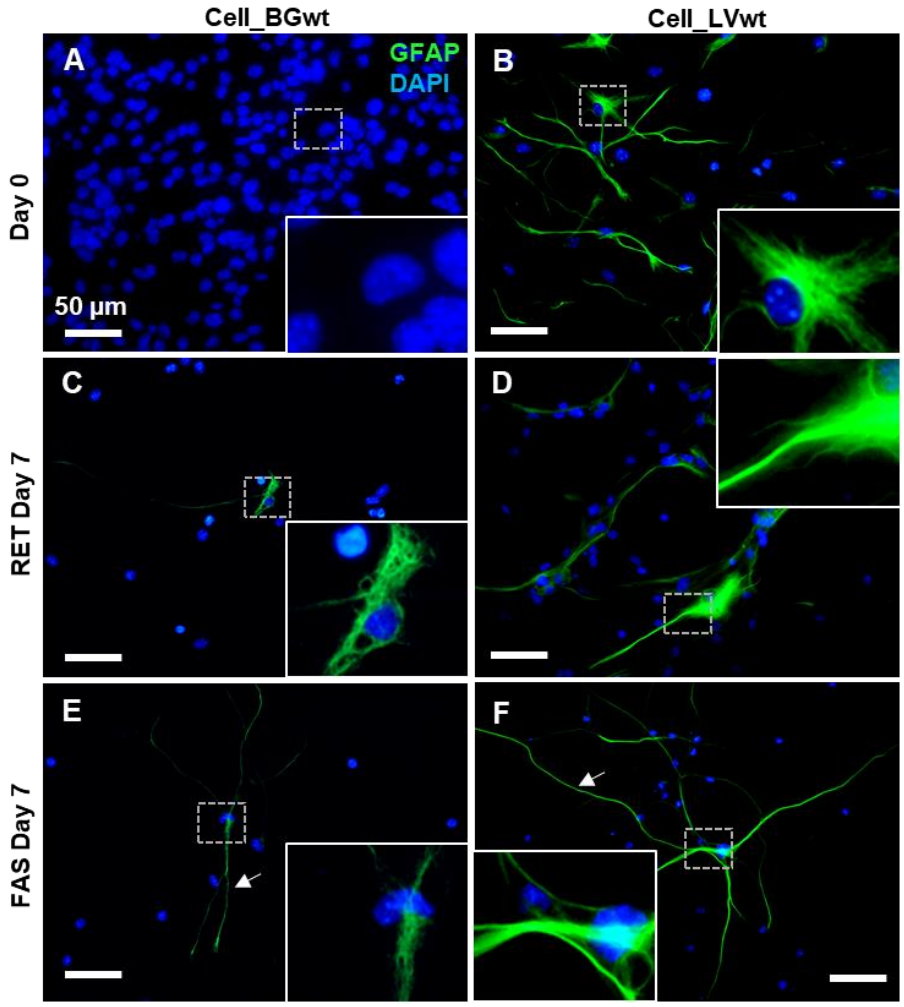


Figure 5.6: Immunofluorescence detection of GFAP (green) in (A, C and E) Cell_BGwt and (B, D and F) Cell_LVwt at (A and B) day 0, (C and D) day 7 of RET-treatment and (E and F) day 7 of FAS-treatment. DAPI (blue) was used as nuclei counterstain. Arrows show GFAP positive radial outgrowth of FAS-treated cells.

Next, the samples were stained for the glial marker S100b. Most of the Cell_BGwt_D0 expressed S100b (83.12 ± 6.78%) (Figure 5.7 A) in contrast to Cell_LVwt (12.49 ± 4.81%) (Figure 5.7 B), in line with their expression *in vivo* (Allen's Brain Atlas http://mouse.brain-map.org/). Cell_BGwt and Cell_LVwt maintained S100b detection during RET as well as FAS treatment (Figure 5.7 C-F), however, both cell types showed much more complex glial morphology with multiple extensions only during FAS treatment (Figure 5.7 E and F). Also, S100b detection was

found to be localised strongly in the nuclear region of cells found in day 0 and day 7 of FAS-treated NSCs but not in RET-treated NSCs (Figure 5.7 A-F), suggesting the presence of oligodendroglial progenitors as per previously published suggestions (Deloulme et al., 2004). Taken together, these results suggest that BG-NSCs can respond to FAS-treatment producing few GFAP cells with radial-like extensions and a larger proportion of S100b cells with mature morphology.

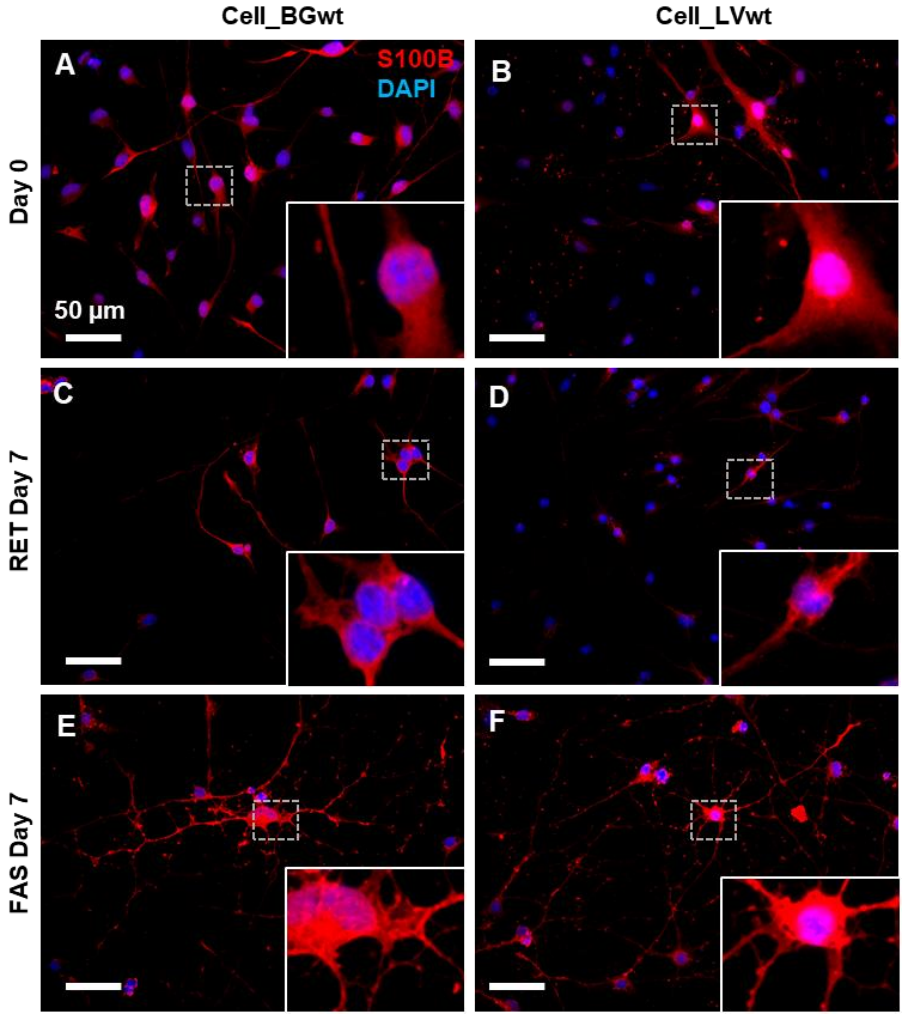


Figure 5.7: Immunofluorescence detection of S100b (red) in (A, C and E) Cell_BGwt and (B, D and F) Cell_LVwt at (A and B) day 0, (C and D) day 7 of RET-treatment and (E and F) day 7 of FAS-treatment. DAPI (blue) was used as nuclei counterstain.

5.3.3. *In vivo* response of BG in pcd^{5J} mouse

To investigate the *in vivo* properties of BG, immunostained images of mouse cerebellum tissue sections were used. In adult wildtype (WT) mice, BG population adjacent to PCs in the PCL expressed the NSC markers Sox1, Sox2 and Sox9, and the radial glial markers GFAP and BLBP (Figure 5.8 A-E).

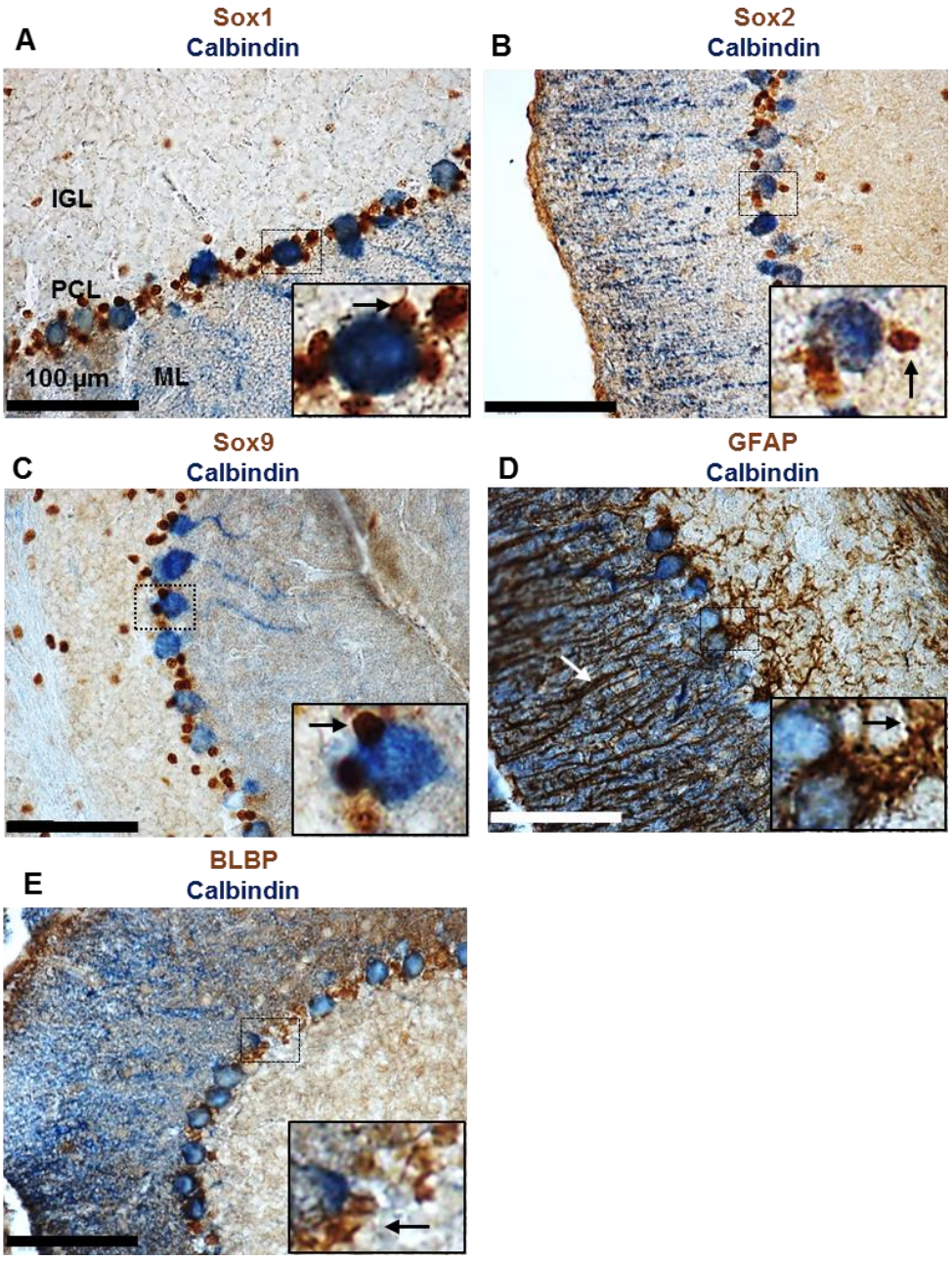


Figure 5.8: Expression of NSC associated markers in the BG of adult mice. Double immunostaining of (A) Sox1, (B) Sox2, (C) Sox9, (D) GFAP and (E) BLBP (brown) with Calbindin (blue) showing the BG population (arrows) situated in PCL adjacent to Purkinje neurons. Black arrows point to the BG. IGL, internal granular layer; ML, molecular layer; PCL, Purkinje cell layer. Staining performed by SS, Images captured by SS and ZN (adapted from Salih, 2016).

Proliferating NSCs *in vivo* can be marked by nestin and Ki67 detection (Kee et al., 2002; Suslov et al., 2002). However, no nestin or Ki67 was detected in PCL of adult WT mice suggesting that BG-NSCs might not proliferate under normal conditions (Figure 5.9 A and B). Alternatively,

database searches using Allen's Brain Atlas (https://www.brain-map.org/) resulted in mixed interpretations where Nestin expression was observed in the PCL of coronal sections but not sagittal sections of adult mice cerebellum (Figure 5.9 C-F). These results suggested that BG most likely consist of a quiescent population of adult NSCs in the cerebellum.

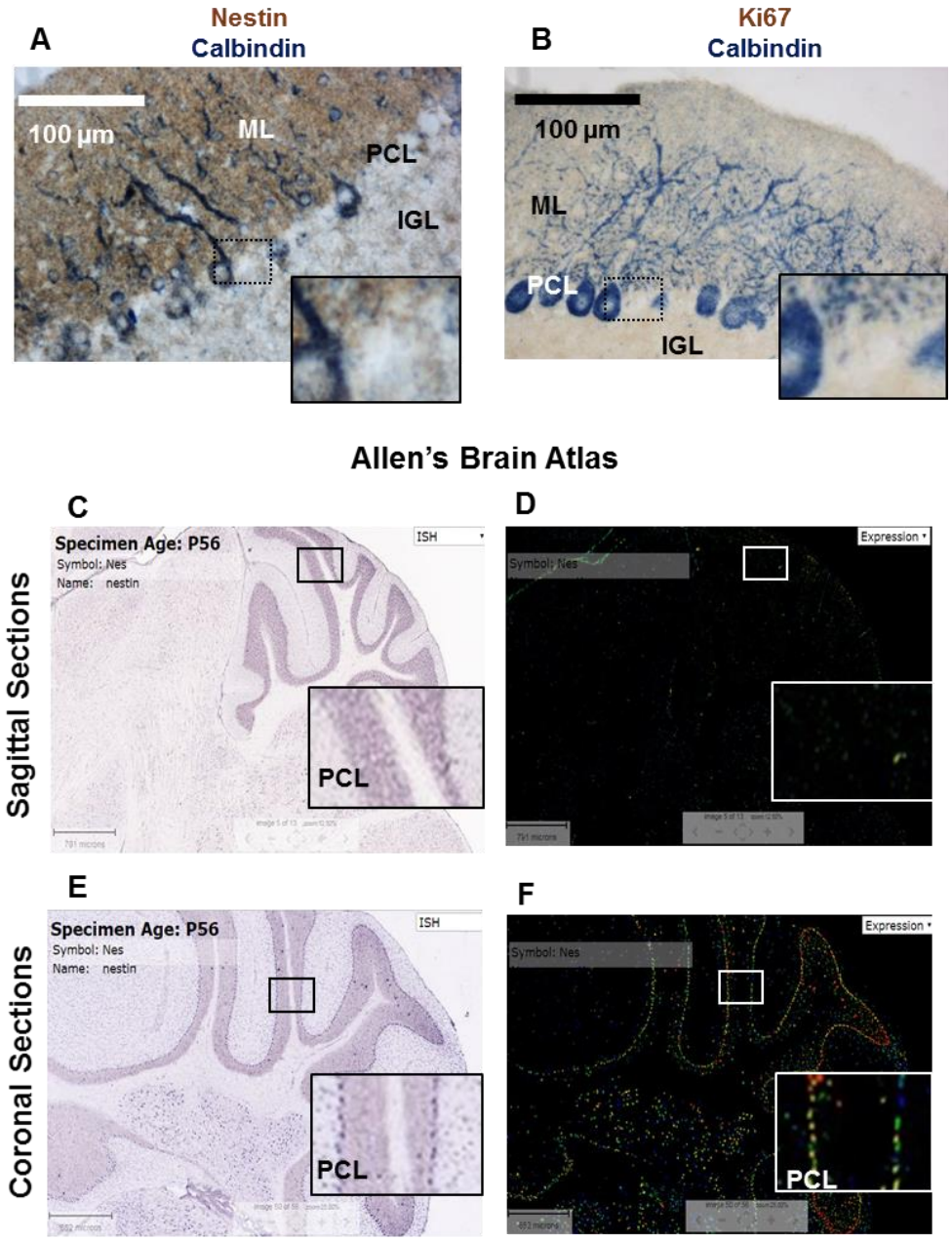


Figure 5.9: Double immunostaining of (A) Nestin and (B) Ki67 (both brown) with Calbindin (blue) in the adult mouse cerebellum. Nestin detection (C and E- In situ hybridisation; D and F- Expression) in (C and D) sagittal and (D and F) coronal sections of adult mouse brain from Allen's Brain Atlas Database. IGL, internal granular layer; ML, molecular layer; PCL, Purkinje cell layer. (A and B) Sections stained by SS, sections imaged by SS and ZN (adapted from Salih, 2016).

To study the *in vivo* response of BG during neurodegeneration, a Purkinje cell denegation (*pcd*^{5J}) mutant model was used (Chakrabarti et al., 2006). *pcd*^{5J} is an autosomal recessive mutation where the insertion

of a single GAC triplet encoding an aspartic acid residue at position 775 of *Nna1* gene causes the death of virtually all PCs by third to fourth postnatal week (Chakrabarti et al., 2006). *pcd* mutants have been reported to lose 25% to 50% of total PCs in the culmen and pyramis vermis of the cerebellum by P25 (Mullen et al., 1976). Despite the lack of PCs in 3 to 4-month old *pcd* mice, large number of synaptic inputs in the ML, and other cell types, are still intact (eg: a significant proportion of Granule cells (GCs) remain) which allows for cell transplantation, reactive gliosis and behavioural studies due to PC loss in mice (Wang and Morgan, 2007).

To investigate the response of BG during PC insult, immunostained images of cerebellum of *pcd*^{5J} mice were quantified for the number of BG present at postnatal day P104 (a late stage of PC insult) (Figure 5.10 A). Double immunostaining for Calbindin with Sox1, Sox2, and Sox9 indicated that although PC were lost at P104 in the mutant mice, Sox-positive BG were still numerous (Figure 5.10 A). Quantification of Sox-positive cells in mutant cerebellum showed a significant increase after P104 compared to WT controls (Figure 5.10 B), indicating an increase in the Sox-positive BG population in response to PC insult.

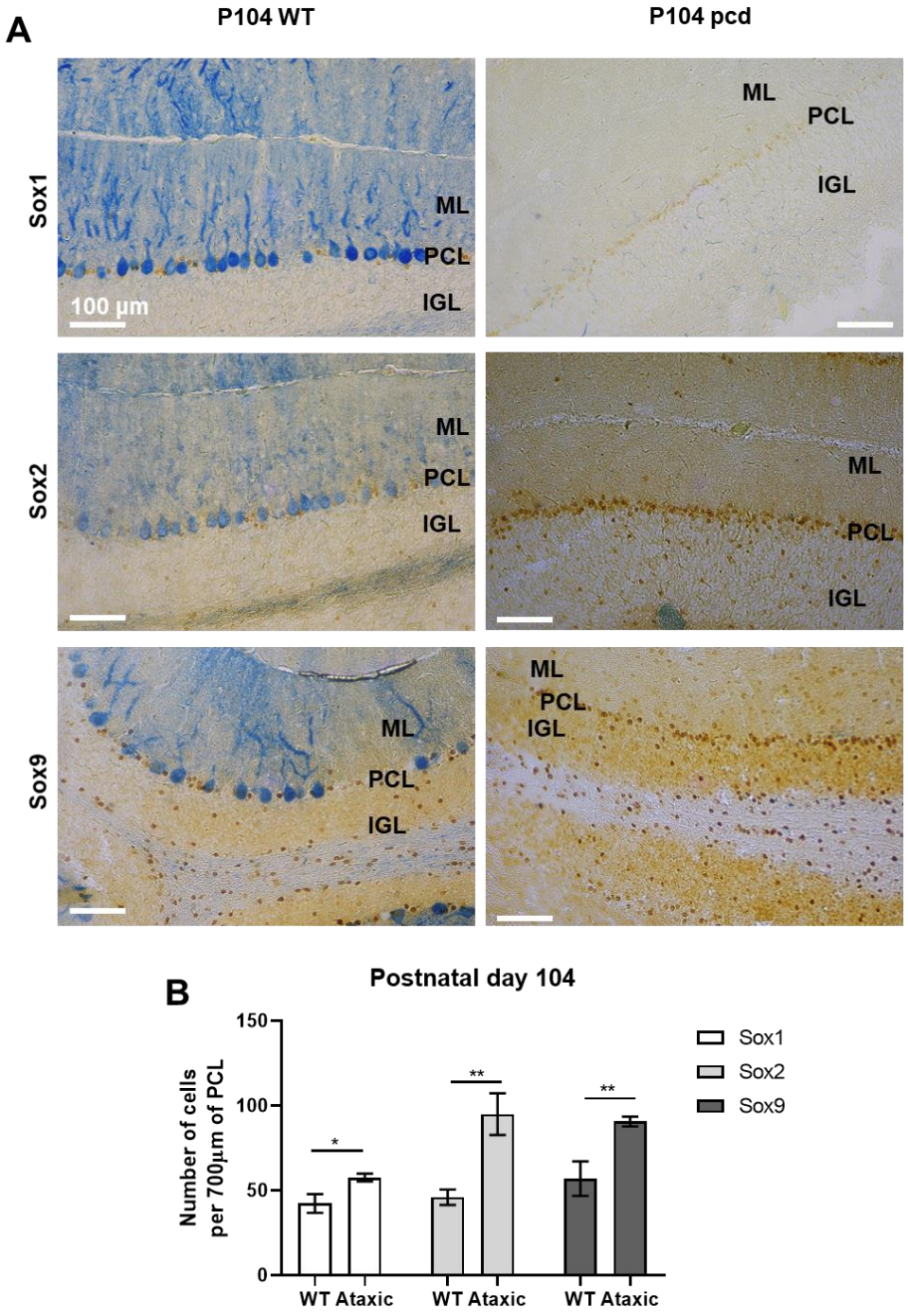


Figure 5.10: (A) Expression of Sox1, Sox2 and Sox9 in postnatal day 104 *pcd* mutant mice. (A) Double immunostaining of Sox1, Sox2, Sox9, (brown) with Calbindin (blue) showing the Bergmann glial population situated in PCL adjacent to Purkinje neurons in *pcd* mutant and WT control mice on P104, n = 3. (B) Quantitation of Sox1, Sox2, Sox9 in the PCL of mice cerebellum on P104 (Mean ± SD). WT- Wildtype, Ataxic (*pcd5J*) mutant mice. Scale bar = 100 µm. IGL, internal granular layer; ML, molecular layer; PCL, Purkinje cell layer. WT – wildtype. IGL, internal granular layer; ML, molecular layer; PCL, Purkinje cell layer. WT – wildtype, P-postnatal day. Sections stained by SS, sections imaged and analysed by ZN.

To investigate if the BG displayed signs of reactive gliosis under PC insult *in vivo*, GFAP immunostained images were analysed at P100 (a late

stage of PC insult). Calbindin and GFAP double immunostained images showed a clearly strong GFAP detection in P100 mutant cerebellum with vacuolar regions, suggesting gliosis, in contrast to WT cerebellum (Figure 5.11 A and B).

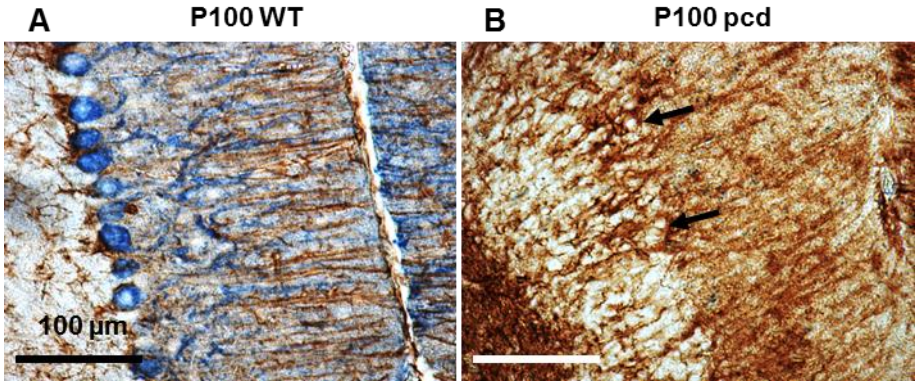


Figure 5.11: Double immunostaining of GFAP (brown) with Calbindin (blue) showing the BG fibres situated in ML of (A) WT and (B) pcd mutant cerebellum at P100. Black arrows show vacuole formation in the PCL fibres in the cerebellum of pcd mutant. BG, Bergmann glia; IGL, internal granular layer; ML, molecular layer; PCL, Purkinje cell layer. WT – wildtype, P-postnatal day. Sections stained by SS, sections imaged by SS and ZN (adapted from Salih, 2016).

5.3.4. Neuronal response, cellular uptake and localisation of Cell_BGwt derived EVs in neuronal culture system

To determine the optimal concentration of EVs required for neuronal response study, EV_BGwt_D0 were added to 2-DN cultures from day 4 to day 10 of differentiation every 48 hours with either undiluted (1x) or diluted (0.1x and 0.01x) amount of EVs (diluted from stock EV isolates). (Refer to section 5.2 for justification of this dilution). These dilutions will contain different number of EVs depending on the surface area of cell

culture flask or plate (refer Table 5.1). Note: Please refer to Table 2.1 for the sample nomenclatures.

Table 5.1: Concentration of EVs isolated from BG-NSCs used for neuronal cell response study (Mean ± SEM; n=6).

1x stock concentration	**Total EVs from 75 cm^2**		**Total EVs for 2 cm^2**		**Total EVs for 0.3 cm^2**	
	Volume (µl)	**EV count**	**Volume (µl)**	**EV count**	**Volume (µl)**	**EV count**
EV_BGwt_D0	1000	1.8 ± 0.1 x 10^{13}	26.7	4.8 ± 0.3 x 10^{11}	4	7.2 ± 0.4 x 10^{10}

The response of 2-DN cultures to EV_BGwt_D0 was similar to their response to EV_LVwt_D0 that was observed in section 5.32 and 5.33. EV_BGwt_D0 also showed increased metabolic activity of 2-DN cultures at day 10 along with the presence of neuronal bodies (similar to control cells in 2-DN cultures without added EVs) only when 0.1x dilution of EVs were used (Figure 5.12 A and B).

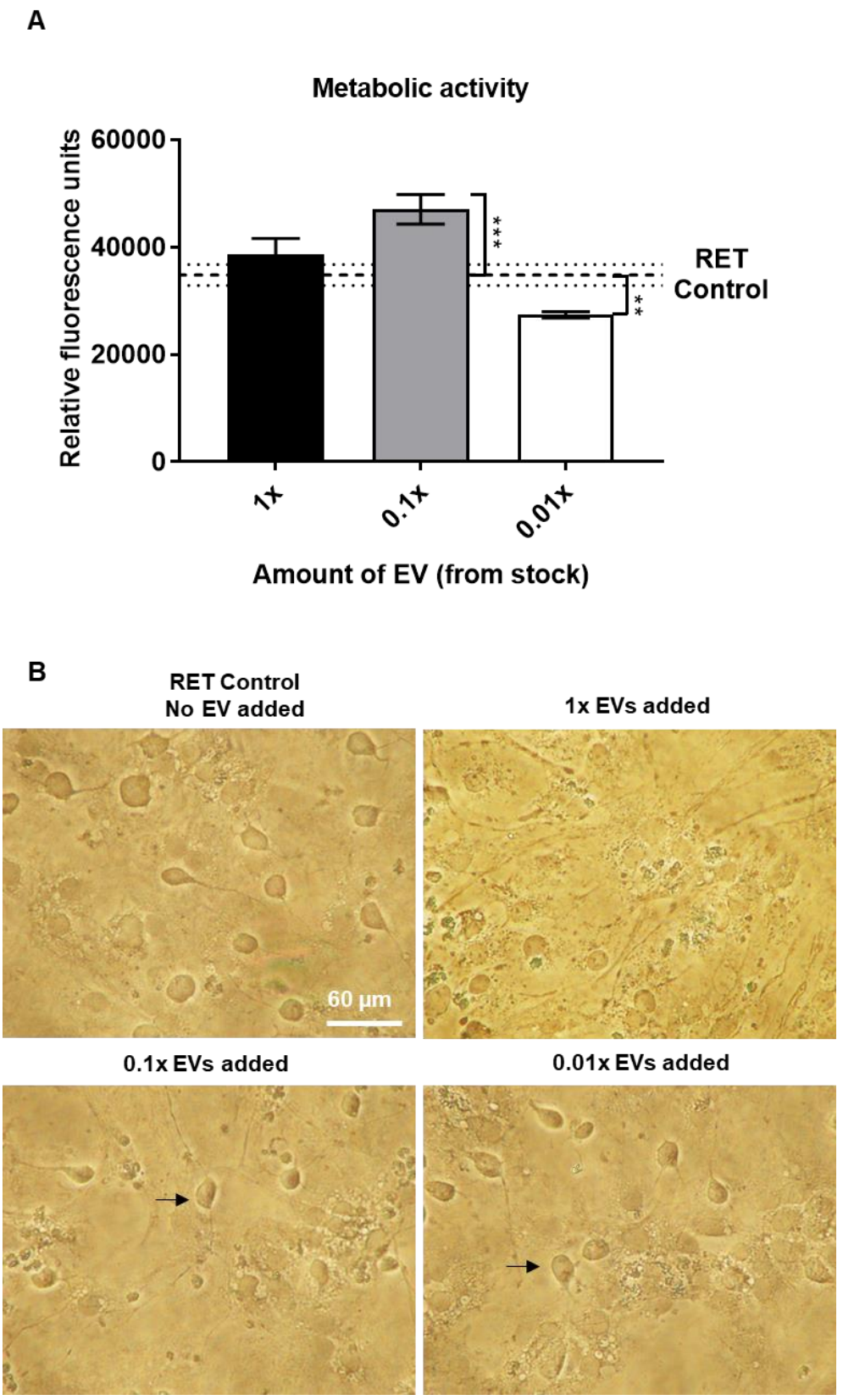


Figure 5.12: (A) Metabolic assay and (B) brightfield imaging of Cell_LVwt_RET under different stock concentrations of EVs derived from Cell_BGwt on day 10. Black arrows show neuronal-like cells. One-way ANOVA Tukey's multiple comparison test, n=3, (*) p<0.05.

Samples were then stained for βIII-Tubulin to assess the neuronal changes in cultures in response to added EVs. Qualitative analysis using MetaXpress neuronal outgrowth analysis module of immunofluorescence images suggested an increase in total neuronal processes per image for 2-DN cultures incubated with EV_BGwt_D0 compared to control wells with no added EVs (Figure 5.13 A-E).

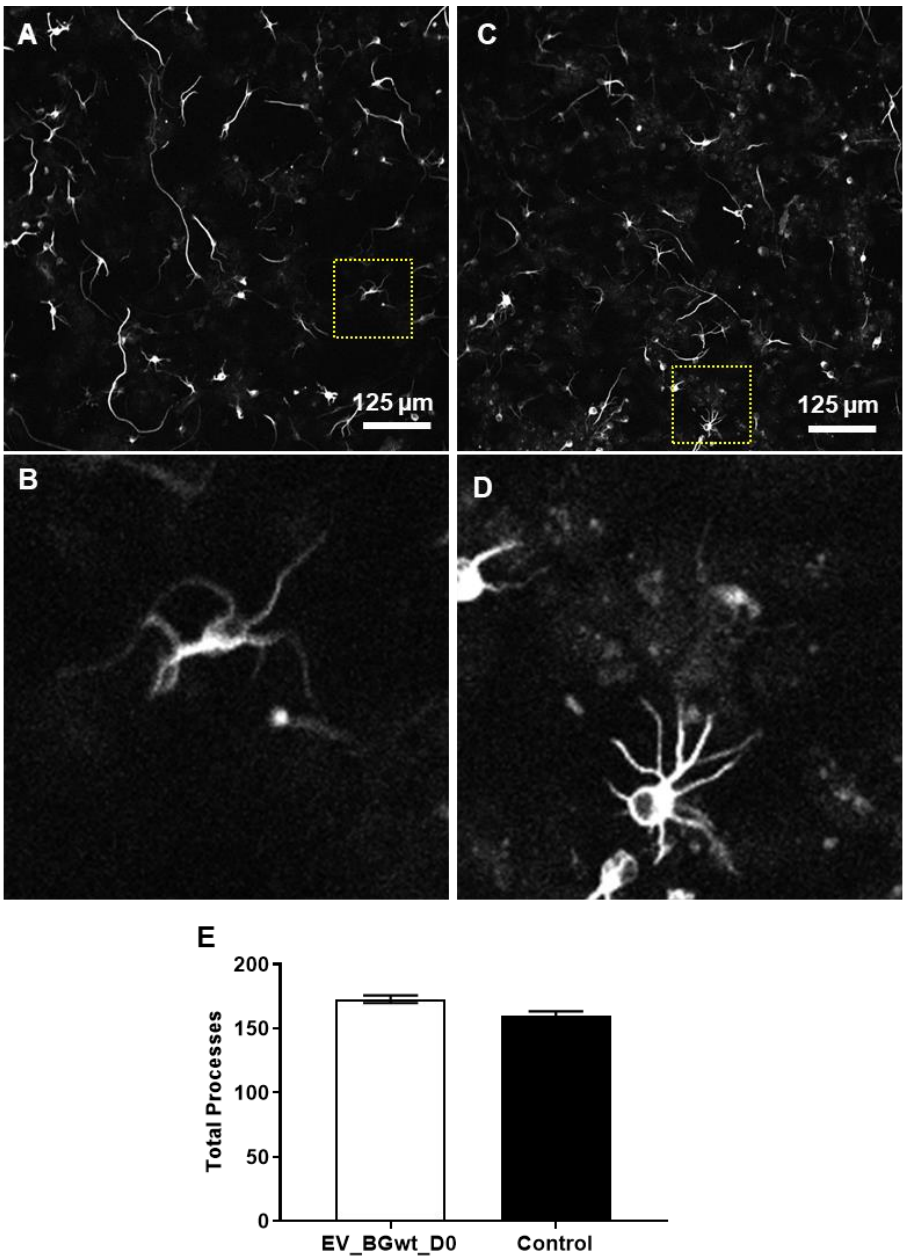


Figure 5.13: Changes in number of neuronal processes upon addition of EV_BGwt_D0 (day 10). Immunofluorescence images of βIII-Tubulin positive cells in (A) no EV added controls ((B) showing zoomed in image of a neuron in (A)) and (C) EV_BGwt_D0 added cells ((D) shows zoomed in image of neuron in (C)) of 2-DN cultures. (E) Quantitation of total neuronal processes per image. Mean ± SD, n=2.

To confirm if the increase in neuronal outgrowth was associated with cellular uptake of EVs in culture, samples stained with βIII-Tubulin and GFAP and analysed for colocalization of DiD-labelled EVs within cells. Immunofluorescence images confirmed the colocalization of DiD with

cells in EV treated samples but no DiD signal from control cultures, confirming the uptake of DiD-labelled EVs (Figure 5.14 A-D). It was noted that majority of cells (79.28 ± 6.08% of DAPI nuclei and their perinuclear region) were associated with DiD detection; 15.08 ± 5.09% and 10.67 ± 0.82% of total cells were positive for GFAP and βIII-Tubulin, respectively and most them (90.60 ± 9.11% of total GFAP cells and 63.98 ± 5.84% of total βIII-Tubulin cells) colocalized with DiD detection (Figure 5.14 C and E). These results confirmed that EV_BGwt_D0 were actively taken up by 2-DN cultures during neuronal differentiation and this was associated with an increase in total neuronal processes.

Next, 3D localisation of DiD detection were analysed to investigate if the added EVs showed axonal or intracellular association with βIII-Tubulin neurons in culture. Confocal z-stack images showed detected DiD to be associated with axonal regions of neurons (Figure 5.14 F). 3-D reconstruction by Zen image analysis platform confirmed the partial detection of DiD within axons (Figure 5.14 F and G). Taken together, these results suggested that EVs derived from BG-NSCs may interact with neurons in culture in a similar way to EVs derived from LV-NSCs - either via direct internalisation or via axonal contact, or indirectly via neighbouring cells.

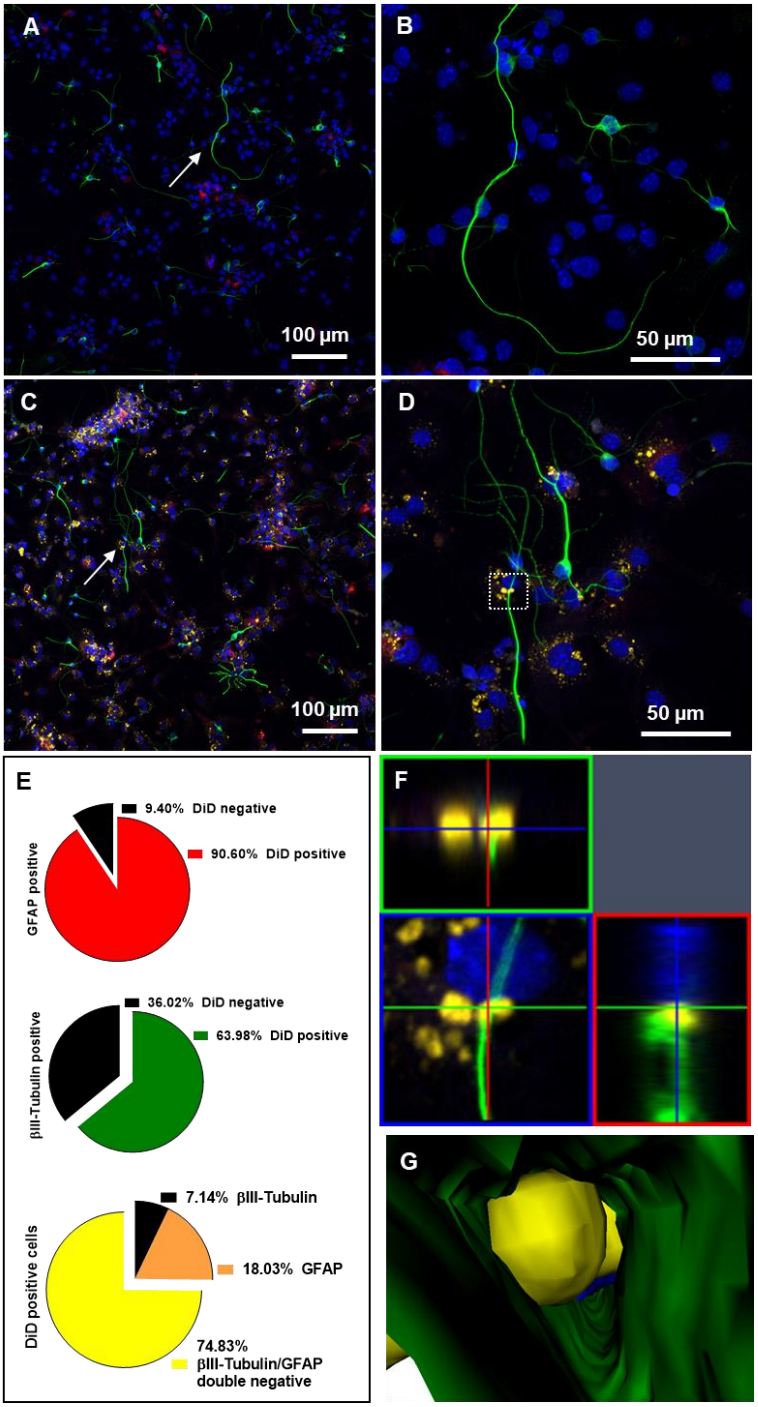


Figure 5.14: Immunofluorescence and subsequent 3-D reconstruction imaging of EV_BGwt_D0 uptake by 2-DN cultures (day 10). Immunofluorescence images of βIII-Tubulin (green), GFAP (red) and DiD (yellow) in (A) no added EV control cells and ((B) zoomed in image of neurons marked by white arrow in (A)) and (C)) EV_BGwt_D0 added cells ((D) shows zoomed in image of neuron in (C)) of 2-DN cultures. (E) Population estimation of DiD localised cells from (C). Cells with DiD detection within the perinuclear (radius = 5 µm; for DAPI-only cells) and/or cytoplasmic regions (for green or red cells) were confirmed as DiD+ve cells. Vacuolar region (for GFAP+ve cells) and axonal. (F) Orthogonal view of the boxed region shown in (D) to localise DiD detection near axons. (G) Snapshot from reconstructed 3-D movie of DiD detection associated with the axon image of (E).

5.3.5. Particle size distribution, concentration and secretion rate of EVs derived from Cell_BGwt

In order to characterise the EVs secreted by BG-NSCs, EVs from undifferentiated and differentiated Cell_BGwt were isolated and characterised using d-STORM approach. PSD analysis indicated a decrease in EVs of <50 nm in sizes (EV_BGwt_D0, 13 ± 0.7 x 10^{12}; EV_BGwt_RET, 4.4 ± 1.4 x 10^{12}; EV_BGwt_FAS, 0.4 ± 0.01 x10^{12}; Mean ± SEM) (Figure 5.15 A-C), and a decrease in total EVs isolated from day 4 differentiating BG-NSCs compared to their day 0 counterparts (Figure 5.16 A).

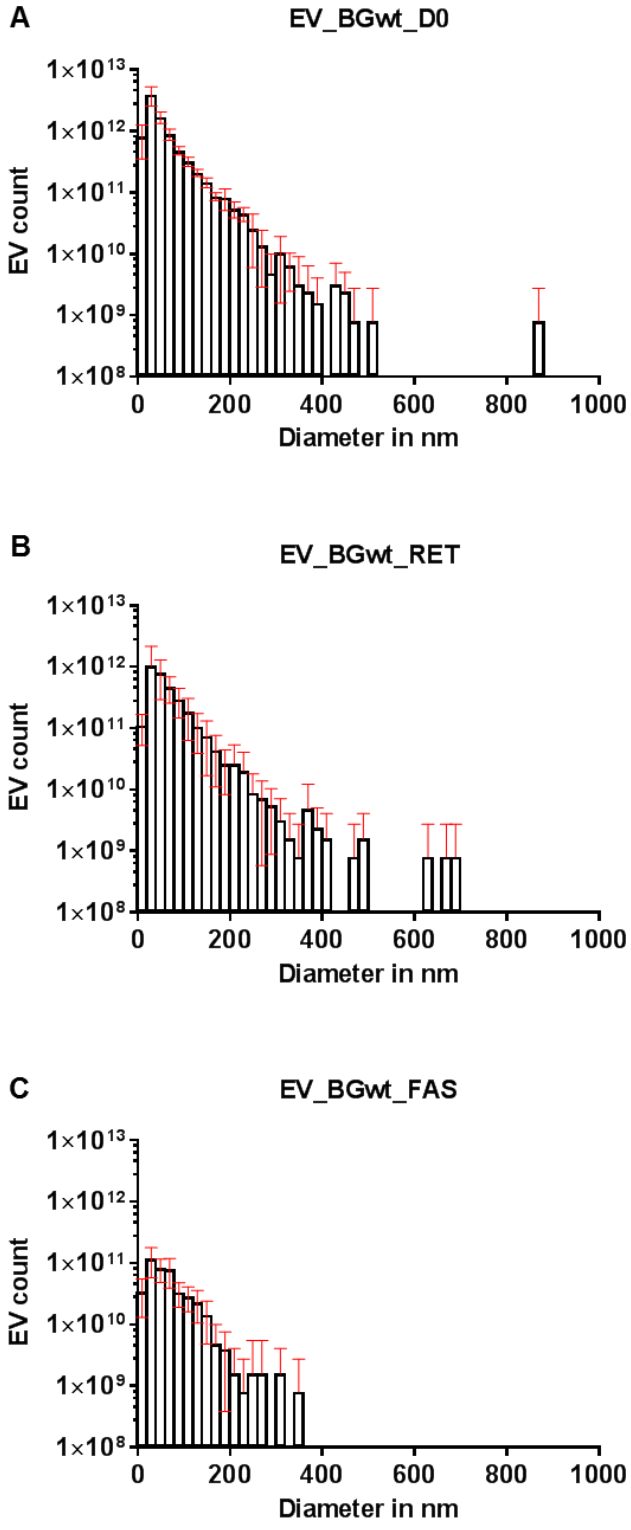


Figure 5.15: Particle size distribution analysis of EVs derived from Cell_BGwt using d-STORM at (A) day 0, (B) day 4 RET-treated and (C) day 4 FAS-treated. (Mean ± SD), n=3.

Indeed, RET- and FAS-treated Cell_BGwt generated significantly less number of EVs in total compared untreated cells (Figure 5.16 A). However, only FAS-treatment significantly decreased the EV release per cell during differentiation (Figure 5.16 B). Both RET- and FAS-treatment resulted in the release of EVs with significantly bigger sizes compared to untreated cells (Figure 5.16 C). These results highlighted the changes in EV secretion and size range during the differentiation of BG-NSCs.

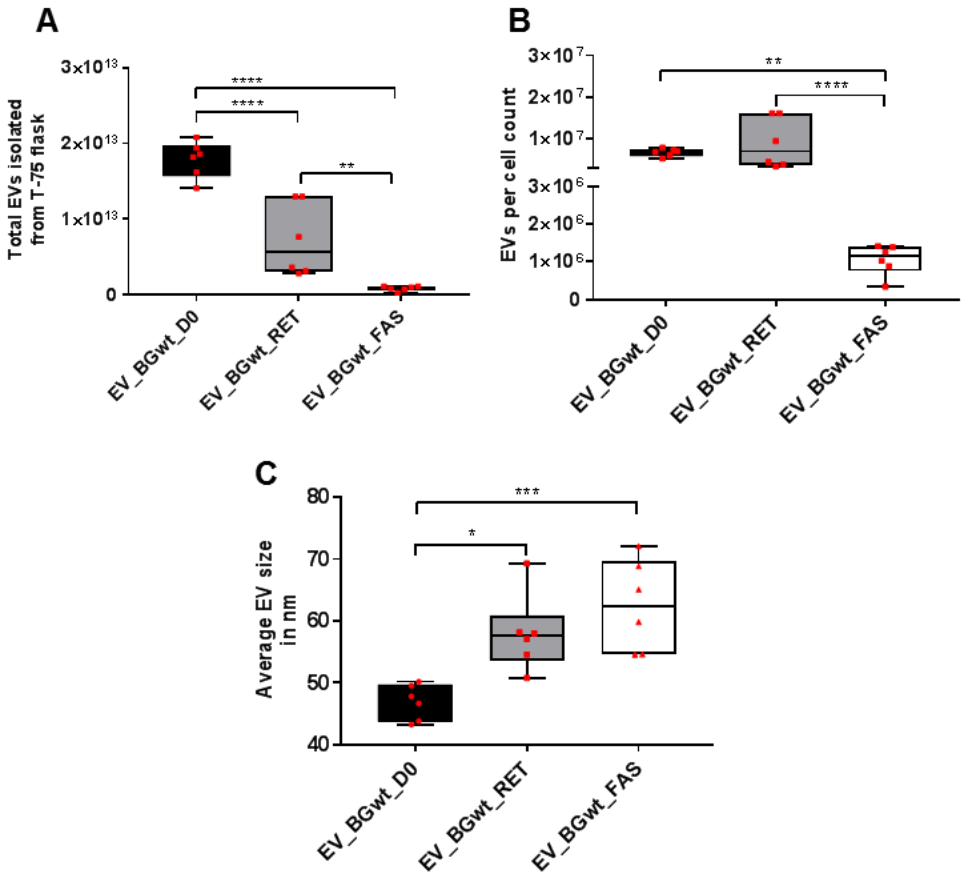


Figure 5.16: Average concentration and size determination of Cell_BGwt derived-EVs. (A) Total EVs isolated from differentiating BG-NSCs. (B) Average EVs secreted per BG-NSCs during differentiation. (C) Average size of EVs isolated from differentiating BG-NSCs. One-way ANOVA tukey's multiple comparison test. (Mean ± SD), n=3, (*) p<0.05.

At their undifferentiated state, it was found that Cell_BGwt secreted EVs of significantly lower sizes compared to Cell_LVwt (Figure 5.17 A).

Interestingly, it was also found that Cell_BGwt secreted 10-fold more EVs per cell compared to Cell_LVwt or Cell_LVsg (Figure 5.17 B). These results suggested that BG-NSCs had distinct EV secretion profile compared to LV-NSCs.

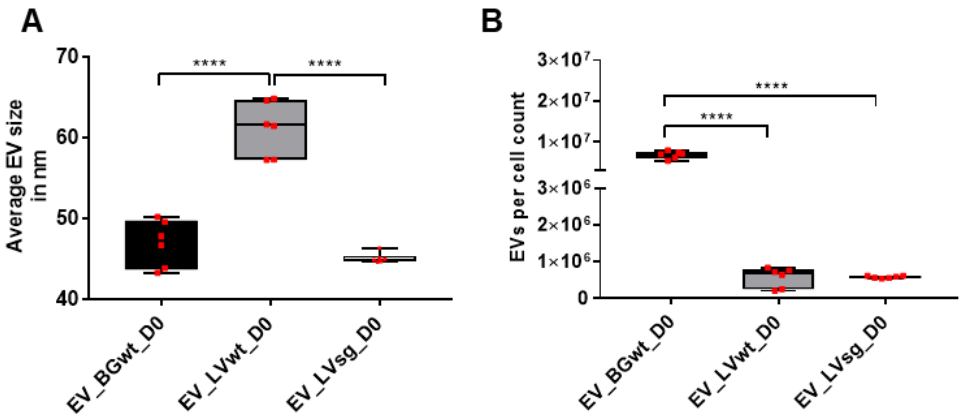


Figure 5.17: (A) Average size of EVs and (B) Average EV released per cell by Cell_LVwt and Cell_BGwt. Student's test. (Mean ± SD), n=3, (*) p<0.05.

5.4. Discussion

This chapter focused on characterising cellular and acellular properties of BG-NSCs using the protocols optimised in previous chapters.

5.4.1. Distinct stem cell properties of BG

Recent studies have highlighted that NSCs are a heterogenous population of glial cells, within the same region as well as different regions of the mammalian CNS (Ihrie and Alvarez-Buylla, 2011; Klein et al., 2005). In this study, it is shown that isolated BGs not only display the conventional *in vitro*-NSC characteristics, but also that they can be distinguished from NSCs isolated from the SVZ region of the CNS.

Consistent with a previous study involving mice and human cerebellum tissue samples (Alcock and Sottile, 2009), here it is observed that the BG in the adult mouse CB express the NSC markers Sox1, Sox2 and Sox9. Interestingly, BG also show morphological characteristics similar to developmental radial glia (Koirala and Corfas, 2010). *In vivo*, BG fibres extend radially along the parallel fibres in the ML towards the pia, similar to the radial extensions of embryonic radial glial NSCs, and here it is shown that BG express radial glial markers including GFAP and BLBP (Yamada and Watanabe, 2002). Since radial glia are embryonic NSCs, our results imply that BG are a rare persistence of radial glial NSC into adulthood in the vertebrate CNS.

A previous study has reported that adult cerebellum-derived NSCs (CB-NSCs) from the adult (>P42) and postnatal (P0) mice failed to functionally integrate into the SVZ neurogenic niche (Klein et al., 2005). Accordingly, CB-NSCs failed to migrate into the olfactory bulb, generated a majority of GFAP positive astrocytes and showed low efficiency of neuronal differentiation into TAG1 positive cells, thereby retaining cerebellar identity (Klein et al., 2005). On the other hand, SVZ-NSCs showed structural integration into the cerebellum but produced a majority of astrocytes and no cerebellar neurons (Klein et al., 2005). Here it is shown that the Cell_BGwt show differences in- 1) growth rate, 2) morphological properties and adherence to tissue culture plastic, 3) S100b expression, 4) EV secretion rate, and 5) viability and neuronal body soma size during differentiation in culture, compared to Cell_LVwt. These observations are incidental with independent reports which suggest that NSCs derived from the cerebellum have distinct intrinsic regional identity compared to SVZ derived NSCs (Klein et al., 2005).

5.4.2. BG-NSCs display the potential to produce cerebellar neurons

Here, it is shown that BG-NSCs can express the neuronal markers βIII-Tubulin and Calbindin, and the glial markers GFAP and S100b during *in vitro* differentiation. These markers, excluding S100b, were detected only at very low levels (<1%). Moreover, other cerebellar neuronal markers including (TAG1 and NeuN for GCs of the cerebellum) were not tested. Therefore, although this study shows the potential of BG-NSCs to

produce neurons, the extent and diversity of differentiation of these NSCs, along with the optimal culture conditions for their analysis, are still unclear.

Studies reporting the neuronal differentiation ability of adult BG to PCs are limited. PCs are reported to be technically challenging to be differentiated *in vitro*. Previous studies have reported the maturation of embryonic and adult CB-NSCs to Calbindin positive PCs *in vitro* when cultured on feeder layers of dissociated E15.5 mouse rhombic lip tissue containing GCs (Klein et al., 2005; Muguruma et al., 2010, 2015). A following study had suggested the use of fetal cerebellum slices for the maturation of PC progenitors to attain electrophysiologically mature PCs (Wang et al., 2015b). However, adult NSCs failed to generate PCs *in vivo* and their efficiency to produce PCs *in vitro* is poor (4.3 ± 0.7%) (Klein et al., 2005)

Here it is shown that Cell_BGwt can be differentiated on Geltrex coated coverslips up to 7 days *in vitro* resulting in large neuronal bodies compared to Cell_LVwt, which is a characteristic of PCs *in vivo* (Herndon, 1963). Although BG-NSC derived cells express Calbindin in their neural extensions in contrast to LV-NSC derived cultures, only very few cells expressed Calbindin (<1%) and no cells showed mature PC morphology with dendritic branching. This could be due to the poor supporting ability of Geltrex for PC differentiation *in vitro* as adequate supporting niche reminiscent of the *in vivo* cerebellar cortex might be needed with respect to previous reports (Klein et al., 2005; Muguruma et

al., 2010, 2015; Wang et al., 2015b). In addition to structural support derived from feeder layer and slice culture systems, acellular components of cerebellar tissues including EVs can be involved in neuronal differentiation of PCs. Therefore, future research involving optimising and dissecting the cellular and acellular requirements of adult BG culture and differentiation will be necessary to uncover their PC differentiation abilities to be studied *in vitro*. Furthermore, BG differentiation into other cerebellar neurons including glutamatergic GCs and GABAergic interneurons using immunostaining experiments.

5.4.3. Nestin is an activated stem-cell state of adult BG

Nestin is known to be a marker for both slow dividing and proliferating NSCs of the adult SVZ (Faiz et al., 2015; Hendrickson et al., 2011). A recent study investigating neurogenesis in the adult cerebellum has reported a Nestin-Sox2 double positive cell present in the PCL of adult mice cerebellum (Ahlfeld et al., 2017). However, no Nestin positive cells in the PCL were found in the adult CB used in this study. Alternative analysis using Allen's Brain Atlas (https://www.brain-map.org/) resulted in mixed interpretations where Nestin RNA expression was observed in the PCL of coronal sections but not sagittal sections of adult mice cerebellum. There is also a lack of evidence for Nestin expressing BGs in the adult mammalian cerebellum under normal physiological conditions.

However, mature BG are known to express Nestin transiently in response to embryonic PC grafts in pcd mice (Sotelo et al., 1994). Additionally, studies in adult zebrafish models have shown that Nestin expression is induced in the cerebellum upon injury and that Nestin positive cells can differentiate to replace lost neurons (Kaslin et al., 2013, 2017). Recently, it has been shown that Nestin positive cells from the postnatal PCL, where BG reside, undergo adaptive reprogramming to replenish irradiated cells in the EGL of developing mouse cerebellum (Wojcinski et al., 2017). Finally, here it is shown that Nestin is detected at higher levels at both day 0 and day 7 of differentiation *in vitro* in Cell_BGwt in contrast to Cell_LVwt. These reports speculate that Nestin might be able to prime BG to an 'activated stem cell-like state' that can proliferate and produce neurons *in vivo* and *in vitro*. Future investigations using genetic lineage tracing techniques including the Cre-LoxP system can help uncover the properties of Nestin expressing adult BG with respect to activation and control of neurogenesis in the cerebellum (Dubois et al., 2006; Tsien, 2016).

5.4.4. BG can be a source of reactive glial stem cells

Reactive glia are proliferating glial cells including astrocytes and oligodendrocytes which are often found after lesion or stab wound injury in animal models (Pekny and Nilsson, 2005). These cells express NSC markers *in vivo* and have shown potential to generate neurons *in vitro* (Götz et al., 2015). However, the *in vivo* potential of reactive glia to produce neurons is still unclear. For instance, a recent study has

reported that GFAP labelled reactive astrocytes from cortical stab wound lesions generated neurospheres and produced βIII-Tubulin positive neurons, GFAP positive astrocytes and O4 positive oligodendrocytes *in vitro*, but did not produce any neurons *in vivo* (Shimada et al., 2012). In this study, BG showed hallmark properties of *in vivo* reactive astrocytes including increase in number and strong GFAP expression. However, the extent of their neurogenic potential *in vivo* is unclear. Although here it is shown that BG can produce βIII-Tubulin and Calbindin positive neurons *in vitro*, this property might not be extendable to *in vivo* without external stimulation such as genetic manipulation (Aravantinou-Fatorou et al., 2015; Faiz et al., 2015; Shimada et al., 2012). Recently, retroviral vectors carrying a NeuroD1 or Sox2 and Mash1 have been used to successfully reprogram reactive astrocytes and pericytes, respectively, into functional neurons *in vivo* (Guo et al., 2014; Karow et al., 2012). Therefore, although reactive glia are not commonly observed to produce neurons *in vivo*, future studies involving genetic manipulation of reactive BG to produce PCs and GCs can provide insights into their potential to promote recovery by cellular replacement in ataxic patients.

5.5. Conclusion

This chapter focused on characterising the cellular and acellular properties of BG-NSCs *in vitro* and *in vivo*. Here, differentiation characteristics of BG-NSCs were revealed, including their ability to express the PC specific marker Calbindin during *in vitro* cultures. Cell_BGwt were responsive to FAS and showed distinctive glial morphology with increase in S100b expression. Moreover, it was shown that BG respond to *in vivo* PC insult and show reactive glial characteristics including increase in number and GFAP expression. Furthermore, acellular properties of BG-NSCs were revealed here. Cell_BGwt derived EVs were actively taken in by 2-DN system and appears to promote neuronal outgrowth. It was also discovered that Cell_BGwt secreted a large amount of EVs compared to Cell_LVsg and Cell_LVwt. This chapter thus provided intriguing insights into the properties of BG-NSCs, which in the future, can be useful to develop therapeutic strategies for cerebellum repair.

6. Effect of low-power sonication on isolated extracellular vesicles in addition to disaggregation

6.1. Introduction

Aggregation of EVs has been reported to pose technical challenges in characterising EVs (Bosch et al., 2016; Linares et al., 2015). Recent studies have suggested low-power sonication as a useful method to disaggregate EVs prior to analysis (Ansa-Addo et al., 2010; Maas et al., 2014). Therefore, in the previous chapters, all EV samples were sonicated with low-power sonication setting (Bioruptor Diagenode) prior to characterisation and EV response studies to avoid aggregation.

Sonication of EVs has been reported to also disrupt and generate pore formation in EV membranes which has been used to load cargo into EVs (Kim et al., 2016). Also, the sonication technique is primarily used for shredding cellular structures including cell membrane, EVs, chromatin, DNA (Alvarez-Cubero et al., 2018; Hosseini-Beheshti et al., 2012; Yang et al., 2015). It is also important to note that there are inconsistencies in the final power output between ‘low-power’ modes of different sonicator instruments, which can reduce reproducibility in EV research. Given the range of physical effects of sonication on cellular structures, it is necessary to investigate the changes in functional effect of EVs due to

the sonication step used in this study 4.3.5 and 5.3.4 (EV response studies), beyond the intended effect of disaggregation of EVs.

6.2. Aims

This chapter has 3 aims.

The first aim was to investigate the changes in PSD of EVs induced by low-power sonication using the new d-STORM approach, NTA and DLS.

The second aim was to investigate the changes in membrane morphology of EVs using cryo-TEM.

The third aim was to compare sonicated and non-sonicated EVs derived from NSCs in their effect to promote neuronal outgrowth in 2DN culture.

6.3. Results

6.3.1. Effect of sonication on disaggregation of EVs analysed by TEM

To investigate the presence of aggregates and the effect of sonication upon disaggregation of EVs, samples were analysed under TEM. EV samples were fixed and embedded on EM grids as previously described (Nizamudeen et al., 2018a) unless mentioned otherwise. TEM images of EV samples on holey carbon grids showed that sonication results in a lower propensity for large aggregates to form on EM grids (Figure 6.1 A and B) compared to non-sonicated samples. To aid the visualisation of single EVs, samples were diluted (1 in 100) and embedded onto graphene oxide TEM grids. Here, sonicated EVs (sEVs) showed an increase in particles below 50 nm in size (184.67 ± 9.29 particles/3.625 μm^2) compared to non-sonicated EVs (nsEVs) (113.33 nm ± 23.02 particles/3.625 μm^2) (data presented as Mean ± SD). However, it was noted that the contrast of particles <50 nm in sEVs was reduced compared to nsEVs (Figure 6.1 C and D).

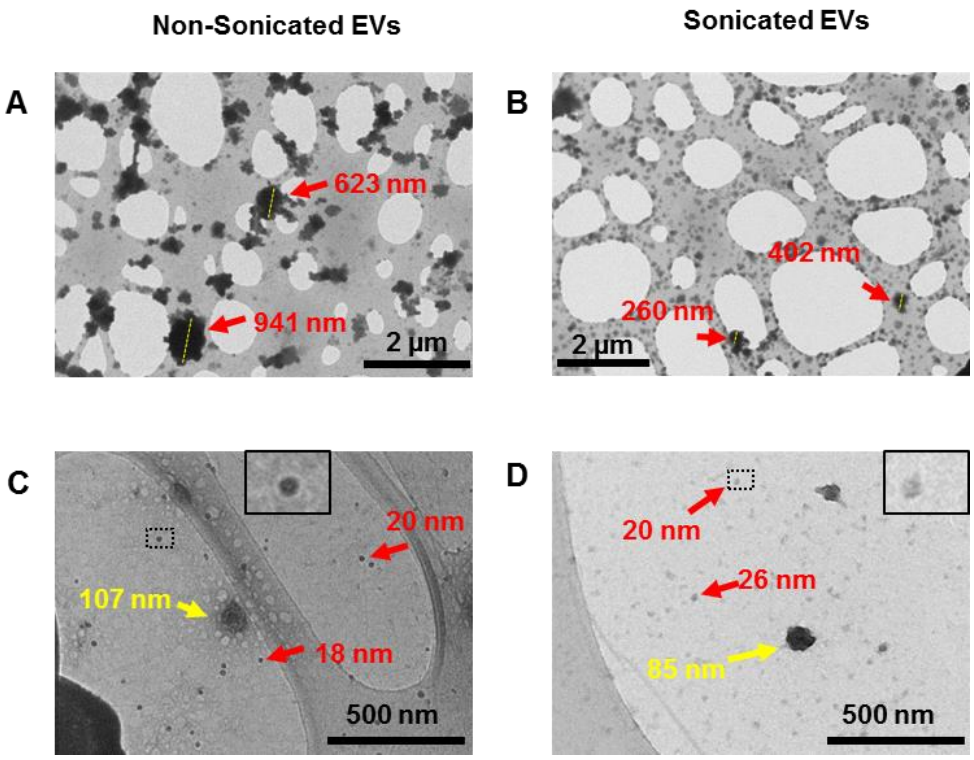


Figure 6.1: TEM images of non-sonicated (ns) and sonicated (s) EVs. (a) Non-sonicated and (b) sonicated EVs embedded onto holey carbon grids. Red arrows indicate aggregate-like structures. (c) Ns- and (d) s- EVs diluted and embedded on graphene oxide grids. Red arrows show EVs below 50 nm in size. Yellow arrows show EVs above 80 nm in size. Magnifications – (a) 11.5K, (b) 9.9K, (c), (d) 16.5K. TEM performed and images captured by KS and ZA.

6.3.2. Effect of sonication on EV distribution analysed by DLS, NTA and d-STORM imaging

To investigate if sonication resulted in changes in PSD of isolated EVs, DLS, NTA and d-STORM techniques were employed in parallel. DLS analysis displays an increase in the proportion of particles below 200 nm in size in sEVs as compared to nsEVs (Figure 7.2 A and B). Similar to DLS analysis, NTA also detected an increase in the proportion of particles below 200 nm in size for sEVs compared to nsEVs (Figure 7.2 C and D).

To confirm the suggestion by DLS and NTA techniques, d-STORM approach was used. Prior to d-STORM imaging, wide-field snapshots were taken using TIRF mode for optimal focus where sEVs showed increased background fluorescence (Figure 7.2 E and F). This suggested an increase in DiD particles with low intensity due to sonication. Subsequent d-STORM imaging detected a striking increase in particles below 50 nm in size (Mean ± SD: sEV 11.8 ± 0.5 x 10^{12}; nsEV 6.08 ± 0.5 x 10^{12}) (Figure 7.2 G and H), in line with TEM images and an overall increase in EV particle count in sEVs ((1.68 ± 0.066) x 10^{13} particles/ml) compared to nsEVs ((0.94 ± 0.074) x10^{13} particles/ml) (data presented as Mean ± SD).

DLS, NTA and d-STORM detected a reduction in the average size of EVs post-sonication, although the specific size values varied significantly between techniques (refer Table 6.1). Taken together, these results confirmed that low-power sonication increased the number of smaller EVs, particularly in the particle population below 50 nm in size.

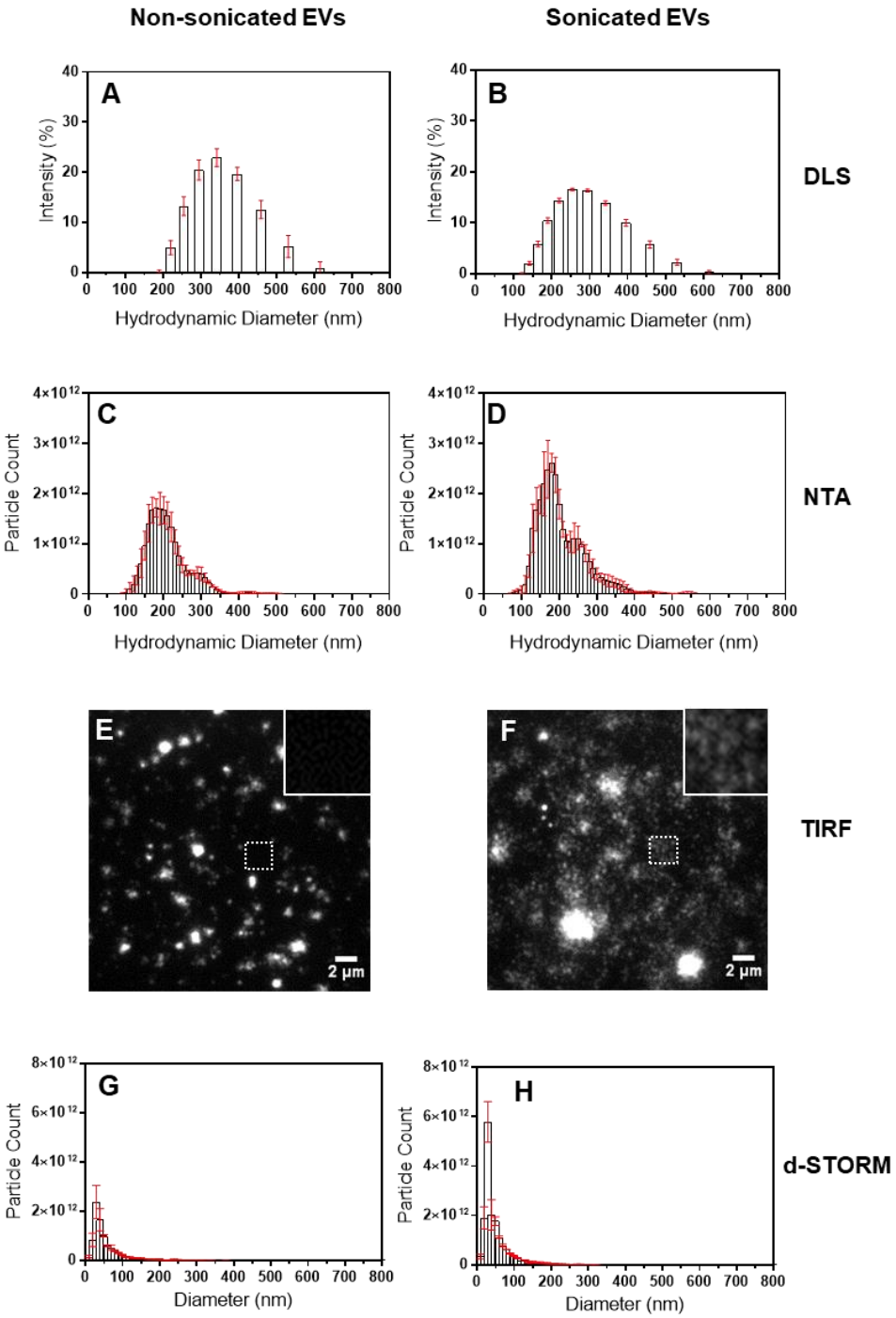


Figure 6.2: Characterisation of (A, C, E and G) ns- and (B, F and H) s- EVs by (A and B) DLS, (C and D) NTA, (E and F) TIRF and (G and H) d-STORM. (n=3, Mean ± SD)

Table 6.1: Average size of EVs calculated by DLS, NTA and d-STORM techniques

Technique	Non-Sonicated EVs	Sonicated EVs
DLS (Z. Average Hydrodynamic Diameter ± SD (nm))	346.9 ± 1.518	287.1 ± 4.085
NTA (Mean Hydrodynamic Diameter ± SD (nm))	209.9 ± 55.4	205.8 ± 63.4
D-STORM (Mean Diameter ± SD (nm))	58.77 ± 2.83	48.11 ± 1.56

6.3.3. Effect of sonication on EV membrane morphology analysed by cryo-TEM

Under cryo-TEM imaging, nsEV samples consisted of a heterogeneous population with respect to size, shape, contrast and defined border (Figure 6.3 A-D). nsEVs were observed to contain vesicular structures with a visible (vm_EV) or without visible (nvm_EV) membranes, resembling lipid-bilayered EVs and lipoproteins (Figure 6.3 A), respectively according to published reports (Yuana et al., 2013). nsEV sample contained vm_EVs of 100 to 500 nm in sizes which were either singular, multi-vesicular concentric (Figure 6.3 A) or multi-vesicular non-concentric (Figure 6.3 B) in nature with clear visibility of each membrane layers.

EVs with disorganised features near the membrane were often observed in nsEVs (Figure 6.3 A and C), which could be due to the filtration and membrane affinity-based EV isolation procedures used in this study.

Interestingly, EVs bigger than 500 nm in sizes with non-spherical shapes were also observed (Figure 6.3 C) suggesting that EVs are likely to be semi-fluid in nature, as is common with other lipid structures, and enable particles to morph, allowing passage through a 0.45 µm pore whilst maintaining its overall surface area and volume. Additionally, tubular structures with m_EV like membrane features over 2 µm in length were observed (Figure 6.3 D). These results suggested that diameter estimation analysis of EVs is restricted to spherical shaped EVs. Some m_EVs contained spot-like features within them suggesting presence of electron-dense cargo (Figure 6.3 D). The nvm_EVs observed in nsEVs showed a heterogeneous population differing in contrast and size suggesting heterogeneity within lipoprotein structures (Figure 6.3 D).

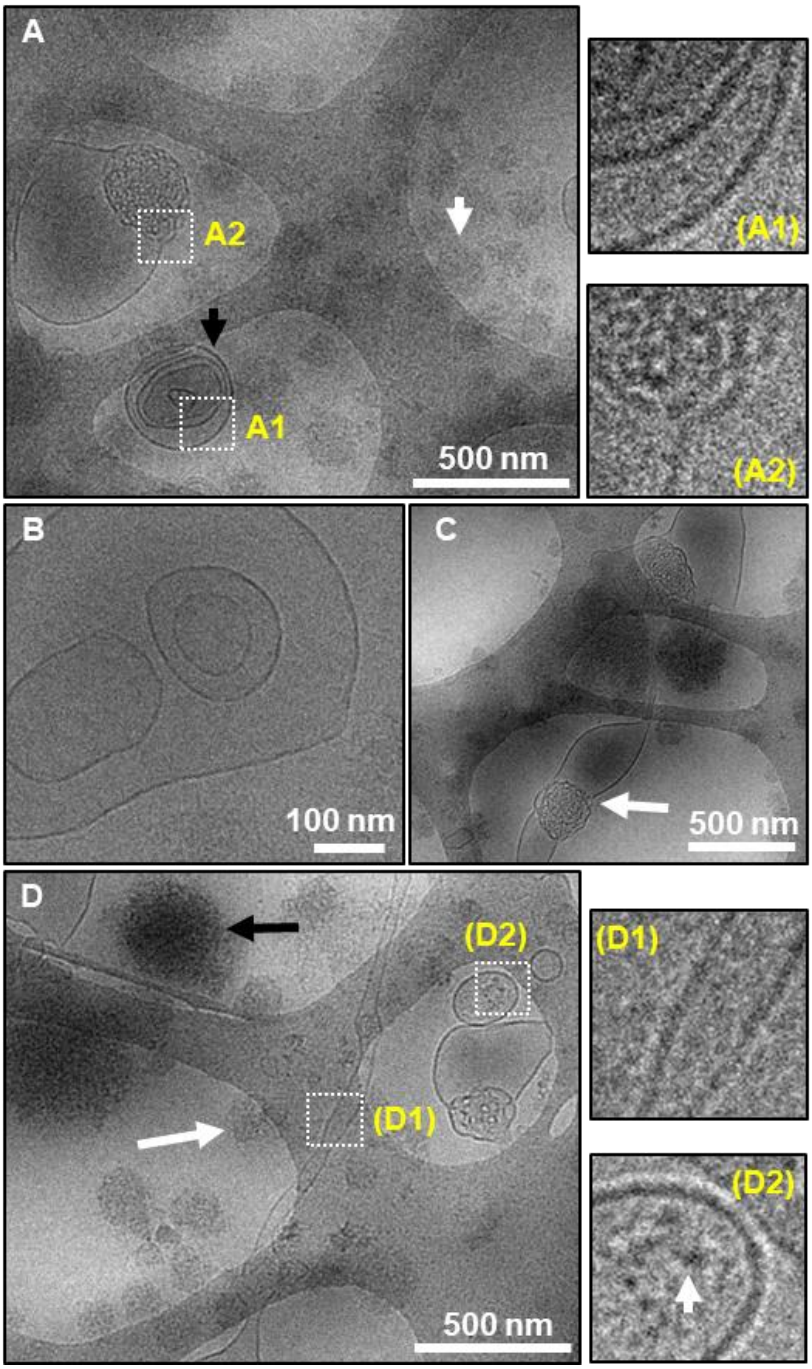


Figure 6.3: Cryo-TEM images of non-sonicated MSC-derived EV samples. (A) Image showing multiple EVs with (black arrow) or without (white arrow) a clear membrane border. Zoomed in area showing (A1) an EV with multiple concentric EVs inside it and (A2) an EV with membrane disorganisation. (B) A multi-vesicular non-concentric EV. (C) Image showing an EV structure bigger than 500 nm in size with disorganised shape and membrane. (D) Image showing (D1) a tubular EV-structure with defined border and (D2) an EV with electron-dense features inside (Arrow in zoomed in image of (D1) shows features with high electron contrast within an EV). Arrows in (D) show round structures with no clear membrane either with (black arrow) high electron contrast or (white arrow) low electron contrast. Cryo-TEM performed by CP (assisted by ZN). Images captured by CP.

Similar to nsEVs, sEVs contained a heterogeneous population of nvm_EVs (Figure 6.4 A) and smaller vm_EVs of 20 nm in sizes were observed (Figure 6.4 B). However, in contrast to nsEVs, larger vm_EVs were rarely found (Figure 6.4 A and B) suggesting that sonication resulted in reduction of vm_EVs of 100 to 500 nm in size. Also, in some 200 nm vesicular structures, a vesicular membrane border with low contrast was noted, suggesting membrane damage (Figure 6.4 C and D). These results suggest that low-power sonication can have damaging effects on a sub-population of EVs that show defined membrane under cryo-TEM, which can ultimately result in bias in EV characterisation towards nvm_EVs, which have been confirmed to be lipoproteins (Karimi et al., 2018; Yuana et al., 2013; Zabeo et al., 2017) by recent studies.

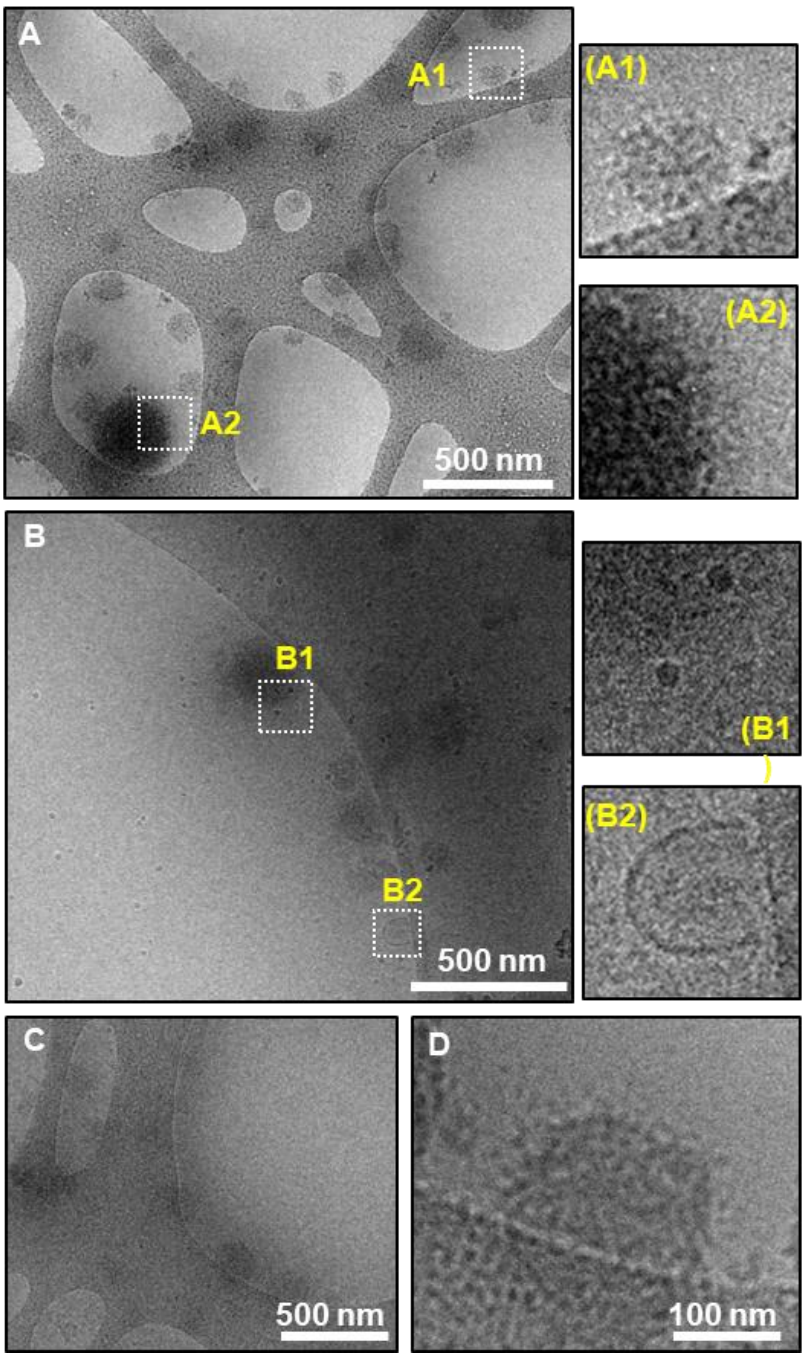


Figure 6.4: Cryo-TEM images of sonicated MSC-derived EV samples. (A) Image showing multiple EVs without a clear membrane border having either (A1) low contrast or (A2) high contrast. (B) Image showing (B1) multiple 20 nm sized EVs with border-like features and (B2) portion of an EV structure with clear membrane border. (C) Image showing EV-like structures with faint membrane border (arrow). (D) Higher magnification image of arrowed object in (C). Cryo-TEM performed by CP (assisted by ZN). Images captured by CP.

6.3.4. Flow cytometry analysis of cellular uptake of sonicated vs non-sonicated EVs

To investigate if the changes in size and morphology of EVs due to sonication resulted in a differential functional effect, MSCs cultured in 6 well tissue culture plates were incubated with nsEVs or sEVs (for 6 hours) of the same number (1 x 10^{10} particles per 9 cm^2; as counted by d-STORM) or the same volume (5 µl per 9 cm^2) (Figure 6.5). Since d-STORM has revealed an increase in particle count after sonication of EVs, sEV samples will contain more particles per volume compared to nsEV samples, which could account for increase in cellular uptake of particles. Samples were then trypsinized and analysed using flow cytometry. It was observed that MSCs incubated with sEVs had lower population of DiD positive cells compared to MSCs incubated with nsEVs when added at both, the same amount (Figure 6.5 A and B) as well as the same volume (Figure 6.5 C and D). This indicated that low-power sonication reduced the efficiency of uptake of EVs by MSCs in culture.

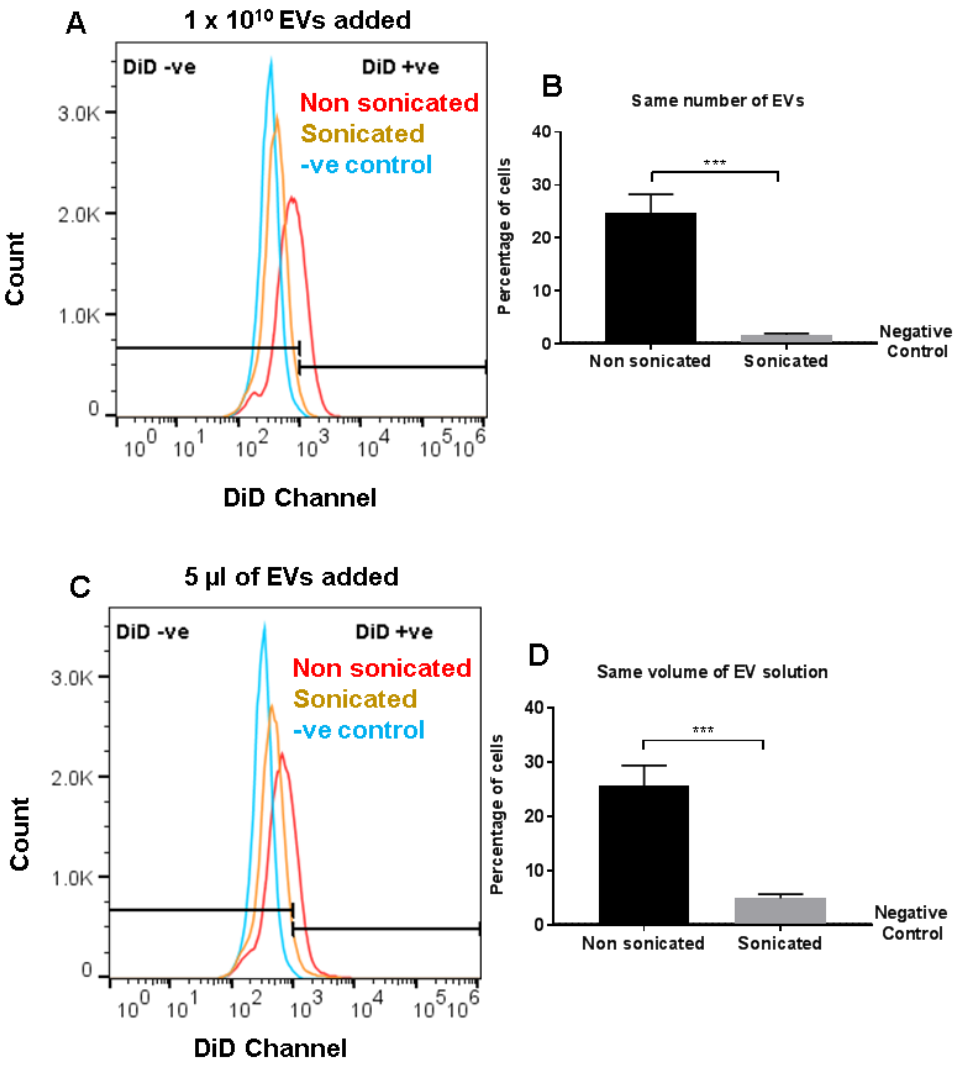


Figure 6.5: Cellular uptake of EVs by MSCs analysed by flow cytometry. DiD-labelled EVs added at (A and B) 1 x 10^{10} particles per 9 cm^2 or (C and D) 5 µl per 9 cm^2. (A and C) Histogram plot of fluorescence detected in live cells after EV incubation compared to negative control (MSCs with no EVs added). (B and D) Quantification of cells containing EVs after 6-hour incubation. Students t test, (Mean ± SD), n =3 (*) p<0.05. Flow cytometry performed by DO, analysed by ZN.

6.3.5. Neuronal response, cellular uptake and localisation of sonicated vs non-sonicated NSC derived EVs in a 2-D neuronal culture system

To further investigate the functional differences between the nsEVs and sEVs, the EV response study from previous sections (5.3.4 and 4.3.5) were repeated with non-sonicated (ns-) EVs isolated from Cell_LVwt_D0

and Cell_BGwt_D0 and compared with sonicated (s-) EVs. Experimental set up was similar. Briefly, DiD- labelled EVs from undifferentiated BG- and LV-NSCs were isolated and divided into sonicated and non-sonicated groups. EVs were added to 2DN culture system (Cell_LVwt_RET) from day 4 to day 10 where medium was refreshed with fresh EVs every 48 hours. Note: Please refer to table 2.1 for nomenclature; a prefix of ‘s’ or ‘ns’ will be used here to denote sonicated and non-sonicated samples, respectively.

Metabolic analysis showed that nsEVs from both, Cell_LVwt_D0 and Cell_BGwt_D0, at 0.1x concentration, increased the metabolic activity of 2-DN cultures, similar to their sEV counterparts, compared to no EV controls (Figure 6.6 A). No significant difference was observed between the metabolic activity of 2-DN cultures incubated with sEVs and nsEVs from both LV- and BG-NSCs (Figure 6.6 A). Brightfield images showed the presence of neuronal bodies in all nsEV and sEV treated cultures (Figure 6.6 B).

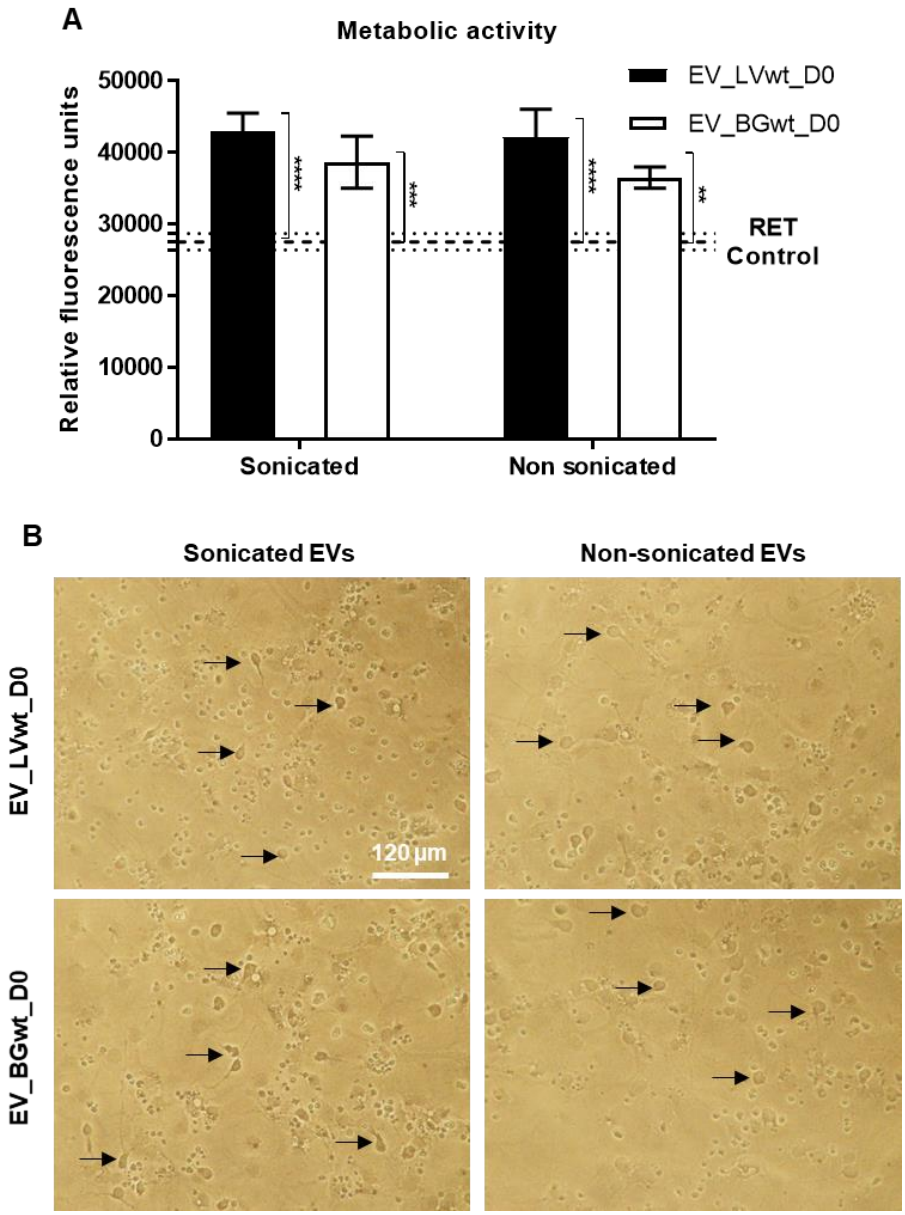


Figure 6.6: (A) Metabolic assay and (B) brightfield imaging of Cell_LVwt_RET under the incubation of 0.1x concentration of sonicated vs non-sonicated EVs derived from Cell_LVwt_D0 and Cell_BGwt_D0 (day 10). Black arrows show neuronal bodies. One-way ANOVA Tukey's multiple comparison test, (Mean ± SD), n=3, (*) p<0.05.

To assess the changes in neuronal outgrowth, samples were stained with βIII-Tubulin and counted for cells associated with 5 or more neuronal extensions (5x neurons). 2-DN cultures treated with sEVs from LV- and BG-NSCs showed increase in the number of 5x neurons compared to no EV treated controls (Figure 6.7 A-C and F), consistent with previous

observations. Interestingly, significant background detection for βIII-Tubulin was observed in sEV_LVwt_D0 treated cells compared to other samples (Figure 6.7 B). 2-DN cultures treated with nsEVs from LV- and BG-NSCs did not show any increase in the number of 5x neurons compared to no EV treated controls (Figure 6.7 D-F). These results suggested that sonicated EVs, when added to 2-DN, did not promote drastic changes in the metabolic activity or the number of neuronal bodies in culture but promoted significant changes in the neuronal outgrowth of neurons in 2-DN cultures, in contrast to the effect of non-sonicated EVs.

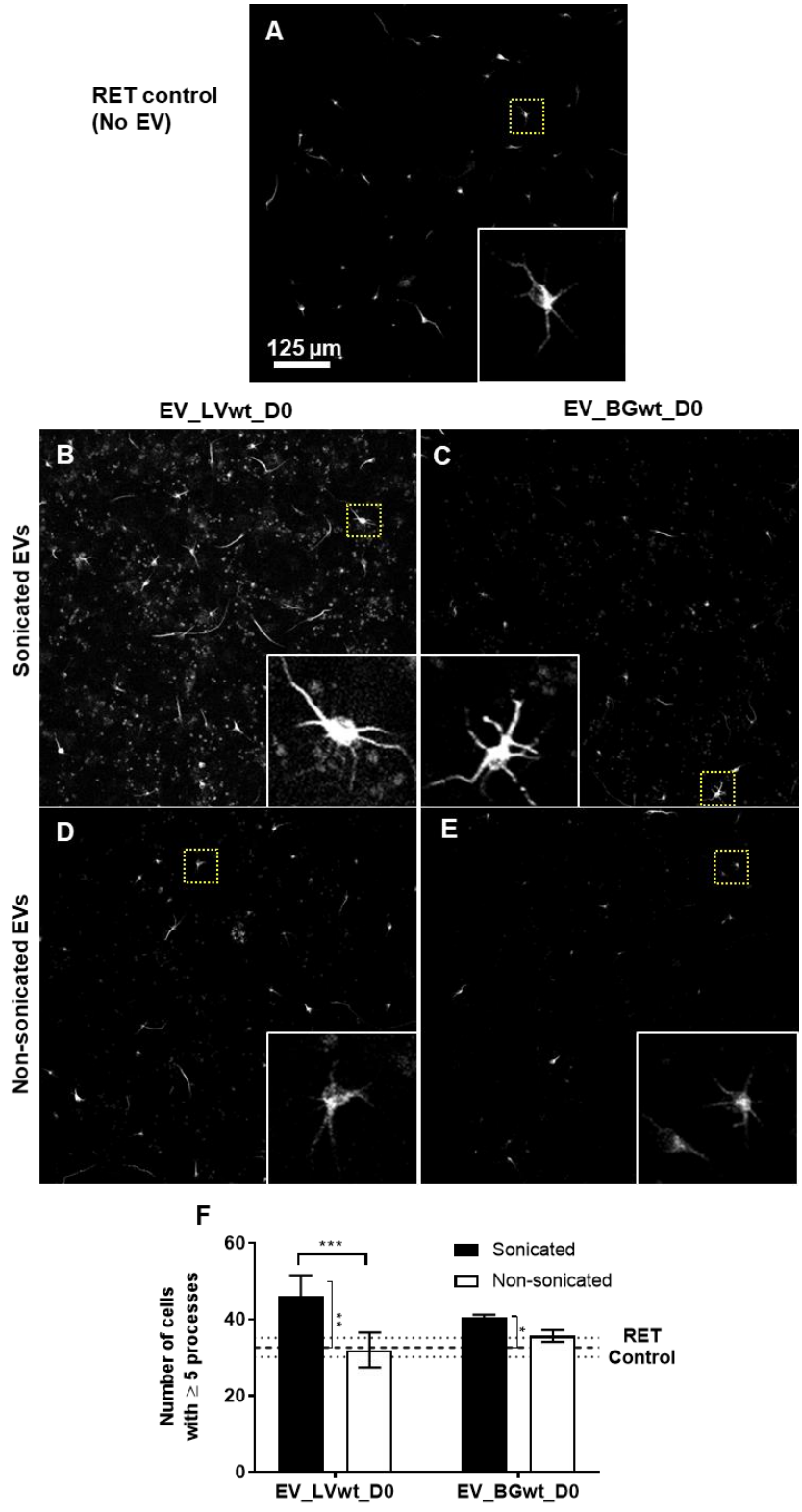


Figure 6.7: Changes in number of neuronal processes upon addition of sonicated (s-) vs non-sonicated (ns-) NSC-derived EVs (day 10). Immunofluorescence images of βIII-Tubulin positive cells of Cell_LVwt_RET culture in (A) no EV added controls, (B) sEV_LVwt_D0 added, (C) sEV_BGwt_D0 added, (D) nsEV_LVwt_D0 added, and (E) nsEV_BGwt_D0 added samples (day 10). Zoomed in boxes show neurons with multiple processes. (E) Quantitation of cells with ≥ 5 processes. One-way ANOVA Tukey's multiple comparison test, (Mean ± SD), n=3, (*) p<0.05.

Next, intercellular localisation of EVs was assessed. Immunohistochemical analysis showed that nsEV_LVwt_D0 were localised to βIII-Tubulin positive, GFAP positive, and largely to βIII-Tubulin and GFAP double negative cells in the 2-DN cultures (Figure 6.8 A-D). ImageJ particle analysis showed that DiD intensity was higher in 2-DN cultures incubated with sEV_LVwt_D0 compared to their non-sonicated counterparts (Figure 6.8 E-G). However, the total number of DiD positive particles were significantly higher in 2-DN cultures incubated with nsEV_LVwt_d0 compared to their sonicated counterparts (Figure 6.8 E, F and H).

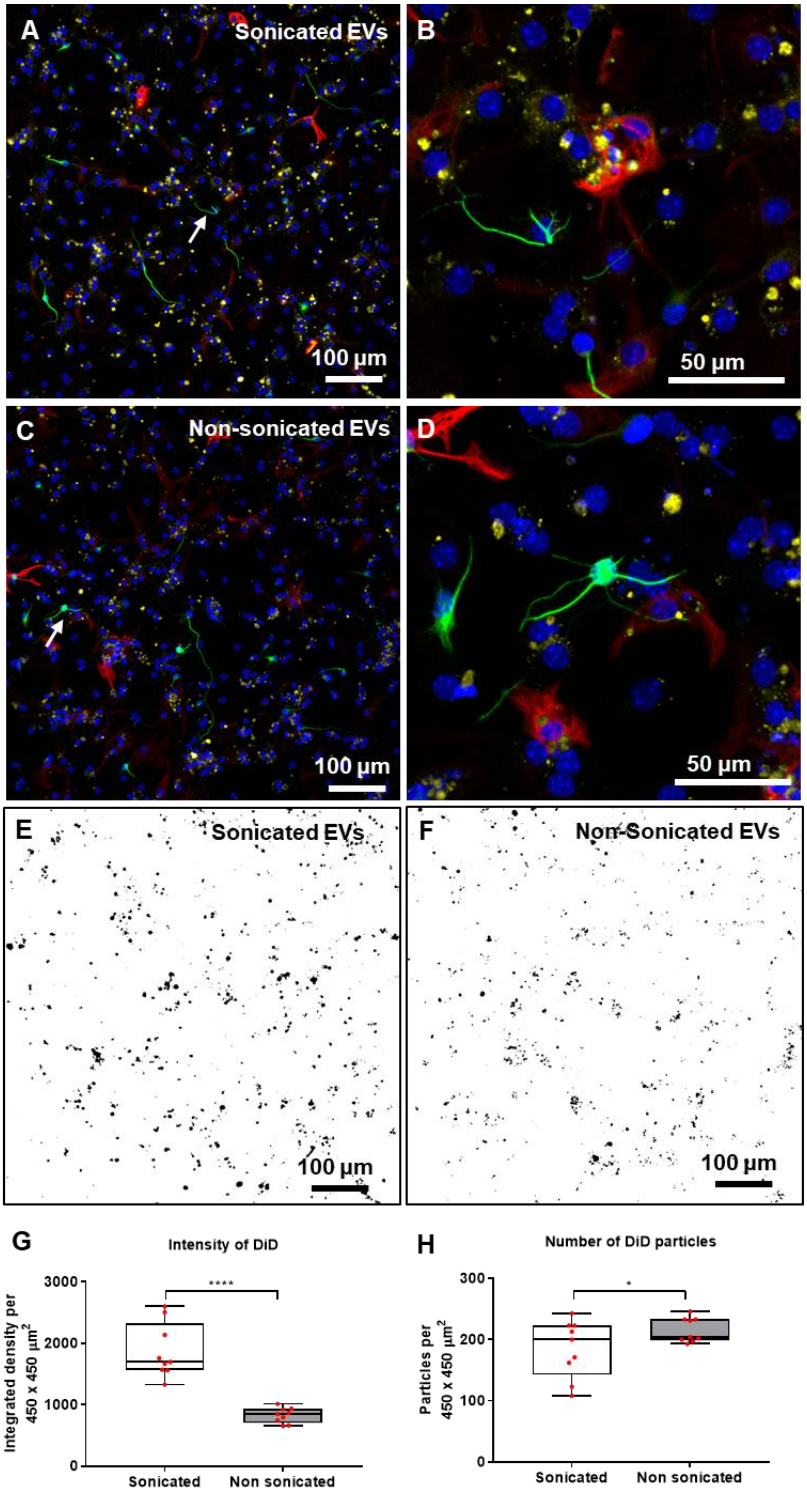


Figure 6.8: Immunofluorescence images of EV_LVwt_D0 uptake by Cell_LVwt_RET (day 10). βIII-Tubulin (green), GFAP (red) and DiD (yellow) in neuronal cultures of Cell_LVwt_RET incubated with (A) sonicated ((B) zoomed in image of arrow marked area from (A)), and (C) non-sonicated ((D) zoomed in image of arrow marked area from (C)) EV_LVwt_D0. ImageJ thresholding of DiD channel for (E) sonicated (in (A)) and (F) non-sonicated (in (C)) EVs taken up by Cell_LVwt_RET. (G-H) Quantitation of (G) DiD intensity and (F) number of DiD particles in (E) and (F). ImageJ thresholding: Min 40, Max 255. Students t-test, one-tailed, (Mean ± SD), n=9, (*) p<0.05.

Subsequent analysis of EV response in 2-DN cultures for EV_BGwt_D0 showed that both s- and ns-EVs were localised in majority of cells in the 2-DN cultures similar to EV_LVwt_D0 (Figure 6.9 A-D). It was also observed that DiD intensity as well as particle number was higher in 2-DN cultures incubated with nsEV_BGwt_D0 compared to their sonicated counterpart (Figure 6.9 E-H). This suggested that low-power sonication of NSC-derived EVs resulted in reduced cellular uptake of EVs in the 2-DN cultures. Note: 3D imaging was not done here and therefore, colocalization of DiD-labelled EVs with DAPI (on nuclei or perinuclear), βIII-Tubulin or GFAP was used as a surrogate measure of cellular uptake.

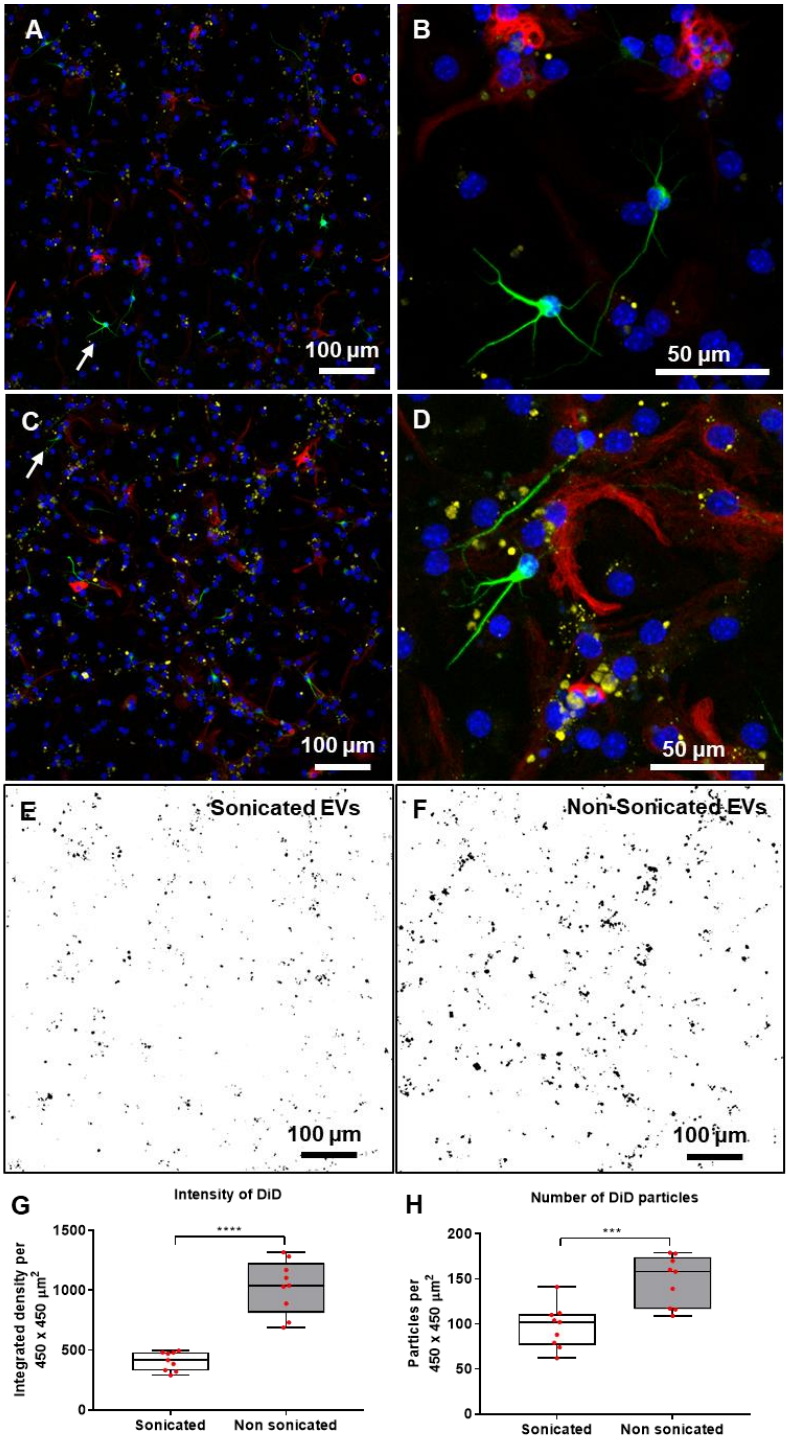


Figure 6.9: Immunofluorescence images of EV_BGwt_D0 uptake by Cell_LVwt_RET (day 10). βIII-Tubulin (green), GFAP (red) and DiD (yellow) in neuronal cultures of Cell_LVwt_RET incubated with (A) sonicated ((B) zoomed in image of arrow marked area from (A)), and (C) non-sonicated ((D) zoomed in image of arrow marked area from (C)) EV_BGwt_D0. ImageJ thresholding of DiD channel for (E) sonicated (in (A)) and (F) non-sonicated (in (C)) EVs taken up by Cell_LVwt_RET. (G-H) Quantitation of (G) DiD intensity and (F) number of DiD particles in (E) and (F). ImageJ thresholding: Min 40, Max 255. Students t-test, one-tailed, (Mean ± SD), n=9, (*) p<0.05.

6.4. Discussion

6.4.1. EVs are a heterogeneous population containing vesicles with varying shape and membrane properties.

In addition to protein heterogeneity, EVs isolated from cells and tissues have been reported to be highly heterogeneous in nature with variations in cargo, size, shape, morphology and structure (Höög and Lötvall, 2015; Karimi et al., 2018; Marcoux et al., 2016; van Niel et al., 2018; Willms et al., 2018; Zabeo et al., 2017). EVs including exosomes are generally known to consist of a lipid bilayer membrane, similar to their parent cell membrane (Villarroya-Beltri et al., 2014). However, lipid structures analysed using d-STORM and spherical structures observed under EM might not all be lipid bi-layered vesicles. EM images of MSC-derived EVs showed presence of a large amount of spherical structures without a cup-shaped morphology under TEM, nor a clear visible lipid membrane under cryo-TEM. Based on morphological and protein assays, recent reports have suggested that these structures are lipoproteins, which range between 5 to 1200 nm in size, primarily transport lipids, and are usually co-isolated with lipid bi-layered EVs from biological fluids (Karimi et al., 2018; Yuana et al., 2013). Future studies can use density cushion size exclusion chromatography columns to purify bi-layered EVs from lipoproteins in EV isolates and reveal functional differences between them (Karimi et al., 2018). Furthermore, cryo-TEM experiments showed that EV samples contained multi-vesicular, tubular and non-spherical

vm_EVs as reported in recent reports (Höög and Lötvall, 2015; Yuana et al., 2013; Zabeo et al., 2017). Interestingly, it was noted that EVs might possess a semi-fluidic nature as EVs of 500 to 1000 nm in sizes have passed through the 450 nm filtering step and also contain tubular vm_EVs of over 2 µm in length. On the other hand, these effects might be due to a damaging influence of membrane-affinity columns on EV membrane properties during isolation procedure, compared to density cushion ultracentrifugation isolation of EVs (Yuana et al., 2013; Zabeo et al., 2017). Nevertheless, it is unclear whether the shape of vm_EVs are related to any of their differential functionality. However, future d-STORM and cryo-TEM experiments in combination with immuno-tagging of protein molecules might be able to investigate the dependence of shape in the diversity of biological EVs.

6.4.2. Sonication of EVs may bias the EV sample towards lipoproteins

Low-power sonication has been generally used to promote disaggregation of isolated EVs prior to analysis (Ansa-Addo et al., 2010; Maas et al., 2014). However, there is a lack of studies reporting the optimal sonication settings for EV research. Here it was observed that the lowest power option of Bioruptor sonicator with 3 x 10 second cycles, which was attempted to disaggregate EVs, was enough to reduce the number of vm_EVs, possibly through membrane damage. A study investigating exosomal delivery of Tau protein in primary neurons has reported that sonication of exosomes using Sonoplus Ultrasonic

homogenizer at 20% amplitude for 10 seconds can inhibit their cellular uptake and delivery (Wang et al., 2017). This suggests that disruption of EV membrane by sonication may lead to inhibition of its structural and biological functions. Interestingly, it was shown here that sonication of EVs lead to increase in neuronal outgrowth in NSCs, in contrast to their non-sonicated counterparts, suggesting that sonication can promote positive as well as negative effects on recipient cells.

It was also noted that nvm_EVs which correspond to lipoprotein structures according to previous reports (Yuana et al., 2013), did not show similar disfigurement or reduction due to low-power sonication, suggesting that vm_EV might be more sensitive to low-power sonication compared to other nvm_EVs. A recent study has reported the use of 10-minute sonication prior to NTA analysis of EVs, and the TEM images of EV samples showed low-contrast vesicular structures positive for exosomal marker-TSG101, and therefore were considered as exosomes (Martins et al., 2018). Here it was shown that sEVs from MSCs are positive for TSG101 but lack CD63 (shown by dot blot) and vm_EVs (shown by cryo-TEM). It is possible that sonication resulted in loss of m_EVs and that TSG101 can be expressed by lipoprotein EVs, thereby providing false-positive results for vm_EV confirmation. An independent study has suggested that non-cup-shaped-low contrast structures under TEM, and nvm_EVs under cryo-TEM, are likely to be lipoproteins co-isolated with EVs which mimic the size range and protein markers of exosomes (Karimi et al., 2018; Yuana et al., 2013). This suggests that

non-optimised sonication might bias sample analysis to lipoproteins by reducing the number of vm_EVs

6.4.3. Unmonitored sonication leads to variability in EV research

This study shows that low-power sonication (used at Bioruptor Diagenode's settings) can induce functional changes to isolated EVs. MSC-derived sEVs showed reduction in cellular uptake as confirmed by flow cytometry analysis, compared to their nsEV counterparts. A similar observation was made in NSC-derived EVs response study where total DiD particles taken in by cells were lower when sEVs were used compared to nsEVs. Moreover, nsEVs derived from NSCs did not promote improved neuronal outgrowth of 2-DN cultures, in contrast to their sEVs counterparts. This suggested that the changes on EVs induced by low-power sonication had an overall positive effect on neuronal differentiation. For now, it is unclear whether reduction of membrane bi-layered EVs or release of EV cargo had promoted the neuronal outgrowth.

Additionally, an interesting observation was made here that requires further investigation. Here it was also shown that DiD detection intensity (in 2DN culture during EV response studies) did not always correlate with number of DiD particles. 2-DN cultures showed stronger DiD detection when incubated with sEV_LVwt_D0 when compared to their nsEV counterparts, although they contained a lower number of DiD particles compared to nsEVs. Moreover, contrastingly, 2-DN cultures incubated

with sEV_BGwt_D0 showed lower DiD particle as well as intensity detection, compared to their nsEV counterparts. One possible reason could be that majority of DiD-labelled EVs can be recruited via the endosomal pathway into the lysosomal compartments for degradation or recycling via phagocytosis, micropinocytosis or receptor-/raft-mediated endocytosis (McKelvey et al., 2015). This can lead to accumulation of DiD-labelled lipid molecules in subcellular organelles which may result in changes in detected intensity and size due to accumulation of DiD. It is unclear whether low-power sonication induces a change in EV trafficking after uptake by 2-DN cultures and if this is depending on the source of EVs- from LV- or BG-NSCs. However, as mentioned earlier, future immunostaining experiments including co-localisation of EVs with endosomal markers such as ESCRT proteins, and lysosome markers such as LAMP-1 or Lysotracker kit (Invitrogen) will provide further information on the fate of added NSC-derived EVs in neuronal cultures.

Taken together, this suggests that non-optimised sonication without cryo-EM confirmation, may lead to variability in EV research including its biomarker expression and biological functions. Therefore, there is a need for considering the standardisation and outcome of sonication as a technique to disaggregate EVs, along with proteomic and immunoblotting analysis purified lipoproteins, to reduce variability in functional studies in the field of EV biology. Nevertheless, these results suggested that BG-NSC derived EVs can promote neuronal outgrowth and that low-power sonication used in this study is crucial for this effect.

6.5. Conclusion

This chapter focused on the investigating the effect of low-power sonication of EVs and its effect on the PSD, membrane morphology and cellular uptake of NSC-derived EVs by an *in vitro* neuronal culture system. It was revealed that low-power sonication can promote unintended effects such as increase in smaller particles, disruption of EV membrane, and decrease in cellular uptake of EVs. Finally, it was also revealed that low-power sonication was crucial for NSC-derived EVs to induce neuronal outgrowth in a 2DN culture system.

7. Concluding discussion and future perspectives

7.1. Investigating the effect of fasudil on primary NSCs

Fasudil is a clinically accepted ROCK inhibitor used for treating neurological disorders including SAH (reviewed in Chen et al., 2013). It has been recently shown the potential to differentiate C17.2 cerebellar neural progenitor cells (Chen et al., 2015), and mobilize SVZ-NSCs *in vivo* (Ding et al., 2010), suggesting that NSCs are responsive to fasudil. This project further explored the effect of fasudil on primary NSCs from the SVZ, the LV-NSCs, and NSCs from the cerebellum, the BG-NSCs.

7.1.1. Fasudil as a pro-neuroglial agent to investigate gliogenesis *in vitro*

Here it was shown that fasudil treatment promoted a radial-gliogenic phenotype in LV-NSCs *in vitro*. FAS-treated postnatal Cell_LVsg underwent INM-like migration and expressed high levels of the glial marker GFAP at day 2 *in vitro*. Moreover, FAS-treatment showed reduced expression of the neuronal marker βIII-tubulin in postnatal Cell_LVsg, compared to their RET treated counterparts. Prolonged FAS-treatment in adult Cell_LVsg showed similar effects as well. FAS-treatment increased S100b expression of Cell_BGwt which showed complex glial morphology compared to their RET treated counterparts.

These results suggested that fasudil primarily promoted a gliogenic phenotype of primary NSCs. Future research will focus on in-depth characterisation of glial phenotypes produced by FAS-treated LV-NSCs using multiple astrocyte markers including GLAST and ALDH1L1 (Perego et al., 2000; Yoon et al., 2017), and oligodendroglial markers including MBP, Olig1/4 and NG2 (Robinson et al., 2014).

Also, FAS-treated LV-NSCs can provide as 2-D model to investigate INM-like migration of neural cells *in vitro*, a biomechanical phenotype shown by developmental radial glia *in vivo* (Glaser and Brüstle, 2005; Spear and Erickson, 2012b, 2012a). On the other hand, FAS-treated C17.2 cells differentiated into βIII-tubulin positive neurons and did not show properties of radial-like glia, consistent with previous observations (Chen et al., 2015). This suggested that the radial-like gliogenic differentiation effect of fasudil might be specific to LV-NSCs and can depend on the cell of origin. This study did not look into the migratory properties of BG-NSCs during FAS-treatment. Therefore, further research in testing the effect of fasudil on multiple NSC and neural progenitor populations from the CNS will be necessary to reveal the differential effect of fasudil on neurogenesis in different regions of the CNS.

7.1.2. Rho-ROCK cascade as an NSC modulating signalling pathway

The results from this study also suggest that fasudil's target, the Rho/ROCK cascade, could be an important NSC regulatory pathway.

Activation of ROCK has been reported to result in decreased axonal regeneration which causes variety of neurological dysfunctions (Liu et al., 2015b), but its role in neurogenesis is largely unknown. Given that SVZ-NSCs were responsive to fasudil both *in vivo* (Ding et al., 2010) and *in vitro*, it can be speculated that ROCK can modulate NSC behaviour. Indeed, several ROCK inhibitors including C3, Y27632 and fasudil have shown to improve symptoms associated with neurological dysfunctions including spinal cord injury and ischaemia (Kubo et al., 2008). Also, other ROCK inhibitors including C3 transferase and Y27632 have been reported to promote differentiation of NSCs *in vitro* (Gu et al., 2013; Jia et al., 2016).

By exploring the differentiation effect of the ROCK inhibitor, fasudil, this study supports the previously suggested hypothesis that Rho-ROCK pathway can regulate NSCs. However, this study did not include the investigation of the signalling pathways modulated by fasudil to promote its effect on NSCs. Therefore, future experiments comparing the effect of multiple ROCK inhibitors, analysing downstream signalling pathways affected by ROCK inhibition *in vitro* and *in vivo*, would shed light into the possible role of Rho-ROCK cascade in NSC homeostasis. Furthermore, fasudil has also been suggested to inhibit other functional kinases including protein kinase N1, protein kinase C, cyclic nucleotide dependant protein kinases (PKA and PKG) and Ca2+/calmodulin dependant MLC kinase in a concentration dependant manner, which can result in off-target effects with respect to ROCK inhibition (Asano et al., 1989; Dugan et al., 1999; Fajardo et al., 2014; Scott, 1991). It will

therefore be necessary to investigate to what extent ROCK inhibition might be the main mechanism for the fasudil-mediated gliogenic differentiation observed in NSCs, in order to further exploit this pharmacological pathway and its potential to regulate and control stem cell populations for CNS repair strategies.

7.2. D-STORM approach can be used to study EVs

EVs are being considered as one of the most important cell-cell communication mechanisms in the body (reviewed in van Niel et al., 2018). However, due to wide range of EVs secreted by cells, ranging approximately from 30 nm to 1 µm, it is quite challenging to characterise EVs isolated in the lab (reviewed in van Niel et al., 2018). Particularly, the gold standard techniques of EM have been reported to be time consuming and lead to variability in EV research, and the conventional high-throughput techniques have posed technical challenges in sensitivity due to sample heterogeneity in size (Anderson et al., 2015; Dragovic et al., 2011; Erdbrügger and Lannigan, 2016; Filipe et al., 2010; Gardiner et al., 2013). This project aimed to provide an alternative solution to characterise EVs using an approach that used lipid dye (DiD) and d-STORM super resolution imaging technique, that could address the limitations of conventional techniques used to characterise EVs (Figure 7.1).

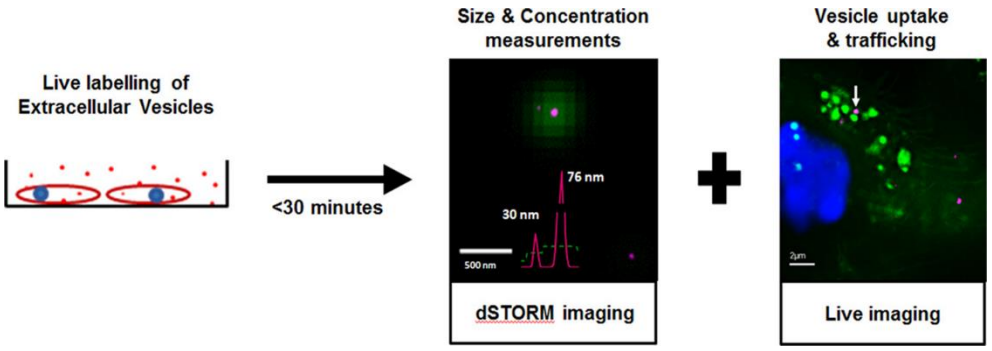


Figure 7.1: Schematic flowchart of the d-STORM approach used in this study to characterise EVs. D-STORM: direct Stochastic optical reconstruction microscopy, EV: Extracellular vesicles.

7.2.1. D-STORM proves advantageous over conventional high-throughput techniques for EV characterisation

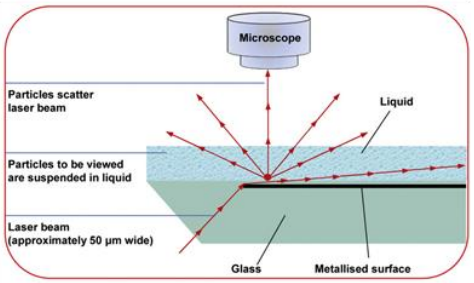
Here it is shown that d-STORM was able to locate DiD-labelled EV isolated from MSCs and NSCs, and provide PSD and particle count in a rapid and sensitive manner. Using the commonly used conventional techniques including TEM, NTA and TRPS, samples were confirmed to contain EVs. By comparing the experimental time between techniques, d-STORM provided an advantage over conventional techniques as it took less than 30 minutes to image and produce results. Given the resolution limit of approximately 20 to 30 nm (Rust et al., 2006), d-STORM was an efficient alternative to conventional techniques for quick EV characterisation for PSD and concentration. On the other hand, the DiD-labelling was shown to be a reliable marker for all isolated EVs (Shim et al., 2012). Moreover, DiD-labelled EVs were actively taken up by cells in culture, which could be tracked using confocal imaging and live-imaging. Here, it was also demonstrated how d-STORM approach can

be used to monitor changes in EV secretion rate and EV size during differentiation of NSCs *in vitro*, highlighting the downstream applicability of the approach. Future research will be focused on developing the d-STORM approach by including co-localisation of DiD with EV specific markers such as CD63, CD89, TSG101 and CD9 to confirm the purity, nature and heterogeneity of EVs labelled with DiD.

Interestingly, here, d-STORM analysis showed that majority of EVs were under 100 nm in size, in contrast to analysis by conventional techniques. It is important to consider the differences in the working principle of each technique used (Figure 7.2). TEM is a direct visualisation technique where the sample processing steps including fixing and dehydration can promote undesired morphological changes on EVs (Momen-Heravi et al., 2012). Cryo-TEM avoids fixation but immediate blotting prior to cryo-plunging of EM grids in cryo-TEM sample preparation can promote dilution effect of EV sample size on grids which can introduce reduction in EV population that is to be imaged. NTA and TRPS are indirect techniques which can be limited in sensitivity of detection of EVs due to the high polydispersity in size in an EV isolate (Anderson et al., 2015; Dragovic et al., 2011; Erdbrügger and Lannigan, 2016; Filipe et al., 2010; Gardiner et al., 2013). The d-STORM approach used here, for instance, is based on the efficiency of the photo-switchable molecules to bind EVs and the assumption that all DiD positive EVs are electrostatically pulled down on the poly-L-lysine coated glass-bottom dish surface prior to imaging. Future technical developments will investigate the fluorescent properties of DiD molecule and optimise the surface coating of glass

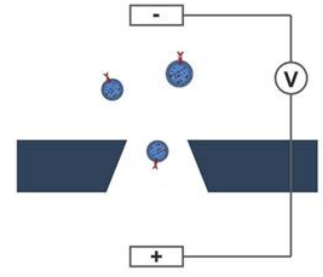
dishes to further validate the reproducibility of the d-STORM approach.

Nanosight (NTA)



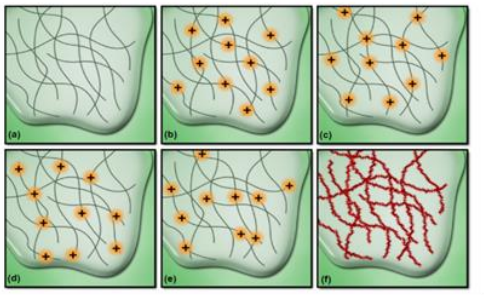
The differential scattering of light by EVs in Brownian motion allows them to be tracked in real time. NTA is high-throughput but has limited range as larger EVs will scatter more light and underestimate the presence of smaller EVs.

qNANO (TRPS)



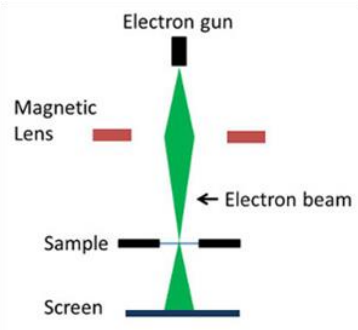
The differential blocking current by EVs when they pass through nanopores allows them to be detected. TRPS is high-throughput but as limited range per analysis due to nanopore size per run.

STORM



The fluorescently tagged EV membrane allows it to be imaged using fluorescence imaging. D-STORM is high-throughput, provides increased resolution (upto 20 nm). STORM has good range and speed but does not provide structural information of EVs

EM



Provides the best resolution to visualise EVs for structural analysis but is not high-throughput

Figure 7.2: Summary of EV characterisation techniques used in this study, with their key advantages and disadvantages. NTA: Nanoparticle tracking analysis, TRPS: Tunable resistive pulse sensing, d-STORM: direct Stochastic optical reconstruction microscopy, EM: Electron microscopy. (NTA and TRPS images adapted from Dragovic et al., 2011; Maas et al., 2014, respectively). STORM image adapted from www.microscopyu.com (Nikon).

7.2.2. Methods of choice for characterising EVs

Here it was observed that low-power sonication can shift the PSD of EV isolates to smaller sizes, as described by results from d-STORM, NTA and DLS, supporting the general assumption that low-power sonication promotes disaggregation of large clumps of EVs. However, under cryo-TEM imaging, it was found that low power sonication reduced the amount of vm_EVs, suggesting a damage to EV lipid membrane, and sample bias towards lipoprotein-like structures (Yuana et al., 2013). Taken together, the results speculate that low-power sonication resulted in fragmentation of larger vm_EVs which were detected as smaller EVs and promoted a shift in PSD when observed under d-STORM, NTA and DLS. This ultimately suggests that a combination of techniques is crucial to accurately characterise EVs. Future work, for instance, can focus on characterising the PSD and concentration using d-STORM, morphological properties using cryo-TEM, and cargo properties using protein detection (immuno-electron/d-STORM/blot). This could ultimately contribute to establishing technical assessments needed to characterise EVs and provide for the better understanding of EV biology (Lötvall et al., 2014).

7.3. Bergmann glial stimulation as a potential cerebellum repair strategy

Over the last fifteen years, multiple studies have supported the presence of NSCs in the adult cerebellum (Ahlfeld et al., 2017; Alcock and Sottile, 2009; Klein et al., 2005; Lee et al., 2005; Sottile et al., 2006). Recently, the BG population has gained a lot of interest as the rare radial glial NSCs in the adult cerebellum (Ahlfeld et al., 2017; Alcock and Sottile, 2009), capable of effective neurogenesis, at least *in vitro* (Alcock and Sottile, 2009). However, little is known about its *in vivo* potential in cerebellar neurogenesis. In this project, the NSC properties and potential of BG have been explored, the results of which support previous observations, and also provide further insights into BG stemness.

7.3.1. *In vitro* NSC potential of BG

Here it is shown that neurosphere forming BG can be isolated *in vitro* and differentiated into cerebellar neural lineages, confirming their NSC potential. Importantly, it is consistent with the earlier observations and published reports of NSCs isolated from adult mouse cerebellum (Alcock and Sottile, 2009; Klein et al., 2005; Lee et al., 2005). Although Cell_BGwt showed the ability to differentiate into neuronal and glial lineages, further analysis for neuronal subtypes produced by BG was not done in this study. The cerebellum contains multiple cell types including parenchymal astrocytes, oligodendrocytes, GABAergic interneurons, glutamatergic GCs and deep cerebellar nuclei neurons (Leto et al., 2006,

2016). Proceeding from the findings from this study, future work will be to perform in-depth analysis of the different types of neural cells produced by BG *in vitro*. To do this, experiments including prolonged differentiation of BG-NSCs (much more than 7 days, which was used in this study) should be performed and immunostained for markers specific for other multiple cerebellar neurons (Muguruma et al., 2015). Several studies have suggested the use of feeder layer or cerebellar tissue slices for healthy culture of cerebellar progenitors *in vitro* (Klein et al., 2005; Wang et al., 2015b). Therefore, a combination of culture optimisation, using co-culture or 3-D tissue culture, and drug screening for lineage differentiation of different cerebellar neural subtypes, would be necessary to understand the BG neurogenesis *in vitro* (Figure 7.3).

Here it was shown that BG-NSCs can promote neuronal outgrowth via secretion of EVs, similar to LV-NSCs. Interestingly, it was found that NSC-derived EVs required to be sonicated to produce significant neuronal outgrowth in neurons *in vitro*. This study did not investigate further into the proteomic (mass spectrometry) and nucleotide (RNA sequencing) profiles of sonicated and non-sonicated EVs which could provide further information about the functional effect of EVs. Also, live-tracking of EVs coupled with multiple EV machinery markers could provide information about the fate of EVs, for instance, differences in lysosome degradation of sonicated vs non-sonicated EVs, which would correlate with their resulting effect in recipient cells.

7.3.2. The distinct NSC properties of BG

Here it is shown that BG-NSCs can be distinguished from LV-NSCs. Consistent with previous observations, here Cell_BGwt showed a slower doubling time and greater adherence to plastic, compared to Cell_LVwt (Alcock and Sottile, 2009). Here it was also observed that Cell_BGwt show low Calbindin detection primarily in the neural extensions, in contrast to Cell_LVwt. Moreover, using a highly sensitive EV characterisation technique, it is shown that Cell_BGwt produce ten times more EVs than Cell_LVwt. These observations are consistent with the hypothesis that NSCs from cerebellum harbour regionally distinct properties (Klein et al., 2005). It could be possible to speculate that NSCs that have been discovered in multiple non-neurogenic sites in the brain including the hypothalamus and the spinal cord, would also harbour regionally distinct NSC properties (Pellegrino et al., 2018; Robins et al., 2013; Sabelström et al., 2014). Therefore, it would be important to understand the innate differences in neurogenic potential of different NSC populations in the adult brain to understand their neurogenic limits.

7.3.3. BG heterogeneity *in vivo*

Although speculative, it is unclear whether the expression of Sox1, Sox2 and Sox9 markers represent distinct subpopulations of BG. Recent reports investigating BG and PC maturation showed that a population of BG expressing NPY-GFP were localised mainly in lobules VI/VII and IX/X, implying a heterogeneity within BG patterning since early development (Reeber et al., 2018). Moreover, a recent study has

reported that only a subset of Sox2 positive cells in the adult cerebellar PCL intermingled within the BG population are S100B negative, express Nestin and undergo neurogenesis to produce NEUN positive neurons in the adult mice cerebellum (Ahlfeld et al., 2017). It has been reported that the adult SVZ harbours a variety of NSCs including slow-cycling radial like type-B1 cells, transient amplifying type-C cells and migrating type-A cells, showing a high degree in organisation and control of adult neurogenesis (Ihrie and Alvarez-Buylla, 2011). Although the analysis done here was not sufficient to investigate the heterogeneity of BGs, future investigations can look into this via intra-clonal molecular phenotyping of neurospheres *in vitro*, followed by *in vivo* birth-dating analysis of BG which can provide more information into the control of neurogenesis in the adult cerebellum (Couillard-Despres et al., 2011; De Marchis and Puche, 2012; Kuhn et al., 1996; Suslov et al., 2002).

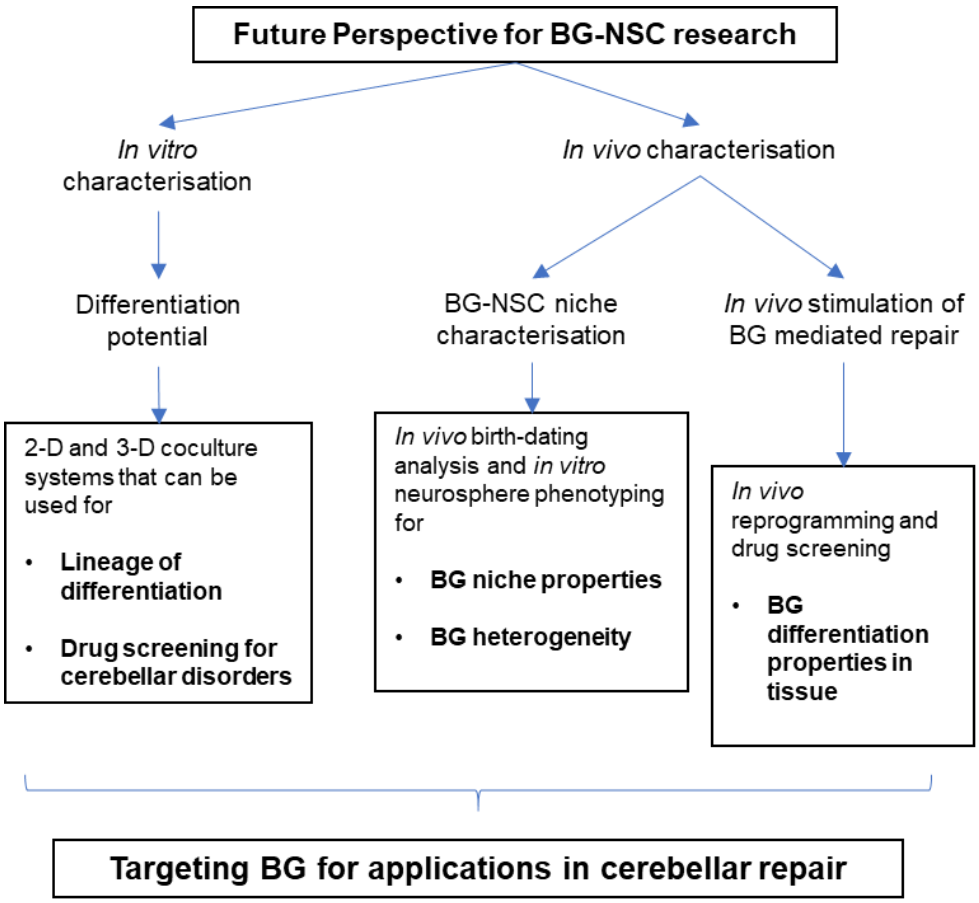


Figure 7.3: Flowchart depicting future perspective for BG-NSC research. BG-Bergmann glia.

8. Final conclusion

This study focused on investigating the neural stem cell (NSC) potential of the Bergmann glia (BG) derived from the adult mouse cerebellum. To do this, innovative approaches to study the cellular and acellular properties of NSCs were developed.

The fasudil-based medium developed in this study was used to assess the differentiation of BG-NSC *in vitro*. It was shown that fasudil can be used to study glial features including radial-morphology and radial -like movement of NSCs *in vitro*. Future investigations into mechanism of fasudil effect on NSCs can contribute to disease modelling of gliogenesis.

The d-STORM-based approach developed in this study provides rapid and efficient alternative to characterise stem cell-derived extracellular vesicles (EVs) including BG-NSC derived EVs. This approach was used to investigate the size distribution and concentration of NSC derived EVs for experiments including neuronal response and EV secretion profile determination. Here it was shown that the d-STORM approach has multiple downstream applications in cell biology including investigating EV-trafficking.

This study showed that BG-NSCs can differentiate into neurons and glia *in vitro*. *In vivo* analysis showed that BG responded to PC insult by showing characteristics involved with reactive glia including increase in cell number and strong GFAP expression. BG-NSCs secreted EVs which

were able to promote outgrowth of neurons in culture, suggesting that BG-NSCs can support neuronal growth in an acellular manner. It was further shown that low-power sonication of BG-NSC derived EVs was crucial to promote the observed neuronal outgrowth in culture; it was demonstrated that low-power sonication can introduce additional effects including increase in EVs below 50 nm, disruption of EV membrane properties and decrease in cellular uptake of EVs. Hence, this study suggested that BG can be a target for treating cerebellar neurodegeneration and that future investigations into neurogenic potential of BG is required.

Taken together, this thesis provides insights into the stem cell properties of BG in the adult mouse cerebellum which would contribute to understanding and potentially stimulating cerebellar regeneration to treating ataxic disorders in the future. The methodologies developed in this study will directly contribute to the investigate of NSC biology and EV characterisation, contributing to the fields of regenerative medicine, cancer biology and therapeutic neuroscience.

9. References

Abe, H., Watanabe, M., Yamakuni, T., Kuwano, R., Takahashi, Y., and Kondo, H. (1992). Localization of gene expression of calbindin in the brain of adult rats. Neurosci. Lett. *138*, 211–215.

Agnarsson, B., Lundgren, A., Gunnarsson, A., Rabe, M., Kunze, A., Mapar, M., Simonsson, L., Bally, M., Zhdanov, V.P., and Höök, F. (2015). Evanescent Light-Scattering Microscopy for Label-Free Interfacial Imaging: From Single Sub-100 nm Vesicles to Live Cells. ACS Nano *9*, 11849–11862.

Agostini, M., Romeo, F., Inoue, S., Niklison-Chirou, M.V., Elia, A.J., Dinsdale, D., Morone, N., Knight, R.A., Mak, T.W., and Melino, G. (2016). Metabolic reprogramming during neuronal differentiation. Cell Death Differ *23*, 1502–1514.

Ahlfeld, J., Filser, S., Schmidt, F., Wefers, A.K., Merk, D.J., Glaß, R., Herms, J., and Schüller, U. (2017). Neurogenesis from Sox2 expressing cells in the adult cerebellar cortex. Sci. Rep. *7*, 6137.

Alcock, J., and Sottile, V. (2009). Dynamic distribution and stem cell characteristics of Sox1-expressing cells in the cerebellar cortex. Cell Res. *19*, 1324–1333.

Alcock, J., Lowe, J., England, T., Bath, P., and Sottile, V. (2009). Expression of Sox1, Sox2 and Sox9 is maintained in adult human cerebellar cortex. Neurosci. Lett. *450*, 114–116.

Al-Nasiry, S., Geusens, N., Hanssens, M., Luyten, C., and Pijnenborg, R. (2007). The use of Alamar Blue assay for quantitative analysis of viability, migration and invasion of choriocarcinoma cells. Hum. Reprod. Oxf. Engl. *22*, 1304–1309.

Altman, J., and Das, G.D. (1966). Autoradiographic and histological studies of postnatal neurogenesis. I. A longitudinal investigation of the kinetics, migration and transformation of cells incorporating tritiated thymidine in neonate rats, with special reference to postnatal neurogenesis in some brain regions. J. Comp. Neurol. *126*, 337–389.

Alvarez-Cubero, M.J., Santiago, O., Martínez-Labarga, C., Martínez-García, B., Díaz, R.M.-, Rubio-Roldan, A., Pérez-Gutiérrez, A.M., Carmona-Saez, P., Lorente, J.A., and Martinez-Gonzalez, L.J. (2018). Methodology for Y Chromosome Capture: A complete genome sequence of Y chromosome using flow cytometry, laser microdissection and magnetic streptavidin-beads. Sci. Rep. *8*, 9436.

Ambrogini, P., Lattanzi, D., Ciuffoli, S., Agostini, D., Bertini, L., Stocchi, V., Santi, S., and Cuppini, R. (2004). Morpho-functional characterization

of neuronal cells at different stages of maturation in granule cell layer of adult rat dentate gyrus. Brain Res. *1017*, 21–31.

Anderson, W., Lane, R., Korbie, D., and Trau, M. (2015). Observations of Tunable Resistive Pulse Sensing for Exosome Analysis: Improving System Sensitivity and Stability. Langmuir *31*, 6577–6587.

Ansa-Addo, E.A., Lange, S., Stratton, D., Antwi-Baffour, S., Cestari, I., Ramirez, M.I., McCrossan, M.V., and Inal, J.M. (2010). Human Plasma Membrane-Derived Vesicles Halt Proliferation and Induce Differentiation of THP-1 Acute Monocytic Leukemia Cells. J. Immunol. 1001656.

Aravantinou-Fatorou, K., Ortega, F., Chroni-Tzartou, D., Antoniou, N., Poulopoulou, C., Politis, P.K., Berninger, B., Matsas, R., and Thomaidou, D. (2015). CEND1 and NEUROGENIN2 Reprogram Mouse Astrocytes and Embryonic Fibroblasts to Induced Neural Precursors and Differentiated Neurons. Stem Cell Rep. *5*, 405–418.

Arias-Carrion, T.-F.Y. and O. (2011). Adult Neurogenesis in the Hypothalamus: Evidence, Functions and Implications.

Asano, T., Suzuki, T., Tsuchiya, M., Satoh, S., Ikegaki, I., Shibuya, M., Suzuki, Y., and Hidaka, H. (1989). Vasodilator actions of HA1077 in vitro and in vivo putatively mediated by the inhibition of protein kinase. Br J Pharmacol *98*, 1091–1100.

Aubert, J., Stavridis, M.P., Tweedie, S., O'Reilly, M., Vierlinger, K., Li, M., Ghazal, P., Pratt, T., Mason, J.O., Roy, D., Smith, A., (2003). Screening for mammalian neural genes via fluorescence-activated cell sorter purification of neural precursors from Sox1-gfp knock-in mice. PNAS 100.

Bahrini, I., Song, J., Diez, D., and Hanayama, R. (2015). Neuronal exosomes facilitate synaptic pruning by up-regulating complement factors in microglia. Sci. Rep. *5*, 7989.

Baietti, M.F., Zhang, Z., Mortier, E., Melchior, A., Degeest, G., Geeraerts, A., Ivarsson, Y., Depoortere, F., Coomans, C., Vermeiren, E., et al. (2012). Syndecan–syntenin–ALIX regulates the biogenesis of exosomes. Nat. Cell Biol. *14*, 677–685.

Baker, E.W., Platt, S.R., Lau, V.W., Grace, H.E., Holmes, S.P., Wang, L., Duberstein, K.J., Howerth, E.W., Kinder, H.A., Stice, S.L., et al. (2017). Induced Pluripotent Stem Cell-Derived Neural Stem Cell Therapy Enhances Recovery in an Ischemic Stroke Pig Model. Sci. Rep. *7*, 10075.

Bakhti, M., Winter, C., and Simons, M. (2011). Inhibition of Myelin Membrane Sheath Formation by Oligodendrocyte-derived Exosome-like Vesicles. J. Biol. Chem. *286*, 787–796.

Bani-Yaghoub, M., Tremblay, R.G., Lei, J.X., Zhang, D., Zurakowski, B., Sandhu, J.K., Smith, B., Ribecco-Lutkiewicz, M., Kennedy, J., and Walker, P.R. (2006). Role of Sox2 in the development of the mouse neocortex. Dev. Biol. *295*, 52–66.

Barraud, P., Thompson, L., Kirik, D., Björklund, A., and Parmar, M. (2005). Isolation and characterization of neural precursor cells from the Sox1–GFP reporter mouse. Eur. J. Neurosci. *22*, 1555–1569.

Barski, J.J., Hartmann, J., Rose, C.R., Hoebeek, F., Mörl, K., Noll-Hussong, M., Zeeuw, C.I.D., Konnerth, A., and Meyer, M. (2003). Calbindin in Cerebellar Purkinje Cells Is a Critical Determinant of the Precision of Motor Coordination. J. Neurosci. *23*, 3469–3477.

Bede, P., Elamin, M., Byrne, S., McLaughlin, R.L., Kenna, K., Vajda, A., Fagan, A., Bradley, D.G., and Hardiman, O. (2015). Patterns of cerebral and cerebellar white matter degeneration in ALS. J. Neurol. Neurosurg. Psychiatry *86*, 468–470.

Bellamy, T.C. (2006). Interactions between Purkinje neurones and Bergmann glia. Cerebellum Lond. Engl. *5*, 116–126.

Berardocco, M., Radeghieri, A., Busatto, S., Gallorini, M., Raggi, C., Gissi, C., D'Agnano, I., Bergese, P., Felsani, A., and Berardi, A.C. (2017). RNA-seq reveals distinctive RNA profiles of small extracellular vesicles from different human liver cancer cell lines. Oncotarget *8*, 82920–82939.

Bernardos, R.L., Barthel, L.K., Meyers, J.R., Raymond, P.A., (2007). Late-Stage Neuronal Progenitors in the Retina Are Radial Müller Glia That Function as Retinal Stem Cells. J. Neurosci. 27, 7028–7040.

Bianco, F., Pravettoni, E., Colombo, A., Schenk, U., Möller, T., Matteoli, M., and Verderio, C. (2005). Astrocyte-Derived ATP Induces Vesicle Shedding and IL-1β Release from Microglia. J. Immunol. *174*, 7268–7277.

Biebl, M., Cooper, C.M., Winkler, J., and Kuhn, H.G. (2000). Analysis of neurogenesis and programmed cell death reveals a self-renewing capacity in the adult rat brain. Neurosci. Lett. *291*, 17–20.

Bignami, A., and Dahl, D. (1974). Astrocyte-specific protein and radial glia in the cerebral cortex of newborn rat. Nature *252*, 55–56.

Billinge, E.R., Broom, M., and Platt, M. (2014). Monitoring Aptamer–Protein Interactions Using Tunable Resistive Pulse Sensing. Anal. Chem. *86*, 1030–1037.

Boldrini, M., Fulmore, C.A., Tartt, A.N., Simeon, L.R., Pavlova, I., Poposka, V., Rosoklija, G.B., Stankov, A., Arango, V., Dwork, A.J., et al. (2018). Human Hippocampal Neurogenesis Persists throughout Aging. Cell Stem Cell *22*, 589-599.e5.

Boncler, M., Różalski, M., Krajewska, U., Podsędek, A., and Watala, C. (2014). Comparison of PrestoBlue and MTT assays of cellular viability in the assessment of anti-proliferative effects of plant extracts on human endothelial cells. J. Pharmacol. Toxicol. Methods *69*, 9–16.

Bonifacino, J.S., and Glick, B.S. (2004). The mechanisms of vesicle budding and fusion. Cell *116*, 153–166.

Braun, S.M.G., and Jessberger, S. (2013). Adult neurogenesis in the mammalian brain. Front. Biol. *8*, 295–304.

Brown, J.P., Couillard-Després, S., Cooper-Kuhn, C.M., Winkler, J., Aigner, L., and Kuhn, H.G. (2003). Transient expression of doublecortin during adult neurogenesis. J. Comp. Neurol. *467*, 1–10.

Buckner, R.L. (2013). The cerebellum and cognitive function: 25 years of insight from anatomy and neuroimaging. Neuron *80*, 807–815.

Buffo, A., and Rossi, F. (2013). Origin, lineage and function of cerebellar glia. Prog. Neurobiol. *109*, 42–63.

Cahoy, J.D., Emery, B., Kaushal, A., Foo, L.C., Zamanian, J.L., Christopherson, K.S., Xing, Y., Lubischer, J.L., Krieg, P.A., Krupenko, S.A., et al. (2008). A Transcriptome Database for Astrocytes, Neurons, and Oligodendrocytes: A New Resource for Understanding Brain Development and Function. J. Neurosci. *28*, 264–278.

Cai, H., Reinisch, K., and Ferro-Novick, S. (2007). Coats, tethers, Rabs, and SNAREs work together to mediate the intracellular destination of a transport vesicle. Dev. Cell *12*, 671–682.

Campbell, K., and Götz, M. (2002). Radial glia: multi-purpose cells for vertebrate brain development. Trends Neurosci *25*, 235–238.

Caponnetto, F., Manini, I., Skrap, M., Palmai-Pallag, T., Di Loreto, C., Beltrami, A.P., Cesselli, D., and Ferrari, E. (2017). Size-dependent cellular uptake of exosomes. Nanomedicine Nanotechnol. Biol. Med. *13*, 1011–1020.

Carayon, K., Chaoui, K., Ronzier, E., Lazar, I., Bertrand-Michel, J., Roques, V., Balor, S., Terce, F., Lopez, A., Salomé, L., et al. (2011). Proteolipidic Composition of Exosomes Changes during Reticulocyte Maturation. J. Biol. Chem. *286*, 34426–34439.

Cerminara, N.L., Lang, E.J., Sillitoe, R.V., and Apps, R. (2015). Redefining the cerebellar cortex as an assembly of non-uniform Purkinje cell microcircuits. Nat. Rev. Neurosci. *16*, 79–93.

Chakrabarti, L., Neal, J.T., Miles, M., Martinez, R.A., Smith, A.C., Sopher, B.L., and Spada, A.R.L. (2006). The Purkinje cell degeneration 5J mutation is a single amino acid insertion that destabilizes Nna1 protein. Mamm. Genome *17*, 103–110.

Chen, B., Li, Q., Zhao, B., and Wang, Y. (2017). Stem Cell-Derived Extracellular Vesicles as a Novel Potential Therapeutic Tool for Tissue Repair. STEM CELLS Transl. Med. *6*, 1753–1758.

Chen, C., Zong, S., Wang, Z., Lu, J., Zhu, D., Zhang, Y., and Cui, Y. (2016). Imaging and Intracellular Tracking of Cancer-Derived Exosomes Using Single-Molecule Localization-Based Super-Resolution Microscope. ACS Appl. Mater. Interfaces *8*, 25825–25833.

Chen, C., Zong, S., Wang, Z., Lu, J., Zhu, D., Zhang, Y., Zhang, R., and Cui, Y. (2018). Visualization and intracellular dynamic tracking of exosomes and exosomal miRNAs using single molecule localization microscopy. Nanoscale *10*, 5154–5162.

Chen, M., Liu, A., Ouyang, Y., Huang, Y., Chao, X., and Pi, R. (2013). Fasudil and its analogs: a new powerful weapon in the long war against central nervous system disorders? Expert Opin Investig Drugs *22*, 537–550.

Chen, S., Luo, M., Zhao, Y., Zhang, Y., He, M., Cai, W., and Liu, A. (2015). Fasudil Stimulates Neurite Outgrowth and Promotes Differentiation in C17.2 Neural Stem Cells by Modulating Notch Signalling but not Autophagy. Cell Physiol Biochem *36*, 531–541.

Chivet, M., Hemming, F., Pernet-Gallay, K., Fraboulet, S., and Sadoul, R. (2012). Emerging role of neuronal exosomes in the central nervous system. Front. Physiol. *3*.

Chung, S.-H., Marzban, H., Croci, L., Consalez, G.G., and Hawkes, R. (2008). Purkinje cell subtype specification in the cerebellar cortex: early B-cell factor 2 acts to repress the zebrin II-positive Purkinje cell phenotype. Neuroscience *153*, 721–732.

Cimadamore, F., Amador-Arjona, A., Chen, C., Huang, C.-T., and Terskikh, A.V. (2013). SOX2–LIN28/let-7 pathway regulates proliferation and neurogenesis in neural precursors. Proc. Natl. Acad. Sci. *110*, E3017–E3026.

Collins, P.Y., Patel, V., Joestl, S.S., March, D., Insel, T.R., Daar, A.S., Scientific Advisory Board and the Executive Committee of the Grand Challenges on Global Mental Health, Anderson, W., Dhansay, M.A., Phillips, A., et al. (2011). Grand challenges in global mental health. Nature *475*, 27–30.

Compagnucci, C., Barresi, S., Petrini, S., Billuart, P., Piccini, G., Chiurazzi, P., Alfieri, P., Bertini, E., and Zanni, G. (2016). Rho Kinase Inhibition Is Essential During In Vitro Neurogenesis and Promotes Phenotypic Rescue of Human Induced Pluripotent Stem Cell-Derived Neurons With Oligophrenin-1 Loss of Function. Stem Cells Transl Med *5*, 860–869.

Contreras-Naranjo, J.C., Wu, H.-J., and Ugaz, V.M. (2017). Microfluidics for exosome isolation and analysis: enabling liquid biopsy for personalized medicine. Lab. Chip *17*, 3558–3577.

Cossetti, C., Iraci, N., Mercer, T.R., Leonardi, T., Alpi, E., Drago, D., Alfaro-Cervello, C., Saini, H.K., Davis, M.P., Schaeffer, J., et al. (2014). Extracellular Vesicles from Neural Stem Cells Transfer IFN-γ via Ifngr1 to Activate Stat1 Signaling in Target Cells. Mol. Cell *56*, 193–204.

Couillard-Despres, S., Vreys, R., Aigner, L., and Van der Linden, A. (2011). In vivo monitoring of adult neurogenesis in health and disease. Front. Neurosci. *5*, 67.

Coumans, F.A., van der Pol, E., Boing, A.N., Hajji, N., Sturk, G., van Leeuwen, T.G., and Nieuwland, R. (2014). Reproducible extracellular vesicle size and concentration determination with tunable resistive pulse sensing. J Extracell Vesicles *3*, 25922.

De Luca, A., Parmigiani, E., Tosatto, G., Martire, S., Hoshino, M., Buffo, A., Leto, K., and Rossi, F. (2015). Exogenous Sonic hedgehog modulates the pool of GABAergic interneurons during cerebellar development. Cerebellum Lond. Engl. *14*, 72–85.

De Luca, A., Cerrato, V., Fucà, E., Parmigiani, E., Buffo, A., and Leto, K. (2016). Sonic hedgehog patterning during cerebellar development. Cell. Mol. Life Sci. CMLS *73*, 291–303.

De Marchis, S., and Puche, A.C. (2012). Cellular Imaging and Emerging Technologies for Adult Neurogenesis Research. Front. Neurosci. *6*.

De Zeeuw, C.I., Hoogland, T.M., (2015). Reappraisal of Bergmann glial cells as modulators of cerebellar circuit function. Front Cell Neurosci 9.

Del Bene, F. (2011). Interkinetic nuclear migration: cell cycle on the move. EMBO J. *30*, 1676–1677.

Deloulme, J.C., Raponi, E., Gentil, B.J., Bertacchi, N., Marks, A., Labourdette, G., and Baudier, J. (2004). Nuclear expression of S100B in oligodendrocyte progenitor cells correlates with differentiation toward the oligodendroglial lineage and modulates oligodendrocytes maturation. Mol. Cell. Neurosci. *27*, 453–465.

Dempsey, G.T., Vaughan, J.C., Chen, K.H., Bates, M., and Zhuang, X. (2011). Evaluation of fluorophores for optimal performance in localization-based super-resolution imaging. Nat. Methods *8*, 1027–1036.

Deng, L., Li, G., Li, R., Liu, Q., He, Q., and Zhang, J. (2010). Rho-kinase inhibitor, fasudil, suppresses glioblastoma cell line progression in vitro and in vivo. Cancer Biol. Ther. *9*, 875–884.

Ding, J., Li, Q.Y., Yu, J.Z., Wang, X., Sun, C.H., Lu, C.Z., and Xiao, B.G. (2010). Fasudil, a Rho kinase inhibitor, drives mobilization of adult neural stem cells after hypoxia/reoxygenation injury in mice. Mol Cell Neurosci *43*, 201–208.

Doetsch, F. (2003). The glial identity of neural stem cells. Nat Neurosci *6*, 1127–1134.

Doetsch, F., and Alvarez-Buylla, A. (1996). Network of tangential pathways for neuronal migration in adult mammalian brain. Proc. Natl. Acad. Sci. *93*, 14895–14900.

Doetsch, F., Caille, I., Lim, D.A., Garcia-Verdugo, J.M., and Alvarez-Buylla, A. (1999). Subventricular zone astrocytes are neural stem cells in the adult mammalian brain. Cell *97*, 703–716.

Dragovic, R.A., Gardiner, C., Brooks, A.S., Tannetta, D.S., Ferguson, D.J.P., Hole, P., Carr, B., Redman, C.W.G., Harris, A.L., Dobson, P.J., et al. (2011). Sizing and phenotyping of cellular vesicles using Nanoparticle Tracking Analysis. Nanomedicine Nanotechnol. Biol. Med. *7*, 780–788.

Dubois, N.C., Hofmann, D., Kaloulis, K., Bishop, J.M., and Trumpp, A. (2006). Nestin-Cre transgenic mouse line Nes-Cre1 mediates highly efficient Cre/loxP mediated recombination in the nervous system, kidney, and somite-derived tissues. Genes. N. Y. N 2000 *44*, 355–360.

Dudok, B., Barna, L., Ledri, M., Szabó, S.I., Szabadits, E., Pintér, B., Woodhams, S.G., Henstridge, C.M., Balla, G.Y., Nyilas, R., et al. (2015). Cell-specific STORM super-resolution imaging reveals nanoscale organization of cannabinoid signaling. Nat. Neurosci. *18*, 75–86.

Dugan, L.L., Kim, J.S., Zhang, Y., Bart, R.D., Sun, Y., Holtzman, D.M., and Gutmann, D.H. (1999). Differential effects of cAMP in neurons and astrocytes role of B-raf. J. Biol. Chem. *274*, 25842–25848.

Eiraku, M., Tohgo, A., Ono, K., Kaneko, M., Fujishima, K., Hirano, T., and Kengaku, M. (2005). DNER acts as a neuron-specific Notch ligand during Bergmann glial development. Nat. Neurosci. *8*, 873–880.

Elkabetz, Y., Panagiotakos, G., Al Shamy, G., Socci, N.D., Tabar, V., Studer, L., (2008). Human ES cell-derived neural rosettes reveal a functionally distinct early neural stem cell stage. Genes & development 22, 152–65.

Episkopou, V. (2005). SOX2 functions in adult neural stem cells. Trends Neurosci *28*, 219–221.

Erdbrügger, U., and Lannigan, J. (2016). Analytical challenges of extracellular vesicle detection: A comparison of different techniques. Cytom. Part J. Int. Soc. Anal. Cytol. *89*, 123–134.

Faiz, M., Sachewsky, N., Gascón, S., Bang, K.W.A., Morshead, C.M., and Nagy, A. (2015). Adult Neural Stem Cells from the Subventricular Zone Give Rise to Reactive Astrocytes in the Cortex after Stroke. Cell Stem Cell *17*, 624–634.

Fajardo, A.M., Piazza, G.A., and Tinsley, H.N. (2014). The role of cyclic nucleotide signaling pathways in cancer: targets for prevention and treatment. Cancers *6*, 436–458.

Filipe, V., Hawe, A., and Jiskoot, W. (2010). Critical Evaluation of Nanoparticle Tracking Analysis (NTA) by NanoSight for the Measurement of Nanoparticles and Protein Aggregates. Pharm. Res. *27*, 796–810.

Fleming, J., and Chiang, C. (2015). The Purkinje neuron: A central orchestrator of cerebellar neurogenesis. Neurogenesis *2*.

Fleming, J.T., He, W., Hao, C., Ketova, T., Pan, F.C., Wright, C.C.V., Litingtung, Y., and Chiang, C. (2013). The Purkinje Neuron Acts as a Central Regulator of Spatially and Functionally Distinct Cerebellar Precursors. Dev. Cell *27*, 278–292.

Foo, L.C., Allen, N.J., Bushong, E.A., Ventura, P.B., Chung, W.-S., Zhou, L., Cahoy, J.D., Daneman, R., Zong, H., Ellisman, M.H., et al. (2011). Development of a Method for the Purification and Culture of Rodent Astrocytes. Neuron *71*, 799–811.

Fröhlich Dominik, Kuo Wen Ping, Frühbeis Carsten, Sun Jyh-Jang, Zehendner Christoph M., Luhmann Heiko J., Pinto Sheena, Toedling Joern, Trotter Jacqueline, and Krämer-Albers Eva-Maria (2014). Multifaceted effects of oligodendroglial exosomes on neurons: impact on neuronal firing rate, signal transduction and gene regulation. Philos. Trans. R. Soc. B Biol. Sci. *369*, 20130510.

Frühbeis, C., Fröhlich, D., Kuo, W.P., Amphornrat, J., Thilemann, S., Saab, A.S., Kirchhoff, F., Möbius, W., Goebbels, S., Nave, K.-A., et al. (2013). Neurotransmitter-Triggered Transfer of Exosomes Mediates Oligodendrocyte–Neuron Communication. PLOS Biol. *11*, e1001604.

Fujita, Y., and Yamashita, T. (2014). Axon growth inhibition by RhoA/ROCK in the central nervous system. Front. Neurosci. *8*.

Furuta, T., Miyaki, S., Ishitobi, H., Ogura, T., Kato, Y., Kamei, N., Miyado, K., Higashi, Y., and Ochi, M. (2016). Mesenchymal Stem Cell-Derived Exosomes Promote Fracture Healing in a Mouse Model. Stem Cells Transl. Med. *5*, 1620–1630.

Gabrielli, M., Battista, N., Riganti, L., Prada, I., Antonucci, F., Cantone, L., Matteoli, M., Maccarrone, M., and Verderio, C. (2015). Active endocannabinoids are secreted on extracellular membrane vesicles. EMBO Rep. *16*, 213–220.

Gage, F.H., and Temple, S. (2013). Neural Stem Cells: Generating and Regenerating the Brain. Neuron *80*, 588–601.

Gallagher, S., Winston, S.E., Fuller, S.A., and Hurrell, J.G.R. (2008). Immunoblotting and immunodetection. Curr. Protoc. Mol. Biol. *Chapter 10*, Unit 10.8.

Garcia-Segura, L.M., Baetens, D., Roth, J., Norman, A.W., and Orci, L. (1984). Immunohistochemical mapping of calcium-binding protein immunoreactivity in the rat central nervous system. Brain Res. *296*, 75–86.

Gardiner, C., Ferreira, Y.J., Dragovic, R.A., Redman, C.W.G., and Sargent, I.L. (2013). Extracellular vesicle sizing and enumeration by nanoparticle tracking analysis. J. Extracell. Vesicles *2*, 19671.

Gaub, P., Tedeschi, A., Puttagunta, R., Nguyen, T., Schmandke, A., and Giovanni, S.D. (2010). HDAC inhibition promotes neuronal outgrowth and counteracts growth cone collapse through CBP/p300 and P/CAF-dependent p53 acetylation. Cell Death Differ. *17*, 1392–1408.

Glaser, T., and Brüstle, O. (2005). Retinoic acid induction of ES-cell-derived neurons: the radial glia connection. Trends Neurosci. *28*, 397–400.

Gleeson, J.G., Lin, P.T., Flanagan, L.A., Walsh, C.A., (1999). Doublecortin Is a Microtubule-Associated Protein and Is Expressed Widely by Migrating Neurons. Neuron 23, 257–271.

Glogger, M., Stichler, S., Subota, I., Bertlein, S., Spindler, M.-C., Teßmar, J., Groll, J., Engstler, M., and Fenz, S.F. (2017). Live-cell super-resolution imaging of intrinsically fast moving flagellates. J. Phys. Appl. Phys. *50*, 074004.

Godin, A.G., Lounis, B., and Cognet, L. (2014). Super-resolution Microscopy Approaches for Live Cell Imaging. Biophys. J. *107*, 1777–1784.

Götz, M., Sirko, S., Beckers, J., and Irmler, M. (2015). Reactive astrocytes as neural stem or progenitor cells: In vivo lineage, In vitro potential, and Genome-wide expression analysis. Glia *63*, 1452–1468.

Graham, V., Khudyakov, J., Ellis, P., and Pevny, L. (2003). SOX2 functions to maintain neural progenitor identity. Neuron *39*, 749–765.

Grimaldi, P., Rossi, F., (2006). Lack of neurogenesis in the adult rat cerebellum after Purkinje cell degeneration and growth factor infusion. European Journal of Neuroscience 23, 2657–2668.

Gu, H., Yu, S.P., Gutekunst, C.-A., Gross, R.E., and Wei, L. (2013). Inhibition of the Rho signaling pathway improves neurite outgrowth and

neuronal differentiation of mouse neural stem cells. Int J Physiol Pathophysiol Pharmacol *5*, 11–20.

Guo, C.C., Tan, R., Hodges, J.R., Hu, X., Sami, S., and Hornberger, M. (2016). Network-selective vulnerability of the human cerebellum to Alzheimer's disease and frontotemporal dementia. Brain J. Neurol. *139*, 1527–1538.

Guo, W., Patzlaff, N.E., Jobe, E.M., and Zhao, X. (2012). Isolation of multipotent neural stem or progenitor cells from both the dentate gyrus and subventricular zone of a single adult mouse. Nat. Protoc. *7*, 2005–2012.

Guo, Z., Zhang, L., Wu, Z., Chen, Y., Wang, F., and Chen, G. (2014). In vivo direct reprogramming of reactive glial cells into functional neurons after brain injury and in an Alzheimer's disease model. Cell Stem Cell *14*, 188–202.

Gusel'nikova, V.V., and Korzhevskiy, D.E. (2015). NeuN As a Neuronal Nuclear Antigen and Neuron Differentiation Marker. Acta Naturae *7*, 42–47.

Haga, H., Yan, I.K., Takahashi, K., Matsuda, A., and Patel, T. (2017). Extracellular Vesicles from Bone Marrow-Derived Mesenchymal Stem Cells Improve Survival from Lethal Hepatic Failure in Mice. STEM CELLS Transl. Med. *6*, 1262–1272.

Hatten, M.E., and Heintz, N. (1995). Mechanisms of neural patterning and specification in the developing cerebellum. Annu. Rev. Neurosci. *18*, 385–408.

Heilemann, M., van de Linde, S., Schüttpelz, M., Kasper, R., Seefeldt, B., Mukherjee, A., Tinnefeld, P., and Sauer, M. (2008). Subdiffraction-Resolution Fluorescence Imaging with Conventional Fluorescent Probes. Angew. Chem. Int. Ed. *47*, 6172–6176.

Heinrich, C., Gascón, S., Masserdotti, G., Lepier, A., Sanchez, R., Simon-Ebert, T., Schroeder, T., Götz, M., and Berninger, B. (2011). Generation of subtype-specific neurons from postnatal astroglia of the mouse cerebral cortex. Nat. Protoc. *6*, 214–228.

Heinrich, C., Bergami, M., Gascón, S., Lepier, A., Viganò, F., Dimou, L., Sutor, B., Berninger, B., and Götz, M. (2014). Sox2-Mediated Conversion of NG2 Glia into Induced Neurons in the Injured Adult Cerebral Cortex. Stem Cell Rep. *3*, 1000–1014.

Heizmann, C.W., Fritz, G., and Schäfer, B.W. (2002). S100 proteins: structure, functions and pathology. Front. Biosci. J. Virtual Libr. *7*, d1356-1368.

Hendrickson, M.L., Rao, A.J., Demerdash, O.N.A., and Kalil, R.E. (2011). Expression of Nestin by Neural Cells in the Adult Rat and Human Brain. PLOS ONE *6*, e18535.

Herndon, R.M. (1963). The Fine Structure of the Purkinje Cell. J. Cell Biol. *18*, 167–180.

Herrmann, H., Aebi, U., (2000). Intermediate filaments and their associates: multi-talented structural elements specifying cytoarchitecture and cytodynamics. Curr. Opin. Cell Biol. 12, 79–90.

Holm, M.M., Kaiser, J., and Schwab, M.E. (2018). Extracellular Vesicles: Multimodal Envoys in Neural Maintenance and Repair. Trends Neurosci. *41*, 360–372.

Höög, J.L., and Lötvall, J. (2015). Diversity of extracellular vesicles in human ejaculates revealed by cryo-electron microscopy. J. Extracell. Vesicles *4*, 28680.

Hosseini-Beheshti, E., Pham, S., Adomat, H., Li, N., and Tomlinson Guns, E.S. (2012). Exosomes as Biomarker Enriched Microvesicles: Characterization of Exosomal Proteins Derived from a Panel of Prostate Cell Lines with Distinct AR Phenotypes. Mol. Cell. Proteomics MCP *11*, 863–885.

Hou, S.-W., Liu, C.-Y., Li, Y.-H., Yu, J.-Z., Feng, L., Liu, Y.-T., Guo, M.-F., Xie, Y., Meng, J., Zhang, H.-F., et al. (2012). Fasudil ameliorates disease progression in experimental autoimmune encephalomyelitis, acting possibly through antiinflammatory effect. CNS Neurosci. Ther. *18*, 909–917.

Hu, L., Wang, J., Zhou, X., Xiong, Z., Zhao, J., Yu, R., Huang, F., Zhang, H., and Chen, L. (2016). Exosomes derived from human adipose mensenchymal stem cells accelerates cutaneous wound healing via optimizing the characteristics of fibroblasts. Sci. Rep. *6*, 32993.

Huang, L., Li, Q., Li, H., He, Z., Cheng, Z., Chen, J., and Guo, L. (2009). Inhibition of intracellular Ca 2+ release by a Rho-kinase inhibitor for the treatment of ischemic damage in primary cultured rat hippocampal neurons. Eur J Pharmacol *602*, 238–244.

Hurley, J.H. (2008). ESCRT complexes and the biogenesis of multivesicular bodies. Curr. Opin. Cell Biol. *20*, 4–11.

Hutton, S.R., and Pevny, L.H. (2011). SOX2 expression levels distinguish between neural progenitor populations of the developing dorsal telencephalon. Dev. Biol. *352*, 40–47.

Ihrie, R.A., and Alvarez-Buylla, A. (2011). Lake-front property: a unique germinal niche by the lateral ventricles of the adult brain. Neuron *70*, 674–686.

Iraci, N., Gaude, E., Leonardi, T., Costa, A.S.H., Cossetti, C., Peruzzotti-Jametti, L., Bernstock, J.D., Saini, H.K., Gelati, M., Vescovi, A.L., et al. (2017). Extracellular vesicles are independent metabolic units with asparaginase activity. Nat. Chem. Biol. *13*, 951–955.

Ishida, Y., Kawakami, H., Kitajima, H., Nishiyama, A., Sasai, Y., Inoue, H., and Muguruma, K. (2016). Vulnerability of Purkinje Cells Generated from Spinocerebellar Ataxia Type 6 Patient-Derived iPSCs. Cell Rep. *17*, 1482–1490.

Jablonska, B., Aguirre, A., Raymond, M., Szabo, G., Kitabatake, Y., Sailor, K.A., Ming, G.-L., Song, H., and Gallo, V. (2010). Chordin-induced lineage plasticity of adult SVZ neuroblasts after demyelination. Nat. Neurosci. *13*, 541–550.

Jeyakumar, M., Lee, J.-P., Sibson, N.R., Lowe, J.P., Stuckey, D.J., Tester, K., Fu, G., Newlin, R., Smith, D.A., Snyder, E.Y., et al. (2009). Neural stem cell transplantation benefits a monogenic neurometabolic disorder during the symptomatic phase of disease. Stem Cells Dayt. Ohio *27*, 2362–2370.

Jia, X., Ye, F., Wang, Y., and Feng, D. (2016). ROCK inhibition enhances neurite outgrowth in neural stem cells by upregulating YAP expression in vitro. Neural Regen. Res. *11*, 983.

Jiao, Y., Palmgren, B., Novozhilova, E., Englund Johansson, U., Spieles-Engemann, A.L., Kale, A., Stupp, S.I., and Olivius, P. (2014). BDNF increases survival and neuronal differentiation of human neural precursor cells cotransplanted with a nanofiber gel to the auditory nerve in a rat model of neuronal damage. BioMed Res. Int. *2014*, 356415.

Johansson, C.B., Svensson, M., Wallstedt, L., Janson, A.M., and Frisén, J. (1999). Neural Stem Cells in the Adult Human Brain. Exp. Cell Res. *253*, 733–736.

Jünger, F., Olshausen, P. v, and Rohrbach, A. (2016). Fast, label-free super-resolution live-cell imaging using rotating coherent scattering (ROCS) microscopy. Sci. Rep. *6*, 30393.

Juopperi, T.A., Song, H., and Ming, G. (2011). Modeling neurological diseases using patient-derived induced pluripotent stem cells. Future Neurol. *6*, 363–373.

Juopperi, T.A., Kim, W.R., Chiang, C.-H., Yu, H., Margolis, R.L., Ross, C.A., Ming, G., Song, H., (2012). Astrocytes generated from patient induced pluripotent stem cells recapitulate features of Huntington's disease patient cells. Mol Brain 5, 17.

Karimi, N., Cvjetkovic, A., Jang, S.C., Crescitelli, R., Hosseinpour Feizi, M.A., Nieuwland, R., Lötvall, J., and Lässer, C. (2018). Detailed analysis

of the plasma extracellular vesicle proteome after separation from lipoproteins. Cell. Mol. Life Sci. CMLS *75*, 2873–2886.

Karow, M., Sánchez, R., Schichor, C., Masserdotti, G., Ortega, F., Heinrich, C., Gascón, S., Khan, M.A., Lie, D.C., Dellavalle, A., et al. (2012). Reprogramming of Pericyte-Derived Cells of the Adult Human Brain into Induced Neuronal Cells. Cell Stem Cell *11*, 471–476.

Kaslin, J., Kroehne, V., Benato, F., Argenton, F., and Brand, M. (2013). Development and specification of cerebellar stem and progenitor cells in zebrafish: from embryo to adult. Neural Develop. *8*, 9.

Kaslin, J., Kroehne, V., Ganz, J., Hans, S., and Brand, M. (2017). Distinct roles of neuroepithelial-like and radial glia-like progenitor cells in cerebellar regeneration. Development *144*, 1462–1471.

Katsetos, C.D., Frankfurter, A., Christakos, S., Mancall, E.L., Vlachos, I.N., and Urich, H. (1993). Differential localization of class III, beta-tubulin isotype and calbindin-D28k defines distinct neuronal types in the developing human cerebellar cortex. J. Neuropathol. Exp. Neurol. *52*, 655–666.

Katsuda, T., Tsuchiya, R., Kosaka, N., Yoshioka, Y., Takagaki, K., Oki, K., Takeshita, F., Sakai, Y., Kuroda, M., and Ochiya, T. (2013). Human adipose tissue-derived mesenchymal stem cells secrete functional neprilysin-bound exosomes. Sci. Rep. *3*, 1197.

Kazanis, I., and ffrench-Constant, C. (2011). Extracellular matrix and the neural stem cell niche. Dev. Neurobiol. *71*, 1006–1017.

Kee, N., Sivalingam, S., Boonstra, R., and Wojtowicz, J.M. (2002). The utility of Ki-67 and BrdU as proliferative markers of adult neurogenesis. J. Neurosci. Methods *115*, 97–105.

Kempermann, G., Gage, F.H., Aigner, L., Song, H., Curtis, M.A., Thuret, S., Kuhn, H.G., Jessberger, S., Frankland, P.W., Cameron, H.A., et al. (2018). Human Adult Neurogenesis: Evidence and Remaining Questions. Cell Stem Cell *23*, 25–30.

Kerjan, G., Dolan, J., Haumaitre, C., Schneider-Maunoury, S., Fujisawa, H., Mitchell, K.J., and Chédotal, A. (2005). The transmembrane semaphorin Sema6A controls cerebellar granule cell migration. Nat. Neurosci. *8*, 1516–1524.

Kim, M.S., Haney, M.J., Zhao, Y., Mahajan, V., Deygen, I., Klyachko, N.L., Inskoe, E., Piroyan, A., Sokolsky, M., Okolie, O., et al. (2016). Development of exosome-encapsulated paclitaxel to overcome MDR in cancer cells. Nanomedicine Nanotechnol. Biol. Med. *12*, 655–664.

Klajn, A., Drakulic, D., Tosic, M., Pavkovic, Z., Schwirtlich, M., and Stevanovic, M. (2014). SOX2 overexpression affects neural

differentiation of human pluripotent NT2/D1 cells. Biochem. Mosc. *79*, 1172–1182.

Klein, C., Butt, S.J.B., Machold, R.P., Johnson, J.E., and Fishell, G. (2005). Cerebellum- and forebrain-derived stem cells possess intrinsic regional character. Development *132*, 4497–4508.

Koirala, S., and Corfas, G. (2010). Identification of Novel Glial Genes by Single-Cell Transcriptional Profiling of Bergmann Glial Cells from Mouse Cerebellum. PLoS ONE *5*.

Kriegstein, A., and Alvarez-Buylla, A. (2009). The Glial Nature of Embryonic and Adult Neural Stem Cells. Annu. Rev. Neurosci. *32*, 149–184.

Kriegstein, A.R., Götz, M., (2003). Radial glia diversity: a matter of cell fate. Glia 43, 37–43.

Kubo, T., Yamaguchi, A., Iwata, N., and Yamashita, T. (2008). The therapeutic effects of Rho-ROCK inhibitors on CNS disorders. Ther. Clin. Risk Manag. *4*, 605–615.

Kuhn, H.G., Dickinson-Anson, H., and Gage, F.H. (1996). Neurogenesis in the dentate gyrus of the adult rat: age-related decrease of neuronal progenitor proliferation. J. Neurosci. Off. J. Soc. Neurosci. *16*, 2027–2033.

Kulikova, S., Abatis, M., Heng, C., and Lelievre, V. (2011). Interkinetic nuclear migration. Cell Adhes. Migr. *5*, 277–279.

Lai, A., Kinhal, V., Nuzhat, Z., Menon, R., Rice, G.E., and Salomon, C. (2018). Proteomics Method to Identification of Protein Profiles in Exosomes. Methods Mol. Biol. Clifton NJ *1710*, 139–153.

Lankford, K.L., Arroyo, E.J., Nazimek, K., Bryniarski, K., Askenase, P.W., and Kocsis, J.D. (2018). Intravenously delivered mesenchymal stem cell-derived exosomes target M2-type macrophages in the injured spinal cord. PLOS ONE *13*, e0190358.

Lee, A., Kessler, J.D., Read, T.-A., Kaiser, C., Corbeil, D., Huttner, W.B., Johnson, J.E., and Wechsler-Reya, R.J. (2005). Isolation of neural stem cells from the postnatal cerebellum. Nat. Neurosci. *8*, 723–729.

Leto, K., Carletti, B., Williams, I.M., Magrassi, L., and Rossi, F. (2006). Different Types of Cerebellar GABAergic Interneurons Originate from a Common Pool of Multipotent Progenitor Cells. J. Neurosci. *26*, 11682–11694.

Leto, K., Arancillo, M., Becker, E.B.E., Buffo, A., Chiang, C., Ding, B., Dobyns, W.B., Dusart, I., Haldipur, P., Hatten, M.E., et al. (2016). Consensus Paper: Cerebellar Development. The Cerebellum *15*, 789–828.

Li, B., Antonyak, M.A., Zhang, J., and Cerione, R.A. (2012). RhoA triggers a specific signaling pathway that generates transforming microvesicles in cancer cells. Oncogene *31*, 4740–4749.

Li, J., Imitola, J., Snyder, E.Y., and Sidman, R.L. (2006). Neural Stem Cells Rescue nervous Purkinje Neurons by Restoring Molecular Homeostasis of Tissue Plasminogen Activator and Downstream Targets. J. Neurosci. *26*, 7839–7848.

Lim, J., Hao, T., Shaw, C., Patel, A.J., Szabó, G., Rual, J.-F., Fisk, C.J., Li, N., Smolyar, A., Hill, D.E., et al. (2006). A Protein–Protein Interaction Network for Human Inherited Ataxias and Disorders of Purkinje Cell Degeneration. Cell *125*, 801–814.

Linares, R., Tan, S., Gounou, C., Arraud, N., and Brisson, A.R. (2015). High-speed centrifugation induces aggregation of extracellular vesicles. J. Extracell. Vesicles *4*, 29509.

Lingor, P., Teusch, N., Schwarz, K., Mueller, R., Mack, H., Bahr, M., and Mueller, B.K. (2007). Inhibition of Rho kinase (ROCK) increases neurite outgrowth on chondroitin sulphate proteoglycan in vitro and axonal regeneration in the adult optic nerve in vivo. J Neurochem *103*, 181–189.

Lippman, J.J., Lordkipanidze, T., Buell, M.E., Yoon, S.O., Dunaevsky, A., (2008). Morphogenesis and regulation of Bergmann glial processes during Purkinje cell dendritic spine ensheathment and synaptogenesis. Glia 56, 1463–1477.

Liu, D., Nikoo, M., Boran, G., Zhou, P., and Regenstein, J.M. (2015a). Collagen and gelatin. Annu. Rev. Food Sci. Technol. *6*, 527–557.

Liu, J., Gao, H., and Wang, X. (2015b). The role of the Rho/ROCK signaling pathway in inhibiting axonal regeneration in the central nervous system. Neural Regen. Res. *10*, 1892–1896.

Liu, L., Geisert, E.E., Frankfurter, A., Spano, A.J., Jiang, C.X., Yue, J., Dragatsis, I., and Goldowitz, D. (2007). A transgenic mouse class-III beta tubulin reporter using yellow fluorescent protein. Genes. N. Y. N 2000 *45*, 560–569.

Livak, K.J., Schmittgen, T.D., 2001. Analysis of relative gene expression data using real-time quantitative PCR and the 2-ΔΔCt Method. Methods *25*, 402–408.

Lodish, H., Berk, A., Zipursky, S.L., Matsudaira, P., Baltimore, D., and Darnell, J. (2000). Overview of Neuronal Outgrowth. Mol. Cell Biol. 4th Ed.

Lois, C., and Alvarez-Buylla, A. (1994). Long-distance neuronal migration in the adult mammalian brain. Science *264*, 1145–1148.

Lötvall, J., Hill, A.F., Hochberg, F., Buzás, E.I., Vizio, D.D., Gardiner, C., Gho, Y.S., Kurochkin, I.V., Mathivanan, S., Quesenberry, P., et al. (2014). Minimal experimental requirements for definition of extracellular vesicles and their functions: a position statement from the International Society for Extracellular Vesicles. J. Extracell. Vesicles *3*, 26913.

Maas, S.L.N., Vrij, J.D., and Broekman, M.L.D. (2014). Quantification and Size-profiling of Extracellular Vesicles Using Tunable Resistive Pulse Sensing. JoVE J. Vis. Exp. e51623–e51623.

Maas, S.L.N., Broekman, M.L.D., and de Vrij, J. (2017). Tunable Resistive Pulse Sensing for the Characterization of Extracellular Vesicles. In Exosomes and Microvesicles: Methods and Protocols, A.F. Hill, ed. (New York, NY: Springer New York), pp. 21–33.

MacDonald, L., Baldini, G., and Storrie, B. (2015). Does Super Resolution Fluorescence Microscopy Obsolete Previous Microscopic Approaches to Protein Co-localization? Methods Mol. Biol. Clifton NJ *1270*, 255–275.

Malatesta, P., Appolloni, I., and Calzolari, F. (2008). Radial glia and neural stem cells. Cell Tissue Res. *331*, 165–178.

Manto, M., Bower, J.M., Conforto, A.B., Delgado-García, J.M., da Guarda, S.N.F., Gerwig, M., Habas, C., Hagura, N., Ivry, R.B., Mariën, P., et al. (2012). Consensus paper: roles of the cerebellum in motor control--the diversity of ideas on cerebellar involvement in movement. Cerebellum Lond. Engl. *11*, 457–487.

Mao, F., Wu, Y., Tang, X., Kang, J., Zhang, B., Yan, Y., Qian, H., Zhang, X., and Xu, W. (2017). Exosomes Derived from Human Umbilical Cord Mesenchymal Stem Cells Relieve Inflammatory Bowel Disease in Mice. BioMed Res. Int. *2017*, 5356760.

Marcoux, G., Duchez, A.-C., Cloutier, N., Provost, P., Nigrovic, P.A., and Boilard, E. (2016). Revealing the diversity of extracellular vesicles using high-dimensional flow cytometry analyses. Sci. Rep. *6*, 35928.

Maric, D., and Barker, J.L. (2005). Fluorescence-based sorting of neural stem cells and progenitors. Curr. Protoc. Neurosci. *Chapter 3*, Unit 3.18.

Martins, T.S., Catita, J., Rosa, I.M., Silva, O.A.B. da C. e, and Henriques, A.G. (2018). Exosome isolation from distinct biofluids using precipitation and column-based approaches. PLOS ONE *13*, e0198820.

McKelvey, K.J., Powell, K.L., Ashton, A.W., Morris, J.M., and McCracken, S.A. (2015). Exosomes: Mechanisms of Uptake. J. Circ. Biomark. *4*.

Merkle, F.T., Tramontin, A.D., García-Verdugo, J.M., Alvarez-Buylla, A., (2004). Radial glia give rise to adult neural stem cells in the subventricular zone. PNAS 101, 17528–17532.

Michalczyk, K., Ziman, M., (2005). Nestin structure and predicted function in cellular cytoskeletal organisation. Histol. Histopathol. 20, 665–671.

Mignone, J.L., Kukekov, V., Chiang, A.-S., Steindler, D., and Enikolopov, G. (2004). Neural stem and progenitor cells in nestin-GFP transgenic mice. J. Comp. Neurol. *469*, 311–324.

Ming, G., and Song, H. (2005). Adult neurogenesis in the mammalian central nervous system. Annu. Rev. Neurosci. *28*, 223–250.

Ming, G., and Song, H. (2011). Adult Neurogenesis in the Mammalian Brain: Significant Answers and Significant Questions. Neuron *70*, 687–702.

Miron, V.E., Kuhlmann, T., and Antel, J.P. (2011). Cells of the oligodendroglial lineage, myelination, and remyelination. Biochim. Biophys. Acta BBA - Mol. Basis Dis. *1812*, 184–193.

Miyazaki, T., Yamasaki, M., Hashimoto, K., Kohda, K., Yuzaki, M., Shimamoto, K., Tanaka, K., Kano, M., and Watanabe, M. (2017). Glutamate transporter GLAST controls synaptic wrapping by Bergmann glia and ensures proper wiring of Purkinje cells. Proc. Natl. Acad. Sci. *114*, 7438–7443.

Momen-Heravi, F., Balaj, L., Alian, S., Tigges, J., Toxavidis, V., Ericsson, M., Distel, R.J., Ivanov, A.R., Skog, J., and Kuo, W.P. (2012). Alternative methods for characterization of extracellular vesicles. Front. Physiol. *3*, 354.

Morel, L., Regan, M., Higashimori, H., Ng, S.K., Esau, C., Vidensky, S., Rothstein, J., and Yang, Y. (2013). Neuronal Exosomal miRNA-dependent Translational Regulation of Astroglial Glutamate Transporter GLT1. J. Biol. Chem. *288*, 7105–7116.

Morton, M.C., Neckles, V.N., Seluzicki, C.M., Holmberg, J.C., and Feliciano, D.M. (2018). Neonatal Subventricular Zone Neural Stem Cells Release Extracellular Vesicles that Act as a Microglial Morphogen. Cell Rep. *23*, 78–89.

Muguruma, K., Nishiyama, A., Ono, Y., Miyawaki, H., Mizuhara, E., Hori, S., Kakizuka, A., Obata, K., Yanagawa, Y., Hirano, T., et al. (2010). Ontogeny-recapitulating generation and tissue integration of ES cell–derived Purkinje cells. Nat. Neurosci. *13*, 1171–1180.

Muguruma, K., Nishiyama, A., Kawakami, H., Hashimoto, K., and Sasai, Y. (2015). Self-Organization of Polarized Cerebellar Tissue in 3D Culture of Human Pluripotent Stem Cells. Cell Rep. *10*, 537–550.

Mullen, R.J., Eicher, E.M., and Sidman, R.L. (1976). Purkinje cell degeneration, a new neurological mutation in the mouse. Proc. Natl. Acad. Sci. U. S. A. *73*, 208–212.

Nakamura, H., Katahira, T., Matsunaga, E., and Sato, T. (2005). Isthmus organizer for midbrain and hindbrain development. Brain Res. Brain Res. Rev. *49*, 120–126.

Nakamura, Y., Miyaki, S., Ishitobi, H., Matsuyama, S., Nakasa, T., Kamei, N., Akimoto, T., Higashi, Y., and Ochi, M. (2015). Mesenchymal-stem-cell-derived exosomes accelerate skeletal muscle regeneration. FEBS Lett. *589*, 1257–1265.

Namba, T., Mochizuki, H., Onodera, M., Mizuno, Y., Namiki, H., and Seki, T. (2005). The fate of neural progenitor cells expressing astrocytic and radial glial markers in the postnatal rat dentate gyrus. Eur. J. Neurosci. *22*, 1928–1941.

Neymeyer, V., Tephly, T.R., and Miller, M.W. (1997). Folate and 10-formyltetrahydrofolate dehydrogenase (FDH) expression in the central nervous system of the mature rat. Brain Res. *766*, 195–204.

van Niel, G., D'Angelo, G., and Raposo, G. (2018). Shedding light on the cell biology of extracellular vesicles. Nat. Rev. Mol. Cell Biol. *19*, 213–228.

Niu, W., Zang, T., Smith, D.K., Vue, T.Y., Zou, Y., Bachoo, R., Johnson, J.E., and Zhang, C.-L. (2015). SOX2 Reprograms Resident Astrocytes into Neural Progenitors in the Adult Brain. Stem Cell Rep. *4*, 780–794.

Nizamudeen, Z., Markus, R., Lodge, R., Parmenter, C., Platt, M., Chakrabarti, L., and Sottile, V. (2018a). Rapid and accurate analysis of stem cell-derived extracellular vesicles with super resolution microscopy and live imaging. Biochim. Biophys. Acta BBA - Mol. Cell Res. *1865*, 1891–1900.

Nizamudeen, Z.A., Chakrabarti, L., and Sottile, V. (2018b). Exposure to the ROCK inhibitor fasudil promotes gliogenesis of neural stem cells in vitro. Stem Cell Res. *28*, 75–86.

Obernier, K., Tong, C.K., and Alvarez-Buylla, A. (2014). Restricted nature of adult neural stem cells: re-evaluation of their potential for brain repair. Front. Neurosci. *8*.

Okamoto, H., Yoshio, T., Kaneko, H., and Yamanaka, H. (2010). Inhibition of NF-kappaB signaling by fasudil as a potential therapeutic strategy for rheumatoid arthritis. Arthritis Rheum *62*, 82–92.

Olesen, J., Gustavsson, A., Svensson, M., Wittchen, H.-U., Jönsson, B., CDBE2010 study group, and European Brain Council (2012). The economic cost of brain disorders in Europe. Eur. J. Neurol. *19*, 155–162.

Ostrowski, M., Carmo, N.B., Krumeich, S., Fanget, I., Raposo, G., Savina, A., Moita, C.F., Schauer, K., Hume, A.N., Freitas, R.P., et al. (2010). Rab27a and Rab27b control different steps of the exosome secretion pathway. Nat. Cell Biol. *12*, 19–30; sup pp 1-13.

Pekny, M., and Nilsson, M. (2005). Astrocyte activation and reactive gliosis. Glia *50*, 427–434.

Pellegrino, G., Trubert, C., Terrien, J., Pifferi, F., Leroy, D., Loyens, A., Migaud, M., Baroncini, M., Maurage, C.-A., Fontaine, C., et al. (2018). A comparative study of the neural stem cell niche in the adult hypothalamus of human, mouse, rat and gray mouse lemur (Microcebus murinus). J. Comp. Neurol. *526*, 1419–1443.

Perego, C., Vanoni, C., Bossi, M., Massari, S., Basudev, H., Longhi, R., and Pietrini, G. (2000). The GLT-1 and GLAST Glutamate Transporters Are Expressed on Morphologically Distinct Astrocytes and Regulated by Neuronal Activity in Primary Hippocampal Cocultures. J. Neurochem. *75*, 1076–1084.

Petreanu, L., and Alvarez-Buylla, A. (2002). Maturation and Death of Adult-Born Olfactory Bulb Granule Neurons: Role of Olfaction. J. Neurosci. *22*, 6106–6113.

Pevny, L.H., Sockanathan, S., Placzek, M., and Lovell-Badge, R. (1998). A role for SOX1 in neural determination. Dev. Camb. Engl. *125*, 1967–1978.

Pfisterer, U., and Khodosevich, K. (2017). Neuronal survival in the brain: neuron type-specific mechanisms. Cell Death Dis. *8*, e2643.

van der Pol, E., Coumans, F. a. W., Grootemaat, A.E., Gardiner, C., Sargent, I.L., Harrison, P., Sturk, A., van Leeuwen, T.G., and Nieuwland, R. (2014). Particle size distribution of exosomes and microvesicles determined by transmission electron microscopy, flow cytometry, nanoparticle tracking analysis, and resistive pulse sensing. J. Thromb. Haemost. JTH *12*, 1182–1192.

Prada, I., Gabrielli, M., Turola, E., Iorio, A., D'Arrigo, G., Parolisi, R., De Luca, M., Pacifici, M., Bastoni, M., Lombardi, M., et al. (2018). Glia-to-neuron transfer of miRNAs via extracellular vesicles: a new mechanism underlying inflammation-induced synaptic alterations. Acta Neuropathol. (Berl.) *135*, 529–550.

Purves, D., Augustine, G.J., Fitzpatrick, D., Katz, L.C., LaMantia, A.-S., McNamara, J.O., and Williams, S.M. (2001). Circuits within the Cerebellum. Neurosci. 2nd Ed.

Raponi, E., Agenes, F., Delphin, C., Assard, N., Baudier, J., Legraverend, C., and Deloulme, J.-C. (2007). S100B expression defines a state in which GFAP-expressing cells lose their neural stem cell potential and acquire a more mature developmental stage. Glia *55*, 165–177.

Reeber, S.L., Arancillo, M., and Sillitoe, R.V. (2018). Bergmann Glia are Patterned into Topographic Molecular Zones in the Developing and Adult Mouse Cerebellum. Cerebellum Lond. Engl. *17*, 392–403.

Reichenbach, A., Siegel, A., Rickmann, M., Wolff, J.R., Noone, D., and Robinson, S.R. (1995). Distribution of Bergmann glial somata and processes: implications for function. J. Hirnforsch. *36*, 509–517.

Rikitake, Y., Kim, H.-H., Huang, Z., Seto, M., Yano, K., Asano, T., Moskowitz, M.A., and Liao, J.K. (2005). Inhibition of Rho kinase (ROCK) leads to increased cerebral blood flow and stroke protection. Stroke *36*, 2251–2257.

Robins, S.C., Stewart, I., McNay, D.E., Taylor, V., Giachino, C., Goetz, M., Ninkovic, J., Briancon, N., Maratos-Flier, E., Flier, J.S., et al. (2013). alpha-Tanycytes of the adult hypothalamic third ventricle include distinct populations of FGF-responsive neural progenitors. Nat Commun *4*, 2049.

Robinson, A.P., Rodgers, J.M., Goings, G.E., and Miller, S.D. (2014). Characterization of Oligodendroglial Populations in Mouse Demyelinating Disease Using Flow Cytometry: Clues for MS Pathogenesis. PLoS ONE *9*.

Roloff, F., Scheiblich, H., Dewitz, C., Dempewolf, S., Stern, M., and Bicker, G. (2015). Enhanced neurite outgrowth of human model (NT2) neurons by small-molecule inhibitors of Rho/ROCK signaling. PLOS ONE *10*, e0118536.

Rüb, U., Hoche, F., Brunt, E.R., Heinsen, H., Seidel, K., Del Turco, D., Paulson, H.L., Bohl, J., von Gall, C., Vonsattel, J.-P., et al. (2013). Degeneration of the cerebellum in Huntington's disease (HD): possible relevance for the clinical picture and potential gateway to pathological mechanisms of the disease process. Brain Pathol. Zurich Switz. *23*, 165–177.

Ruiz i Altaba, A., Palma, V., and Dahmane, N. (2002). Hedgehog–GLI signaling and the growth of the brain. Nat. Rev. Neurosci. *3*, 24–33.

Rust, M.J., Bates, M., and Zhuang, X. (2006). Sub-diffraction-limit imaging by stochastic optical reconstruction microscopy (STORM). Nat. Methods *3*, 793–796.

Ryder, E.F., Snyder, E.Y., and Cepko, C.L. (1990). Establishment and characterization of multipotent neural cell lines using retrovirus vector-mediated oncogene transfer. J. Neurobiol. *21*, 356–375.

Ryu, J.R., Hong, C.J., Kim, J.Y., Kim, E.-K., Sun, W., and Yu, S.-W. (2016). Control of adult neurogenesis by programmed cell death in the mammalian brain. Mol. Brain *9*.

Sabelström, H., Stenudd, M., and Frisén, J. (2014). Neural stem cells in the adult spinal cord. Exp. Neurol. *260*, 44–49.

Saha, K., Keung, A.J., Irwin, E.F., Li, Y., Little, L., Schaffer, D.V., and Healy, K.E. (2008). Substrate Modulus Directs Neural Stem Cell Behavior. Biophys. J. *95*, 4426–4438.

Salih, S. (2016). Investigating the existence of neural stem cells in the adult mouse cerebellum and third ventricle. Thesis (PhD), University of Nottingham.

Sanai, N., Nguyen, T., Ihrie, R.A., Mirzadeh, Z., Tsai, H.-H., Wong, M., Gupta, N., Berger, M.S., Huang, E., Garcia-Verdugo, J.-M., et al. (2011). Corridors of migrating neurons in the human brain and their decline during infancy. Nature *478*, 382–386.

Sato, T., Asamitsu, K., Yang, J.P., Takahashi, N., Tetsuka, T., Yoneyama, A., Kanagawa, A., and Okamoto, T. (1998). Inhibition of human immunodeficiency virus type 1 replication by a bioavailable serine/threonine kinase inhibitor, fasudil hydrochloride. AIDS Res Hum Retroviruses *14*, 293–298.

Scott, J.D. (1991). Cyclic nucleotide-dependent protein kinases. Pharmacol Ther *50*, 123–145.

Segura, E., Amigorena, S., and Théry, C. (2005). Mature dendritic cells secrete exosomes with strong ability to induce antigen-specific effector immune responses. Blood Cells. Mol. Dis. *35*, 89–93.

Seri, B., García-Verdugo, J.M., Collado-Morente, L., McEwen, B.S., and Alvarez-Buylla, A. (2004). Cell types, lineage, and architecture of the germinal zone in the adult dentate gyrus. J. Comp. Neurol. *478*, 359–378.

Seto, Y., Nakatani, T., Masuyama, N., Taya, S., Kumai, M., Minaki, Y., Hamaguchi, A., Inoue, Y.U., Inoue, T., Miyashita, S., et al. (2014). Temporal identity transition from Purkinje cell progenitors to GABAergic interneuron progenitors in the cerebellum. Nat. Commun. *5*, 3337.

Sharma, S., Rasool, H.I., Palanisamy, V., Mathisen, C., Schmidt, M., Wong, D.T., and Gimzewski, J.K. (2010). Structural-Mechanical Characterization of Nanoparticle Exosomes in Human Saliva, Using Correlative AFM, FESEM, and Force Spectroscopy. ACS Nano *4*, 1921–1926.

Sharma, S., Gillespie, B.M., Palanisamy, V., and Gimzewski, J.K. (2011). Quantitative Nanostructural and Single-Molecule Force Spectroscopy Biomolecular Analysis of Human-Saliva-Derived Exosomes. Langmuir *27*, 14394–14400.

Shim, S.-H., Xia, C., Zhong, G., Babcock, H.P., Vaughan, J.C., Huang, B., Wang, X., Xu, C., Bi, G.-Q., and Zhuang, X. (2012). Super-resolution fluorescence imaging of organelles in live cells with photoswitchable membrane probes. Proc. Natl. Acad. Sci. *109*, 13978–13983.

Shimada, I.S., LeComte, M.D., Granger, J.C., Quinlan, N.J., and Spees, J.L. (2012). Self-renewal and differentiation of reactive astrocyte-derived neural stem/progenitor cells isolated from the cortical peri-infarct area after stroke. J. Neurosci. Off. J. Soc. Neurosci. *32*, 7926–7940.

Sillitoe, R.V., Gopal, N., and Joyner, A.L. (2009). Embryonic origins of ZebrinII parasagittal stripes and establishment of topographic Purkinje cell projections. Neuroscience *162*, 574–588.

Sitar, S., Kejžar, A., Pahovnik, D., Kogej, K., Tušek-Žnidarič, M., Lenassi, M., and Žagar, E. (2015). Size Characterization and Quantification of Exosomes by Asymmetrical-Flow Field-Flow Fractionation. Anal. Chem. *87*, 9225–9233.

Snyder, E.Y., Deitcher, D.L., Walsh, C., Arnold-Aldea, S., Hartwieg, E.A., and Cepko, C.L. (1992). Multipotent neural cell lines can engraft and participate in development of mouse cerebellum. Cell *68*, 33–51.

Sorrells, S.F., Paredes, M.F., Cebrian-Silla, A., Sandoval, K., Qi, D., Kelley, K.W., James, D., Mayer, S., Chang, J., Auguste, K.I., et al. (2018). Human hippocampal neurogenesis drops sharply in children to undetectable levels in adults. Nature *555*, 377–381.

Sotelo, C., Alvarado-Mallart, R.M., Frain, M., and Vernet, M. (1994). Molecular plasticity of adult Bergmann fibers is associated with radial migration of grafted Purkinje cells. J Neurosci *14*, 124–133.

Sottile, V., Li, M., and Scotting, P.J. (2006). Stem cell marker expression in the Bergmann glia population of the adult mouse brain. Brain Res *1099*, 8–17.

Spear, P.C., and Erickson, C.A. (2012a). Interkinetic nuclear migration: a mysterious process in search of a function. Dev. Growth Differ. *54*, 306–316.

Spear, P.C., and Erickson, C.A. (2012b). Apical movement during interkinetic nuclear migration is a two-step process. Dev. Biol. *370*, 33–41.

Stone, M.B., Shelby, S.A., and Veatch, S.L. (2017). Super-Resolution Microscopy: Shedding Light on the Cellular Plasma Membrane. Chem. Rev. *117*, 7457–7477.

Su, J. (2015). Label-Free Single Exosome Detection Using Frequency-Locked Microtoroid Optical Resonators. ACS Photonics *2*, 1241–1245.

Su, X., Guan, W., Yu, Y.-C., and Fu, Y. (2014). Cerebellar stem cells do not produce neurons and astrocytes in adult mouse. Biochem. Biophys. Res. Commun. *450*, 378–383.

Sunabori, T., Tokunaga, A., Nagai, T., Sawamoto, K., Okabe, M., Miyawaki, A., Matsuzaki, Y., Miyata, T., and Okano, H. (2008). Cell-

cycle-specific nestin expression coordinates with morphological changes in embryonic cortical neural progenitors. J. Cell Sci. *121*, 1204–1212.

Suslov, O.N., Kukekov, V.G., Ignatova, T.N., and Steindler, D.A. (2002). Neural stem cell heterogeneity demonstrated by molecular phenotyping of clonal neurospheres. Proc. Natl. Acad. Sci. U. S. A. *99*, 14506–14511.

Sutherland, M.L., Delaney, T.A., and Noebels, J.L. (1996). Glutamate transporter mRNA expression in proliferative zones of the developing and adult murine CNS. J. Neurosci. *16*, 2191–2207.

Szatanek, R., Baj-Krzyworzeka, M., Zimoch, J., Lekka, M., Siedlar, M., and Baran, J. (2017). The Methods of Choice for Extracellular Vesicles (EVs) Characterization. Int. J. Mol. Sci. *18*.

Takata, M., Tanaka, H., Kimura, M., Nagahara, Y., Tanaka, K., Kawasaki, K., Seto, M., Tsuruma, K., Shimazawa, M., and Hara, H. (2013). Fasudil, a rho kinase inhibitor, limits motor neuron loss in experimental models of amyotrophic lateral sclerosis. Br J Pharmacol *170*, 341–351.

Tam, J., and Merino, D. (2015). Stochastic optical reconstruction microscopy (STORM) in comparison with stimulated emission depletion (STED) and other imaging methods. J. Neurochem. *135*, 643–658.

Tamai, K., Tanaka, N., Nakano, T., Kakazu, E., Kondo, Y., Inoue, J., Shiina, M., Fukushima, K., Hoshino, T., Sano, K., et al. (2010). Exosome secretion of dendritic cells is regulated by Hrs, an ESCRT-0 protein. Biochem. Biophys. Res. Commun. *399*, 384–390.

Tamura, R., Uemoto, S., and Tabata, Y. (2016). Immunosuppressive effect of mesenchymal stem cell-derived exosomes on a concanavalin A-induced liver injury model. Inflamm. Regen. *36*, 26.

Tan, B.-T., Wang, L., Li, S., Long, Z.-Y., Wu, Y.-M., and Liu, Y. (2015). Retinoic acid induced the differentiation of neural stem cells from embryonic spinal cord into functional neurons in vitro. Int. J. Clin. Exp. Pathol. *8*, 8129–8135.

Tan, C.Y., Lai, R.C., Wong, W., Dan, Y.Y., Lim, S.-K., and Ho, H.K. (2014). Mesenchymal stem cell-derived exosomes promote hepatic regeneration in drug-induced liver injury models. Stem Cell Res. Ther. *5*, 76.

Tatenhorst, L., Eckermann, K., Dambeck, V., Fonseca-Ornelas, L., Walle, H., Lopes da Fonseca, T., Koch, J.C., Becker, S., Tonges, L., Bahr, M., et al. (2016). Fasudil attenuates aggregation of alpha-synuclein in models of Parkinson's disease. Acta Neuropathol Commun *4*, 39.

Théry, C., Amigorena, S., Raposo, G., and Clayton, A. (2006). Isolation and characterization of exosomes from cell culture supernatants and biological fluids. Curr. Protoc. Cell Biol. *Chapter 3*, Unit 3.22.

Tian, T., Zhu, Y.-L., Hu, F.-H., Wang, Y.-Y., Huang, N.-P., and Xiao, Z.-D. (2013). Dynamics of exosome internalization and trafficking. J. Cell. Physiol. *228*, 1487–1495.

Tian, T., Zhang, H.-X., He, C.-P., Fan, S., Zhu, Y.-L., Qi, C., Huang, N.-P., Xiao, Z.-D., Lu, Z.-H., Tannous, B.A., et al. (2018a). Surface functionalized exosomes as targeted drug delivery vehicles for cerebral ischemia therapy. Biomaterials *150*, 137–149.

Tian, Y., Ma, L., Gong, M., Su, G., Zhu, S., Zhang, W., Wang, S., Li, Z., Chen, C., Li, L., et al. (2018b). Protein Profiling and Sizing of Extracellular Vesicles from Colorectal Cancer Patients via Flow Cytometry. ACS Nano *12*, 671–680.

Tilson, S.G., Haley, E.M., Triantafillu, U.L., Dozier, D.A., Langford, C.P., Gillespie, G.Y., and Kim, Y. (2015). ROCK Inhibition Facilitates In Vitro Expansion of Glioblastoma Stem-Like Cells. PLOS ONE *10*, e0132823.

Tonges, L., Frank, T., Tatenhorst, L., Saal, K.A., Koch, J.C., Szego, E.M., Bahr, M., Weishaupt, J.H., and Lingor, P. (2012). Inhibition of rho kinase enhances survival of dopaminergic neurons and attenuates axonal loss in a mouse model of Parkinson's disease. Brain *135*, 3355–3370.

Tsien, J.Z. (2016). Cre-Lox Neurogenetics: 20 Years of Versatile Applications in Brain Research and Counting…. Front. Genet. *7*.

Tuoriniemi, J., Johnsson, A.-C.J.H., Holmberg, J.P., Gustafsson, S., Gallego-Urrea, J.A., Olsson, E., Pettersson, J.B.C., and Hassellöv, M. (2014). Intermethod comparison of the particle size distributions of colloidal silica nanoparticles. Sci. Technol. Adv. Mater. *15*, 035009.

Underwood, J.G., Boutz, P.L., Dougherty, J.D., Stoilov, P., Black, D.L., (2005). Homologues of the Caenorhabditis elegans Fox-1 Protein Are Neuronal Splicing Regulators in Mammals. Mol Cell Biol 25, 10005–10016.

Valadi, H., Ekström, K., Bossios, A., Sjöstrand, M., Lee, J.J., and Lötvall, J.O. (2007). Exosome-mediated transfer of mRNAs and microRNAs is a novel mechanism of genetic exchange between cells. Nat. Cell Biol. *9*, 654–659.

Venere, M., Han, Y.-G., Bell, R., Song, J.S., Alvarez-Buylla, A., and Blelloch, R. (2012). Sox1 marks an activated neural stem/progenitor cell in the hippocampus. Development *139*, 3938–3949.

Villarroya-Beltri, C., Baixauli, F., Gutiérrez-Vázquez, C., Sánchez-Madrid, F., and Mittelbrunn, M. (2014). Sorting it out: Regulation of exosome loading. Semin. Cancer Biol. *28*, 3–13.

Vogel, A., Upadhya, R., and Shetty, A.K. (2018). Neural stem cell derived extracellular vesicles: Attributes and prospects for treating neurodegenerative disorders. EBioMedicine *38*, 273–282.

Wang, F., Xu, Q., Wang, W., Takano, T., Nedergaard, M., (2012). Bergmann glia modulate cerebellar Purkinje cell bistability via Ca2+-dependent K+ uptake. PNAS 109, 7911–7916.

Wang, T., and Morgan, J.I. (2007). The Purkinje cell degeneration (pcd) mouse: An unexpected molecular link between neuronal degeneration and regeneration. Brain Res *1140*, 26–40.

Wang, Q., Yang, L., and Wang, Y. (2015a). Enhanced differentiation of neural stem cells to neurons and promotion of neurite outgrowth by oxygen–glucose deprivation. Int. J. Dev. Neurosci. *43*, 50–57.

Wang, S., Cesca, F., Loers, G., Schweizer, M., Buck, F., Benfenati, F., Schachner, M., and Kleene, R. (2011). Synapsin I Is an Oligomannose-Carrying Glycoprotein, Acts As an Oligomannose-Binding Lectin, and Promotes Neurite Outgrowth and Neuronal Survival When Released via Glia-Derived Exosomes. J. Neurosci. *31*, 7275–7290.

Wang, S., Wang, B., Pan, N., Fu, L., Wang, C., Song, G., An, J., Liu, Z., Zhu, W., Guan, Y., et al. (2015b). Differentiation of human induced pluripotent stem cells to mature functional Purkinje neurons. Sci. Rep. *5*, 9232.

Wang, W., Osenbroch, P., Skinnes, R., Esbensen, Y., Bjørås, M., and Eide, L. (2010). Mitochondrial DNA integrity is essential for mitochondrial maturation during differentiation of neural stem cells. Stem Cells Dayt. Ohio *28*, 2195–2204.

Wang, Y., Balaji, V., Kaniyappan, S., Krüger, L., Irsen, S., Tepper, K., Chandupatla, R., Maetzler, W., Schneider, A., Mandelkow, E., et al. (2017). The release and trans-synaptic transmission of Tau via exosomes. Mol. Neurodegener. *12*, 5.

Webb, R.L., Kaiser, E.E., Scoville, S.L., Thompson, T.A., Fatima, S., Pandya, C., Sriram, K., Swetenburg, R.L., Vaibhav, K., Arbab, A.S., et al. (2018). Human Neural Stem Cell Extracellular Vesicles Improve Tissue and Functional Recovery in the Murine Thromboembolic Stroke Model. Transl. Stroke Res. *9*, 530–539.

Webb Robin L., Kaiser Erin E., Jurgielewicz Brian J., Spellicy Samantha, Scoville Shelley L., Thompson Tyler A., Swetenburg Raymond L., Hess David C., West Franklin D., and Stice Steven L. (2018). Human Neural Stem Cell Extracellular Vesicles Improve Recovery in a Porcine Model of Ischemic Stroke. Stroke *49*, 1248–1256.

Wegel, E., Göhler, A., Lagerholm, B.C., Wainman, A., Uphoff, S., Kaufmann, R., and Dobbie, I.M. (2016). Imaging cellular structures in super-resolution with SIM, STED and Localisation Microscopy: A practical comparison. Sci. Rep. *6*, 27290.

White, J.J., and Sillitoe, R.V. (2013). Development of the cerebellum: from gene expression patterns to circuit maps. Wiley Interdiscip. Rev. Dev. Biol. *2*, 149–164.

Willms, E., Johansson, H.J., Mäger, I., Lee, Y., Blomberg, K.E.M., Sadik, M., Alaarg, A., Smith, C.E., Lehtiö, J., and Andaloussi, S.E. (2016). Cells release subpopulations of exosomes with distinct molecular and biological properties. Sci. Rep. *6*, 22519.

Willms, E., Cabañas, C., Mäger, I., Wood, M.J.A., and Vader, P. (2018). Extracellular Vesicle Heterogeneity: Subpopulations, Isolation Techniques, and Diverse Functions in Cancer Progression. Front. Immunol. *9*.

Winner, B., Cooper-Kuhn, C.M., Aigner, R., Winkler, J., and Kuhn, H.G. (2002). Long-term survival and cell death of newly generated neurons in the adult rat olfactory bulb. Eur. J. Neurosci. *16*, 1681–1689.

Wojcinski, A., Lawton, A.K., Bayin, N.S., Lao, Z., Stephen, D.N., and Joyner, A.L. (2017). Cerebellar granule cell replenishment postinjury by adaptive reprogramming of Nestin+ progenitors. Nat. Neurosci. *20*, 1361–1370.

Wood, H.B., and Episkopou, V. (1999). Comparative expression of the mouse Sox1, Sox2 and Sox3 genes from pre-gastrulation to early somite stages. Mech. Dev. *86*, 197–201.

Wu, T., and Hallett, M. (2013). The cerebellum in Parkinson's disease. Brain *136*, 696–709.

Wu, J., Qu, Z., Fei, Z.-W., Wu, J.-H., and Jiang, C.-P. (2017). Role of stem cell-derived exosomes in cancer. Oncol. Lett. *13*, 2855–2866.

Wu, Y., Deng, W., and Klinke, D.J. (2015). Exosomes: Improved methods to characterize their morphology, RNA content, and surface protein biomarkers. The Analyst *140*, 6631–6642.

Xu, B., Zhang, Y., Du, X.-F., Li, J., Zi, H.-X., Bu, J.-W., Yan, Y., Han, H., and Du, J.-L. (2017). Neurons secrete miR-132-containing exosomes to regulate brain vascular integrity. Cell Res *27*, 882–897.

Yagi, Y., Ohkubo, T., Kawaji, H., Machida, A., Miyata, H., Goda, S., Roy, S., Hayashizaki, Y., Suzuki, H., and Yokota, T. (2017). Next-generation sequencing-based small RNA profiling of cerebrospinal fluid exosomes. Neurosci. Lett. *636*, 48–57.

Yamada, K., and Watanabe, M. (2002). Cytodifferentiation of bergmann glia and its relationship with purkinje cells. Anat. Sci. Int. *77*, 94–108.

Yamashita, K., Kotani, Y., Nakajima, Y., Shimazawa, M., Yoshimura, S., Nakashima, S., Iwama, T., and Hara, H. (2007). Fasudil, a Rho kinase

(ROCK) inhibitor, protects against ischemic neuronal damage in vitro and in vivo by acting directly on neurons. Brain Res *1154*, 215–224.

Yang, H., Linden, S.B., Wang, J., Yu, J., Nelson, D.C., and Wei, H. (2015). A chimeolysin with extended-spectrum streptococcal host range found by an induced lysis-based rapid screening method. Sci. Rep. *5*, 17257.

Yang, H.K.C., Sundholm-Peters, N.L., Goings, G.E., Walker, A.S., Hyland, K., and Szele, F.G. (2004). Distribution of doublecortin expressing cells near the lateral ventricles in the adult mouse brain. J. Neurosci. Res. *76*, 282–295.

Ying, H., Biroc, S.L., Li, W.W., Alicke, B., Xuan, J.A., Pagila, R., Ohashi, Y., Okada, T., Kamata, Y., and Dinter, H. (2006). The Rho kinase inhibitor fasudil inhibits tumor progression in human and rat tumor models. Mol Cancer Ther *5*, 2158–2164.

Yoon, H., Walters, G., Paulsen, A.R., and Scarisbrick, I.A. (2017). Astrocyte heterogeneity across the brain and spinal cord occurs developmentally, in adulthood and in response to demyelination. PLoS ONE *12*.

Yoshioka, Y., Konishi, Y., Kosaka, N., Katsuda, T., Kato, T., and Ochiya, T. (2013). Comparative marker analysis of extracellular vesicles in different human cancer types. J. Extracell. Vesicles *2*, 20424.

Yuana, Y., Koning, R.I., Kuil, M.E., Rensen, P.C.N., Koster, A.J., Bertina, R.M., and Osanto, S. (2013). Cryo-electron microscopy of extracellular vesicles in fresh plasma. J. Extracell. Vesicles *2*, 21494.

Yuasa, S. (1996). Bergmann glial development in the mouse cerebellum as revealed by tenascin expression. Anat. Embryol. (Berl.) *194*, 223–234.

Zabeo, D., Cvjetkovic, A., Lässer, C., Schorb, M., Lötvall, J., and Höög, J.L. (2017). Exosomes purified from a single cell type have diverse morphology. J. Extracell. Vesicles *6*, 1329476.

Zaim, M., and Isik, S. (2018). DNA topoisomerase IIβ stimulates neurite outgrowth in neural differentiated human mesenchymal stem cells through regulation of Rho-GTPases (RhoA/Rock2 pathway) and Nurr1 expression. Stem Cell Res. Ther. *9*, 114.

Zhang, J., and Jiao, J. (2015). Molecular Biomarkers for Embryonic and Adult Neural Stem Cell and Neurogenesis. BioMed Res. Int. *2015*.

Zhang, B., Yin, Y., Lai, R.C., and Lim, S.K. (2014). Immunotherapeutic potential of extracellular vesicles. Front. Immunol. *5*.

Zhang, Y., Liu, J., Yao, S., Li, F., Xin, L., Lai, M., Bracchi-Ricard, V., Xu, H., Yen, W., Meng, W., et al. (2012). Nuclear factor kappa B signaling

initiates early differentiation of neural stem cells. Stem Cells *30*, 510–524.

Zhang, Y., Kim, M.S., Jia, B., Yan, J., Zuniga-Hertz, J.P., Han, C., and Cai, D. (2017). Hypothalamic stem cells control ageing speed partly through exosomal miRNAs. Nature *548*, 52–57.

Zhao, S., Nichols, J., Smith, A.G., and Li, M. (2004). SoxB transcription factors specify neuroectodermal lineage choice in ES cells. Mol. Cell. Neurosci. *27*, 332–342.

Zhou, Z.-D., Kumari, U., Xiao, Z.-C., and Tan, E.-K. (2010). Notch as a molecular switch in neural stem cells. IUBMB Life *62*, 618–623.

van der Zwaag, D., Vanparijs, N., Wijnands, S., De Rycke, R., De Geest, B.G., and Albertazzi, L. (2016). Super Resolution Imaging of Nanoparticles Cellular Uptake and Trafficking. ACS Appl. Mater. Interfaces *8*, 6391–6399.

10. Appendix document

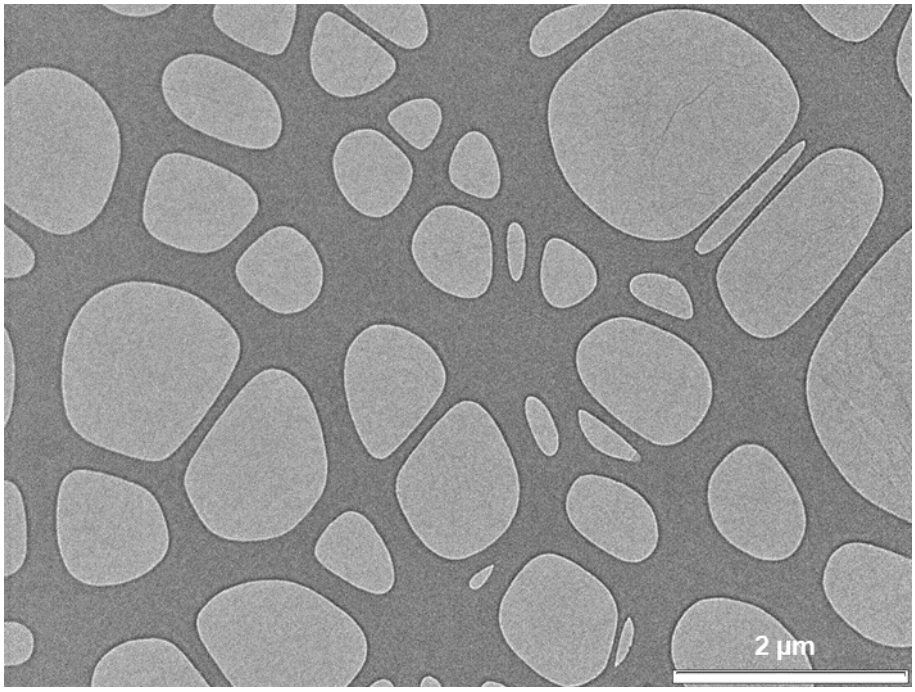


Figure 10.1: TEM of EV negative control grid. Grids were processed with fixation and negative staining as mentioned in methods but without addition of EV sample.

Table 10.1: Details of antibodies used for immunostaining experiments

Antibody	Specificity	Host	Dilution	Catalogue	Company
Nestin	anti-mouse	Mouse	1:50	Rat401	Dako
Sox2	anti-mouse	Rabbit	1:500	AB5603	EMD Millipore
βIII-Tubulin	anti-mouse	Rabbit	1:1000	Ab18207	Abcam
GFAP	anti-mouse	Mouse	1:250	MA515086	Invitrogen
DCX	anti-mouse	Rabbit	1:500	4604S	Cell Signalling
NeuN	anti-mouse	Mouse	1:500	MAB377	EMD Millipore
Calbindin	anti-mouse	Mouse	1:500	C9848	Sigma
L7	anti-mouse	Mouse	1:500	Sc137064	Santa cruz
GFP	anti-GFP	Goat	1:250	GTX26662	GeneTex
HRP	Anti-goat	goat	1:200	Not provided by SS	Sigma
HRP	Anti-mouse	mouse	1:200	Not provided by SS	Sigma
Alexa fluor-647	anti-rabbit	Goat	1:500	A21244	Life technologies
Alexa fluor -594	anti-rabbit	Goat	1:20	R37117	Life technologies
Alexa fluor -594	anti-mouse	Goat	1:500	A11032	Life technologies

Alexa fluor - 488	anti-rabbit	Goat	1:500	A11008	Life technologies
Alexa fluor - 488	anti-mouse	Goat	1:500	A11001	Life technologies

Table 10.2: List of primers used in RT-PCR

Primer	Forward	Reverse
Clathrin6 K	GACAGTGCCATCATGAATCC	TTTGTGCTTCTGGAGGAAAGAA
Nestin	AGAGTCAGATCGCTCAGATCC	GCAGAGTCCTGTATGTAGCCAC
Sox2	GGCGGCAACCAGAAGAACAG	GCTTGGCCTCGTCGATGAAC
GFAP	CTCAATGCTGGCTTCAAGGAG	GGATCTCCTCCTCCAGCGA
βIII-tub	GGCCTCCTCTCACAAGTATGT	CAGGGAATCGAAGGGAGGTG

Table 10.3: Primers used for qPCR

Primer	Forward	Reverse
Clathrin6 K	AGATTCTGCCCATTCGCTTTC	TCAGTGCAATCACTTTGCTGG
Nestin	AGAGTCAGATCGCTCAGATC	GCAGAGTCCTGTATGTAGCCAC
Sox2	GGCGGCAACCAGAAGAACAG	GCTTGGCCTCGTCGATGAAC
GFAP	GAGGAGTGGTATCGGTCTAAGTTTG	GCCGCTCTAGGGACTCGTT
βIII-tub	GCGCCTTTGGACACCTATTCA	GCCCTCCGTATAGTGCCCT

Table 10.4: Details of antibodies used for immunoblotting experiments.

Antibody	Specificity	host	Dilution	Catalogue	Company
CD63	anti-mouse	Mouse	1:50	Sc5275	Santa cruz
Tsg101	anti-mouse	Mouse	1:50	Sc7694	Santa cruz
GM130	anti-mouse	Mouse	1:50	Sc55590	A Santa cruz
HRP-conjugate	anti-mouse	Horse	1:1000	PI2000	Vector Labs

1. Macro 1

```
/*
 * This Macro
 *
 *
 *      Rewritten for v 1.5d
 *
 *      measures the size of the exosomes.
 *      exports the results in a txt file
 *      exports the generated outline image of the objects (exosomes)
 *      saves the Summary into a text file
 *      the first line in the result file is showing the total area of the image.
 *      (note: the objects touching the edge of the image are excluded)
 *
 *      If published -Please
 *      Quote : "The nuclei measurments were done with a custom written macro in Fiji."
 *      Acknowledgements: "We thank for Robert Markus and Ricardo Figueroa for witing the automated measurement macro."
 */


//setBatchMode(true);
```

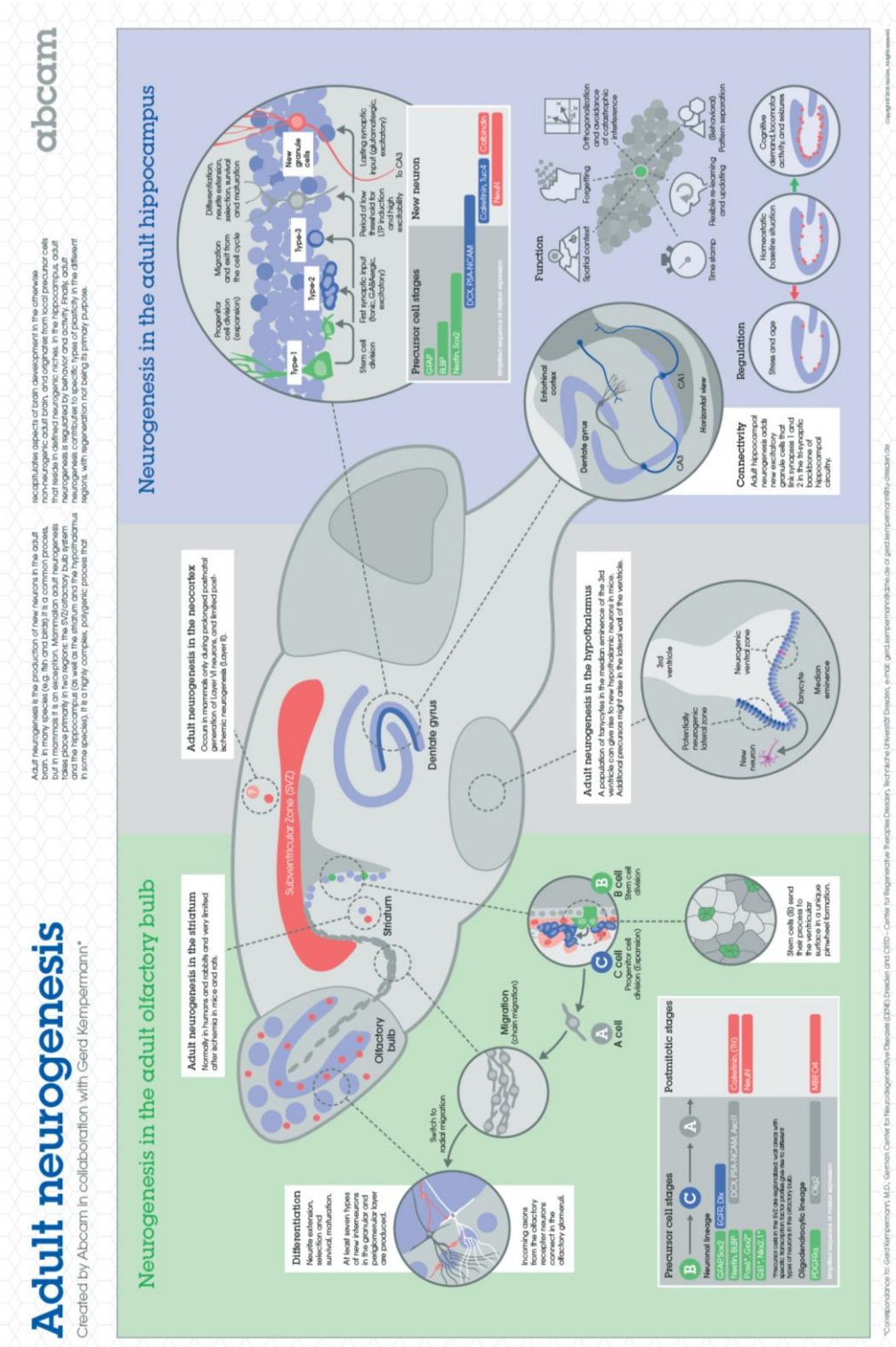
```
22. run("Clear Results");
23. //roiManager("Delete");
24.
25. title=getTitle();
26. ImageID = getImageID();
27. //run("8-bit");
28. delimiters =".";
29. stringResult = split(title, delimiters);
30. title2=stringResult[0];
31.     selectImage(ImageID);
32.     run("Measure");
33.     s=nSlices();
34.     run("Duplicate...", "title="+title2+"_mask duplicate range=1-
    "+s+"");
35.     //run("8-bit");
36.     run("Gaussian Blur...", "sigma=3");
37.     run("Unsharp Mask...", "radius=3 mask=0.9");
38.     run("Set Scale...", "distance=1 known=5 pixel=1 unit=nm global");
39.     run("Auto Threshold", "method=Default white");
40.    run("Invert");
41.
42.     //run("Set Measurements...", "area shape stack decimal=2");
43.
44.     //roiManager("Delete");
45.
```

```
46.  run("Set Measurements...", "area mean min perimeter shape
     redirect=None decimal=2");
47.  run("Analyze Particles...", "  show=Outlines display exclude clear
     summarize add");
48.
49.  saveAs("Tiff",File.directory()+title2+"mask");
50.
51. saveAs("Results",File.directory()+title2+"Results");
52.
53. //This section shows it in a log woindow and saves the results in a
     summary file
54.
55. selectWindow("Results");
56. a=0;
57. n=nResults;
58. n=n-1;
59. a = getResult("Area", 0);
60. print("Total area: ",a);
61. print("Number of Exosomes: ",n);
62. selectWindow("Log");
63. saveAs("Results",File.directory()+title2+"Summary");
64.
65. showStatus ("Done");
66.
67.
```

```
68.
69. //setBatchMode(false);
70.
```

Appendix PDF file 1:

Available from https://www.abcam.com/neuroscience/adult-neurogenesis-poster



Appendix excel file 1

Excel template used to perform qPCR analysis: https://bitesizebio.com/24894/4-easy-steps-to-analyze-your-qpcr-data-using-double-delta-ct-analysis/

Appendix video file:

https://www.sciencedirect.com/science/article/pii/S0167488918304129#ec0005

Appendix video file 2:

https://www.sciencedirect.com/science/article/pii/S187350611830045X?via%3Dihub#ec0010

Appendix video file 3:

https://www.sciencedirect.com/science/article/pii/S187350611830045X#ec0015

Appendix video file 4:

https://www.sciencedirect.com/science/article/pii/S187350611830045X#ec0020

Appendix video file 5:

https://www.sciencedirect.com/science/article/pii/S0167488918304129#ec0010